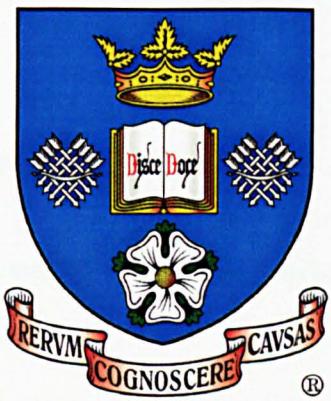

Identification of Nonlinear Processes in Space Plasma Turbulence

Ian Bates

A thesis submitted for the degree of Doctor of Philosophy in the

Department of Automatic Control and Systems Engineering,

University of Sheffield,

U.K.

September, 2002

Acknowledgements

I would like to thank, in no particular order,

- All members of the Space Systems Group for their help over the past period, particular thanks to Hugo, Misha and Simon,
- Almost a sister group the Applied Maths Department should not go unmentioned, in particular Chris (and friends) for providing me with squash fodder,
- My family, in particular my parents and my brother for helping me in ways only family can including, but not exclusively, driving me up the wall, but for sure always being there,
- My friends for just being around, what more can I say,
- And finally Paul and Michela should not go unmentioned, least of all for the part they played in bringing Joanna and myself together.

Bringing me nicely to my dedication,

For Joanna.

Abstract

Frequency domain analysis tools have been developed to analyse simultaneous multi-point measurements of developed space plasma turbulence.

The Coherence Length technique enables the scale length for plasma wave structures to be measured from magnetic field measurements. The coherence length defines a length scale for the measurement of wave phenomena. Single satellite measurements can be used, the technique becoming more reliable with higher numbers of satellites.

The technique is used to identify coherence lengths for waves observed in the magnetic field near the bow shock by the dual *AMPTE-UKS/AMPTE-IRM* satellites, and for mirror wave structures observed in the magnetic field in the magnetosheath by the dual *ISEE-1/ISEE-2* satellites.

The Transfer Function Estimation technique enables the transfer of energy between plasma waves to be measured, from simultaneous dual-point measurements, resulting in linear growth / damping rates and second-order wave coupling. The technique is improved by replacing the Least Squares method for inversion with Regularisation.

The technique is applied to simultaneous magnetic field measurements near the bow shock by the *AMPTE-UKS/AMPTE-IRM* satellites, where a linear instability in the wave field is identified, which is attributed to an ion anisotropy instability, and accompanying sequence of second-order three-wave coupling processes is also identified, which dissipates the energy from the linear instability.

The Wave vector Determination technique enables the identification of wave vectors from simultaneous four-point measurements. The availability of four-point measurements means that the reliance on Minimum Variance Analysis, and that of only being able to use magnetic field measurements, is removed, the wave vector can be determined unambiguously directly from the magnetic field measurements. The technique can identify between waves of different frequency, and waves at the same frequency but propagating in different directions.

The technique is applied to simultaneous observations of the electric field by the four-point

Cluster II satellites, enabling the determination of the wave vector and the identification of a mirror mode structure, solely from the electric field measurements.

Chapter 1 introduces the solar-terrestrial environment, briefly describing exploration of this environment by man-made satellites and listing some aims of the analysis of data collected by the satellites. Chapter 2 elaborates on what is meant by data analysis; Spectral Transforms are introduced and described, with a comparison made between Fourier Transforms and Wavelet Transforms, before a review is made of current data analysis techniques for satellite data. Chapter 3 defines and focuses attention on the objectives of this thesis, which are addressed in the following three chapters. Chapter 4 investigates the coherence length of plasma waves through use of the Wavelet Transform and the Fourier Shift Theorem. Chapter 5 makes estimates of wave Transfer Functions, replacing an established Least Squares inversion technique with a Regularisation inversion. Chapter 6 uses a method to determine wave propagation directions, from multi-satellite data, that has not been applied before due to the lack of availability of suitable data sets. Chapter 7 summarises the preceding chapters. The Appendices contain reprints of papers resulting from, and relating to, this research.

Executive Summary

Aims

This thesis explores possible ways to extract information available from multi-spacecraft missions by developing analysis techniques to exploit the information contained in multi-satellite datasets to further the physical understanding of the nature of the near-Earth environment.

Objectives

The following techniques have been identified for development,

- Use of multi-spacecraft data to gain coherence lengths, or scale sizes, of wave phenomena in space plasma,
- Use of multi-spacecraft data to understand energy transfer processes between waves,
- Use of multi-spacecraft data to extract wave frequency and propagation characteristics.

Achievements

The objectives have been attained,

- A technique for determining the coherence length of plasma waves from single, dual or multi-satellite data has been found and developed,
- A Transfer Function Estimation technique has been developed for plasmas containing dispersive waves, with the addition of an improved inversion technique,

- A wave vector propagation determination technique has been developed, by extending a method available for dual satellites, and found to be successful.

Publications

This research has resulted in publications,

Refereed

D. McCaffrey, I. Bates, M. A. Balikhin, H. St. C. K. Alleyne, M. Dunlop, and W. Baumjohann, Experimental method for the identification of dispersive three-wave coupling in space plasma, *Advances in Space Research*, 25(7/8):1571–1577, 1999

M. A. Balikhin, I. Bates, S. Walker, Identification of Linear and Nonlinear Processes in Space Plasma Turbulence data, *Advances in Space Research*, 2001

Conference Proceedings

I. Bates, M. A. Balikhin, H. St. C. K. Alleyne, and M. Andre, Minimum-variance free determination of magnetosheath wave propagation vectors, In *SP-492 Multipoint Measurements versus Theory*. ESA, 2001

I. Bates and M. A. Balikhin, Coherence lengths of low frequency turbulence at the bow shock and in the magnetosheath, In *SP-449 Multiscale/Multipoint Plasma Measurements*. ESA, 2000

Contents

List of Figures

Chapter 1

Motivation

1.1 The Solar-terrestrial Environment

An understanding of the global near-earth environment is needed to appreciate the interplay between the variety of processes that transport energy around the system. This section will describe briefly the main regions, and some main processes for coupling and energy transfer.

1.1.1 The Sun and Solar Wind

The Sun is the source of energy in our solar system. It rotates and radiates energy. The solar corona is a hot, tenuous fully ionised plasma. In the solar corona there are dissipation of currents, flares and eruptions. Then there is the solar wind, a thermal expansion of the hot solar corona into the cool interplanetary space. Interwoven between the plasma particles (mainly protons and electrons) there is the Interplanetary Magnetic Field (IMF). The coronal expansion is not isotropic. There are fast (not much more than 900 km/s) and slow (around 300 km/s) solar wind flows. Rotation of the Sun causes the magnetic field lines to become twisted and form what is called the Parker Spiral (Figure 1.1). Near Earth, the field lines are roughly 45 degrees in the ecliptic.

Near Earth the solar wind flow is supersonic, that is has a velocity greater than the fast MHD

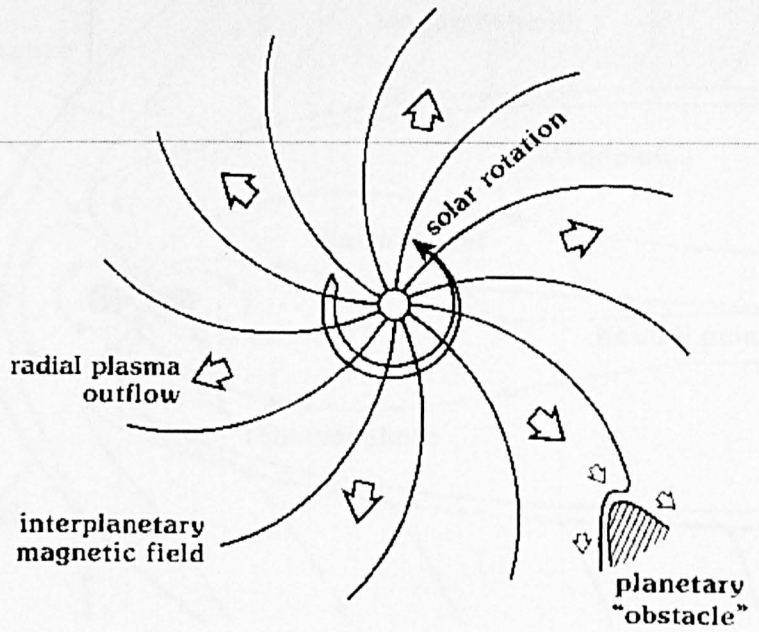

Figure 1.1: The Interplanetary Magnetic Field (IMF).

wave velocity (the Mach number being roughly 1.5-10) . The flow is radial, however the magnetic field is twisted to roughly 45 degrees in the ecliptic plane. The Earth and it's magnetic bubble of terrestrial plasma presents an obstacle to the solar wind flow; the IMF is "frozen-inside" the solar plasma and a consequence of the so-called "frozen-in" theorem is that different magnetised plasmas do not mix. Structure is formed, namely the Earth's Magnetosphere (Figure 1.2). This structure consists of a sequence of collisionless boundary layers which govern energy transport in the system.

1.1.2 The Earth's Magnetosphere

The Bow Shock (BS) is formed by the interaction and subsequent deceleration of the supersonic solar wind flow and Earth. Upstream from the BS flow is supersonic, downstream it is sub-sonic. The BS stands roughly 15 Earth radii upstream from the Earth. The BS boundary forms a roughly parabolic surface.

The physical nature of this shock region can be classified by three parameters, plasma beta (β), Magnetosonic Mach number and θ_{B_n}. The plasma beta is the ratio between thermal and magnetic pressure and is indicative of the level of turbulence expected near the shock. The BS is classified

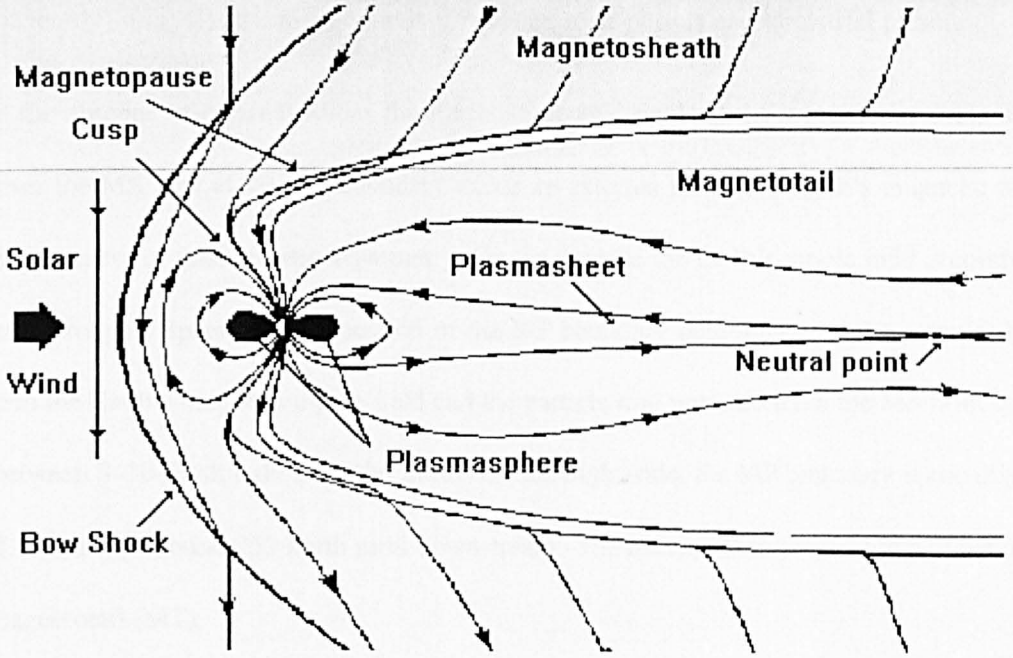

Figure 1.2: The Magnetosphere.

as supercritical (subcritical) when the magnetosonic Mach number is greater (less) than the First Critical Mach number, i.e. the Mach number at which the downstream flow speed parallel to the shock normal equals the downstream sound speed [Newbury and Russell, 1996]. The angle the IMF makes with the normal to the BS surface, θ_{B_n}, also determines the physics of the BS. Regions where $\theta_{B_n} \leq 45^\circ$ are termed quasi-parallel shocks. Regions where $\theta_{B_n} \geq 45^\circ$ are termed quasi-perpendicular shocks. Both are regions where wave activity and particle heating occur, from the formation of a foreshock region, produced by reflected ions or waves generated at the shock front. Quasi-perpendicular shocks have an "abrupt" shock structure. Quasi-parallel shocks have an extended structure.

Behind the BS, downstream of the Sun, the solar wind flow is sub-sonic. This region is the Magnetosheath (MS). It is a transition region for the solar wind before it encounters the obstacle Earth presents to the flow. In the MS the orientation of the IMF changes from it's solar orientation near the BS to one "draped" around the Earth, around the Magnetopause. Solar Wind structures can propagate past the BS and through the MS, towards Earth. The Magnetopause (MP) is a boundary, around the Earth's Magnetosphere, between the IMF and the Earth's magnetic field, formed by the condition that a magnetic field is "frozen-in" solar-terrestrial plasmas and that different plasmas do

not (generally) mix. It is the main boundary between solar plasma and terrestrial plasma.

In the absence of external forces the Earth's magnetic field would approximate a dipole field. However the MS flow at the MP boundary exerts an external force, the Earth's magnetic field deforming because of this, causing asymmetry. On the dayside the Earth's dipole field is compressed, becoming roughly spherical, the location of the MP boundary determined by the pressure balance between the Earth's magnetic dipole field and the particle ram pressure from the MS flow, typically it is between 8–10 Earth radii from the Earth. On the night-side, the MP boundary is roughly cylindrical, extending around 250 Earth radii downstream. The interior of the nightside MP boundary is the Magnetotail (MT).

The MP is leaky, energy from the MS flow is not completely deflected around the Earth by the MP boundary, some energy can pass through the MP boundary into the Magnetosphere. There are many processes by which this can happen, influenced mainly by the IMF z-component.

Under southward IMF the dayside MP boundary becomes magnetically open, by a classic mechanism called Reconnection, allowing MS plasma to enter the Earth's Magnetosphere. Reconnection is a topological rearrangement of opposing magnetic field lines, releasing magnetic field energy as plasma kinetic and thermal energy, substantial energy input can cause storms.

Under northward IMF conditions, the dayside MP boundary remains magnetically closed, but energy can be transferred across the boundary by pressure variations perturbing the MP boundary, increasing the Earth's dipole magnetic field, initiating Sudden Impulse/Sudden Storm Commencements (SI/SSCs). Other mechanisms may act to transfer energy across the MP boundary, such as the Kelvin-Helmholtz instability, by setting up surface waves on the MP boundary. Northward IMF conditions may also lead to reconnection occurring at the Magnetotail lobes, possibly influencing regions called the Polar Cusps.

The Polar Cusps are regions of depressed field strength above the Earth's magnetic poles, between the dayside MP from the nightside MP. They form not-so-strong boundaries between solar

wind and MS plasma populations. The cusps are also leaky. They have a low profile yet are one of the most direct means for MS plasma to enter the Earth's Magnetosphere, direct entry in the sense that the number flux of plasma particles is high and they retain most of their original energy characteristics. Essentially they "funnel" plasma particles towards the Magnetosphere, giving rise to dayside auroral precipitation, and "diffuse" aurora.

On the nightside, the interaction between the MP and the MS flow stretches out the Earth's dipole field, forming the Earth's Magnetotail (MT). It extends many (roughly 250) Earth radii downstream of the Earth. The north lobe and south lobe are separated by a region called the plasmasheet, defined as a region of closed magnetic field lines in the equatorial magnetotail. The structure of the magnetotail is strongly influenced by reconnection. When this occurs it leads to major restructuring of the MT, the onset of substorms, resulting in discrete aurorae, as plasma particles are accelerated Earthward in the plasmasheet, with a "plasmoid" being ejected in the tail downstream, a "blob" of accelerated plasma confined by closed field lines.

Nearer Earth, the Plasmasphere is a region of plasma that co-rotates with the Earth. It can couple with and can be considered an extension of the Ionosphere. Between and partially overlapping the Plasmasphere and the Plasmasheet are the Radiation Belts and the Ring Current. The Outer Radiation Belt consists mainly of electrons, lies typically between 3-9 Earth radii, with maximum electron energies at a distance of 4 Earth Radii, and is dynamic, being strongly related with geomagnetic storms. The Inner Radiation Belt consists mainly of protons, lies typically between 1-3 Earth radii, with maximum proton energies occurring around 2 Earth radii, and is influenced a little by storms. It is reasonably stable. The Ring Current, typically lies between 2-7 Earth radii, contains geomagnetically trapped ions and electrons drifting around Earth, overlaps the Radiation Belts, with maximum energies around 4 Earth radii, energies which intensify during solar wind initiated storms.

The Ionosphere is a dense, weakly-ionised lower boundary on the system. It is reflective for most radio waves. Precipitating / injected plasma particles entering the Earth upper-atmosphere, ionise neutrals, which then emit visible light as they relax, forming visible aurorae.

Summary

The near-earth environment is structured by the interaction of the solar wind plasma and terrestrial plasma. This interaction forms various regions, and energy is transported around these regions. There are many processes that transfer energy around the system, the main source for this energy is the solar wind. The transfer of energy around, and coupling with, this system is of interest. There are a variety of means that are used, including waves, instabilities, magnetic reconnection and particle acceleration.

1.2 In-situ Satellite Measurements of Space Plasmas

Understanding of the near-earth environment comes from scientific enquiry, and experimental observations form an important part of this process, by using them to validate current theories and stimulate ideas for new theories. Space plasmas are unique in that they allow observation of plasmas unattainable in laboratory conditions.

The Bow shock and magnetosheath have been identified as particular regions of interest. Remote sensing of far regions, i.e the bow shock and the magnetosheath, is not so easy, for the level of observation needed to understand further these regions it is necessary to take in-situ measurements.

1.2.1 Multi-Instrument Studies

Initial exploration of the solar terrestrial region was made by single satellites, often with limited instrumentation. Increasing knowledge fed back into the design of satellite missions led to the improvement and fine-tuning of satellite instrumentation, forming the basis for multi-instrument studies.

A single solar wind / magnetosphere satellite would carry many instruments to measure particular features of the environment. Solar plasma contains EM fields and particles.

For the EM fields, there would be instruments like fluxgate magnetometers to measure the low frequency / DC magnetic fields. There would be electric dipole antennas to measure the low frequency / DC electric fields. The low frequency fields are usually measured as a field intensity versus time. Electric dipole antennas can also be used to measure higher frequency wave activity, complemented by search coil magnetometers measuring higher frequency wave activity in the magnetic field. Such measurements would be returned as frequency spectra versus time.

To measure the plasma there would be low and high energy instruments, returning quantities including particle populations and the magnitude and direction of particle fluxes. Langmuir probes would be used, by biasing the probe to obtain a potential/current curve, to obtain electron temperature and density.

Analysis of single satellite measurements can be made in many ways. There is first the simple time-domain inspection of the measurements. It is possible to identify things like boundary crossings, from changes in field strength between regions, and particular energetic particle events, by increases / decreases in particle flux. It is possible, for some measurements, in particular low frequency field measurements, to convert them to the frequency domain, one method being the Fast Fourier Transform (FFT). This is a more natural approach when considering waves. It is possible then to inspect Power Spectral Densities (PSDs), identifying frequency ranges of high energy. These measurements, can of course, be compared with each other, for using low frequency magnetic field data to identify a boundary crossing, such as the Bow Shock, then looking in the particle data to inspect any changes in particle flux.

Single satellite measurements are useful, they reveal some information about the regions they measure, however some information remains hidden.

1.2.2 Multi-Satellite Studies

It is possible to entertain the idea that most regions of space have been, at one time or another, sampled by a single satellite under a variety of conditions. It is now not a case of what and where,

but a case of *how*, the solar terrestrial region is sampled, that can lead to further understanding of this region.

Single satellite missions progressed to coordinated single satellite missions, to simultaneous dual satellite missions to the simultaneous multi-satellite missions of today, establishing multi-satellite studies.

Simplest of all is the case where data from two separate satellite missions can be compared. Care of course needs to be taken that data from both satellites, for the interval considered, is available, and that they were suitably located for the study to be meaningful (e.g. *Voyager*, *ACE/Interball*, *ISEE 1/2* and *ISEE 3*). Usually they were not very close to each other and large scale features were studied, e.g. interplanetary shocks. If more detailed analysis was required then the possible different sampling rates of the satellite instruments needed to be dealt with.

More advanced multi-point studies were made possible by the development of dual satellite missions. These consisted of two satellites containing instruments taking similar or comparable measurements placed in similar orbits, typically close to each other (of the order of 100's of kilometers) enabling studies of smaller scale features. Missions such as these included *AMPTE UKS/IRM* and *ISEE1/2*.

More recently the order of the multi in multi-point satellite missions is increasing. The successful launch of the *CLUSTER II* mission in the summer of 2000 provided (and at the time of writing is still providing) four-point measurements. It is exactly this type of dataset that is considered in this thesis.

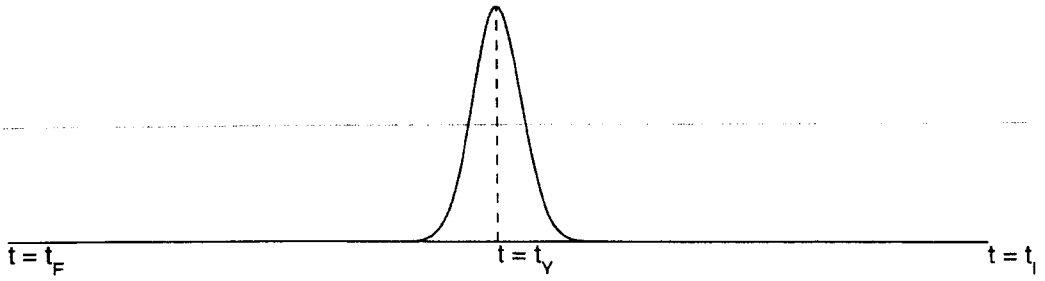

(a) First journey. The weather is fine in Edinburgh. As the day progresses and the train nears York, the skies become a little darker, then it rains quite heavily. As the train leaves York and moves South, the skies begin to clear and by Doncaster it is sunny again. It remains sunny all the way to London.

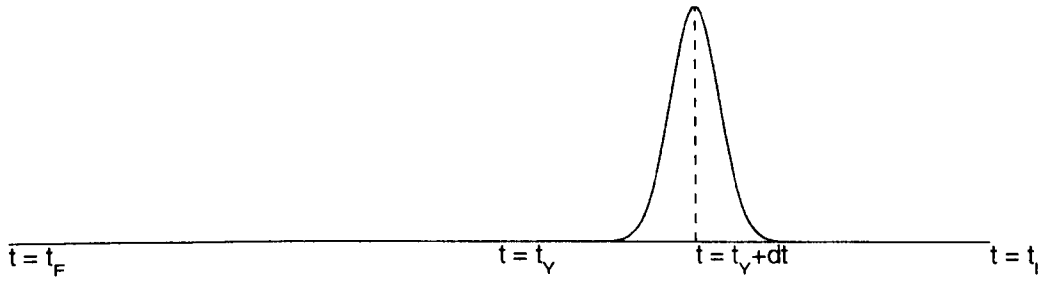

(b) Second journey. The weather starts fine, gets cloudy and starts to rain over Doncaster, then clears and stays fine all the way to London.

Figure 1.3: Example of the spatio-temporal ambiguity. Representation of amount of rainfall observed on a train journey, y-axis representing precipitation intensity. Do observations correlate with where, when, or both.

1.3 Some aims of multi-point analysis

1.3.1 Spatio-temporal ambiguity

Satellite motion is determined by orbital mechanics, there is no escape from the fact that the satellite position changes with time. This introduces the spatial-temporal ambiguity: when an event is seen in the measurements, such as an abrupt change in a particular quantity, is it explained by the location of the satellite, the time the satellite is taking measurements, or a mixture of both?

To clarify this point consider a train journey from Edinburgh to London. The first journey starts with good weather, it starts raining near York, then the weather clears after Doncaster and is fine all the way to London (a representation of this can be seen in Figure 1.3(a)). Two interpretations can be made from this journey, each equally valid.

- It rains *only* in York, *all* the time (localised in space)
- It rains *everywhere*, but only at a *particular* time (localised in time)

Which is true? From this one observation, this one set of measurements, it is not possible to distinguish between the two cases. This is an example of the spatio-temporal ambiguity. More information is needed to, at least partially, remove the ambiguity, by either supporting one interpretation over another, or creating need for a new interpretation.

So consider now a journey along the same route, but made a few hours later. Again the weather starts fine, but the bad weather is now seen around Doncaster, before clearing and then staying fine all the way to London. This is represented in Figure 1.3(b). From this observation, neither of the above can be argued to be true. A third interpretation is possible,

- It rains over an area that changes with time (localised in time *and* space)

This interpretation implies motion of some kind which calls for further interpretation and analysis.

Information to remove the spatio-temporal ambiguity can be gained from extra sets of measurements. For in-situ space plasma observations this means using more than one satellite.

1.3.2 Coherence Length

The type of multi-point study is characterised by the relative separation of the satellites. For a coordinated multi-point study, the satellites are typically from separate missions, their relative separations usually large, e.g. solar wind studies, and changing over time. For a simultaneous multi-point study the satellites involved are usually from the same mission and their relative separations are usually small, of the order of 100s of kilometers. The size of the phenomena in these studies is restricted to the order of the separation scale. This introduces the idea of scale size in multi-point studies.

The large scale structure of the solar-terrestrial environment has been explored and is generally well understood. It was thought that going to smaller scales would not be so interesting (exceptions

being of course boundaries, i.e. the Bow shock and the magnetopause). However studies with small scale satellite missions have shown a wealth of phenomena that should be explored at even smaller scales. An example being reconnection, large scale reconfiguration of magnetic field lines occurs, with the reconnection site being very small, maybe even of the order of electron gyroradii.

As scale size reduces from larger, e.g. the Sun, the Earth and the bow shock, to smaller scales, e.g. sub-region scales and boundary widths, wave phenomena begin to be observed. Now scale size not only corresponds to the wavelength of the waves, but how long it is possible to observe them, or *coherence length*. Consider a pair of satellites, closely separated in the sense they observe the same local wave-field. What is the extent of the local wave-field? How far can these satellites be separated, and still measure the same wave-field? There will be a certain separation over which the two satellites will not observe the same wave-field, e.g. a satellite located upstream in the solar wind is not observing the same wave-field as one sitting inside the Earth's inner magnetosphere. For a not-so-extreme example there are regions where the plasma flow becomes turbulent, e.g. in the magnetosheath, and turbulence is stationary in the statistical sense, only on very short scales, if it can be said to be stationary at all. There will be a limit on the extent of a turbulent plasma wave.

1.3.3 Energy transfer

Of importance when studying turbulent plasmas is the dissipation and transfer of energy in the plasma. Being able to measure this energy transfer helps identify the possible physical mechanisms involved.

Transfer functions are used in system identification as models for systems, they contain information representing how the system responds to given conditions, this knowledge can be used to assist in a physical interpretation of the system model.

Multi-point plasma turbulence measurements can be viewed in the system identification framework as inputs and outputs of the turbulent plasma system. Viewed as a system identification problem suitable analysis can reveal the properties of the turbulent plasma.

This kind of analysis is only possible with simultaneous multi-point measurements as usually their separation is within the coherence length of the waves. Other data sets, from co-ordinated multi-point studies for example, are not suitable as usually their separation is greater than the coherence length of the waves so this analysis is not meaningful.

1.3.4 Directions

There are three spatial dimensions. Single satellites can only ever represent a single point in this space. Dual satellites individually provide two points, when considered together a line can be drawn through their points and a single direction is defined. Adding more satellites, and treating them collectively, increases the dimensions covered. With four satellites, it is possible to cover the whole three dimensional space.

Waves are present in space plasma, Multi-point measurements give the possibility to measure their propagation direction, of use when finding wave modes.

This unambiguous determination, without any *a priori* assumptions, is not possible with anything less than four-point measurements.

Chapter 2

Review

2.1 Spectral transforms, Wavelet and Fourier

Spectral Transforms give information about waves. The Fourier Transform is a well known spectral transform and is well established. The Wavelet Transform however is a reasonably modern introduction, with the localisation in space and time of it's basis functions making it more suitable for the analysis of plasma turbulence which, by it's nature, is also localised spatially and temporally.

This section presents the mathematical definitions of wavelets and wavelet transforms and comparisons are made between them and sinusoids and Fourier transforms.

Examples intending to aid the interpretation of wavelet transforms are given along with showing the effect that altering the width of the Morlet wavelet has on the transform.

2.1.1 Wavelets and Wavelet Transforms

Sinusoids and Wavelets

Generally, sinusoids are infinite in extent over the time domain and are characterised by a frequency parameter ω, interpreted as a frequency. Figure 2.1 shows three sinusoids with different frequencies.

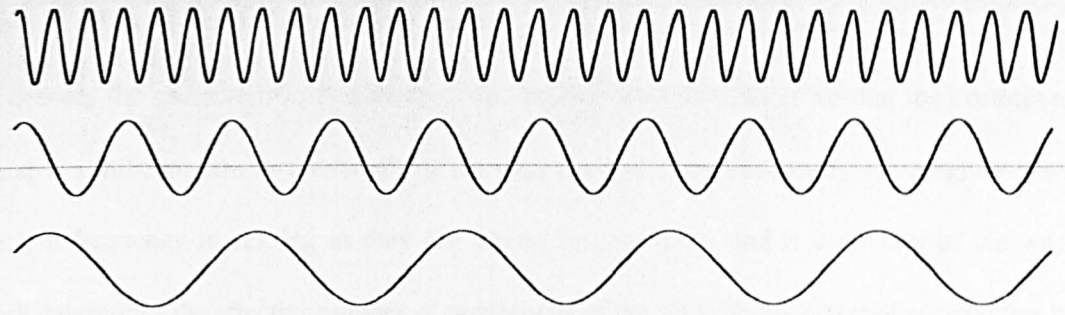

Figure 2.1: Plot of three sinusoids. The frequencies are in the ratio 1:2:4.

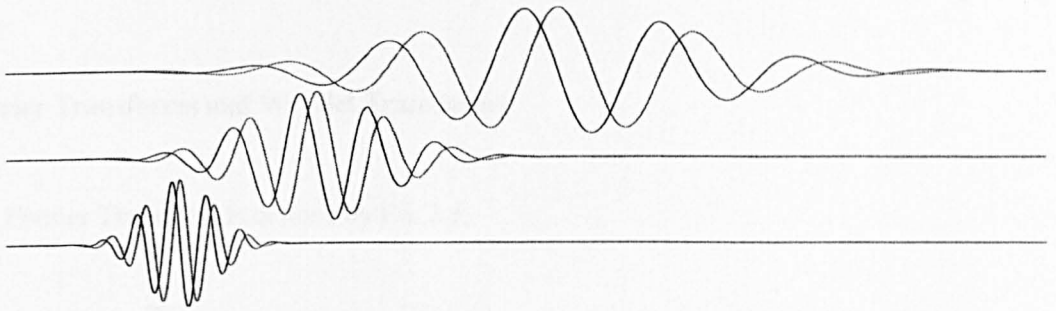

Figure 2.2: Plot of three wavelets. The parameters scale (α) and translation (τ) are in the ratio 1:2:4 and 1:4:9 respectively.

Wavelets are characterised by two parameters α and τ which can be interpreted as an instantaneous frequency $\frac{1}{\alpha}$ and time τ. They are finite in extent and are localised in the time domain around τ. Figure 2.2 shows three wavelets with different parameters.

These wavelets are generated from a mother wavelet $h(t)$ by a translation and dilation operation $t \rightarrow \frac{t-\tau}{\alpha}$, giving the daughter wavelets the form $h_{\alpha,\tau}(t) = \frac{1}{\sqrt{\alpha}} h\left(\frac{t-\tau}{\alpha}\right)$.

Different wavelets exist, e.g. the Haar wavelet and the Mexican Hat wavelet, however the choice of the Morlet wavelet is made without further comment other than that they offer a reasonable trade-off between complexity and desirable features. Eq. 2.1 shows the mother Morlet wavelet and Eq. 2.2 shows the daughter Morlet wavelets [Holter, 1995]. These wavelets are complex sinusoids with a Gaussian envelope,

$$h(t) = \frac{1}{\sqrt{2\pi\sigma}} \exp(i\omega_0 t) \exp\left(-\frac{t^2}{2\sigma^2}\right) \tag{2.1}$$

$$h_{\alpha,\tau}(t) = \frac{1}{\sqrt{2\pi\sigma\alpha}} \exp\left[i\omega_0\left(\frac{t-\tau}{\alpha}\right)\right] \exp\left[-\frac{1}{2\sigma^2}\left(\frac{t-\tau}{\alpha}\right)^2\right] \tag{2.2}$$

where as before t, α and τ denote time and the general wavelet parameters, for the Morlet wavelets ω_0 denotes the characteristic frequency of the mother wavelet (chosen so that the corresponding period is similar in size to the length of the data interval to be examined, the daughter wavelets effective frequency increasing as they are scaled successively), and σ the width of the wavelet, which determines the effective number of oscillations of the wavelet (the effect of varying this width is mentioned briefly in Section 2.1.5, Page 19).

Fourier Transforms and Wavelet Transforms

The Fourier Transform is defined by Eq. 2.3,

$$F(\omega) = \int_{-\infty}^{\infty} f(t)\, e^{-i\omega t} dt \tag{2.3}$$

where $f(t)$ is the signal and $e^{-i\omega t}$ is the complex sinusoid. This transformation moves a signal from the time domain to the frequency domain. The transformation works by multiplying the signal with a complex sinusoid of a known frequency. If there is any part of the signal containing the same frequency as the complex sinusoid a constant term is introduced that the integration operation picks up. Any other features of the signal are in effect averaged to zero. Doing this process for all the frequencies of interest results in the frequency components present in the signal to be detected.

A Wavelet Transform is defined by Eq. 2.4,

$$W(\alpha, \tau) = \int_{-\infty}^{\infty} f(t)\, \overline{h_{\alpha,\tau}(t)} dt \tag{2.4}$$

where $\overline{h_{\alpha,\tau}(t)}$ is the daughter wavelet, with $\bar{}$ denoting complex conjugation. The transformation is similar in operation to the Fourier Transform; if any part of the signal resembles a wavelet, then the multiplication and integration process will produce a non-zero value for the given parameters α and τ.

The sinusoid used in the Fourier Transform has only one parameter, ω, and the result of the

transformation is a function only of that single parameter. The wavelet transform used in Eq. 2.4 has two parameters, α and τ, and the transform resulting from the use of the wavelet also inherits those two parameters. These parameters are interpreted as an instantaneous frequency ($\frac{1}{\alpha}$) and time (τ).

More information on wavelets can be obtained from Akanso [1992], Burrus [1998], Daubechies [1992], Vettereli [1995].

2.1.2 Wavelet Transforms with Fourier Transforms

The Fourier transform is a very well known analysis tool and it is useful to be able to write the wavelet transform in terms of the Fourier transform. From a computational view efficient Fourier Transform algorithms have been written and it is prudent to make use of them instead.

Individual Wavelet coefficients, the main goal for calculating a Wavelet transform, can be evaluated as time domain integrals,

$$W(\alpha,\tau) = \int_{-\infty}^{\infty} f(t)\overline{h(\alpha,\tau,t)}dt \tag{2.5}$$

where f is the signal of interest, t is the time-domain parameter, $h(\alpha,\tau,t)$ is the daughter wavelet, α,τ are the Wavelet-domain scale and translation parameters, and W is the Wavelet coefficient.

The equation used in the *MATLAB* code developed for the Wavelet transform evaluates the Wavelet coefficients with a Fourier domain representation,

$$W(\alpha,\tau) = \sqrt{\alpha}\mathcal{F}^{-1}\left\{\mathcal{F}\left\{f(t),\omega\right\}\mathcal{F}\left\{h(t),\alpha\omega\right\}\right\} \tag{2.6}$$

where $\mathcal{F}\{\}$ is the Fourier Transform, $\mathcal{F}^{-1}\{\}$ the inverse Fourier Transform, f the signal to be transformed, h the Mother Wavelet, and α, τ the wavelet scale and translation parameters.

This second equation (Eq. 2.6) has advantages over the first (Eq. 2.5), mainly that efficient algorithms have been developed to calculate Fourier transforms and the direct calculation of Eq. 2.5

can take a long time, certainly when compared with the calculation time of Eq. 2.6. The remainder of this subsection will show the derivation of Eq. 2.6.

The daughter wavelet $h(\alpha, \tau, t)$ can be written as $h_\alpha(t-\tau)$, where $h_\alpha(t) = \frac{1}{\sqrt{\alpha}} h\left(\frac{t}{\alpha}\right)$, and noting that given Eq. 2.2 $\overline{h_\alpha(t)} = h_\alpha(-t)$, Eq. 2.5 becomes,

$$\begin{aligned} WT(\alpha,\tau) &= \int_{-\infty}^{\infty} f(t)\overline{h_\alpha(t-\tau)}dt \\ &= \int_{-\infty}^{\infty} f(t)h_\alpha(\tau-t)dt \end{aligned} \tag{2.7}$$

The RHS is the convolution of f and h_α, $f * h_\alpha$. By the Fourier Transform theorem for the Fourier Transform of the convolution of two functions, $\mathcal{F}\{f*g\} = \mathcal{F}\{f\}\mathcal{F}\{g\}$, taking the Fourier Transform of Eq. 2.7 shows that,

$$\mathcal{F}\{WT(\alpha,\tau),\omega\} = \mathcal{F}\{f(t),\omega\}\mathcal{F}\{h_\alpha(t),\omega\}$$

By the Fourier Transform Scaling Theorem, the second term on the RHS becomes,

$$\begin{aligned} \mathcal{F}\{h_\alpha(t),\omega\} &= \mathcal{F}\left\{\frac{1}{\sqrt{\alpha}}h\left(\frac{t}{\alpha}\right),\omega\right\} \\ &= \sqrt{\alpha}\mathcal{F}\{h(t),\alpha\omega\} \end{aligned}$$

giving,

$$\mathcal{F}\{WT(\alpha,\tau),\omega\} = \sqrt{\alpha}\mathcal{F}\{f(t),\omega\}\mathcal{F}\{h(t),\alpha\omega\}$$

which, by taking inverse Fourier Transforms of both sides, leads to Eq. 2.6.

2.1.3 Notes on sampling a continuous signal

There are limits on the highest and lowest frequency that can be resolved when dealing with discrete time signals. These limits are found to be dependent on the sampling rate of the signal and the number of sampling periods in the signal.

The limit on the highest frequency is given by the Nyquist sampling theorem as $f_s/2$, where f_s is the sampling rate. For extra security the highest frequency is taken to be $f_s/4$.

The limit on the lowest frequency varies with the length of the time series. The assumption that the lowest frequency must fit two complete cycles into the length of the time series leads to the frequency being $2f_s/N$, where N is the number of sampling periods in the time series. These limits impose constraints of the valid scales used by the wavelets.

2.1.4 Notes on ensemble averaging

When using Fourier Transforms it is typical to generate ensembles, and average over the ensembles, to improve the statistical robustness of the calculation. To generate ensembles a windowing technique is used, where the data is divided into (possibly overlapping) sections, each subjected to a FFT. Problems arise with sectioning data for FFT, non-continuous data create edge effects, so a windowing algorithm is performed to reduce the effect of spurious frequency components appearing. The ensembling is then performed over these windowed FFTs,

$$X(\omega) \rightarrow X(\omega, k)$$

$$\langle X(\omega) \rangle = \frac{1}{N} \sum_k X(\omega, k) = \langle X(\omega, k) \rangle_k$$

where k is the index over each window used in the ensemble.

Spectral transforms can be made using the Wavelet Transform. Essentially this gives an instan-

taneous spectral transform,

$$X(\omega) \rightarrow X(\omega, t)$$

$$\langle X(\omega) \rangle = \frac{1}{N} \sum_t X(\omega, t) = \langle X(\omega, t) \rangle_t$$

where t represents time. In terms of ensembles the Wavelet Transform provides as many as there are samples, enabling ensemble averaging over time, also the possibility of defining *instantaneous* spectral functions, e.g. the auto power spectral density can be defined as,

$$G_{xx}(\omega, t) = X(\omega, t)\overline{X}(\omega, t) \tag{2.8}$$

2.1.5 Interpretation

In this section a number of artificially generated signals are considered. Their Fourier and Wavelet transforms are examined to demonstrate how to interpret Wavelet Transform plots and to show the potential advantages Wavelet Transforms offer over Fourier Transforms.

First consider a sine wave of frequency 100 mHz, sampled at 1 Hz for 1000 seconds. The magnitude plot is shown in Figure 2.3. The Fourier Transform is shown in Figure 2.4. From this figure the 100 mHz component can clearly be seen.

The wavelet transform plot is shown in Figure 2.5. The Mother wavelet characteristic frequency ω_0 is $\frac{2\pi}{1000} \approx 6$ mHz. For this figure the width parameter $\sigma = 2$. The wavelet translation parameter τ is shown along the horizontal axis, in units of time. The wavelet scale parameter α is represented as a frequency, $f = \frac{1}{\alpha}$, and is shown along the vertical axis, in units of Hz.

A distinct band can be seen at 100 mHz extending over the time range, indicating the wavelet transform has also detected the frequency component. Also, added time information is given but the range is rather blurred, i.e. it is hard to distinguish exactly the start and end times of the 100 mHz component.

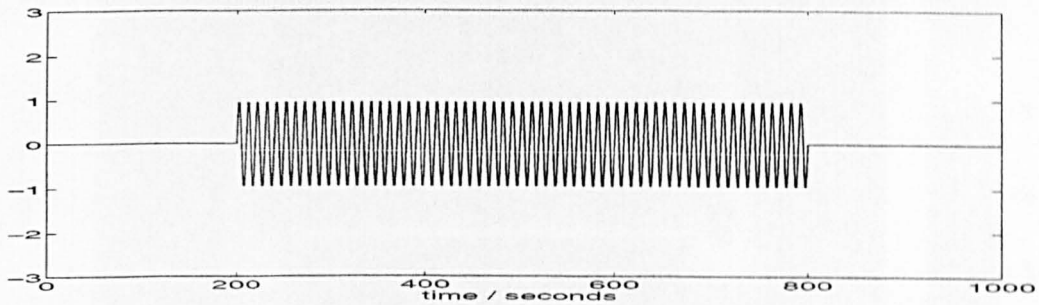

Figure 2.3: Magnitude plot of a 100 mHz sinusoid. The sinusoid is constrained to the time range [200, 800] seconds.

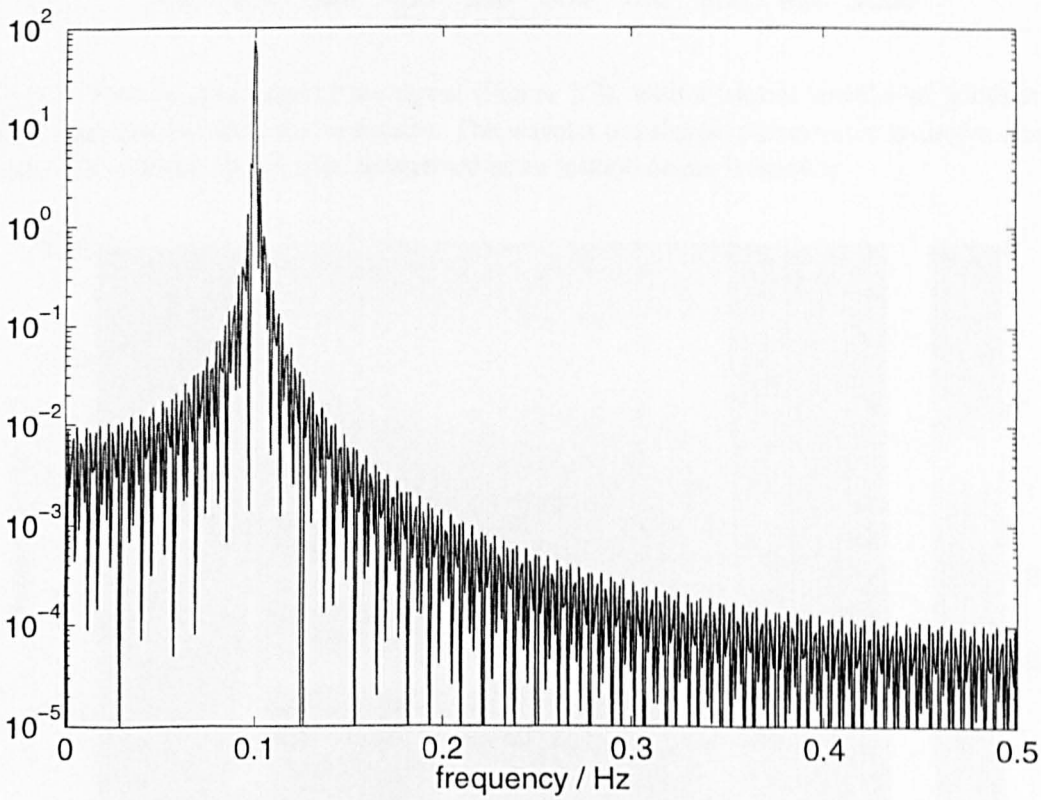

Figure 2.4: Fourier Transform of the signal shown in Figure 2.3.

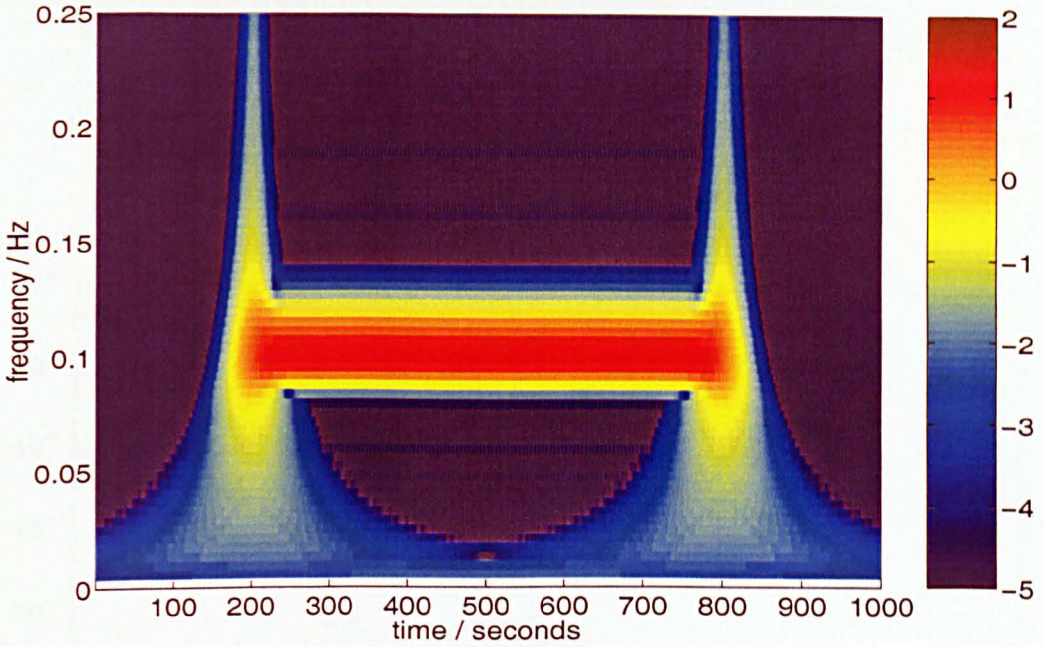

Figure 2.5: Wavelet transform of the signal (Figure 2.3), with a Morlet wavelet of width $\sigma = 2$, and with characterisic scale $\omega_0 \approx 6$ rad/s. The wavelet translation parameter τ is shown along the abscissa. The ordinate shows $1/\alpha$, interpreted as an instantaneous frequency.

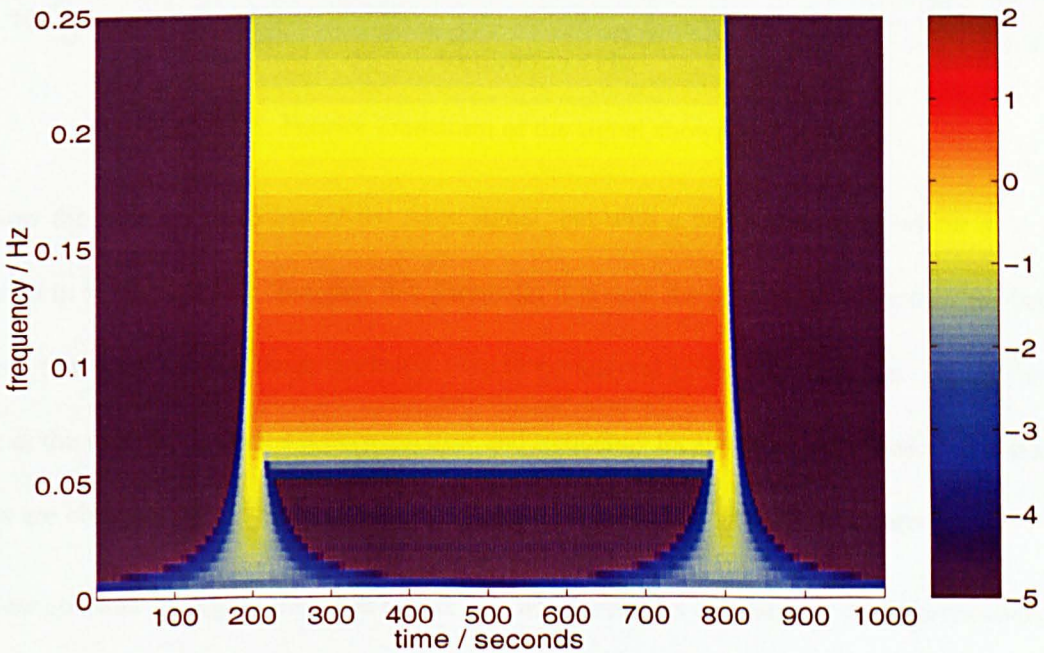

Figure 2.6: Wavelet transform of the signal shown in Figure 2.3, with a Morlet wavelet of width $\sigma = 1/2$, and with characterisic scale $\omega_0 \approx 6$ rad/s. The wavelet translation parameter τ is shown along the abscissa. The ordinate shows $1/\alpha$, interpreted as an instantaneous frequency.

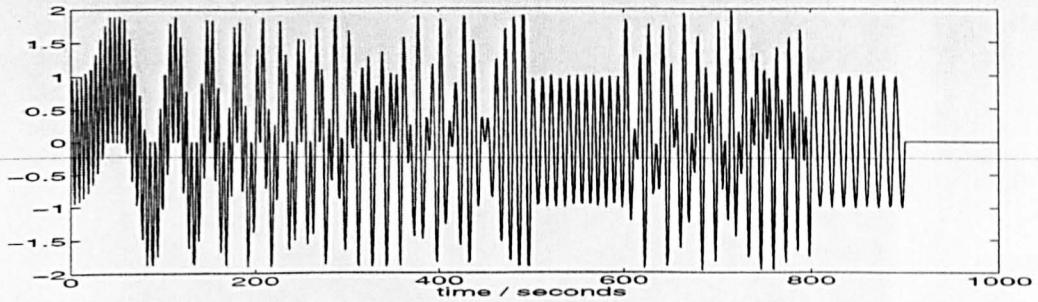

Figure 2.7: Magnitude plot of a superposition of four sinusoids.

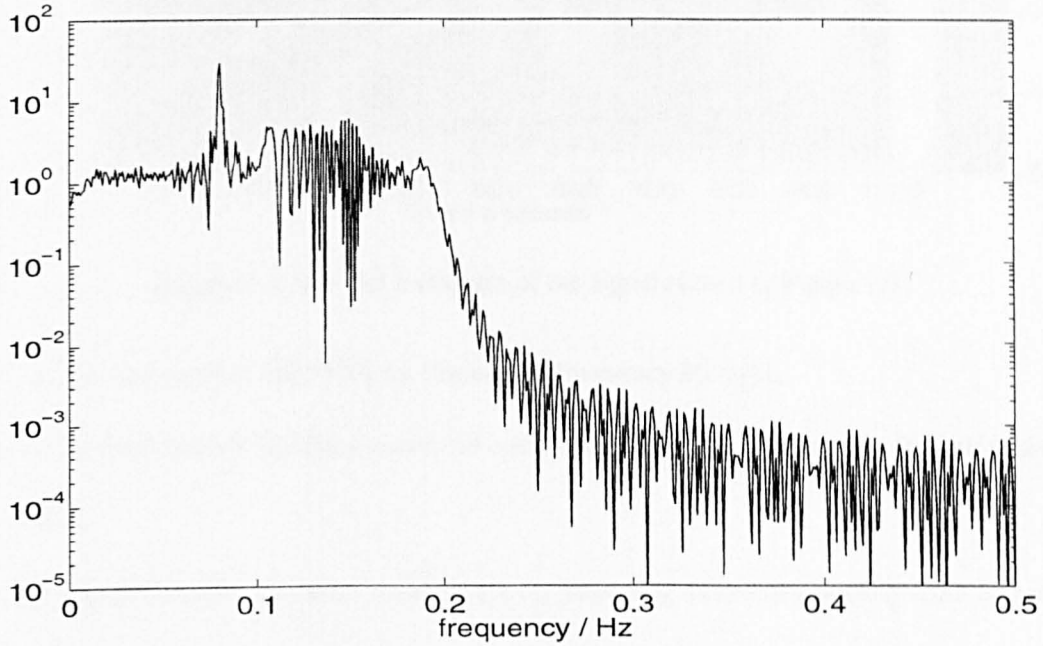

Figure 2.8: Fourier Transform of the signal shown in Figure 2.7.

Now the Wavelet transform of the same signal, but with a width parameter where $\sigma = 1/2$, is shown in Figure 2.6. By changing this parameter it is now the frequency range that has become blurred, however the time range is clearly seen to be interval [200, 800] seconds. By varying the width of the wavelets, a trade-off between time and frequency localisation can be made. Satisfactory results are obtained by setting the width parameter $\sigma = 1$ and this value is used throughout.

Now consider the signal shown in Figure 2.7, which consists of a number of different sinusoids. It is difficult to see on inspection the nature of the underlying waves. Inspection of the Fourier transform (Figure 2.8) also does not help. The wavelet transform, shown in Figure 2.9, is more revealing.

The position of the maxima indicate the presence of three different sinusoids,

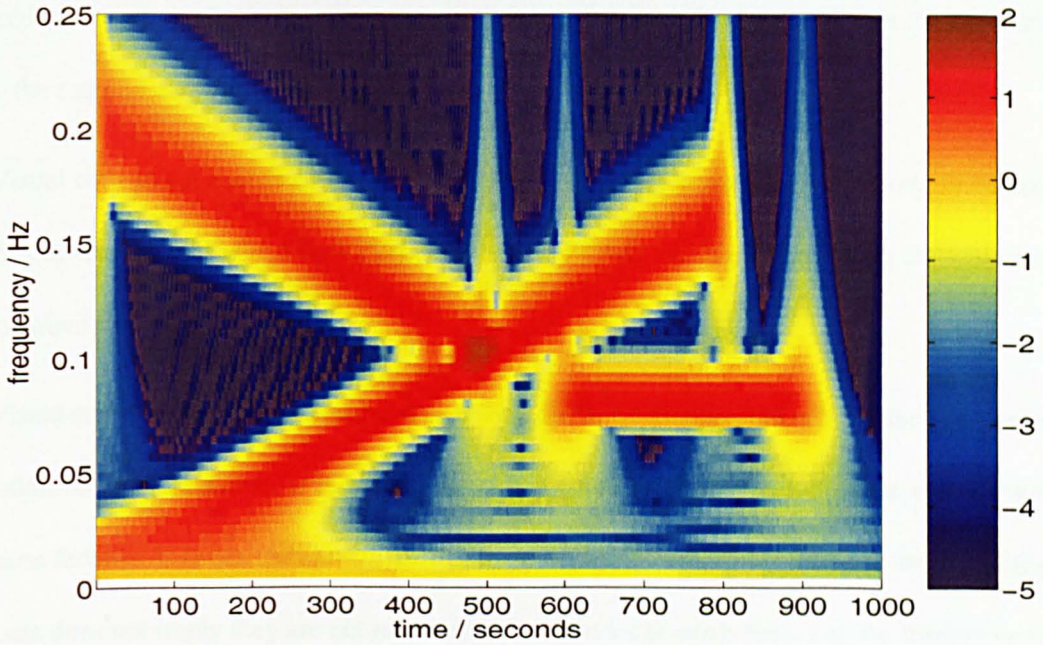

Figure 2.9: Wavelet transform of the signal shown in Figure 2.7.

- on the time interval [600 900] s a sinusoid of frequency 80 mHz,
- on the time interval [0 800] s a sinusoid with frequency increasing linearly from 0 mHz to 150 mHz,
- on the time interval [0 500] s a sinusoid with frequency decreasing linearly from 200 mHz to 100 mHz.

2.2 Data Analysis Techniques

The study of multi-point measurements is not new, there exist a variety of techniques for extracting information from the datasets, many using a spectral transform to use wave information instead of signal level information.

2.2.1 Correlation

Correlation can be useful to visually inspect data, and compare multi-point measurements side by side, plot by plot. For events such as boundary crossings, a clear crossing can be distinguished from a boundary moving back and forwards across the satellite array by whether the measurements are

ordered or nested, the former implying a boundary moving back and forwards over the array and the latter the satellite array crossing over the boundary.

Visual correlation can be used to say something of the scale size, as in the work by Fazakerley and Southwood [1994] where dual *ISEE* magnetic field data was used to examine the scale sizes of mirror wave structures.

Visual correlation is only useful for waves when there are distinct monochromatic waves present. The addition of more waves, as is usually the case for turbulent plasma, makes the identification of common features between data sets difficult. There being no common features between multi-point data sets does not imply they are not measuring the same local wave-field, e.g. for dispersive waves it is most probable that the time domain signal is changing continuously, further analysis would be needed.

It is wrong to assume that data sets are not coherent based on there being no visual correlation.

2.2.2 (Linear) Coherence Function

Visual correlation cannot be used to identify when two data sets are measuring the same phenomena. A statistic that can be found instead is the linear coherence function [Bendat and Piersol, 1986],

$$\gamma^2(\omega) = \frac{|G_{xy}(\omega)|^2}{G_{xx}(\omega)G_{yy}(\omega)} \tag{2.9}$$

where $G_{xy}(\omega)$, $G_{xx}(\omega)$ and $G_{yy}(\omega)$ are the cross and (two) auto power spectral density functions respectively, which given the spectral transform ensembles $X(\omega,k)$ and $Y(\omega,k)$ can be calculated as,

$$\begin{aligned} G_{xy}(\omega) &= \left\langle X(\omega,k)\overline{Y(\omega,k)}\right\rangle_k \\ G_{xx}(\omega) &= \left\langle X(\omega,k)\overline{X(\omega,k)}\right\rangle_k \\ G_{yy}(\omega) &= \left\langle Y(\omega,k)\overline{Y(\omega,k)}\right\rangle_k \end{aligned} \tag{2.10}$$

where $^{-}$ denotes complex conjugation and the ensemble averaging is as mentioned in Section 2.1.4, Page 18.

The value of $\gamma^2(\omega)$ varies from 0, for no coherence, to 1, for complete coherence.

This is a general equation and can be applied to many situations. It can be used as a test for stationarity of a time series. A stationary time series means statistics derived from the signal are not dependent on the particular interval chosen. For coherence functions defined on many subintervals stationarity can be concluded if values of the coherence function remain constant. When the coherence level changes the signal is not stationary (by the definition of stationarity), but with the coherence function information about which waves contribute to the non-stationarity is indicated by the regions where the coherence function changes, increasing values of coherence indicate waves becoming coherent, decreasing values of the coherency indicate waves becoming incoherent.

The phase of the cross power spectral density function, G_{xy}, gives information about the phase difference between the signals, which for the case of multi-point satellite measurements leads to information about the dispersion of plasma waves [Balikhin et al., 1997a, 2001b, deWit et al., 1995]. The phase of the cross power spectral density function only becomes a valid measurement for high values of the coherence function; the phase when the coherence is low is meaningless as the waves are not coherent.

Use is made of this function in Chapter 4, and is explained in more detail there.

2.2.3 Coherence Length

The ideas that coherent data sets become incoherent leads to the notion of a coherence length, a scale size that can represent the limit between the coherence and incoherence of data sets. Attempts to derive this quantity experimentally have been made by Le et al. [1993] using *ISEE* data, by examining the cross spectral widths of various waves, over different *ISEE* separations, concluding that magnetosheath waves, of periods 30, 15 and 3 seconds, remain coherent within two to three

wavelengths.

Problems with their method include that long data intervals were necessary to obtain decent spectra for the spectral width calculations, only monochromatic waves could be studied as clear spectral peaks were needed, and many data sets had to be considered to get good enough statistics for the calculations. *ISEE* data sets suit these requirements, but the restrictions make it difficult to apply the technique to other data sets.

2.2.4 Higher-order Coherence Functions

Techniques based on the estimation of the bi- and tri- coherence have been the main tool for the identification of nonlinear processes in space plasma turbulence. The bicoherence method is based on the resonance conditions for three wave interactions (or for four wave interactions in the tricoherence case). The frequencies and the corresponding wave vectors of waves involved in such an interaction must satisfy resonance conditions in any frame of reference [Sagdeev and Galeev, 1969],

$$\omega_1 + \omega_2 = \omega_3 \qquad \mathbf{k}_1 + \mathbf{k}_2 = \mathbf{k}_3 \tag{2.11}$$

The phases of the interacting waves (denoted by ϕ_i) should also be related,

$$\phi_1 + \phi_2 - \phi_3 = \text{const.} \tag{2.12}$$

If such a phase relation is statistically established then this can be considered as an indicator of a nonlinear interaction between the corresponding waves.

The bicoherence function is a tool to validate the phase relation Eq. 2.12. Let us consider a real, stationary signal $X(t)$. The bi-spectrum $\mathcal{B}(f_1, f_2)$ of $X(t)$ is defined as,

$$\mathcal{B}(f_1, f_2) = \langle X(f_1)X(f_2)X^*(f_1 + f_2)\rangle \tag{2.13}$$

where $X(f_i)$ is the Fourier component at frequency f_i; * denotes complex conjugation and brackets denote ensemble averaging.

The bicoherence function $b(f_1, f_2)$ is the normalised bi-spectrum [deWit and Krasnoselskikh, 1995],

$$b^2(f_1, f_2) = \frac{|B(f_1, f_2)|^2}{\langle |X(f_1)X(f_1)X^*(f_1 + f_2)| \rangle^2} \tag{2.14}$$

where the normalisation factor used is that of Kravtchenko-Berejnoi et al. [1995].

The value of the bicoherence function lies between 0 and 1. Values of the bicoherence close to 1 indicate that Eq. 2.12 is statistically valid. Values of the bicoherence close to 0 indicate statistical independence of the wave phases and hence absence of any nonlinear interaction between the waves.

In spite of the numerous applications of the bicoherence method to the identification of nonlinear processes in various space plasma regions it has significant disadvantages. One of the effects is related to so called *historical nonlinearities*. Let us assume that as the result of some space plasma process a variation in the electro-magnetic field is generated with a shape that differs from an ideal sine wave, and propagates as a stable wave, without any energy transfer between plasma modes. The phases of the various spectral components which compose such a structure are not independent. Therefore the application of the bicoherence will indicate numerous multi-wave coupling processes which do not take place in reality. It will instead identify the nonlinear process which took place in the past when the wave was generated. The bicoherence is not able to distinguish between this case and processes of energy transfer between scales of turbulence. This was illustrated by Walker et al. [2000] where the application of bicoherence to periodic stationary non-sinusoidal waves has been investigated.

In conclusion methods based on the bi- or tri- coherence can not provide reliable results in the identification of nonlinear processes in space plasma turbulence. The other more reliable methods are based on system identification, the *black box* approach, described later in this chapter.

2.2.5 Minimum Variance Analysis

This technique, abbreviated MVA, is not a multi-point analysis technique in the pure sense; however it is of importance as it can be used with other multi-point techniques as an independent verification.

The result of MVA is a direction determination. It was described first by Sonnerup and Cahill [1967]. The method requires 3D vector measurements, the magnetic field being optimal as the requirement $\mathrm{div}\mathbf{B} = 0$ is also used. The algorithm returns information that can be represented by as a 3×3 matrix whose eigenvalues correspond to the degree of variance along each of the directions specified by the corresponding eigenvectors. Ordering the eigenvectors by their eigenvalues, greatest to lowest, allows Maximum, Intermediate, and Minimum variance directions, $\mathbf{e}_{max}$, $\mathbf{e}_{int}$, $\mathbf{e}_{min}$, to be defined. How well defined these directions are is found by comparing the ratios of the eigenvalues. When the eigenvalues are all distinctly different from each other, $\lambda_{min} \ll \lambda_{int} \ll \lambda_{max}$, then each of the directions are well defined. When two or more eigenvalues are of similar value, $\lambda_i \sim \lambda_j$, then the corresponding directions are not well defined, there is degeneracy. The case for a well defined minimum variance direction would be $\lambda_{min} \ll \lambda_{int}, \lambda_{max}$.

In space, for reasonably well defined planar structures, the minimum variance direction $\mathbf{e}_{min}$ corresponds to the normal of the plane, for propagating structures this is the direction of propagation of the structure, e.g. a planar boundary. For cases where the minimum variance direction is not well defined, i.e. there is degeneracy, the propagation direction cannot be determined. Degeneracy compromises the definite determination of the propagation direction [Sonnerup and Schieble, 1998]. This can be dealt with by combining MVA with other complementary analysis techniques [Dunlop et al., 2000, 1995a] but this requires more thought and can be problematic too.

The requirement for having three-dimensional vector measurements means MVA is suitable for magnetic field measurements (flux-gate magnetometers are more than capable of measuring the three components of the magnetic field vector) but is not suitable for electric field measurements which generally only consist of the two components of the electric field lying in the satellite spin plane (as

extending a boom to measure the third component of the electric field vector perpendicular to the spin-plane of a spin-stabilised satellite causes it to become attitude unstable and so is generally not done).

Work by Dunlop et al. [1995a,b], Sonnerup and Schieble [1998] considers the application of MVA to space physics data sets in great detail. A particular application was made by [Horbury et al., 2001], using MVA to determine the orientation of the BS, and comparing the results with a standard model, and that of another multi-point analysis method, the discontinuity analyser, described later. Their results showed that the three techniques determined the boundary orientation in agreement with each other, confidence in one technique alone was not enough, with all three the confidence increased.

MVA for waves needs careful consideration also; it can only be used for magnetic field measurements ($\mathrm{div}\mathbf{B} = 0$), and for cases where there is expected to be a minimum variance direction, meaning it is not possible for linearly polarised waves, for example. Another problem is when waves are propagating in different directions at the same frequency. MVA is unable to distinguish between these directions. Confidence in MVA alone, although accurate in some cases, without complementary analysis cannot be so high.

2.2.6 Dispersion Relation

Phase differencing is a useful technique, and has been applied to plasma wave observations previously, e.g. Balikhin et al. [1997a], Balikhin and Gedalin [1993], Balikhin et al. [1997b], deWit et al. [1995]. The method reveals the magnitude of one of the three wave-vector components, along the direction defined by the displacement between the two measurement devices (i.e. satellites). Finding how this varies with frequency reveals the dispersion of the observed waves.

Assuming the wave-field is composed of plane waves, it can be expressed as,

$$\mathbf{B}(\mathbf{x},t) = \sum_{\omega_i} \alpha(\omega_i) \exp i(\mathbf{k}_i \cdot \mathbf{x} - \omega_i t) \tag{2.15}$$

where $\alpha(\omega_i)$ is the amplitude of the ω_i component and the dispersion relation is given by $\omega_i = \omega(|\mathbf{k}_i|)$ (the phase speed is $\omega_i/|\mathbf{k}_i|$ and the group speed is $|\partial\omega_i/\partial\mathbf{k}_i|$). Writing the phase as $\psi(\mathbf{x},t) = \mathbf{k}\cdot\mathbf{x} - \omega t$ and the phase at the i^{th} satellite as $\psi_i = \psi(\mathbf{x}_i,t)$, it can be shown that the phase difference between the two satellites ψ_{ij} contains information about the projection of $\mathbf{k}$ on the separation vector $\mathbf{x}_{ij}$,

$$\begin{aligned}
\psi_{ij} &= \psi_j - \psi_i \\
&= \psi(\mathbf{x}_j,t) - \psi(\mathbf{x}_i,t) \\
&= (\mathbf{k}\cdot\mathbf{x}_j - \omega t) - (\mathbf{k}\cdot\mathbf{x}_i - \omega t) \\
&= \mathbf{k}\cdot(\mathbf{x}_j - \mathbf{x}_i) \\
&= \mathbf{k}\cdot\mathbf{x}_{ij} \\
&= |\mathbf{x}_{ij}|\, k_{ij}
\end{aligned} \tag{2.16}$$

where $k_{ij} = |\mathbf{k}|\cos\theta_{ij}$ is the magnitude of the projection of the wave vector $\mathbf{k}$ along the direction of the satellite separation vector $\mathbf{x}_{ij}$, and can be seen in Figure 2.10. As a side note, finding the projection of $\mathbf{k}$ on the separation vector between the two satellites places a lower limit on $|\mathbf{k}|$, $0 \le |\cos\theta| \le 1$, therefore $0 \le |\mathbf{k}|\cos\theta \le |\mathbf{k}|$. So k_{ij} is a lower limit for $|\mathbf{k}|$. This also puts in place an upper limit for the wavelength.

To find the phase difference between two datasets spectral transforms are needed. Spectral transforms contain not only magnitude information but also phase information as a function of frequency. The phase difference ψ_{ij} is related to the wave vector projection k_{ij} through Eq. 2.16. The dispersion relation is found by determining the dependence of this wave vector projection with frequency. The phase difference between dual satellite measurements is obtained by one of two

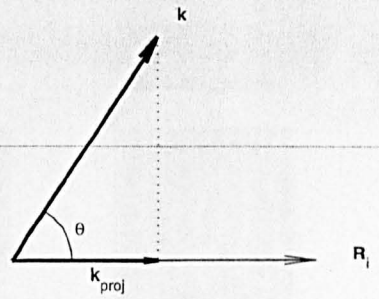

Figure 2.10: **k** projection.

methods.

The first method involves taking Fast Fourier Transforms (FFTs) of the time series and finding the spectral coherence [Bendat and Piersol, 1986]. The phase difference ψ_{ij} is then taken as the phase of the coherence function. Usual windowing and averaging techniques are employed in calculating the coherence.

The second method involves using Wavelet Transforms (WTs). The phase difference is calculated in a similar manner as above, however the extra information provided by the WTs allows a histogram of the phase differences to be constructed. Inspection of the histogram reveals the dispersion of the observed waves.

Use of this second method is made in Chapter 4 and extensively in Chapter 6 so the remainder of this subsection is devoted to a more detailed explanation.

The phase difference is found by taking the difference between the individual wavelet spectral transforms of each of the data sets, see Figure 2.11. After obtaining the phase differences, for each frequency component, the phase differences are distributed into a finite number of bins over the domain $[-\pi, \pi]$, where both a count of the number of phase differences in each bin, and a running total of wave power associated with each phase difference are recorded. This is illustrated in Figure 2.12. The former, simply a count, is useful to see the overall distribution of phase differences, the latter, weighted by wave power, is useful to detect where most of the wave power is located.

An example of a dispersion relation plot, using real satellite data, is shown in Figure 6.2, Page 96, where the abscissa instead of showing the phase difference $\Delta\psi_{ij}$ shows k_{ij}, calculated

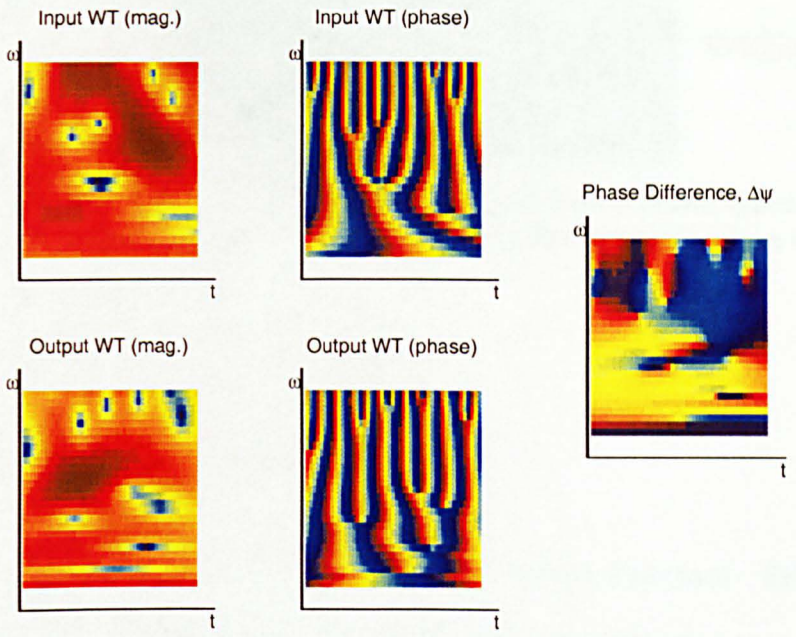

Figure 2.11: Determining the phase difference between dual satellite spectral transforms. A wavelet spectral transform (WT) is made of each of the data sets, the phase difference being just the difference in phase of the two spectral transforms.

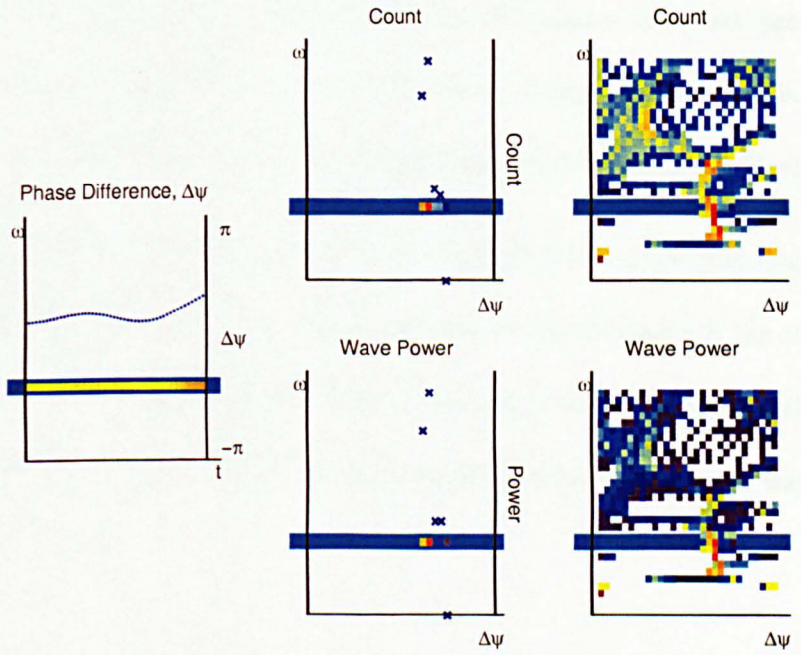

Figure 2.12: Construction of the dispersion histogram. The distribution of phase differences, for each frequency component, are collected in a finite number of bins, on the domain $[-\pi, \pi]$, displayed as both a simple count of the number of phases in the bin (top two panels on the right) and as total wave power associated with the phase differences in the bin (averaged over the two satellites, bottom two panels on the right).

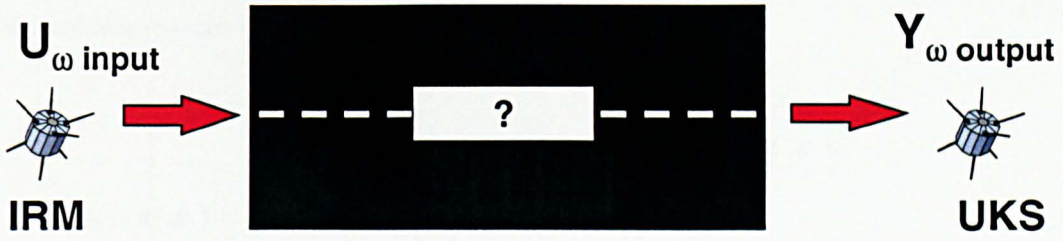

Figure 2.13: Black Box picture. The plasma is considered as an unknown system, a black box, with observable inputs and outputs which can be used to determine properties of the system.

using Eq. 2.16.

2.2.7 Transfer Function Estimation

The foundation for the method lies in a system identification framework. System identification works by treating dynamic systems as black boxes, with measurable inputs and outputs, and using those measurements to discern the nature of the black box (Figure 2.13).

This description is readily applicable to simultaneous dual satellite measurements. To the satellites in their rest-frame the plasma is flowing past them. Waves in the plasma pass the first satellite and then a short while later, after perhaps undergoing some plasma processes, pass the second satellite. The first and second satellite measurements can be thought of respectively as the 'input' and 'output' of the abstract system with the plasma processes represented by the black box.

The transfer function method for analysing turbulent plasma was first proposed by Ritz and Powers [1986]. They took laboratory based measurements of the turbulence at the edge of a Tokamak Plasma Generator with Langmuir probes. The method they used has been adapted to measurements in space plasmas [deWit et al., 1999] and modified to account for dispersive waves in the plasma [McCaffrey et al., 1999].

The problem reduces to solving a system of linear matrix equations,

$$A(t,\omega_i)\cdot\mathbf{x}(\omega_i)=\mathbf{y}(t,\omega_i) \qquad \begin{array}{l} A: m\times n,\quad m\gg n \\ \mathbf{x}: n\times 1 \\ \mathbf{y}: m\times 1 \end{array} \tag{2.17}$$

where ω_i denotes frequency, whose discrete variations over the desired frequency range form the system of equations, A and $\mathbf{y}$ contain the input and output signal spectral information respectively, and $\mathbf{x}$ contains the unknown parameters.

The solution can be found with a Least-Squares (LS) method. This method involves defining a functional $J(\mathbf{x}) = |A\mathbf{x}-\mathbf{y}|^2$ and then by finding the vector that minimises $J(\mathbf{x})$ w.r.t $\mathbf{x}$ the LS solution, $\mathbf{x}_{LS}$, is found. The LS solution has the advantage that it is an unbiased estimator in the sense that if a solution $\mathbf{x}_{LS}$ satisfies $J(\mathbf{x}_{LS}) = 0$ then the solution is accurate. The disadvantage is that when the problem is ill-posed, as the case usually appears to be when dealing with solar-terrestrial data sets, the LS solution has large uncertainties.

The meaning of ill-posed in this context is that the matrix formed by A^TA has entries with widely spaced orders of magnitude, in particular where one or more rows and/or columns contain *all* entries significantly different in magnitude to the other entries. The inversion of such a matrix, possessing no rows or columns identical to the zero vector, is possible; however with such a matrix the errors associated with the solution vector will be large.

This technique is explained further in Chapter 5.

2.2.8 Discontinuity Analyser

This is a technique pioneered by Dunlop and Woodward [1998], Dunlop et al. [1997]. It is used to determine the orientation of propagating shock-like structures (i.e. those where an identifiable shock parameter exists), that are large on the scale of the satellite separation, and may not be so useful for

waves.

The idea is not so complicated, only with deeper consideration the main problems become apparent. When a discontinuity passes a satellite, the satellite will measure the change in parameter(s), e.g. a combination of changes in particle densities or field intensities. As the discontinuity crosses an array of satellites, as is the case with multi-point measurements, each satellite will observe the shock at different times. Information from the time differences and the relative satellite separations can then be used to attempt to determine the orientation (and possibly motion) of the discontinuity.

For the simple case of an ideal planar discontinuity moving at a constant velocity over the satellite array, the normal $\hat{\mathbf{n}}$ and velocity parallel to $\hat{\mathbf{n}}$, V', can be found from the timings and relative positions,

$$V' \begin{bmatrix} t_2 - t_1 \\ t_3 - t_2 \\ t_4 - t_3 \end{bmatrix} = \begin{bmatrix} \mathbf{r}_2 - \mathbf{r}_1 \\ \mathbf{r}_3 - \mathbf{r}_2 \\ \mathbf{r}_4 - \mathbf{r}_3 \end{bmatrix} \cdot \hat{\mathbf{n}} \tag{2.18}$$

The analysis becomes more complicated when considering non-planar boundaries and acceleration of the boundary, and being able to detect which effect is the most apparent to account for the observations [Dunlop and Woodward, 1999].

2.2.9 Curlometer

This is a multi-point analysis technique that truly uses information only available with four-point or more satellites. It has been introduced and developed in Dunlop and Balogh [1993], Robert et al. [1998], Robert and Roux [1990, 1993]. It is a technique that attempts to calculate current flows. It is not a technique that directly deals with waves, but is an example of a technique only possible with multi-point missions.

2.2.10 Wave vector Filtering

This technique has been developed by Glassmeier et al. [2001], Motschmann et al. [1998, 1996], Neubauer and Glassmeier [1990], Pinçon [1995]. It is a multi-point technique used to obtain an estimate for the wave propagation vector $\mathbf{k}$. It is stated that with four-point measurements up to seven waves present simultaneously at the same frequency can be resolved [Motschmann et al., 1996]. This is done by assuming the wave characteristics are represented by the spectral amplitude $\mathbf{b}(\omega, \mathbf{k})$, and proceeding by adopting a filter-bank approach where the problem becomes one of finding optimum filters, which allow particular waves through and absorb all others, which are then used to find corresponding optimum spectral energy density estimates.

As a technique it is maturing, although more detailed studies are needed for the confidence levels of the estimator [Glassmeier et al., 2001].

2.2.11 MHD Mode Filtering

This technique has been developed by, among others, Motschmann and Glassmeier [1995]. This can be considered an extension to the technique described previously, as it builds on the general approach by also assuming a particular model, MHD, and the problem is posed so the solution will be in terms of the eigenmodes of the model, i.e the eigenmodes of the MHD equations.

First the general $\mathbf{k}$-filtering method is applied, to both check the suitability of a particular plasma model for the data, and also to get an estimate for $\mathbf{k}$; and then second the mode decomposition is performed to obtain spectral energy density estimates [Motschmann et al., 1998].

Chapter 3

Statement of Question

The motivation for exploration of our environment is to answer questions we have about that environment. As well as the solar system is understood, there are questions that remain unanswered and lead to more questions.

The aim of this research is to develop advanced data analysis techniques that extract essential features from satellite measurements of space plasmas, that would otherwise remain hidden, enabling the furthering of our knowledge and understanding of the processes that take place in space.

This can be expressed as three main objectives which are addressed, in detail, in the following three chapters.

3.1 Investigation of Coherence Length

By our definition of coherence length, there will be a separation beyond which satellites will stop observing the same local wave-field. A statistical test exists that can measure the degree of coherence between two data sets. If these data sets come from multi-point satellite measurements there will be a separation distance associated with these data sets. For simultaneous multi-point measurements the satellite separation does not change dramatically over short time intervals, to investigate many separation distances very long data sets, which contain many separation lengths, should be used,

which is quite restrictive, so some means to be able to select different separation lengths from a data set would be advantageous. The spatio-temporal ambiguity here helps, not hinders, analysis; wave phase is a function of position and time, and introducing an artificial *time* shift between two data sets can also be thought of as an artificial *positional* shift. Using this idea it is possible to investigate so some degree the coherence length of plasma waves.

3.2 Estimation of Transfer Functions

Multi-point satellite measurements allow changes between small scale events to be observed and measured. As discussed, a useful quantity to know is how energy is exchanged, or transferred, around the plasma system. Instabilities are the usual mechanism, involving particles and waves. Waves can be observed in magnetic and electric field components, and as energy is transferred around the observed wave energies will change. Suitable analysis of the energy changes, as discussed previously, can be made to quantify this energy transfer, the experimentally derived energy transfer functions can then be used to deduce possible physical mechanisms to fit the observations. The algorithm employed by deWit et al. [1999], Kim and Powers [1988], McCaffrey et al. [1999] used a Least Squares inversion technique. This is prone to inaccuracies for the case, as is usually in plasma data, of an ill-posed problem. Modifications to the inversion can be made, and a technique called Regularisation can be used.

3.3 Wave propagation determination

Four-point measurements are the minimum required to unambiguously determine 3D motion. Many techniques have been developed, all with advantages and disadvantages. Phase differencing between spectral components derived from multi-point measurements leads to the determination of the wave vector for the observed waves.

The proposed method is an extension of the dual-satellite method. With four satellites the projec-

tion of the wave propagation direction can be found on three independent satellite separation vectors and hence can be completely determined without using Minimum Variance Analysis (MVA). This lifts the restriction that three-dimensional vector measurements are needed; the method can be used with three-component magnetic field measurements, two-component electric field measurements or one component plasma densities, assuming the wave perturbs those quantities.

Chapter 4

Coherence Length

4.1 Introduction

Single satellite measurements are not able to separate between spatial and temporal variations, so cannot reveal the full composition of linear and nonlinear processes taking place. For these reasons multi-point measurements are required. Measurements of space plasma turbulence reveal that the time series measurements are not stationary. This raises the question over how long, both spatially and temporally, it is reasonable to compare multi satellite measurements. This length is the coherence length. Multi-satellite measurements cannot be used to identify the composition of observed turbulence and its dynamics if the satellite separation exceeds this coherence length. If the distance between the satellites is larger than the coherence length the mutual phase information is lost in the sense that the measurements become effectively independent. The study of coherence lengths is crucial to understand, for given separations, which waves will carry mutual phase information and will be possible to compare with multi-point measurements.

Le et al. [1993] found the coherence lengths for various types of waves measured simultaneously by dual *ISEE* satellites. The coherence length was estimated from the width of the spectral peak of the wave modes studied. Their conclusions were that the distance varies for the type of wave considered, but the number of wavelengths remains roughly constant, stating '*over several wavelengths*'.

The *ISEE* data was used as their method required satellite separations over many length scales and long sequences of data. This criteria is quite demanding, and most satellite data sets are not suitable for this approach.

The Coherence Length method described here uses (at least) dual-point measurements, spectral transforms, the coherence function and the shift theorem, to determine coherent frequency ranges and the spatial / temporal extent of their coherence.

4.2 Exploring the Coherence Function

The technique makes use of the coherence function. As mentioned in Chapter 2 this function indicates coherent and incoherent frequency ranges between two datasets. This section gives insight into how the coherence function detects coherent waves.

Also the ability of the coherence function to detect coherent and incoherent waves, along with sensitivity to signal-to-noise ratio is tested using artificially generated data.

4.2.1 Understanding further the Coherence Function

The coherence function was defined in Section 2.2.2 in terms of cross spectral density functions, and is repeated here for completeness,

$$\gamma^2(\omega) = \frac{|G_{xy}(\omega)|^2}{G_{xx}(\omega)G_{yy}(\omega)} \tag{4.1}$$

where $G_{xy}(\omega)$, $G_{xx}(\omega)$ and $G_{yy}(\omega)$ are the cross and (two) auto power spectral density functions respectively, which given the spectral transform ensembles $X(\omega,k)$ and $Y(\omega,k)$ are calculated as,

$$\begin{aligned} G_{xy}(\omega) &= \langle X(\omega,k)\overline{Y(\omega,k)}\rangle_k \\ G_{xx}(\omega) &= \langle X(\omega,k)\overline{X(\omega,k)}\rangle_k = \langle |X(\omega,k)|^2\rangle_k \\ G_{yy}(\omega) &= \langle Y(\omega,k)\overline{Y(\omega,k)}\rangle_k = \langle |Y(\omega,k)|^2\rangle_k \end{aligned} \tag{4.2}$$

With Fourier Transforms the ensemble averaging is over windows, with wavelet transforms the averaging is done over time.

It is possible to expand the coherence function, using the definitions of cross spectral density functions in Eq. 4.2 and noting that $G_{xy}(\omega)$ is in general a complex number, to show that it is related to the phase difference between the signals, $\delta\theta(\omega)$,

$$\begin{aligned} G_{xy}(\omega) &= \langle X(\omega,k)\overline{Y(\omega,k)}\rangle_k \\ &= \langle |X(\omega,k)||Y(\omega,k)| \exp i\delta\theta(\omega,k)\rangle_k \\ &\leq \langle |X(\omega,k)|\rangle_k \langle |Y(\omega,k)|\rangle_k \langle \exp i\delta\theta(\omega,k)\rangle_k \\ &= \widetilde{X(\omega)}\widetilde{Y(\omega)}\langle \exp i\delta\theta(\omega,k)\rangle_k \end{aligned}$$

where $\widetilde{\ }$ denotes an average value, and noting that $G_{xx} \sim \widetilde{X(\omega)}^2$ and similarly $G_{yy} \sim \widetilde{Y(\omega)}^2$ leads to,

$$\gamma^2(\omega) \leq \left|\langle \exp i\delta\theta(\omega,k)\rangle_k\right|^2 \tag{4.3}$$

The magnitude of the RHS of Eq. 4.3 is always less than or equal to 1.

Interpretation of the coherence function is made easier keeping Eq. 4.3 in mind. When waves are coherent, for each ensemble k, $\delta\theta(\omega,k)$ will remain constant, so the ensemble average $\langle \exp i\delta\theta(\omega,k)\rangle$ will have an absolute value near unity, with phase according to the constant phase difference. How-

ever, if $\delta\theta(\omega,k)$ varies randomly, the ensemble average $\langle \exp i\delta\theta(\omega,k)\rangle$ will have a value near zero, the wave at frequency ω is incoherent.

It is possible to consider an instantaneous coherence function in the sense mentioned in Section 2.1.4,

$$\begin{aligned}\gamma_i^2(\omega,t) &= \frac{|G_{xy}(\omega,t)|^2}{G_{xx}(\omega,t)G_{yy}(\omega,t)} \\ &= \frac{|X(\omega,t)|^2|Y(\omega,t)|^2|\exp i\delta\theta(\omega,t)|^2}{|X(\omega,t)|^2|Y(\omega,t)|^2} \\ &= |\exp i\delta\theta(\omega,t)|^2\end{aligned}$$

The magnitude of this instantaneous coherence will always be unity. Information about the coherence of the waves in the signal can only be found when ensemble averaging,

$$\gamma_i^2(\omega) = |\langle \exp i\delta\theta(\omega,t)\rangle_t|^2 \tag{4.4}$$

which is defining the instantaneous coherence function to be the upper limit in Eq. 4.3. The degree of coherence is found from the ensemble average of the values of $\delta\theta(\omega,t)$.

4.2.2 Surrogate data description

The following data set is not intended to represent a physical system but simply to provide a dataset to explore features of the coherence function.

The surrogate dual-satellite data set is generated as 1000 points with a sample period of 64s.

The input data set contains three frequencies, 0.5, 1.5 and 3 mHz. The output dataset contains three frequency components, 1, 1.5 and 3 mHz, with a constant phase offset between the common frequency components. In addition the 1.5 mHz component, common to both input and output, can have a specified number of random phase changes over the sample interval.

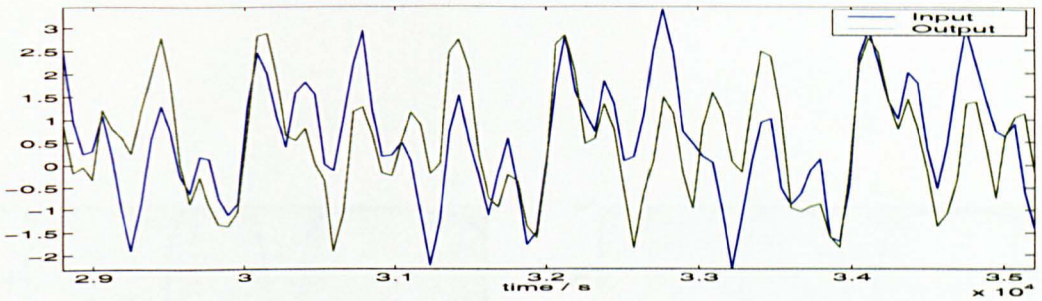

Figure 4.1: Waveforms of the generated signals. The input signal is shown in blue, the output in green.

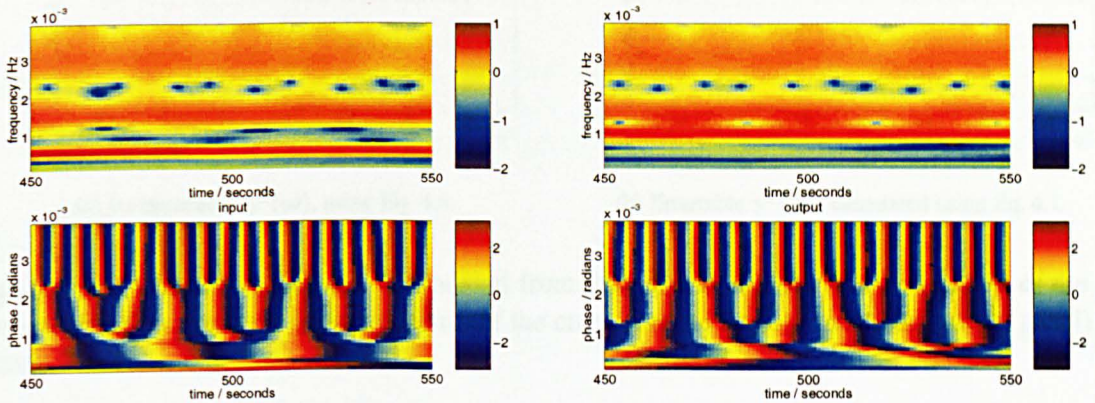

(a) Input.

(b) Output.

Figure 4.2: Wavelet transforms of the generated signals. The magnitude (top panel) and phase (bottom panel) of the transforms are shown.

All waves have the same amplitude. Uncorrelated Gaussian noise can be added to both data sets at a specified signal-to-noise ratio.

An interval of generated waveforms, for a signal-to-noise ratio (SNR) of 1, with the number of phase changes (NPC) zero, can be seen in Figure 4.1. The corresponding wavelet transforms can be seen in Figure 4.2.

The coherence function plot can be seen in Figure 4.3. The figure indicates coherent frequencies near 1.5 mHz and 3 mHz, as expected. Other waves are present in the data set, 0.5 and 1 mHz, they are not present in both input and output simultaneously, they are not expected to be, and are not identified as being, coherent.

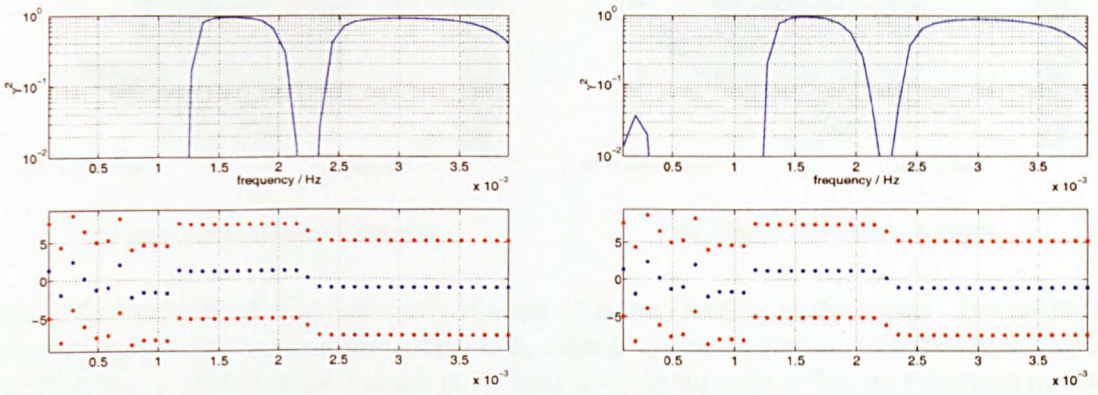

(a) Instantaneous $\gamma^2(\omega)$, using Eq. 4.4.

(b) Ensemble $\gamma^2(\omega)$, calculated using Eq. 4.1.

Figure 4.3: Coherence functions. Calculated from the generated data. The magnitude of the coherence function (top panel) and the phase of the cross spectral density function (bottom panel) are shown.

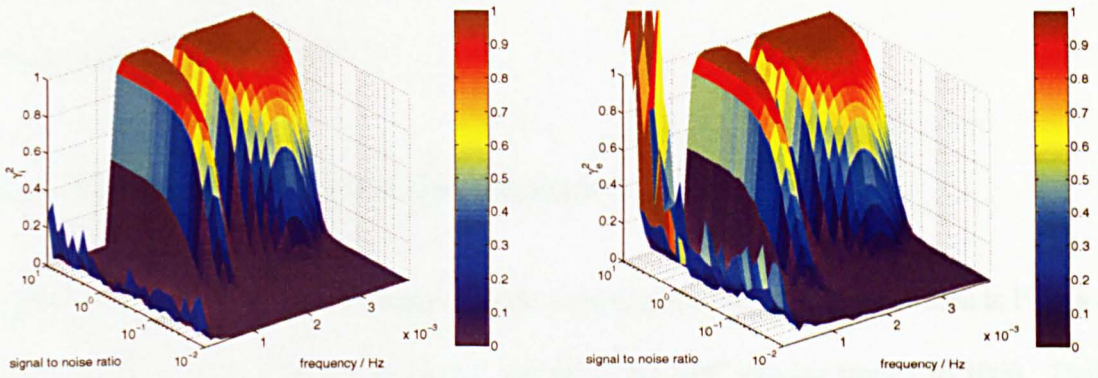

(a) Instantaneous coherence function.

(b) Ensemble coherence function.

Figure 4.4: Variation of coherence with signal to noise ratio. The magnitude of the coherence function is on the vertical axis, plotted against frequency, with the remaining axis containing the signal to noise ratio of the generated signals used to find the coherence function.

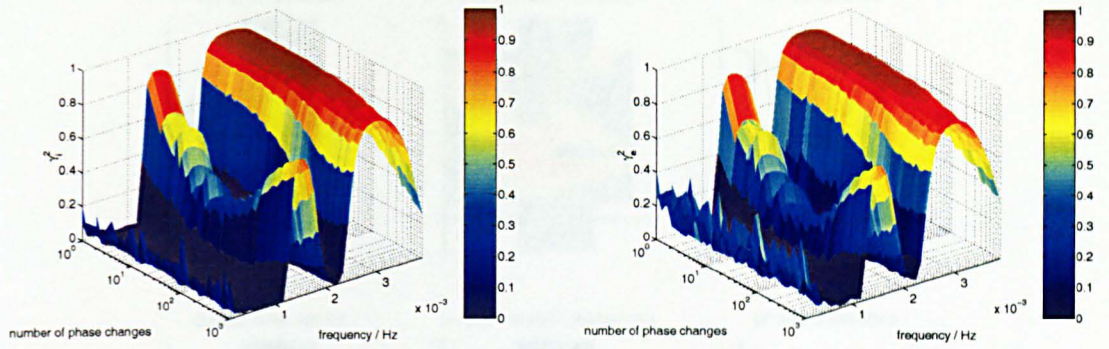

(a) Instantaneous coherence function.

(b) Ensemble coherence function.

Figure 4.5: Variation of coherence with number of phase changes in the signal. The magnitude of the coherence function is on the vertical axis, plotted against frequency, with the remaining axis containing the number of phase changes in the generated signals used to find the coherence function.

4.2.3 Coherence function and noise

The effect of noise can be seen in Figure 4.4. The coherence between data sets is found by varying the signal-to-noise ratio (SNR). The coherence is plotted against frequency and against SNR, with SNR varying between 10 and 10^{-2}, i.e. the relative strength changing from the signal being 10 times stronger, to the noise being 100 times stronger.

Decreasing the SNR from 10 the coherence remains high until it drops through 0.5 at SNR$\sim$0.2 after which it remains low. This shows a robustness against noise for levels of noise up to 4 times stronger than the signal strength.

4.2.4 Coherence function and phase changes

Sensitivity to the number of phase changes in the sampling interval (NPC) can be seen in Figure 4.5. The coherence is plotted against frequency and NPC, for NPC varying from 1 to 1000. The coherence for the 1.5 mHz wave drops below 0.5 for NPC$\sim$10, so a level of just 1% random phase changes in an interval is enough to effect the coherence significantly.

Surprisingly the coherence rises again after NPC$\sim$100. This suggests that somehow the randomness of the phase changes is averaged to zero and the original underlying signal is then identified as

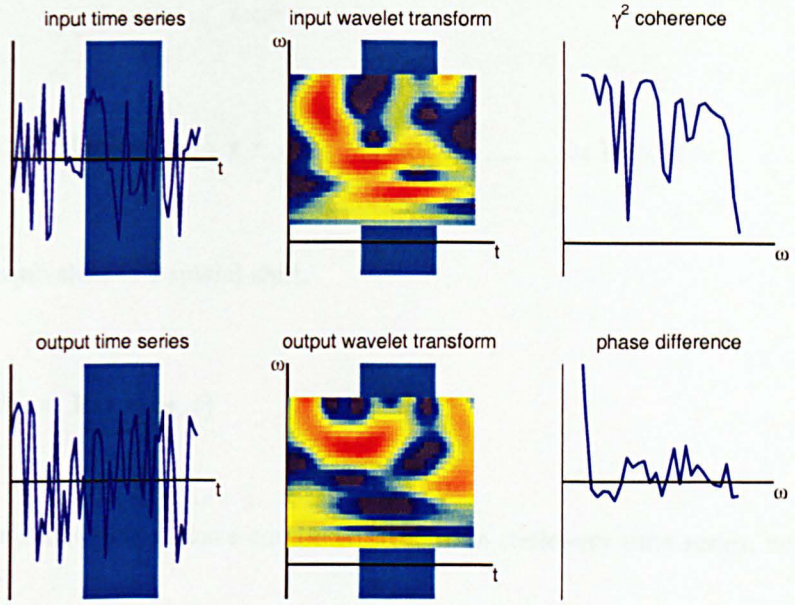

Figure 4.6: Usual coherence calculation. Spectral transforms are taken of the input and output data, which are then used to find the coherence function. Also indicated is the time window over which the coherence function is calculated. In this figure the two windows coincide.

coherent. This is an artifact of the surrogate data set, and not physical.

4.3 Method

For a given pair of satellites calculation of the coherence function gives information about the coherence of the waves for the particular spatial separation of the satellites. This is illustrated in Figure 4.6. From left to right in this figure are input and output data sets, their wavelet transforms, and the coherence calculated between the data sets. Data from the region highlighted is used. This calculation reveals the coherence between the satellites, and is associated with the separation distance of the satellites.

To find how the coherence varies with distance, the satellite separation needs to be changed. Unfortunately significant changes in satellite separations take place on very large scales, e.g. of the order of an orbit, and although it is possible to make repeated coherence calculations for the same region over many orbits, changing conditions due to the orbit period make conclusive comparison difficult.

This method makes use of the shift theorem [Chapman and Dunlop, 1993]. Assuming the wave-

field can be expressed as a sum of plane waves,

$$\mathbf{B}(\mathbf{r},t) = \sum_{\omega} \mathbf{B}(\omega) \exp i(\mathbf{k}.\mathbf{r} - \omega t) \qquad \text{as } \mathbf{k} = \mathbf{k}(\omega) \tag{4.5}$$

a time delay is equivalent to a spatial shift,

$$\mathbf{B}(\mathbf{r}, t - \delta t) = \mathbf{B}(\mathbf{r} + \delta\mathbf{r}, t)$$

as the phase of a time-delayed wave can be written, for a stationary time series, as that of a wave shifted in space,

$$\begin{aligned}
\psi(\mathbf{r}, t - \delta t) &= \mathbf{k} \cdot \mathbf{r} - \omega(t - \delta t) \\
&= \mathbf{k} \cdot \mathbf{r} + \omega\delta t - \omega t \\
&= \mathbf{k} \cdot \mathbf{r} + \mathbf{k} \cdot \delta\mathbf{r} - \omega t \\
&= \mathbf{k} \cdot (\mathbf{r} + \delta\mathbf{r}) - \omega t \\
&= \psi(\mathbf{r} + \delta\mathbf{r}, t)
\end{aligned}$$

where the following relation is used,

$$\begin{aligned}
\omega\delta t &= \mathbf{k} \cdot \delta\mathbf{r} \\
&= |\mathbf{k}||\delta\mathbf{r}| \cos\theta
\end{aligned} \tag{4.6}$$

That is, introducing an artificial time delay between the satellite datasets is equivalent, by the shift theorem, to an artificial spatial shift in separation along the original satellite separation vector.

Calculating the coherence function between two satellite datasets that have an artificially introduced time delay is the same as calculating the coherence function between two satellite data sets that have had an artificial *spatial* shift introduced between them. Thus the path is set for the coherence function to be calculated for arbitrary spatial shifts δr, through arbitrary time shifts δt, by

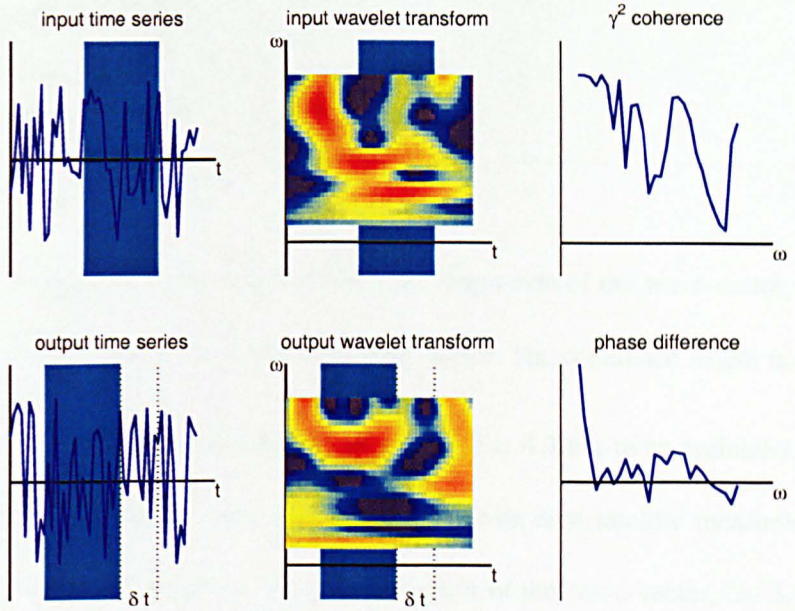

Figure 4.7: Coherence Length calculation. Spectral transforms are taken of the input and output data, which are then used to find the coherence function. Also indicated is the time window over which the coherence function is calculated. In this figure the two windows *do not* coincide, they are shifted by a time of δt (see bottom left and bottom middle panels). The temporal shift is related to a spatial shift by Eq. 4.6.

Eq. 4.6.

This is illustrated in Figure 4.7. Similarly to Figure 4.6, from left to right are input and output data sets, their wavelet transforms, and the coherence calculated between the data sets. Data from the region highlighted is used, where it should be noted that there is a time shift between the input and output data sets. This calculation reveals the coherence between the satellites, for the time shift δt, and is associated with the spatial shift δr given by Eq. 4.6.

4.3.1 Coherence length in kilometers

For an initially coherent wave, assuming a sufficiently large enough interval is chosen, there will be a particular time delay after which the wave becomes incoherent. This is indicated in the coherence function by the value of the coherence for that wave falling below a specified cut-off value. The associated time delay is identified with the *time* over which the wave remains coherent. This in turn

is related to a *length*, by Eq. 4.6,

$$|\delta \mathbf{r}| = \frac{\omega \delta t}{|\mathbf{k}| \cos \theta} \tag{4.7}$$

where δt is the time delay, ω the frequency, $|\mathbf{k}|$ the magnitude of the wave-vector, and θ the angle the wave-vector makes with the satellite separation vector. The coherence length is δr.

In relating the time delay δt to a displacement $|\delta \mathbf{r}|$, Eq. 4.7 has to be evaluated, meaning information about the phase speed of the wave is needed. From dual-satellite measurements it is only possible to estimate the phase speed using a component of the wave-vector, $\omega/|\mathbf{k}| \cos \theta$, a phase speed observed along the satellite separation vector that is in excess of the true phase speed. The phase speed $\omega/|\mathbf{k}| \cos \theta$ is found by calculating the dispersion relation (Section 2.2.6), hence $|\delta \mathbf{r}|$ can be determined.

4.3.2 Coherence length in wavelengths

It is also useful to be able to express the coherence length of a wave as a wavelength multiple,

$$n = \frac{\delta r}{\lambda} \tag{4.8}$$

where δr is the separation distance given by Eq. 4.7 and λ is the wavelength of the wave. For dual satellite measurements it is possible to get information only about the projection of the wave-vector on the satellite separation vector, $k_{proj} = |\mathbf{k}| \cos \theta$. The true wave-vector magnitude is (equal to or) greater than the magnitude of any of its projections, $|\mathbf{k}| \geq k_{proj}$. As a consequence the wavelength calculated from the wave-vector projection will be greater than its true value, $\lambda_{proj} \geq \lambda$, so Eq. 4.8 is a lower limit on the true value of n,

$$n \geq \frac{\delta r}{\lambda_{proj}} \tag{4.9}$$

the RHS of Eq. 4.9 can be rewritten using Eq. 4.7,

$$\frac{\delta r}{\lambda_{proj}} = \frac{\omega \delta t}{k_{proj}\lambda_{proj}} = \frac{\omega \delta t}{2\pi} = f\delta t$$

giving,

$$n \geq f\delta t \tag{4.10}$$

where $f = \omega/2\pi$.

The Shift Theorem is valid only for a stationary time series, it is not justifiable to use for non-stationary data. However it is being used here as a test for stationarity of a time series that is assumed to be initially stationary. The breakdown of stationarity is indicated by the coherence function, for a particular time delay, returning low values, the assumption of stationarity and the validity of the shift theorem for that case is then not asserted as this is the indication that the coherence length of the signal has been reached.

The cut-off that determines the level of coherence required to call a wave coherent is chosen arbitrarily, typically values between 0.5 and 0.8 are used, depending on the sensitivity required. A low cut-off will be sensitive to only strong incoherences; a high cut-off will be sensitive to even the smallest deviations from full coherence.

4.4 Visualisation

Two ways of visualising this coherence length are discussed.

4.4.1 Strong cut-off method

The strong cut-off method is based on the assumption that the coherence function is a decreasing function of frequency, as shown in Figure 4.8, where at an arbitrary frequency ω_0 all frequencies

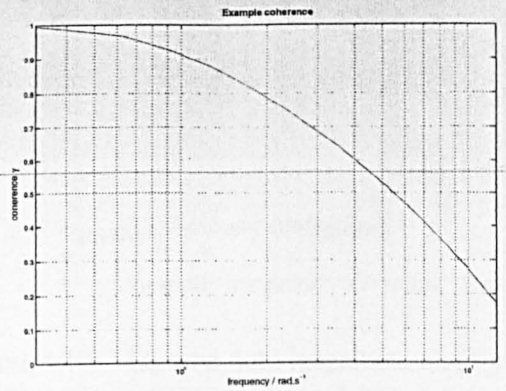

Figure 4.8: Example of a coherence function decreasing positively with frequency.

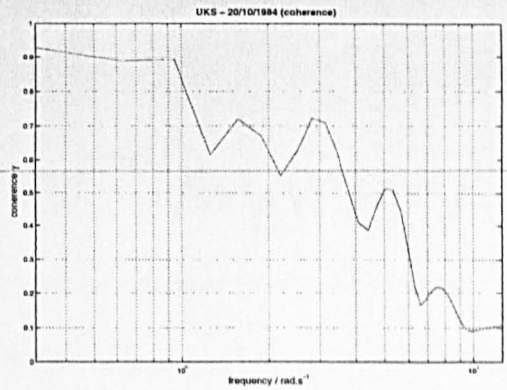

Figure 4.9: Example of a coherence function for real data.

greater have a lower coherence and all frequencies less have a higher coherence,

$$\gamma^2(\omega) > \gamma^2(\omega_0) \qquad \forall \omega < \omega_0$$

$$\gamma^2(\omega) < \gamma^2(\omega_0) \qquad \forall \omega > \omega_0$$

For such a case a cut-off in the sense described above is ideal to define a maximum coherent frequency. For example consider again Figure 4.8. A cut-off value of 0.65 would define a maximum coherent frequency of 3.5 rad/s. All frequencies below this are coherent; above are incoherent.

The coherence length plot is constructed by plotting this maximum coherent frequency on the abscissa against displacement on the ordinate, see e.g. Figure 4.13 on Page 54, where it is understood that this plot defines the boundary between coherent and incoherent waves.

4.4.2 Surf method

While the existence of such coherence functions for real data may be true, coherence functions with localised maxima are more common. Figure 4.9 shows a coherence function calculated with real satellite data. The same cut-off value of 0.65 for this figure would identify five individual frequencies indicating three coherent frequency ranges (0 to 1.1 rad/s, 1.2 to 1.9 rad/s and 2.4 to 3.2 rad/s). Clearly a simple maximum coherent frequency is not enough to describe properly the information in the figure.

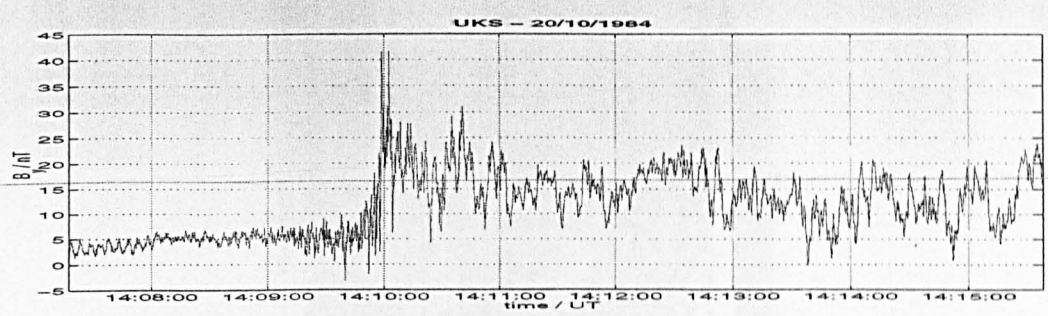

Figure 4.10: Magnetic field magnitude plot for 20/10/1984 around 14:11:00 to 14:14:00 UT (*UKS* satellite shown, *IRM* not shown for clarity).

The visualisation scheme proposed is simply to produce a surface plot of the coherence function, displayed against frequency on the abscissa and against displacement on the ordinate, the value of the coherence function colour-coded according to value, see for example Figure 4.22, Page 59. Maxima (regions where $\gamma^2(\omega, \delta r) \sim 1$) in the surface plot indicate coherent waves, minima (where $\gamma^2(\omega, \delta r) \ll 1$) regions waves are incoherent. This allows easier inspection of coherent frequency ranges and how they change with displacement.

4.5 Applications

The coherence length method is applied to three datasets, determining the characteristic length scales of the waves in each.

4.5.1 Downstream of a quasi-perpendicular bow shock on 20/10/1984

AMPTE UKS/IRM was a dual-satellite mission. It consisted of two spacecraft in an earth orbit, with apogee near 20 earth radii, separated typically a distance of 10^1–10^2 km. A comprehensive description of the mission aims, objectives and instrumentation can be found in IEEE85.

On 20/10/1984 the satellites crossed the bow shock. The magnetic field y-component measured by *UKS* can be seen in Figure 4.10. The satellites were on an inbound section of their orbit, with *UKS* encountering the bow-shock before *IRM*, but as shown in Balikhin et al. [1997b] the waves are propagated by the solar wind flow past *IRM* then to *UKS*, the data sets are ordered for *IRM* as

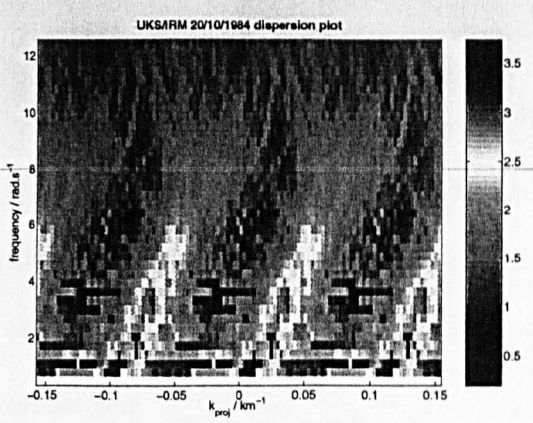

Figure 4.11: Initial dispersion plot for 20/10/1984. Satellite separation distance of 60 km. ω plotted against k_{proj}, the projection of the wave vector on the satellite separation vector. This dispersion is linear, with a phase and group velocity of $\approx$ 100 km/s.

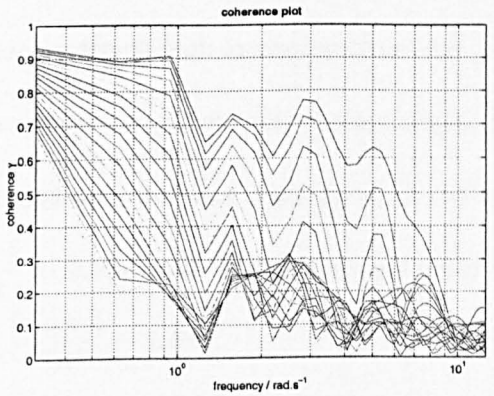

Figure 4.12: Coherence function plots for 20 incremental time delays of 1 s. As the time delay increases the maximum coherent frequency (defined by an arbitrary cut-off value) decreases.

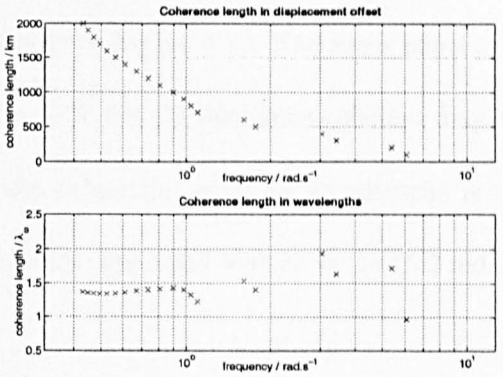

Figure 4.13: Coherence lengths for 20/10/1984. Shown against satellite separation in km (upper panel) and against number of wavelengths (lower panel).

input and *UKS* as output.

The dispersion is shown in Figure 4.11, for the interval 14:10:30 to 14:12:30. Positive k indicates the direction from *IRM* to *UKS*. This dispersion shows a broad width in k, but can be seen to be linear, with a phase velocity $\sim$100 km/s.

The region downstream of the bow-shock is chosen, a 60 s interval starting at 14:11:00 and finishing 14:12:00. A sliding window of 40 s width was used, fixing the *IRM* window and sliding the *UKS* window in steps of $\delta t = 1$ s, for 20 steps. Figure 4.12 shows the coherence functions calculated for different time delays. The general trend is for the tail end of the coherence function to move closer to lower frequencies as the time delay gets larger. This indicates that lower frequency

waves stay coherent over longer temporal distances, and hence over larger spatial distances.

The strong cut-off method is used to visualise the coherence length. For each time delay the coherence function plot is inspected, a maximum coherent frequency is chosen by applying a cut-off, here $\gamma^2_{cutoff} = 0.5$ is chosen. For example the maximum coherent frequency for the delay $\delta t = 1$ s (the first trace in Figure 4.12) is ~ 5.2 rad/s. The plot is constructed by considering the remaining time delays in a similar way.

The phase velocity, from the dispersion in Figure 4.11, is used with Eq. 4.7, to form the relation $\delta r = 100\delta t$. This in turn is used to construct Figure 4.13 (upper panel). This shows a decrease in coherence length with increasing frequency, as suggested by Figure 4.12. The lower panel shows the coherence length in terms of wavelength, using Eq. 4.10. For the maximum coherent frequency identified with the time delay $\delta t = 1$ s (6 rad/s), the coherence length in wavelengths is $n = \frac{6 \times 1}{2\pi} \sim 0.95\lambda$, and for the maximum coherent frequency associated with $\delta t = 2$ s (5.2 rad/s) as $n = \frac{5.2 \times 2}{2\pi} \sim 1.65\lambda$.

Mentioned previously is that this is a conservative estimate for n in the sense that this is a lower bound on n; the true value will be greater. This figure shows that waves measured in the interval described remain coherent at least over one and a half wavelengths.

This result is not surprising as the region behind the bow-shock is expected to be turbulent and to exhibit non-stationary behaviour, a low coherence length is not unexpected. This method has determined this length experimentally.

4.5.2 Upstream of a quasi-parallel bow shock on 30/11/1984

Data from the *AMPTE UKS/IRM* dataset is used for an interval on 30/11/1984 between 10:50:00 UT and 11:00:00 UT, where the satellites were located upstream of a quasi-parallel chock. This data interval has been used and described by Schwartz et al. [1992].

The magnitude of y component of the magnetic field measured by *AMPTE UKS* for this interval

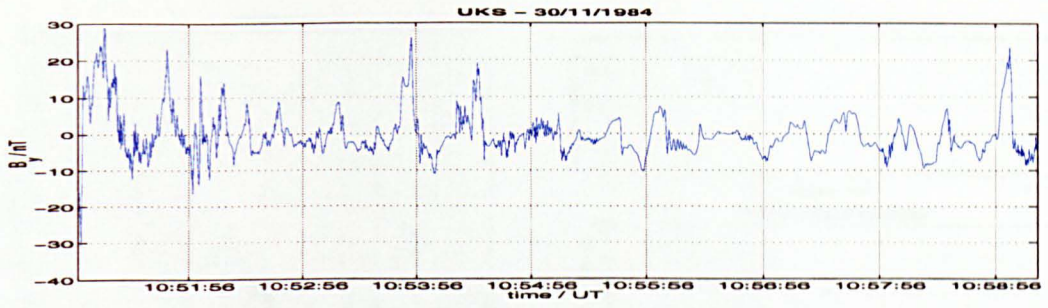

Figure 4.14: Magnetic field magnitude plot for 30/11/1984 10:55:00 to 10:58:00 UT (*UKS* satellite shown, *IRM* not shown for clarity).

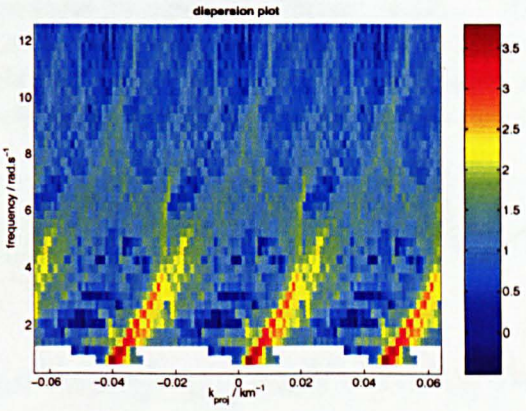

Figure 4.15: Initial dispersion plot for 30/11/1984. Satellite separation distance of 145 km. ω plotted against k_{proj}, the projection of the wave vector on the satellite separation vector. This dispersion is also linear, but with a phase and group velocity of $\approx$ 200 km/s.

is shown in Figure 4.14. In this interval the satellites were separated a distance $\sim$145 km.

For reasons given in Schwartz et al. [1992] (and as also seen from the dispersion in Figure 4.15 as this figure was produced with *UKS* as input and *IRM* as output), waves are propagating from *UKS* to *IRM*, so the data are ordered with *UKS* as input and *IRM* as output.

The dispersion in Figure 4.15 shows a phase speed of 200 km/s in the satellite rest frame.

The interval starting 10:55:30 UT, ending 10:56:30 UT is used to calculate the coherence functions (Figure 4.16) for a sliding window of 40 s width, incremented $\delta t = 1$s for 20 s, fixing the *UKS* window and sliding the *IRM* window. Again the general trend is for the coherence to decrease for increasing time delay.

The coherence length plot shown in Figure 4.17 shows an increase in coherence length for decreasing frequencies (upper panel) and roughly frequency independent coherence lengths in terms of

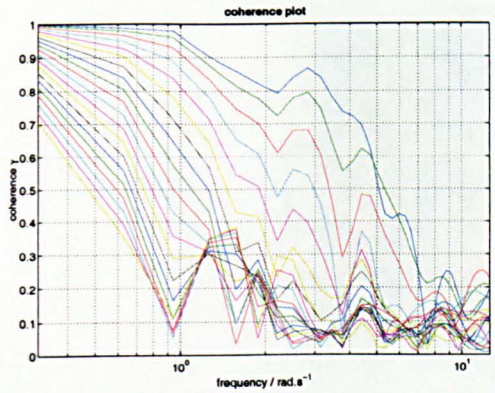

Figure 4.16: Coherence plots for 20 incremental time delays of 1 s. As the time delay increases the maximum coherent frequency (defined by an arbitrary cut-off value) decreases.

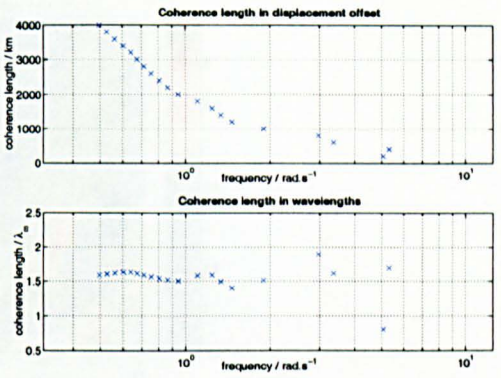

Figure 4.17: Coherence lengths for 30/11/1984. Shown against satellite separation in km (upper panel) and against number of wavelengths (lower panel).

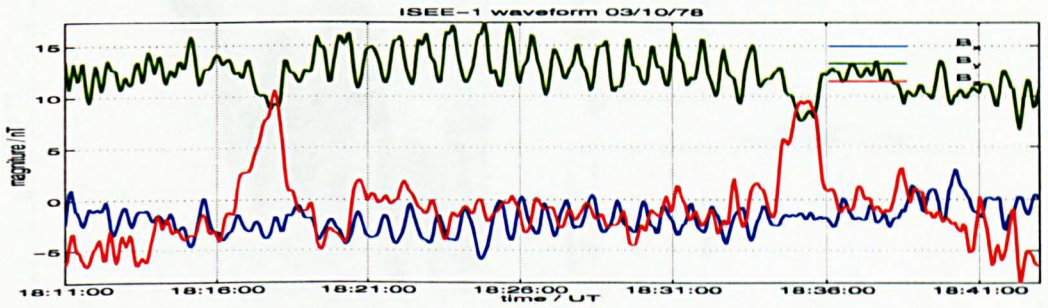

Figure 4.18: *ISEE-1* magnetic field measurements for 03/10/1978. The mirror structure can be seen between 18:19 and 18:35 UT (clearest in B_y).

wavelength (lower panel), the length ratio being on average no less than one and a half wavelengths.

4.5.3 Mirror waves in the magnetosheath

This data set is used to illustrate the surf method for visualising the coherence length.

The data intervals are the same as those found and studied by Fazakerley and Southwood [1994]. They found the data sets by looking through dual *ISEE* satellite measurements for obvious mirror wave signatures in the magnetic field. Their studies attempted to understand the spatial scale and orientation of the mirror structures. The two intervals of data were from 08/11/1977 and 03/10/1978. The magnetic field data shown is averaged over 4 seconds.

The magnetic field waveform measured by *ISEE-1* on 03/10/1978 for the interval 18:11:00 UT to 18:41:00 UT is shown in Figure 4.18. The mirror structure can be seen between 18:19:00 UT and

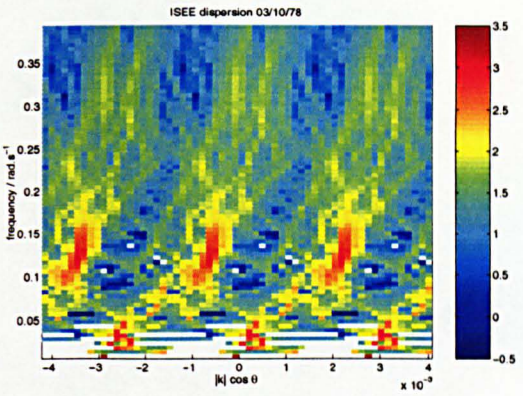

Figure 4.19: Dispersion relation for the 1978 data. These waves have a velocity in the satellite rest frame of approximately 70 km/s. The average satellite separation distance was 2232 km.

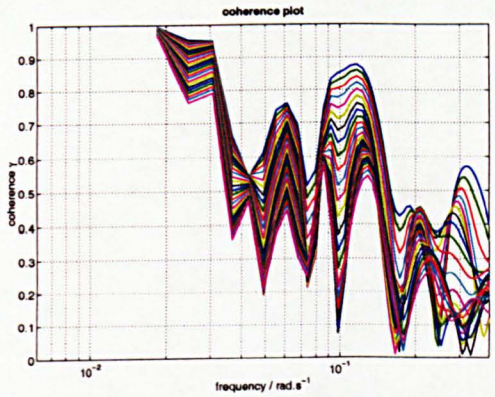

Figure 4.20: Coherence functions for *ISEE* magnetosheath waves observed in 1978. A 120 s sliding window was used, with steps $\delta t = 20$s.

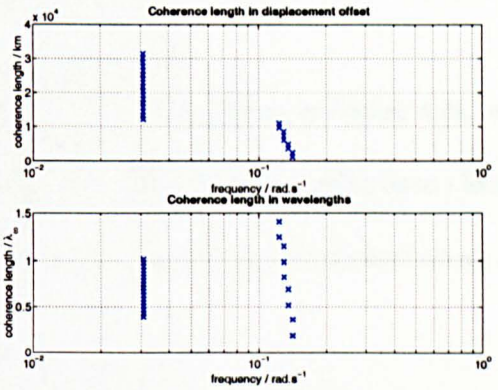

Figure 4.21: Coherence lengths for *ISEE* magnetosheath waves observed in 1978. Shown plotted against virtual satellite separation (top panel) and against number of wavelengths (bottom panel).

18:35:00 UT.

The interval chosen for analysis is the 10 minute period 18:21:00 UT to 18:31:00 UT. The satellite separation for this interval was 2232 km. The dispersion (Figure 4.19) shows a very broad branch, identifying the region corresponding to the mirror wave period of $\sim$ 50s ($\omega = 2\pi \times 0.02 \sim$ 0.125 rad/s) gives a phase speed of 70 km/s. The dispersion plot was constructed so that positive values along the abscissa indicate the direction from *ISEE-2* to *ISEE-1*. This figures shows waves propagating in the direction from *ISEE-2* to *ISEE-1*.

The ordering of the satellites can be made by inspecting the dispersion, *ISEE-2* is chosen as input, *ISEE-1* as output. A 120s sliding window is used, fixing the *ISEE-2* window and sliding the *ISEE-1* window in increments of $\delta t = 20$s. The coherence functions are shown in Figure 4.20.

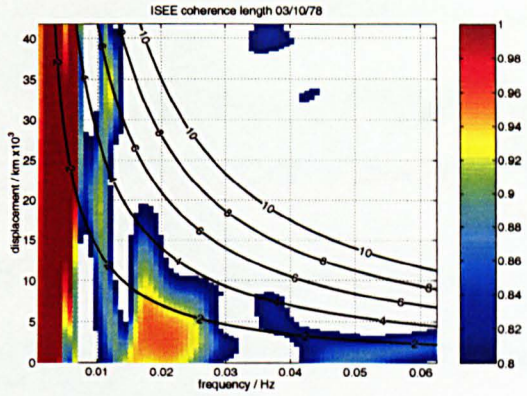

Figure 4.22: Coherence length surface plot for the 1978 data. The low frequency turbulence can be seen to be coherent over the range examined. The dominant frequency in the 1978 data corresponding to the mirror structure remains coherent over a spatial size up to 20×10^3 km, corresponding to roughly 5 wavelengths.

Using the strong cut-off method the coherence length found is shown in Figure 4.21, where a cut-off of 0.7 is used. Interpreting this figure, the indication is low frequency waves have a longer coherence length than higher frequency waves but in terms of wavelengths the coherent waves remain coherent for around one wavelength.

Figure 4.21 does not show all the information that can be obtained from the coherence functions in Figure 4.20, where many local maxima and minima can be seen. A way of visualising this information, as described in Section 4.4.2, is by making a surface plot of the coherence functions. This can be seen in Figure 4.22. Wave frequency is along the abscissa, displacement along the ordinate, and value of the coherence out-of-the-page, with red indicating high coherence. This can be compared with the upper panel of Figure 4.21, but instead of simply indicating the maximum coherent frequency for each time delay as a cross, *all* values of the coherence function are marked, colour-coded by value.

The mirror wave structure, of period 50 s (corresponding to a frequency of 0.02 Hz, 0.126 rad/s) can be seen from Figure 4.22 to be coherent up to distances of 20×10^3 km. There is also a component at frequency 0.01 Hz (0.063 rad/s) that has a high coherence over 40×10^3 km. The detail in Figure 4.20 is preserved, and enables a clearer interpretation of the information.

Superimposed on Figure 4.22 is a contour plot indicating coherence length in terms of wave-

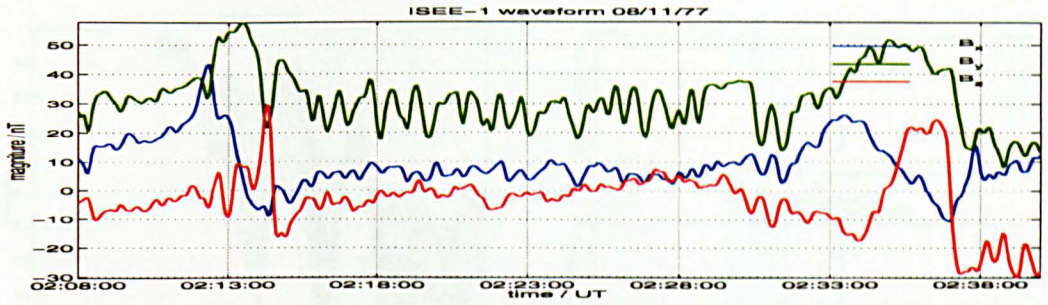

Figure 4.23: *ISEE-1* magnetic field measurements for 08/11/1977. The mirror structure can be seen between 02:16 and 02:32 UT (clearest in B_y).

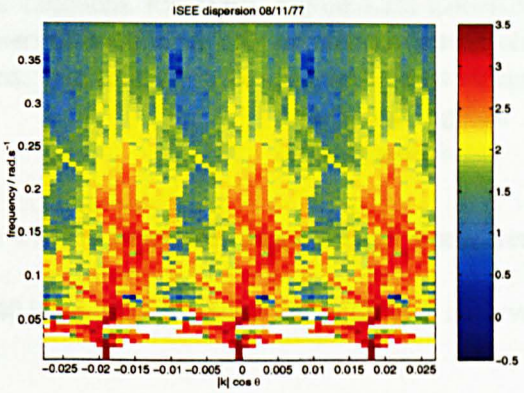

Figure 4.24: Dispersion relation for the 1977 data. These waves have a velocity in the satellite rest frame of approximately 40 km/s. The average satellite separation distance was 339 km.

length. The contours are closely spaced for higher frequencies and spread further for lower frequencies.

The mirror wave structure has a coherence length over 4 wavelengths. From Figure 4.18 the structure appears longer. As shown in Section 4.2.4 the coherence function is sensitive to phase changes, comparing the 5 minute interval to the left and right of 18:26:00 indicates a slight compression of the structure for later times, decreasing the period of oscillation inside the structure, which would also account for the broad width of the peak near f = 0.02 Hz spreading to higher frequencies.

A second interval identified by Fazakerley and Southwood [1994] was on 08/11/1977. *ISEE-1* measurements can be seen in Figure 4.23. The satellites were separated by 339 km. The mirror structure is clear between 02:16:00 UT and 02:32:00 UT, associated with oscillation periods of 50s (frequency 0.02 Hz, 0.126 rad/s).

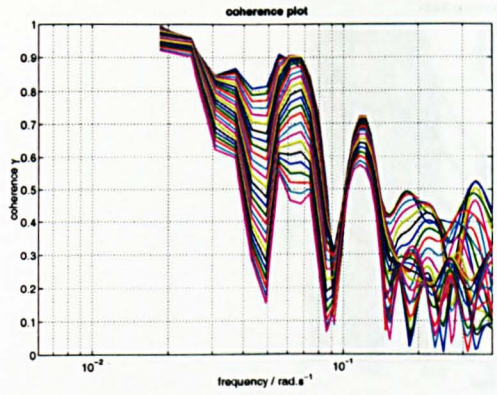

Figure 4.25: Coherence functions for *ISEE* magnetosheath waves observed in 1977. A 120 s sliding window was used, with steps $\delta t = 20$ s.

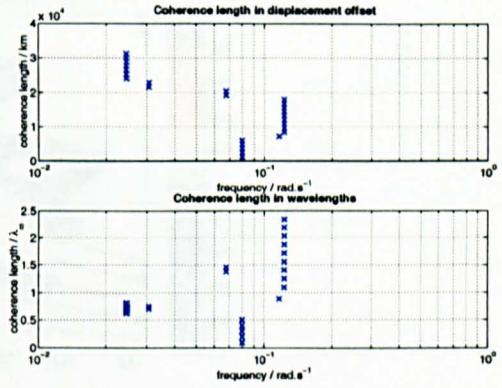

Figure 4.26: Coherence lengths for *ISEE* magnetosheath waves observed in 1977. Shown plotted against virtual satellite separation (top panel) and against number of wavelengths (bottom panel).

The dispersion (Figure 4.24) is very broad but a general linear trend of the dispersion branch indicates a phase speed of 40 km/s. In the satellite frame *ISEE-2* observes the waves before they are swept past to *ISEE-1*.

The time interval 02:18:00 UT to 02:28:00 UT is analysed by a 120s sliding window incremented in delays of $\delta t = 20$s, with the *ISEE-2* window fixed and the *ISEE-1* window free. The coherence functions can be seen in Figure 4.25.

The coherence lengths found using the strong cut-off method, with a cut-off of 0.7, are shown in Figure 4.26. Although both high, the coherence level for the range near $\omega = 0.065$ rad/s (f=0.01 Hz) briefly dips below the coherence for the range $\omega \sim 0.12$ rad/s (f$\sim$0.02 Hz) as δt increases. This not obvious behavior explains the apparent increase in coherent frequency with increasing separation δr (Figure 4.26, upper panel).

This behaviour does not effect the coherence lengths when viewed using the surf method (Figure 4.27). Here the mirror wave structure (corresponding to f$\sim$0.02 Hz, $\omega \sim 0.065$ rad/s) remains coherent over 8 wavelengths.

An interesting feature of this figure is the maxima in the region around $f \sim 0.04$ Hz and $10 \times 10^3 < \delta r < 20 \times 10^3$ km. This indicates a region of coherent waves that initially were not coherent. It could be interpreted physically as an indication that the satellites are near a generating region, the

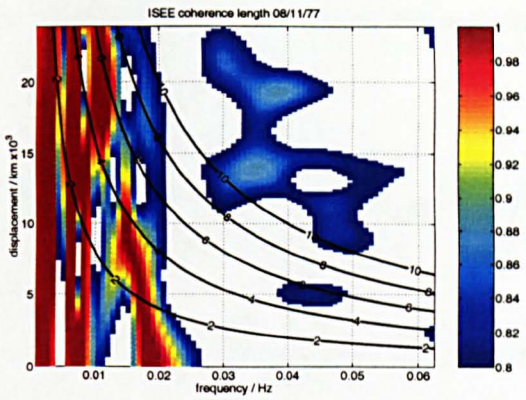

Figure 4.27: Coherence lengths for the 1977 data. The low frequency turbulence can be seen to be coherent over the range examined. The dominant frequency in the 1977 data corresponding to the mirror structure remains coherent over a spatial size up to 15×10^3 km, corresponding to roughly 6 wavelengths.

coherence only becoming apparent further away from the generation region. More likely is that it is a non-physical effect, something similar was seen in Section 4.2.4 when testing the sensitivity of the coherence function to phase changes, a point where the number of phase changes was high yet a the coherence function returned a high value, even though the waves should be deemed incoherent.

4.5.4 Discussion

The datasets were identified by Fazakerley and Southwood [1994] by the criteria that both *ISEE* satellites should show some mirror wave signature in their measurements. For the 1978 interval this criteria was met properly, accounting for the time delay between the satellites (Figure 4.28, lower panel). The waveforms show a good match visually. However for the 1977 data (upper panel) the visual correlation is not so good. Fazakerley and Southwood [1994] argued that it could be explained by considering that one of the satellites could just be skimming the edge of the mirror structure, sampling the structure only intermittently. Continuing with that assumption they made physically sound conclusions. The validity of their claim can be seen in Figure 4.27 as the period corresponding to the mirror waves structure (f$\sim$0.02 Hz) shows as being coherent.

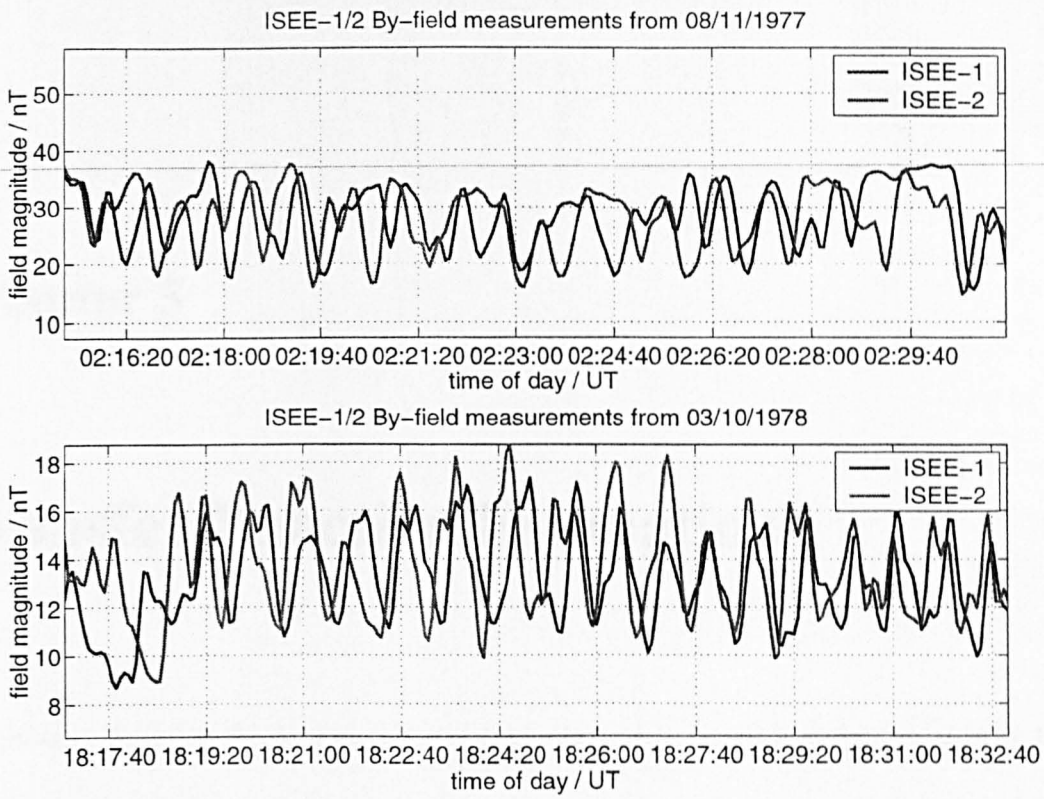

Figure 4.28: Visual correlation of the two mirror waves events identified in the *ISEE* data set. Shown is the 1977 data (top panel) and the 1978 data (bottom panel).

4.6 Summary

A statistical stationarity test is combined with the Shift Theorem to form the basis for a method to derive coherence lengths for waves and structures from (at least) dual satellite measurements. Applications of the method with two different visualisation methods are made with real dual satellite data.

Use of previous satellite measurements to determine this coherence length has implications for future multi-satellite missions. The relation between the waves of interest and their corresponding scale lengths is useful when considering satellite separation strategy. For instance, it is a factor that will influence the *CLUSTER II* measurements.

Chapter 5

Transfer Function Estimation

This chapter describes the development and application of a statistical method to identify linear (wave growth or damping) and second-order (wave-wave) interactions in developed space plasma turbulence.

Information about wave-wave interactions can be obtained by analysing wave signatures in simultaneous dual magnetic field measurements. The necessary parameters are derived, after transforming the measurements to the frequency domain, by applying system identification techniques, using Regularisation methods for the inversion problem.

Dual magnetic field measurements taken just inside the magnetosheath behind the Earth's bow shock, by the *AMPTE UKS* and *AMPTE IRM* satellites, are analysed with this method. A linear instability is identified which is attributed to an ion anisotropy and energy involved with the instability is shown to be redistributed via second order wave interactions to higher frequencies.

5.1 Introduction

A method for analysing turbulent plasma, combining dual-point measurements and frequency domain analysis, was first proposed by Ritz and Powers [1986]. They took laboratory based measurements of the turbulence at the edge of a Tokamak Plasma Generator with Langmuir probes.

Initially they proposed and used an iterative method to solve for the system transfer functions, then they introduced a direct Least Squares solution [Kim and Powers, 1988]. The method they used has been adapted to measurements in space plasmas [deWit et al., 1999] and modified to account for dispersive waves in the plasma [McCaffrey et al., 1999].

As a reminder from Chapter 2, the transfer function estimation method takes a *Black Box* approach to the problem of identifying plasma processes. Progress is made by assuming a form for, and finding parameters of, a suitable model of the plasma system.

A suitable form can be arrived at by a mathematical approach to the problem of the evolution of nonlinear dynamics. Despite the formalism the result is reasonably intuitive. As in deWit et al. [1999] the dynamics of the wave-field $B(x,t)$ can in general be described by,

$$\frac{\partial B(\mathbf{x},t)}{\partial \mathbf{x}} = \mathcal{F}\left(B(\mathbf{x},t)\right) \tag{5.1}$$

where $B(\mathbf{x},t)$ describes the wave-field at position $\mathbf{x}$ and time t, and $\mathcal{F}$ is (in general) a non-linear operator. The simplest case, when the operator $\mathcal{F}$ is linear, the system can be represented by a first order integral,

$$\frac{\partial B(\mathbf{x},t)}{\partial \mathbf{x}} = \int_0^\infty h(\tau)B(\mathbf{x},t-\tau)d\tau$$

where $h(\tau)$ is the impulse response function. This has a convenient frequency domain representation, found by taking Fourier Transforms of both sides,

$$\frac{\partial B(\mathbf{x},\omega)}{\partial \mathbf{x}} = H(\omega)B(\mathbf{x},\omega)$$

where $B(\mathbf{x},\omega)$ is the Fourier Transform of the wave-field, and $H(\omega)$ that of the impulse response function.

For the more general case, when $\mathcal{F}$ contains higher order terms, the system can be represented

as a sum of higher order integrals,

$$\frac{\partial B(\mathbf{x},t)}{\partial \mathbf{x}} = \int_0^\infty h(\tau)B(\mathbf{x},t-\tau)d\tau$$
$$+ \int_0^\infty \int_0^\infty h_2(\tau_1,\tau_2)B(\mathbf{x},t-\tau_1)B(\mathbf{x},t-\tau_2)d\tau_1 d\tau_2$$
$$+ \int_0^\infty \int_0^\infty \int_0^\infty h_3(\tau_1,\tau_2,\tau_3)B(\mathbf{x},t-\tau_1)B(\mathbf{x},t-\tau_2)B(\mathbf{x},t-\tau_3)d\tau_1 d\tau_2 d\tau_3$$
$$+ \cdots$$

where $h_i(\tau_1,\ldots,\tau_i)$ are the (ith) higher order generalisation of the impulse response function. This equation too has a frequency domain form [Rugh, 1981],

$$\frac{\partial B(\mathbf{x},\omega)}{\partial \mathbf{x}} = H(\omega)B(\mathbf{x},\omega)$$
$$+ \int H_2(\omega_1,\omega_2)B(\mathbf{x},\omega_1)B(\mathbf{x},\omega_2)\delta(\omega_1+\omega_2-\omega)d\omega_1$$
$$+ \iint H_3(\omega_1,\omega_2,\omega_3)B(\mathbf{x},\omega_1)B(\mathbf{x},\omega_2)B(\mathbf{x},\omega_3)\delta(\omega_1+\omega_2+\omega_3-\omega)d\omega_1 d\omega_2$$
$$+ \cdots$$

where $H_i(\omega_1,\ldots,\omega_i)$ are known as the ith order kernels of the system.

In the remainder of this chapter it will be understood that the relation $\sum_i \omega_i = \omega$ holds, with this understanding the delta function $\delta(\sum_i \omega_i - \omega)$ can be removed from the integrands.

Proceeding, the frequency domain model is truncated after the second order term,

$$\frac{\partial B(\mathbf{x},\omega)}{\partial \mathbf{x}} = H(\omega)B(\mathbf{x},\omega) + \int H_2(\omega_1,\omega_2)B(\mathbf{x},\omega_1)B(\mathbf{x},\omega_2)d\omega_1 \tag{5.2}$$

Noting that the wave-field $B(\mathbf{x},\omega)$ is a complex quantity with magnitude and phase, the partial

derivative on the LHS can be expanded,

$$\frac{\partial B(\mathbf{x},\omega)}{\partial \mathbf{x}} = |B(\mathbf{x},\omega)| \frac{\partial}{\partial \mathbf{x}} \exp i\psi(\mathbf{x},\omega) + \frac{\partial}{\partial \mathbf{x}} |B(\mathbf{x},\omega)| \cdot \exp i\psi(\mathbf{x},\omega)$$

and each of the two partial derivatives on the RHS of the above equation can be approximated by finite differences,

$$\begin{aligned}
\frac{\partial}{\partial \mathbf{x}} \exp i\psi(\mathbf{x},\omega) &= \exp i\psi(\mathbf{x},\omega) \cdot i \frac{\partial \psi(\mathbf{x},\omega)}{\partial \mathbf{x}} \\
&= \exp i\psi(\mathbf{x},\omega) \cdot i \frac{\psi(\mathbf{x}+\delta\mathbf{x},\omega) - \psi(\mathbf{x},\omega)}{\delta \mathbf{x}} \\
&= \exp i\psi(\mathbf{x},\omega) \cdot i \frac{\delta\psi(\mathbf{x},\omega)}{\delta \mathbf{x}}
\end{aligned}$$

and,

$$\frac{\partial}{\partial \mathbf{x}} |B(\mathbf{x},\omega)| = \frac{|B(\mathbf{x}+\delta\mathbf{x},\omega)| - |B(\mathbf{x},\omega)|}{\delta \mathbf{x}}$$

giving the finite difference approximation for the spatial partial derivative of the wave-field,

$$\frac{\partial B(\mathbf{x},\omega)}{\partial \mathbf{x}} = \exp i\psi(\mathbf{x},\omega) \left[|B(\mathbf{x},\omega)| \cdot i \frac{\delta\psi(\mathbf{x},\omega)}{\delta \mathbf{x}} + \frac{|B(\mathbf{x}+\delta\mathbf{x},\omega)| - |B(\mathbf{x},\omega)|}{\delta \mathbf{x}} \right]$$

Equating this to the truncated system model,

$$\exp i\psi(\mathbf{x},\omega) \left[|B(\mathbf{x},\omega)| \cdot i \frac{\delta\psi(\mathbf{x},\omega)}{\delta \mathbf{x}} + \frac{|B(\mathbf{x}+\delta\mathbf{x},\omega)| - |B(\mathbf{x},\omega)|}{\delta \mathbf{x}} \right] =$$

$$H(\omega)B(\mathbf{x},\omega) + \int H_2(\omega_1,\omega_2)B(\mathbf{x},\omega_1)B(\mathbf{x},\omega_2)d\omega_1$$

and rearranging leads to the new form for the system,

$$B(\mathbf{x}+\delta\mathbf{x},\omega) =$$

$$B(\mathbf{x},\omega)\,(H(\omega)\delta\mathbf{x}+1-i\delta\psi(\mathbf{x},\omega))\exp i\delta\psi(\mathbf{x},\omega)$$

$$+\,\delta\mathbf{x}\exp i\delta\psi(\mathbf{x},\omega)\int H_2(\omega_1,\omega_2)B(\mathbf{x},\omega_1)B(\mathbf{x},\omega_2)d\omega_1$$

or,

$$Y(\mathbf{x},\omega) = L(\omega)U(\mathbf{x},\omega) + \int Q(\omega_1,\omega_2)U(\mathbf{x},\omega_1)U(\mathbf{x},\omega_2)d\omega_1 \tag{5.3}$$

where,

$$Y(\mathbf{x},\omega) = B(\mathbf{x}+\delta\mathbf{x},\omega)$$

$$U(\mathbf{x},\omega) = B(\mathbf{x},\omega)$$

$$L(\omega) = (H(\omega)\delta\mathbf{x}+1-i\delta\psi(\mathbf{x},\omega))\exp i\delta\psi(\mathbf{x},\omega)$$

$$Q(\omega_1,\omega_2) = \delta\mathbf{x}\exp i\delta\psi(\mathbf{x},\omega)H_2(\omega_1,\omega_2)$$

The transfer functions (TFs) $L(\omega)$, $Q(\omega_1,\omega_2)$ appear now instead of the kernels $H_1(\omega)$, $H_2(\omega_1,\omega_2)$. The TFs and the kernels are closely related, although the system properties can still be discussed by considering only the TFs.

This equation expresses the relation between the ω-frequency component at the output satellite to the frequency components measured at the input satellite. That is, as the sum of both a linear modification of the ω component and a combination of frequency components ω_1, ω_2 whose sum is ω.

This is the form used by Ritz and Powers [1986], Ritz et al. [1989] where they considered probes fixed a distance δx apart in a laboratory-based tokamak, and by deWit et al. [1999] where

they considered space satellites separated a fixed distance δx apart. However it is also possible to consider the satellites separated in *time*, and this was the approach taken by McCaffrey et al. [1999].

The reasoning supplied just now to arrive at Eq. 5.3 is the same, only applied to a different wave-field description in Eq. 5.2. Instead of describing the wave-field as $B(\mathbf{x}, \omega)$ the spatial component is exchanged for a temporal one, i.e. the wave-field is described by $B(t, \omega)$, and the truncated system model becomes,

$$\frac{\partial B(t,\omega)}{\partial t} = H(\omega)B(t,\omega) + \int H_2(\omega_1,\omega_2)B(t,\omega_1)B(t,\omega_2)d\omega_1 \tag{5.4}$$

Following the derivation through arrives at the system transfer model Eq. 5.5, but with a temporal difference δt appears instead of a spatial difference $\delta \mathbf{x}$ appearing in the relation between the transfer functions and the kernels,

$$Y(t,\omega) = L(\omega)U(t,\omega) + \int Q(\omega_1,\omega_2)U(t,\omega_1)U(t,\omega_2)d\omega_1 \tag{5.5}$$

remembering the relation $\sum_i \omega_i = \omega$ holds, and where,

$$\begin{aligned} Y(t,\omega) &= B(t+\delta t,\omega) \\ U(t,\omega) &= B(t,\omega) \\ L(\omega) &= (H(\omega)\delta t + 1 - i\delta\psi(t,\omega))\exp i\delta\psi(t,\omega) \\ Q(\omega_1,\omega_2) &= \delta t \exp i\delta\psi(t,\omega)H_2(\omega_1,\omega_2) \end{aligned}$$

This is the significant difference that allowed McCaffrey et al. [1999] to account for dispersion in the wave-field. Waves at different frequencies propagate at different speeds, so different waves take different times to traverse a fixed distance. The dispersion, and phase/group velocities, of the waves can be found using the method in Section 2.2.6, the propagation time for each frequency can be

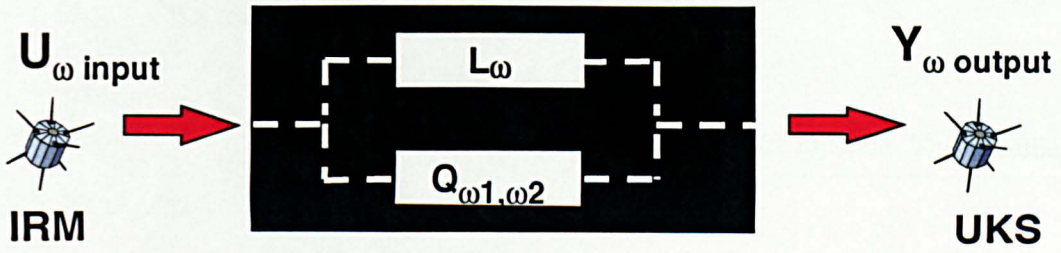

Figure 5.1: L, Q, black box. The form assumed for the plasma system Black Box. $L(\omega)$ modifies the input signal by a (complex valued) factor, $Q(\omega_1, \omega_2)$ modifies the input signal by a factor dependent on the presence, in the input signal, of waves with frequencies ω_1 and ω_2.

found,

$$\delta t(\omega) = \frac{\delta x \cos\theta}{c(\omega)}$$

where δx is the satellite separation distance, $c(\omega)$ is the phase speed of the wave at frequency ω, and $\cos\theta$ the factor accounting for the possibility the wave travels at an angle to the separation vector, a factor inherent with the dispersion calculation.

Eq. 5.5 forms the basis of what follows.

5.2 General Method

The form of the system is found by interpreting Eq. 5.5 in a system identification framework. Also, the integral in Eq. 5.5 is replaced with a discrete summation, as it is understood discrete spectral transforms are now being used. The form of the system transfer function is the sum of a linear and a quadratic transfer function (Figure 5.1).

5.2.1 Interpreting the System Model terms

The first term on the RHS of Eq. 5.5 is interpreted as the linear transfer function. This modifies the input by a gain factor and a phase shift,

$$Y(t,\omega) = L(\omega)U(t,\omega)$$

$$L(\omega) = |L(\omega)| \exp i\angle L(\omega)$$

where L is the linear transfer function, Y, U are the output and input signal spectral transforms, respectively, and ω is the target frequency. The modification appears in the output at the target frequency.

For $|L| = 1$, there is no change in the signal level between the observation points, at the target frequency component. Damping is indicated to occur when $|L| < 1$, and growth when $|L| > 1$. The phase of L, $\angle L$, indicates the amount of phase shift undergone between the observation points. This is related to the dispersion of the waves.

The second term on the RHS of Eq. 5.5 is interpreted as the quadratic transfer function. This also modifies the input with a gain and a phase shift, the modification appearing in the output at the target frequency, but is applied at the input to a linear combination of frequency components whose frequencies combine to the target frequency. By "combine" it is meant the following two relations hold,

$$\omega_1 + \omega_2 = \omega \tag{5.6}$$

$$\omega_1 - \omega_2 = \omega \tag{5.7}$$

where ω_1, ω_2 are the components of the input signal and ω is the target frequency. That is,

$$Y(t,\omega) = \sum_{\omega_1,\omega_2} Q(\omega_1,\omega_2)U(t,\omega_1)U(t,\omega_2)$$

$$Q(\omega_1,\omega_2) = |Q(\omega_1,\omega_2)| \exp i\angle Q(\omega_1,\omega_2)$$

where U, Y are the input and output signal spectral transforms, Q is the quadratic transfer function, ω_1, ω_2 are the input frequency components that combine (by Eq. 5.6, Eq. 5.7) to ω, the target frequency.

Eq. 5.6 is known as the sum interaction. It represents a wave-wave interaction where two waves of lower frequencies interact to produce a wave of a higher frequency. Eq. 5.7 is known as the difference interaction, representing an interaction where two waves produce a wave of frequency lower than at least one of the original waves. Beating is an example of such a phenomena, a superposition of two waves closely separated in frequency produce a wave whose frequency is the difference of the two original waves. These equations can be compared with the resonance conditions, Eq. 2.11. Such interactions are physically sustainable when both the target wave and the initial waves are modes of the plasma system [Krall and Trivelpiece, 1973]. The magnitude of the QTF indicates the strength of the wave-wave coupling. $|Q| \ll 1$ indicates little or no coupling, $|Q| \gg 1$ indicates strong coupling.

The system is solved to find the parameters describing L and Q. The input and output signals are transformed to the frequency domain at a discrete number of frequencies n_ω.

5.2.2 The Inversion Problem

By the process of making a discrete spectral transform, the output signal has been split into n_ω frequency components. By considering one of these components, a target frequency ω, Eq. 5.5 can

be expanded,

$$\begin{aligned} Y(t,\omega) &= L(\omega)U(t,\omega) \\ &+ Q(\omega_1,\omega_2)U(t,\omega_1)U(t,\omega_2) \\ &+ Q(\omega_1',\omega_2')U(t,\omega_1')U(t,\omega_2') \\ &+ \cdots \end{aligned}$$

where $\omega_1, \omega_2, \omega_1', \omega_2'$, ... denote combinations of discrete frequencies satisfying $\sum_i \omega_i = \omega$, and then re-written as a matrix equation for the target frequency ω,

$$\begin{bmatrix} U(t,\omega) & U(t,\omega_1)U(t,\omega_2) & U(t,\omega_1')U(t,\omega_2') & \cdots \end{bmatrix} \begin{bmatrix} L(\omega) \\ Q_\omega(\omega_1,\omega_2) \\ Q_\omega(\omega_1',\omega_2') \\ \vdots \end{bmatrix} = [\, Y(t,\omega) \,] \tag{5.8}$$

that is,

$$A\mathbf{x} = \mathbf{y} \tag{5.9}$$

with,

$$A = \begin{bmatrix} U(t,\omega) & U(t,\omega_1)U(t,\omega_2) & U(t,\omega_1')U(t,\omega_2') & \cdots \end{bmatrix} \qquad m \times n$$

$$\mathbf{x} = \begin{bmatrix} L(\omega) \\ Q_\omega(\omega_1,\omega_2) \\ Q_\omega(\omega_1',\omega_2') \\ \vdots \end{bmatrix} \qquad n \times 1$$

$$\mathbf{y} = [\, Y(t,\omega) \,] \qquad m \times 1$$

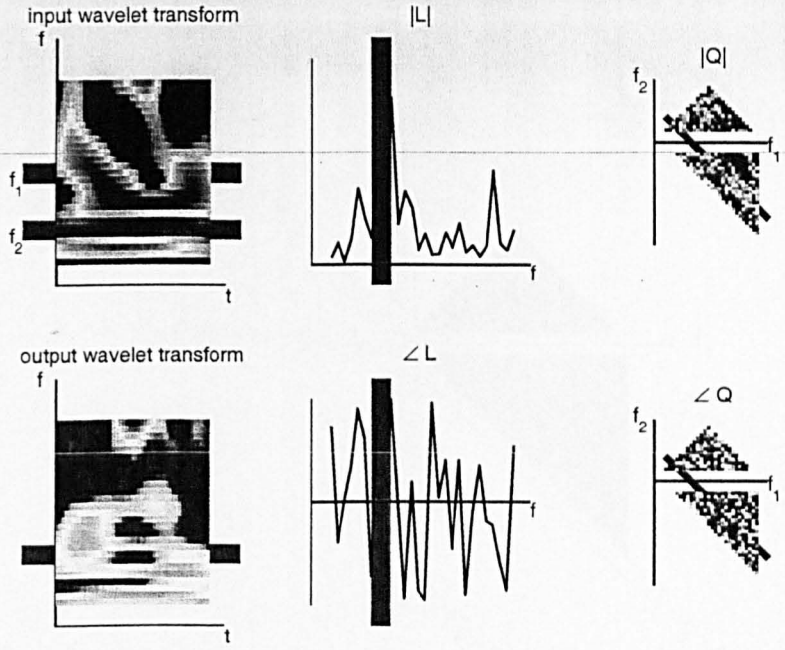

Figure 5.2: Algorithm for calculating the Transfer Functions. Consider a particular target frequency ω. The linear parameter $L(\omega)$ is determined by comparing the spectral magnitude and phase of the ω frequency component in the input and output data sets. The quadratic component $Q(\omega_1, \omega_2)$ is determined, for all pairs of frequencies satisfying $\omega_1 + \omega_2 = \omega$, by comparing the spectral magnitudes and phases of the frequency components ω_1, ω_2 in the input with those of the frequency component ω in the output. These are indicated as the shaded region. The full transfer functions are determined by repeating for all target frequencies.

where A is the matrix of input observations, $\mathbf{y}$ is a vector of observed outputs, $\mathbf{x}$ a vector containing the unknown parameters, m is the number of observations (i.e. for Wavelet Transforms samples in time) and n is the number of parameters to estimate. Again it should be noted that this equation is formed for a fixed target frequency, hence the reason $\mathbf{y}$ has dimensions $(m \times 1)$.

The system can be made over-determined by careful consideration of the length of the time interval and the choice of number of frequency components to split the signal into, that is ensuring there are more observations than unknowns $(m > n)$.

An inversion method is used to solve Eq. 5.9, that is to find the parameters $L(\omega)$, $Q_\omega(\omega_1, \omega_2)$ for the target frequency ω. Solving for one target frequency only provides information for one part of the transfer functions, see Figure 5.2. The process is repeated for all n_ω frequency components to build the whole transfer function.

The inversion is the significant operation. Least Squares has been applied to this problem in

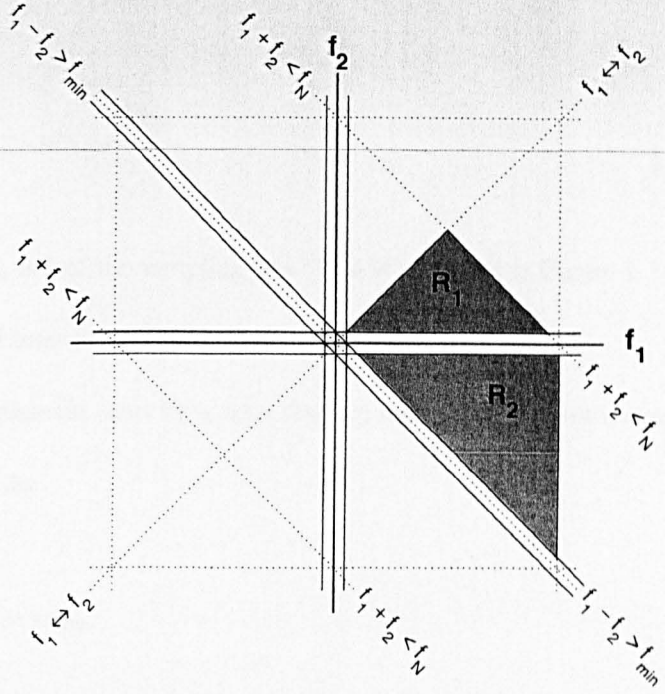

Figure 5.3: Frequency domain region. By considering properties of the data, symmetries and limits on resolvable frequencies, the second-order frequency domain range can be reduced from the full domain to the shaded region.

previous work, here a closely related technique, called Regularisation, is applied to the problem.

5.2.3 Reducing the number of parameters to estimate

For the linear transfer function there will be n_ω (complex) parameters to find. For the quadratic transfer function there will be $\approx n_\omega^2$ parameters. Subsequent terms in Eq. 5.2, if not truncated, would lead to n_ω^k, $k \in 3, 4, 5\ldots$ parameters, increasing exponentially the number of parameters to estimate with each extra term. Inclusion of an arbitrary number of higher order terms can make the method computationally expensive, and can also effect the stability of the solution. For these reasons it is desirable to consider ways to reduce the number of parameters to estimate.

The number or parameters to find can be reduced by considering the limits imposed by the discrete nature of the time series signal, and by observing some frequency symmetries. The frequency domain is reduced to that shown in Figure 5.3.

- The input frequencies must be less than the Nyquist frequency,

$$\omega_1, \omega_2 < \omega_{\text{Nyquist}}$$

where ω_{Nyquist} is half the sampling rate. This is indicated in Figure 5.3 by the horizontal and vertical dotted lines bounding the figure,

- The input frequencies must be greater than the minimum frequency, determined by the length of the time series,

$$\omega_1, \omega_2 > \omega_{\text{min}}$$

where the minimum frequency $f_{\text{min}} = 1/T$. This is indicated by the solid horizontal and vertical lines near the axis,

- The target frequency must be less than the Nyquist frequency. In Eq. 5.6 this gives,

$$\omega_1 + \omega_2 < \omega_{\text{Nyquist}}$$

- The target frequency must be greater than the minimum frequency. In Eq. 5.7 this gives,

$$\omega_1 - \omega_2 > \omega_{\text{min}}$$

- There is symmetry between the interchange of input frequencies, as this interchanges the order of multiplication of the input spectral components, and multiplication is commutative for complex numbers,

$$Q_\omega(\omega_1, \omega_2) = U(\omega_1)U(\omega_2) = U(\omega_2)U(\omega_1) = Q_\omega(\omega_2, \omega_1)$$

This is indicated in Figure 5.3 by the diagonal line marked $f_1 \leftrightarrow f_2$.

Applying these limits and symmetries leaves the shaded region shown in Figure 5.3. R_1 is the sum region, corresponding to the interaction described by Eq. 5.6, and R_2 is the difference region, corresponding to the interaction described by Eq. 5.7.

Truncation of an arbitrary high order system was made to arrive at Eq. 5.5. This clearly reduces the possible number of parameters to estimate, although generally it is not valid to arbitrarily truncate any series expansion, without reasonable cause, as the significance of the truncated terms may be greater than the untruncated terms. However it is possible to argue physically that it is possible to truncate at relatively low order.

The significance of a wave interaction is proportional to the product of the relative amplitudes of the waves involved. Higher order interactions involve higher numbers of waves, so these interactions become relatively less significant than lower order interactions. Waves with a linear dispersion allow second order wave interactions, by the above argument they will be more significant than higher order wave interactions. It follows that for a linearly dispersive wave field there is justification to truncate the model after the second order term.

5.3 Least-Squares Inversion

5.3.1 LS Inversion Method

The method in McCaffrey et al. [1999] and deWit et al. [1999] involved using the standard Least Squares (LS) method. Given the system in Eq. 5.9, the LS method first involves defining a cost function $J(\mathbf{x})$ (Eq. 5.10),

$$\begin{aligned} J &= |A\mathbf{x} - \mathbf{y}|^2 \\ &= (A\mathbf{x} - \mathbf{y})^T (A\mathbf{x} - \mathbf{y}) \end{aligned} \tag{5.10}$$

and then finding a vector, $\mathbf{x}_{LS}$, that minimises the cost function. This is the LS solution, and is found by setting the partial derivative of $J(\mathbf{x})$ w.r.t. $\mathbf{x}^T$ to zero,

$$\frac{\partial J}{\partial \mathbf{x}^T} = 2A^T A\mathbf{x} - 2A^T\mathbf{y} = 0$$

giving,

$$\mathbf{x}_{LS} = (A^T A)^{-1} A^T \mathbf{y} \tag{5.11}$$

The least-Squares (LS) solution has the advantage that it is an unbiased estimator in the sense that if a solution $\mathbf{x}$ is found that sets the functional $J(\mathbf{x}) = 0$ then the solution is accurate. The disadvantage is that when the problem is ill-posed, as the case usually appears to be when dealing with solar-terrestrial data sets, the LS solution has large uncertainties.

5.3.2 Test data description

The analytic forms for known transfer functions are presented here, along with details of how they are used to generate the test data.

The linear transfer function (LTF) was chosen so that the magnitude decreases parabolically, and the phase increases linearly with frequency,

$$|L(\omega)| = \begin{cases} 1 - \beta\omega^2 & \forall\ \omega^2 \leq 1/\beta \\ 0 & \text{otherwise} \end{cases} \qquad \angle L(\omega) = \alpha\omega$$

i.e.

$$L(\omega) = \left(\frac{1-\beta\omega^2}{1+\tan^2\alpha\omega}\right)^{\frac{1}{2}} (1 + i\tan\alpha\omega) \qquad \forall\ \omega^2 \leq 1/\beta \tag{5.12}$$

where β, α are parameters determining the particular scale of the curves.

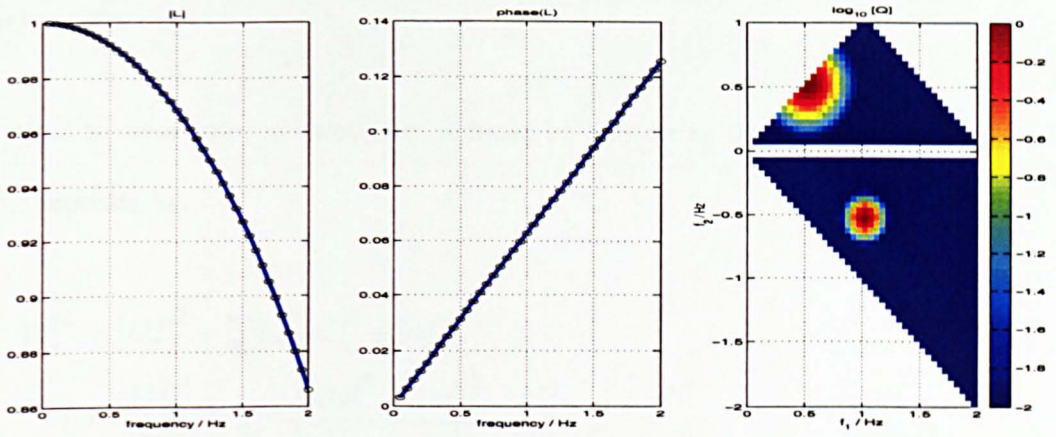

Figure 5.4: Known TFs. These are the transfer functions generated from Eq. 5.12 and Eq. 5.13. From left to right are $|L(\omega)|, \angle L(\omega), |Q(\omega_1, \omega_2)|$.

The quadratic transfer function (QTF) was chosen to consist of a magnitude given by the sum of Gaussian peaks, and to have constant phase,

$$\begin{aligned} |Q(\omega_1, \omega_2)| &= \sum_{i=1}^{N} \beta_i \exp -\frac{(\omega_1 - \omega_{1i})^2}{2\sigma_i^2} \cdot \exp -\frac{(\omega_2 - \omega_{2i})^2}{2\sigma_i^2} \\ &= \sum_{i=1}^{N} \beta_i \prod_{j=1}^{2} \exp -\frac{(\omega_j - \omega_{ij})^2}{2\sigma_i^2} \end{aligned} \tag{5.13}$$

$$\angle Q(\omega_1, \omega_2) = \alpha$$

where N is the number of peaks, β_i, σ_i the magnitude and 'spread' of each peak, and $(\omega_{1i}, \omega_{2i})$ the centre of each peak in frequency space. These transfer functions are shown in Figure 5.4.

The input data is chosen as the wavelet transform of real magnetic field measurements, made by the *AMPTE UKS/IRM* dual satellites and described later. For the purpose of generating surrogate data it is sufficient to say that an arbitrary one minute period ($60 \times 8 = 480$ samples) of the y component magnetic field measured by *AMPTE IRM* is used to find the input wavelet transform, with a frequency mesh $n_\omega = 40$. The output wavelet transform was generated by modifying the input according to the assumed system model (given in Eq. 5.5) with these transfer functions. Noise is introduced into the generation with the addition of a random Gaussian distributed noise term on the RHS of Eq. 5.5, $\alpha\zeta$, where ζ is chosen from a zero-mean unity deviation Gaussian distribution ($\zeta \in \mathcal{N}[0, 1]$), and α varies the signal to noise ratio.

Signal to noise ratio

The signal to noise ratio, in terms of α, is found by considering the relative power each term in Eq. 5.5 provides, i.e.,

$$
\begin{aligned}
|Y|^2 &= |LU|^2 + \sum |QUU|^2 + |\alpha\zeta|^2 \\
1 &= \frac{|LU|^2}{|Y|^2} + \sum \frac{|QUU|^2}{|Y|^2} + \frac{|\alpha\zeta|^2}{|Y|^2} \\
1 &= (1-\beta) + \beta
\end{aligned}
$$

where β is the fraction of power due to the noise term, and $(1-\beta)$ the power due to the the model terms. The noise term, $\beta = \frac{|\alpha\zeta|^2}{|Y|^2}$, can be estimated by considering,

$$
\begin{aligned}
|Y|^2 &\sim 10^2 \\
|\zeta|^2 &\sim 10^1
\end{aligned}
\qquad\qquad
\therefore \frac{|\alpha\zeta|^2}{|Y|^2} \sim \frac{10\alpha^2}{100} = \frac{\alpha^2}{10}
$$

The percentage of noise in the signal, for a given α, is,

$$
\%_{\text{noise}} = 100\frac{\alpha^2}{10} = 10\alpha^2 \tag{5.14}
$$

The input wavelet transform and the generated output wavelet transform are the data sets used in the following.

5.3.3 LS and noise

In this section the TFE method is demonstrated with surrogate data, generated with a known TF. The LS method is shown to extract the known TFs from the surrogate data in the absence of noise, although the estimation in the presence of noise is shown to be not so good.

The first surrogate data set considered is one generated without any noise, $\alpha = 0$. The results

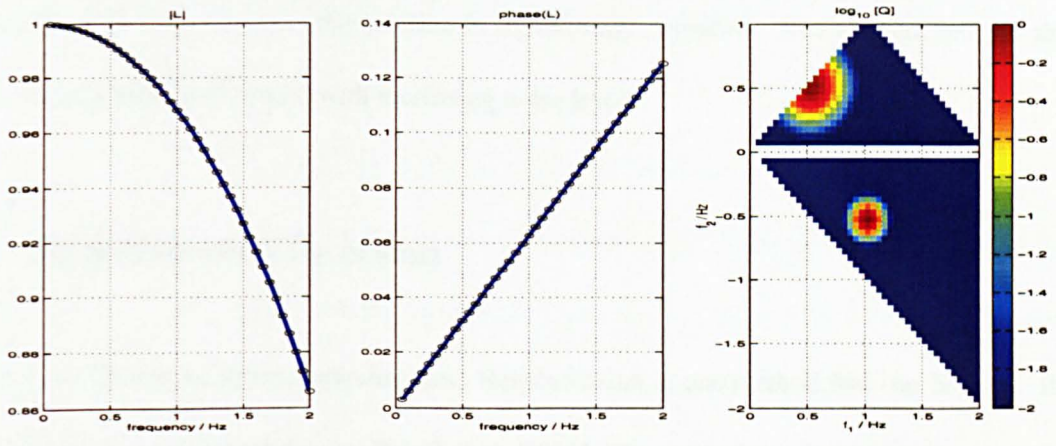

(a) These are the LS estimated transfer functions.

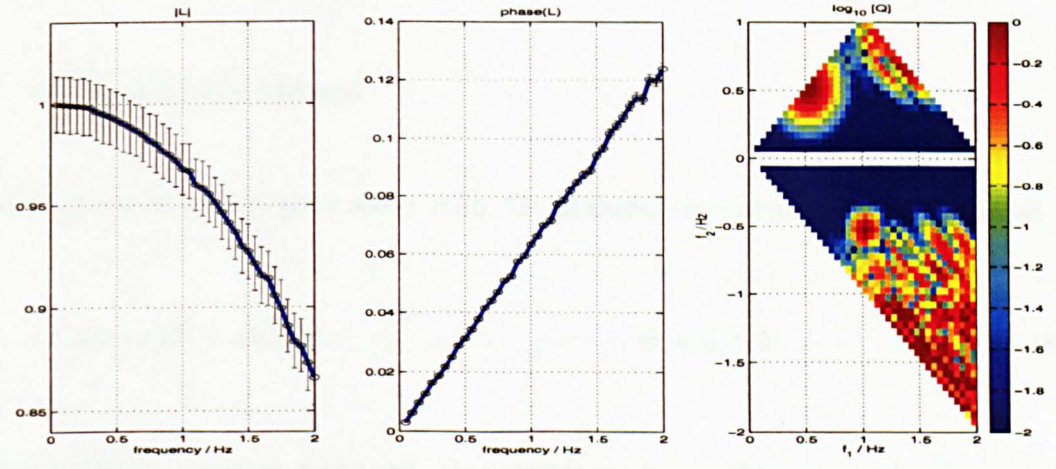

(b) These are the LS estimated transfer functions, with added noise.

Figure 5.5: LS and noise. From left to right, in each figure, are $|L(\omega)|$, $\angle L(\omega)$, $|Q(\omega_1, \omega_2)|$.

using the TFE method are shown in Figure 5.5. The LS inversion results in the TFs shown in Figure 5.5(a). There is a precise and accurate match with the actual TFs (Figure 5.4).

All real systems are effected to some extent by noise. The second data set considered is one generated including the noise term $\alpha\zeta$. The value chosen for α was 0.2, giving the output signal a 0.4% noise content (Eq. 5.14). The estimated TFs can be seen in Figure 5.5(b). Even for such an apparently low level of noise, the solution is significantly degraded. As expected, but not shown here, the degradation increases with increasing noise levels.

5.4 Regularisation Inversion

There exist alternative inversion techniques. Regularisation is one method that can be used. It has been applied to geophysical data by Beloff et al. [2001]. The method can yield improvements to the LS solution when the inversion is ill-posed [Nastasyina-Beloff et al., 2000].

5.4.1 REG Inversion Method

Assuming the same system, given above in Eq. 5.9, an alternative cost function can be formed,

$$J = |A\mathbf{x} - \mathbf{y}|^2 + \alpha \mathbf{x}^T C\mathbf{x} \qquad 0 < \alpha < 1 \tag{5.15}$$

where C is called a stabiliser matrix and α is a tunable parameter. The next step is the same as the LS method, that is the cost function is minimised to find the solution $\mathbf{x}_{REG}$,

$$\frac{\partial J}{\partial \mathbf{x}^T} = 2A^T A\mathbf{x} - 2A^T\mathbf{y} + 2\alpha \mathbf{x}^T C\mathbf{x} = 0$$

giving,

$$(A^T A + \alpha C)\mathbf{x} = A^T \mathbf{y}$$

$$\mathbf{x}_{REG} = (A^T A + \alpha C)^{-1} A^T \mathbf{y} \tag{5.16}$$

This is similar to the LS solution, with the exception that the stabiliser matrix now appears inside the inversion operator.

When a problem is ill-posed, the matrix to invert has eigenvalues separated far away from each other in magnitude, the inversion process becomes unstable, large errors are produced. The inclusion of a stabiliser matrix can act to balance the offset in magnitude of the eigenvalues of the matrix to invert, resulting in a more stable inversion, i.e. smaller errors are produced.

The next step in the Regularisation technique is to find an optimal value of α, α_{opt}. This is done by substituting this solution back into the cost function Eq. 5.15, and minimising w.r.t α,

$$\alpha_{opt} : \left.\frac{\partial J}{\partial \alpha}\right|_{\alpha_{opt}} = 0 \tag{5.17}$$

This in general has no simple analytic solution. Practically a numerical function minimisation routine is used to find the optimum value. Implementations of numerical function minimisation routines can be found in Press et al. [1992].

The REG solution is,

$$\mathbf{x}_{REG} = (A^T A + \alpha_{opt} C)^{-1} A^T \mathbf{y} \tag{5.18}$$

The inclusion of the stabiliser term acts to reduce the errors in the inversion, at the expense of introducing bias into the solution. For $\alpha_{opt} = 0$ the problem reduces to the LS problem, with the same solution as for LS. For α_{opt} near 0, Regularisation is needed to reduce the inversion errors, but

only slightly biasing the solution. For α_{opt} near 1, the need for Regularisation is strong, improvement to the inversion is made, also introducing a strong bias.

5.4.2 Stabiliser Matrix forms

Three forms for the stabiliser matrix are considered.

$$C = I_{n\times n} \tag{5.19}$$

This stabiliser is just the identity matrix, acting by augmenting the diagonal entries of the data matrix by one. The relative change for entries much smaller than one is great, for entries much greater than one the relative change is small, so this stabiliser treats cases where there are diagonal entries much less than one.

$$C = (A^T A)^{-1} \tag{5.20}$$

This stabiliser is the inverse of the data matrix. Here the idea is that this inverse matrix itself contains information weighted accordingly to act to stabilise the inversion in Eq. 5.18.

$$C = \text{diag}\left\{\lambda_i^{\alpha k}\right\} \tag{5.21}$$

An ill-posed problem can be characterised by the eigenvalues if the data matrix being separated over several orders of magnitude. The idea for choosing Eq. 5.21 as the stabiliser matrix comes from the concept of stabilising the inversion by balancing the eigenvalues of the data matrix.

The scaling parameter α also appears in Eq. 5.21. For α near 0 the stabiliser is similar to

the identity matrix stabiliser, Eq. 5.19. For α near 1 the magnitude separation of the eigenvalues becomes more pronounced. A factor k also appears in the exponent of Eq. 5.21. This controls the sensitivity of the eigenvalue changes to α. A value $k = 1/2$ is chosen without further comment.

Each one of these three stabiliser matrices will be shown to improve on the LS solutions, but as described each act in a different manner.

5.4.3 REG and noise

The Transfer Function Estimation (TFE) method is demonstrated with surrogate data, generated by a known Transfer Function (TF). The Regularisation technique (REG), in the presence of noise, is shown to reproduce the known TF more accurately than the LS method.

The data used is the same as described in Section 5.3.2. For the case where there is no noise in the data set the REG method, for all the stabiliser matrices, match the LS solution and reproduce the original TFs. The case where the noise is introduced into the data set is presented here. Again, the noise level is selected with $\alpha = 0.2$ to give a signal noise content of 0.4%.

The REG solutions, for each of the stabiliser matrices in Eq. 5.19, Eq. 5.20, Eq. 5.21, are given in Figure 5.6. The LTF is reproduced, with a similar level of error as the LS solution. However the original form of the TF is maintained. The QTF shows some indication of noise, but the level appears much lower than the LS case.

Ill-posed systems are sensitive to small changes in the data. The case presented here, of adding a low level of noise to the data, illustrates the ill-posed nature of this system. The LS inversion is sensitive to this ill-posed nature; the REG inversion is designed with the ill-posed nature in mind. Here the REG method can be seen to be more appropriate for solving this problem.

The choice of which stabiliser to use, based on this case, is arbitrary. All manage apparently equally well. For individual cases it would be necessary to compare the solutions provided by all three stabiliser matrices to see which is best.

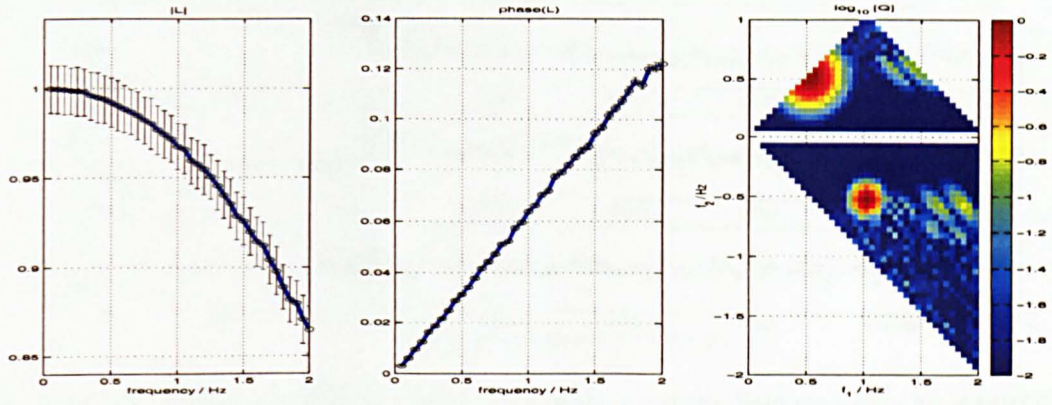

(a) Using the stabiliser matrix given by Eq. 5.19.

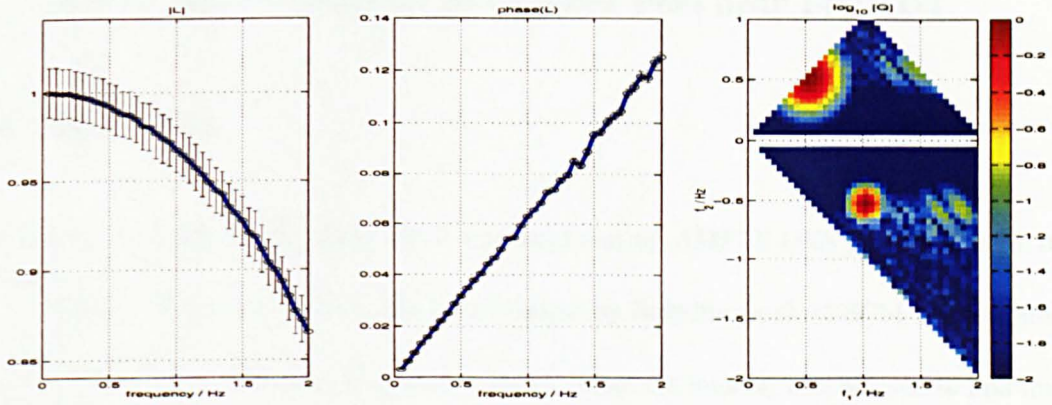

(b) Using the stabiliser matrix given by Eq. 5.20.

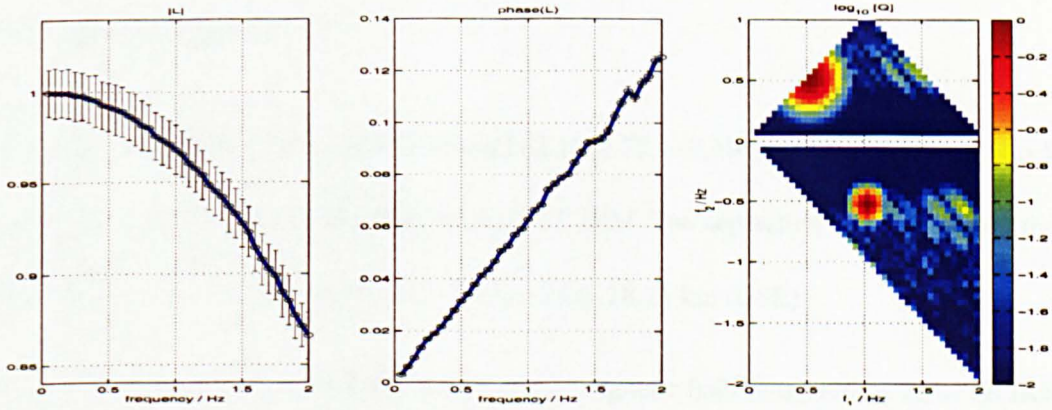

(c) Using the stabiliser matrix given by Eq. 5.21.

Figure 5.6: REG and noise. From left to right, in each figure, are $|L(\omega)|$, $\angle L(\omega)$, $|Q(\omega_1, \omega_2)|$.

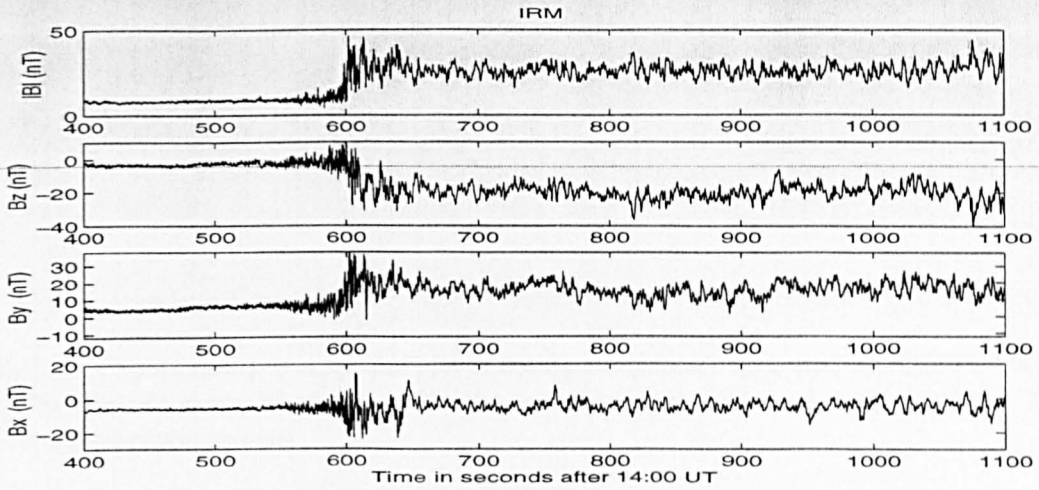

Figure 5.7: Absolute value and three components of the magnetic field measured by *AMPTE IRM* during the bow shock crossing which occurred at about 14:10:00 UT on 20.10.1984. Time scale is in seconds after 14:00:00.

5.5 Bow Shock Crossing on 20 October 1984 near 14:10 UT

5.5.1 Introduction

We consider the Earth's bow shock which was measured by *AMPTE UKS* and *IRM* at 14:10 UT on 20 October 1984. This interval has been studied by Balikhin et al. [1997b] to determine the dispersion of waves downstream of the Bow Shock. Here the interval will be used to find transfer functions in the region, using the method described in this chapter.

5.5.2 Data description

The position of *AMPTE UKS* at 14:10 UT was $(12.19, 0.77, -0.40)$ R_E(GSE). The bow shock was crossed first by *AMPTE UKS* and then by *AMPTE IRM*. The separation vector between the two satellites during the crossing was $\delta\mathbf{r} = (-50.5, -24.6, 18.2)$ km (GSE).

Three components and the absolute values of the magnetic field measured by *AMPTE IRM* are shown in Figure 5.7. The time scale on these figures is seconds after 14:00:00 UT. In the downstream region, waves observed from 650 sec to 1100 sec (corresponding to the time interval from 14:10:50 to 14:18:20 UT) are studied.

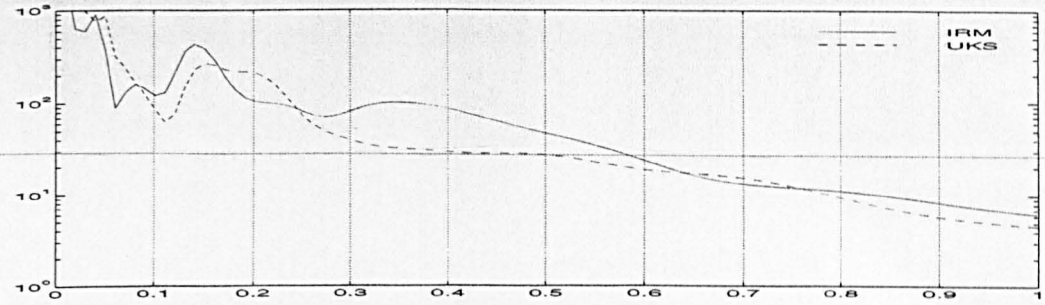

Figure 5.8: Wavelet auto power spectra plot of the B_y components measured by *AMPTE UKS* and *IRM*. The abscissa shows frequency in Hz, the ordinate showing power density in nt^2/Hz. Morlet wavelet transforms were used.

The angle between the upstream magnetic field and the normal to shock front, estimated on the basis of the co-planarity theorem, was $\approx 50°$. Observed features of the turbulence are usual for the quasi-perpendicular shocks. In the foot the main part of the wave energy resides in the frequency range from about one to a few Hz. In this frequency range the waves are whistlers. As the satellite approaches the downstream region, the wave frequency drops. The main energy of the turbulence is present in the downstream region in the frequency range 0–1.5 Hz. These are the waves that are studied here.

The dispersion relation of these waves in the plasma rest frame was obtained by Balikhin et al. [1997b]. These waves are convected by the solar wind flow from *AMPTE IRM* towards *AMPTE UKS*. Thus the *IRM* data set was considered as the input and the *UKS* data set as the output. The y component of the magnetic field is studied in the following.

The B_y^{IRM} and B_y^{UKS} measurements are used to calculate the power spectra (shown in Figure 5.8). The spectra are not smooth but have a number of local maxima. There are regions where the *UKS* spectrum is less than the *IRM* spectrum, indicating there is a decrease of energy contained in those regions as the waves propagate between the satellites. There are regions where the reverse is true, regions where the *UKS* spectrum is greater than the *IRM* spectrum, most notably below 0.1 Hz, near 0.2 Hz and near 0.7 Hz. This indicates an increase of energy contained in those regions. It is not possible from this figure to conclude anything about the mechanisms involved in changing the energy levels.

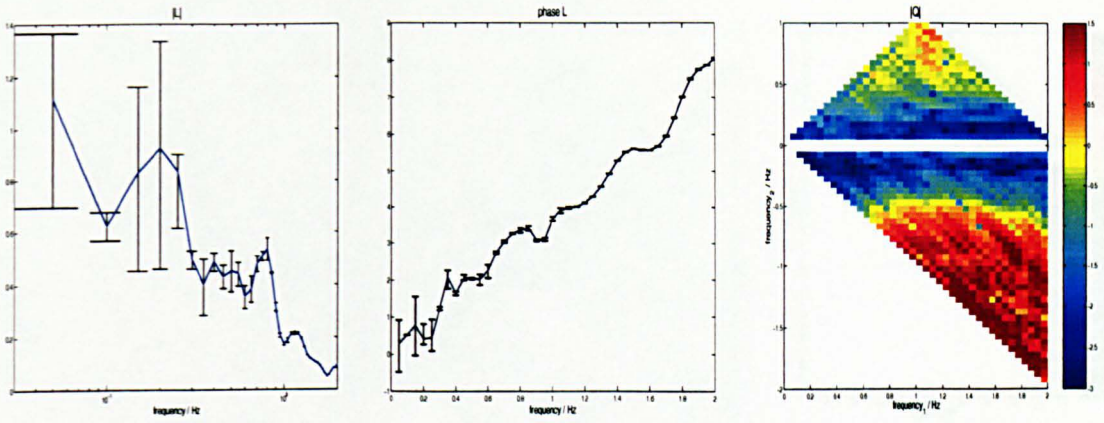

(a) $|L|$. (b) phase(L). (c) $|Q|$.

Figure 5.9: Least Squares Transfer Function Estimates.

5.5.3 Results

The transfer function estimation, described in this chapter, is now made. The results of the LS estimation can be seen in Figure 5.9. The magnitude of the LTF is shown in Figure 5.9(a). It shows, within errors, that waves are linearly damped over almost the whole frequency range. The exception is very low frequency waves (less than 0.1 Hz) and for waves near 0.2 Hz. This corresponds with the inspection of the power spectra earlier. This provides evidence that a linear instability is pumping energy, from the plasma particles , into the wave turbulence in the frequency range $f < 0.1$ Hz and $f \sim 0.2$ Hz. Also observed in the power spectra was the increase in power in the frequency region near 0.7 Hz. There is something to be seen in the LTF in this region, but the LTF does not fully account for the growth inferred from the power spectra.

The phase of the LTF is shown in Figure 5.9(b). It corresponds to the phase shift undergone by the waves as they propagate between the satellites, this is a measure of the dispersion of the waves. This data set has been used by Balikhin et al. [1997b] to find the dispersion, a check can be made that the values here correspond with those in their paper. An intermediate step in Balikhin et al. [1997b] determined the phase gradient for the waves $\frac{\partial \psi}{\partial \omega} = 0.75$ s, which was then used to find the dispersion. From Figure 5.9(b) it is possible to find the same quantity, here it is $\frac{\partial \psi}{\partial \omega} = \frac{8}{2 \times 2\pi} =$ 0.63 s, comparable with the value from Balikhin et al. [1997b]. Also, a check can be made with the

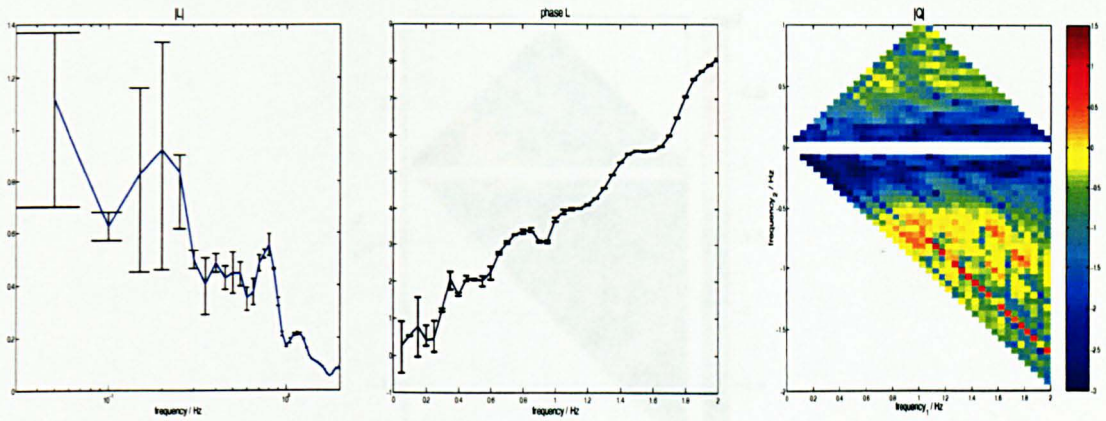

(a) $|L|$. (b) phase(L). (c) $|Q|$.

Figure 5.10: Regularisation Transfer Function Estimates.

dispersion calculated in Section 4.5. The phase speed for the waves in the satellite frame was quoted there as $\frac{\partial \omega}{\partial k_{proj}} \approx 100$ km/s. Here, using Eq. 2.16, the satellite frame phase speed can be estimated as,

$$\frac{\partial \omega}{\partial k_{proj}} = \frac{\partial \omega}{\partial \psi} \frac{\partial \psi}{\partial k_{proj}}$$

With $\frac{\partial \omega}{\partial \psi}$ from above, 1.57 1/s, and $\frac{\partial \psi}{\partial k_{proj}} = \delta r = 59$ km, the satellite frame phase speed is estimated as 93 km/s, again comparable.

The magnitude of the LS QTF is shown in Figure 5.9(c). The estimate does not appear to be so good. The maxima corresponding to the difference interaction region are too similar to the effects observed in Section 5.3.2 when only modest levels of noise were present in a surrogate data set. This highlights the ill-conditioned nature of the problem. Interpretation is possible but no significance can be attributed to the maxima in the difference interaction region, nor the sum interaction region by the same token.

The REG estimates are shown in Figure 5.10. Where similar LTF estimates are made significant improvement can be seen in the QTF estimate. The strongest maxima can be seen in the difference

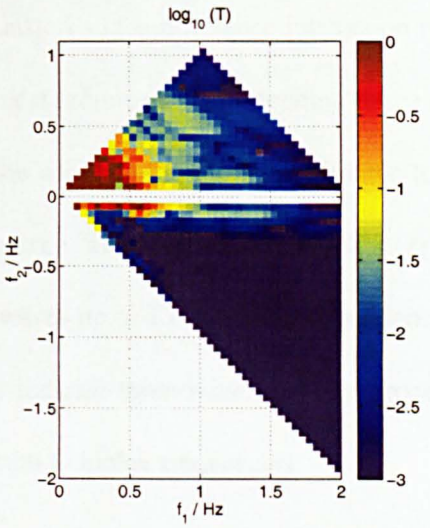

Figure 5.11: Spectral Energy Transfer function.

interaction region, corresponding to wave resonances,

0.9 Hz, 0.7 Hz $\leftrightarrow$ 0.2 Hz

1.7 Hz, 0.7 Hz $\leftrightarrow$ 1.0 Hz

There are also maxima in the sum interaction region,

0.7 Hz, 0.6 Hz $\leftrightarrow$ 1.3 Hz

It was stated in deWit et al. [1999] that interpretation of the quadratic coupling coefficients is rather difficult because of the lack of normalisation. They proceeded to discuss higher order coherence functions Section 2.2.4, but made use of what they termed the Spectral Energy Transfer function, estimated as an ensemble average of spectral moments, to identify regions in the frequency domain where significant energy transfer occurred,

$$T(\omega_1,\omega_2) = \Re\left[\frac{1}{2\delta x}\frac{\langle Y(\omega)\overline{X}(\omega_1)\overline{X}(\omega_2)\rangle\langle\overline{X}(\omega)X(\omega_1)X(\omega_2)\rangle}{\langle|X(\omega_1)X(\omega_2)|^2\rangle}\frac{\langle Y(\omega)\overline{X}(\omega)\rangle}{|\langle Y(\omega)\rangle\overline{X}(\omega)|}\right]$$

where again the relation $\sum_i \omega_i = \omega$, i.e. $\omega_1 + \omega_2 = \omega$, is used.

This quantity has been calculated here, and is shown in Figure 5.11. What is most apparent is the

absence of significant energy transfers in the difference interaction region. Maxima can be seen in the sum interaction region, the most prominent corresponding to the frequency range $0 < f_1 < 1.0$ Hz, $0 < f_2 < 0.5$ Hz, where the waves in those ranges combine to form waves up to 1 Hz, over an order of magnitude drop in energy. The region extends to $0 < f_1 < 1.6$ Hz, $0 < f_2 < 0.8$ Hz, where waves combine to form waves up to 1.6 Hz, when considering another order of magnitude drop in energy. These maxima indicate three-wave coupling processes are redistributing energy from the lower part of the spectrum to higher frequencies.

Although the QTF detects wave resonances in both the sum and interaction regions, only those in the sum region are significant in terms of energy transfer. The resonances may exist in the plasma system, but if there is no energy to excite them their role in the evolution of the plasma system is diminished.

5.5.4 Discussion

It is possible to conclude that high amplitude waves, which have been observed in the region of the magnetosheath adjacent to the Earth's bow shock and which possess a phase velocity close to the velocity of the intermediate waves propagating under the same angle to the magnetic field, are generated as a result of energy pumping via some plasma instabilities into two unstable frequency ranges and there is a subsequent redistribution of this energy via nonlinear wave coupling.

A preliminary comparison of the results of the growth rate value estimation with *AMPTE* plasma measurements show that the proton distribution can be the possible source of the observed instabilities.

Ion data collected by the *AMPTE UKS* satellite is shown in Figure 5.12. The panels, from top to bottom, show ion energy and the direction angles. Near 14:05:00 UT *UKS* sees the solar wind ions, a narrow beam with $E \approx 3$keV/q, $\theta \approx 90°, \phi \approx 180°$. Ions reflected from the bow shock can also be seen, a slightly broader beam with $E \approx 10$keV/q, $\theta \approx 45°, \phi \approx 315°$. As *UKS* encounters the bow shock the count rate increases, and the ions become more scattered in energy and direction.

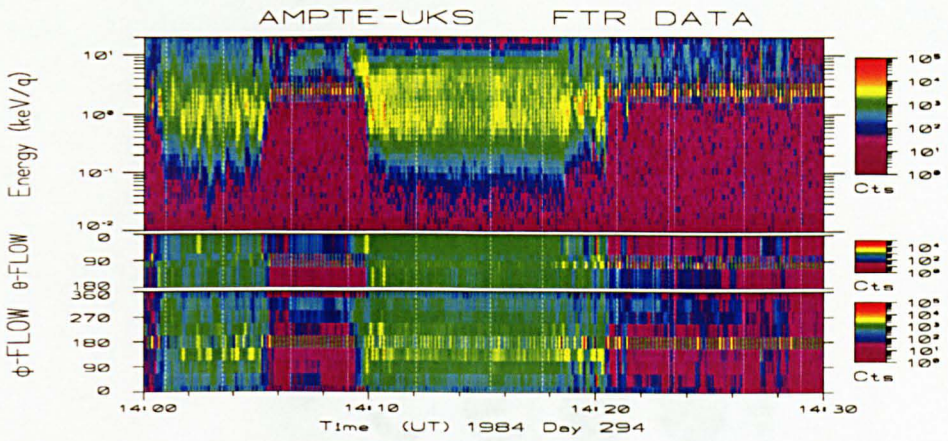

Figure 5.12: FTR *UKS* ion spectrogram.

the *UKS* data is of rather low resolution to determine if there is an ion anisotropy present.

Fortunately *AMPTE IRM* was able to provide cuts through the ion distribution functions with reasonable detail, and are shown in Figure 5.13.

In these figures the solar wind beam and the reflected ion beam can be seen upstream of the bow shock, and the more evenly spread distributions downstream of the shock. Although not so strong it is possible to perceive, in the middle row, a slight anisotropy, the distribution appearing elongated from left to right, and compressed between top and bottom. This could be the linear instability detected in the TF estimations.

5.6 Summary

Significant qualitative and quantitative improvements to the transfer function estimation can be made by using Regularisation techniques compared to LS methods.

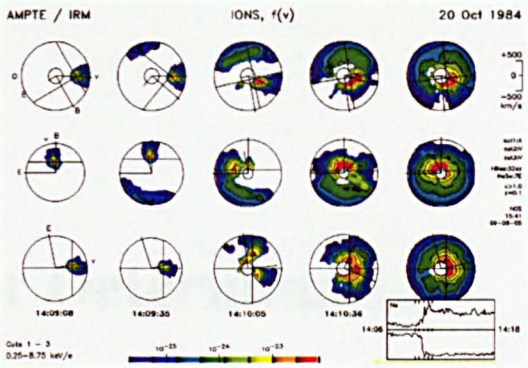

(a) Upstream and leading edge of the shock.

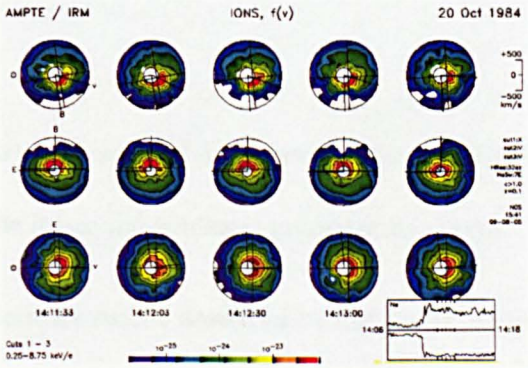

(b) Crossing and trailing edge of the shock.

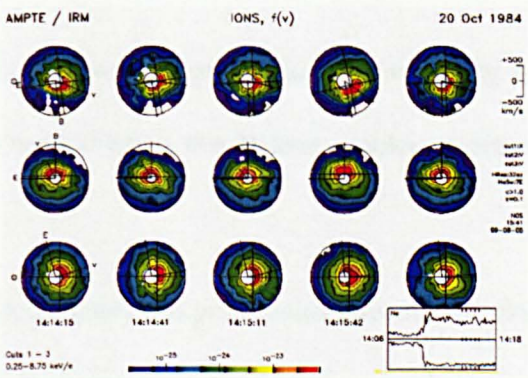

(c) Downstream of the shock.

Figure 5.13: Ion distributions measured during the Bow Shock Crossing.

Chapter 6

Wave-vector Determination

6.1 Introduction

When studying space plasma turbulence finding the propagation characteristics of any waves present is important to understand the linear and nonlinear processes that occur.

The propagation characteristics can be described by finding the wave vector $\mathbf{k}$. The magnitude of the wave vector $|\mathbf{k}|$ gives information about the wavelength of the wave (as $|\mathbf{k}| = 2\pi/\lambda$). The wave propagates in the direction given by the unit vector $\widehat{\mathbf{k}}$.

Single satellite measurements are the least useful for determining the wave vector. But even from these measurements a method exists that at least enables an estimate of the wave direction vector $\widehat{\mathbf{k}}$.

The usual procedure for determining this propagation direction involves minimum variance analysis (MVA). This technique has many limitations, such as not being suitable for plane-polarised waves or for multiple waves at the same frequency, but is the only way of finding the propagation direction from single satellite measurements (see Section 2.2.5).

However the main advantage dual satellite measurements have over single satellite measurements is that information about the magnitude of the wave vector, $|\mathbf{k}|$, can be found using the phase

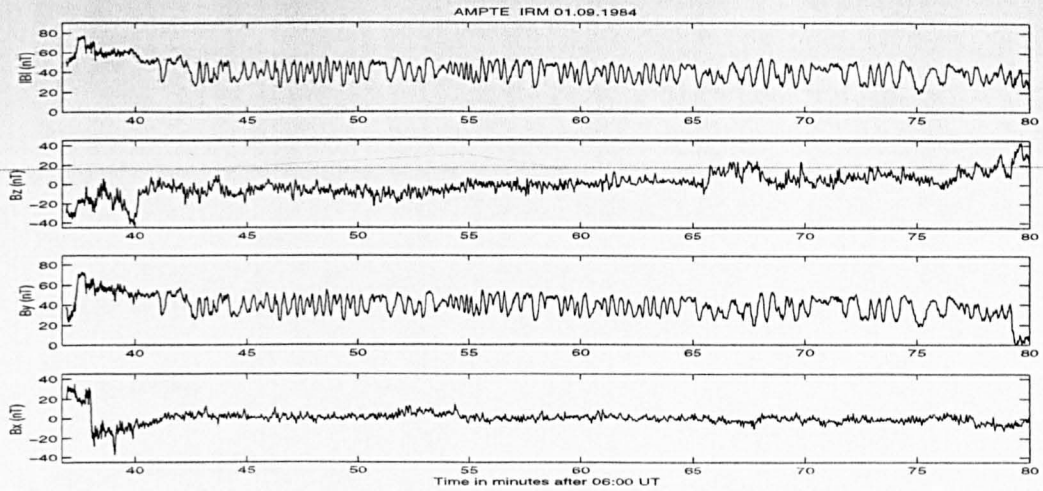

Figure 6.1: *IRM* magnetic field measurements 01/09/1984. The plot shows the time interval 06:35 to 07:35 UT. The *AMPTE* satellites were in the magnetosheath in this time interval. *UKS* magnetic field measurements are also available for this time interval. The magnetic field was sampled at a rate of 8 Hz.

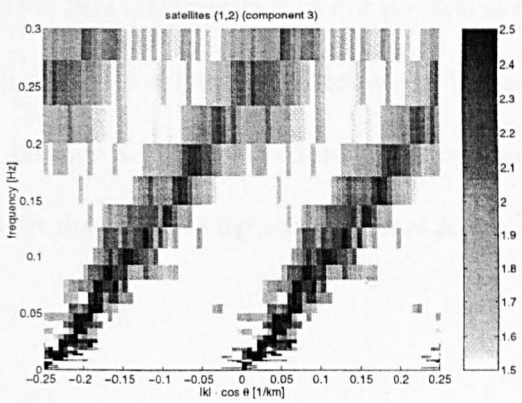

Figure 6.2: Magnetic field wave dispersion 01/09/1984. The time interval 07:05 to 07:15 UT is used for the dispersion calculation.

differencing technique (Section 2.2.5). Recapping briefly, the phase difference between two satellites ψ_{ij} contains information about the projection of $\mathbf{k}$ on the separation vector $\mathbf{x}_{ij}$.

The *AMPTE* satellite mission consisted of dual satellites, *IRM* and *UKS*. Simultaneous magnetic field measurements were taken by each spacecraft. *IRM* measurements of the magnetic field in the magnetosheath on 01/09/1984 are shown in Figure 6.1. *UKS* measurements were also available but are not shown here. This interval has been studied before by Balikhin et al. [2001b].

Figure 6.2 shows the wave dispersion in the magnetic field measured by the *AMPTE* satellites. The figure shows a clear dispersion branch starting from (0,0) and continuing with a phase speed near 6 km/s.

Considering the waves at 0.2 Hz the projection on the satellite separation vector can be seen to be $k_{ij} \approx 0.2$ 1/km. So for these waves the lower bound on $|\mathbf{k}|$ is 0.2 1/km. This also places an upper bound on the phase velocity for these waves,

$$\begin{aligned} V_{\text{phase}} &= \omega/|\mathbf{k}| = 2\pi f/|\mathbf{k}| \\ &\leq \omega/k_{ij} \\ &\leq 2\pi \cdot 0.2/0.2 \\ &\leq 6.3\text{km/s} \end{aligned}$$

This example uses magnetic field measurements so it is possible to apply MVA to the measurements. The analysis reveals the wave propagation direction $\widehat{\mathbf{k}}$. The scalar product of $\widehat{\mathbf{k}}$ and the known satellite separation direction $\widehat{\mathbf{x}}_{ij}$ gives the cosine of the angle between the two directions $\widehat{\mathbf{k}} \cdot \widehat{\mathbf{x}}_{ij} = \cos\theta_{ij}$. From this the magnitude of the wave vector is determined,

$$|\mathbf{k}| = k_{ij}/\widehat{\mathbf{k}} \cdot \widehat{\mathbf{x}}_{ij}$$

Hence $\mathbf{k}$ is fully determined. It must be again noted that this method for determining the full wave vector has uncertainties involved due to the use of MVA, and that MVA can only be used with three-dimensional vector measurements, which generally excludes electric field measurements.

This approach is simple as it is just the spectral phase information which enables this calculation to be made. However it requires phase difference information which is only obtained from multi (at least dual) satellite measurements. Complete $\mathbf{k}$ determination is only possible with at least quad-satellite measurements.

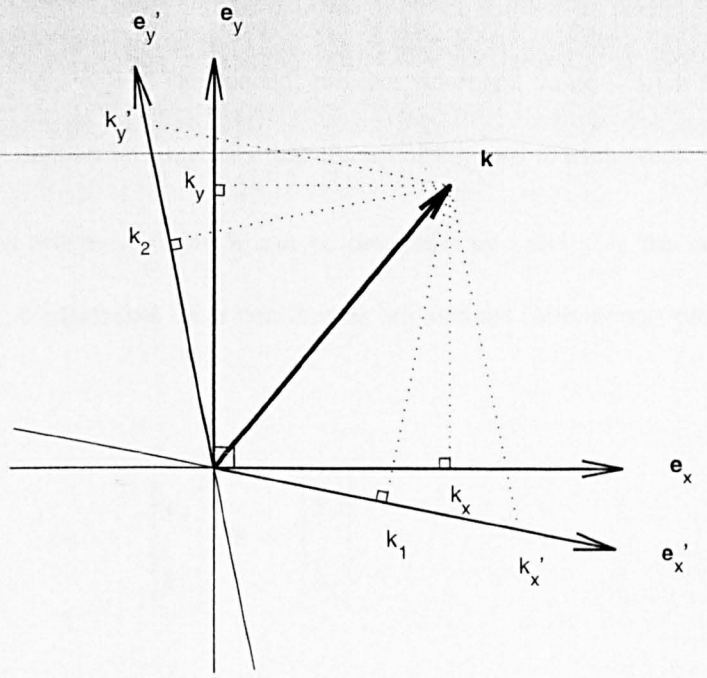

Figure 6.3: **k** in two reference frames, one orthogonal, one non-orthogonal, with relevant coordinates and projections indicated.

6.2 Method

Following the successful launch of the four *CLUSTER II* satellites simultaneous four-point measurements are available enabling, unambiguously, the complete direct determination of the wave propagation direction.

The method is an extension of the dual-satellite method. With four satellites the projection of the wave propagation direction can be found on three independent satellite separation vectors and hence can be completely determined without using MVA. This lifts the restriction that three-dimensional vector measurements are needed; the method can be used with three-component magnetic field measurements and two-component electric field measurements.

6.2.1 Comment on transformations between bases

First attention will be brought to what is meant by vector coordinates and vector projections and why and how they are different.

Figure 6.3 shows a 2D vector **k** in two reference frames. The first, unprimed, reference frame

has the property that is has a basis defined in terms of directions that are perpendicular to each other, i.e. it has an orthogonal basis. The second, primed, reference frame is such that it's basis is not orthogonal, i.e. it is defined by directions that are not orthogonal to each other.

In the unprimed reference frame $\mathbf{k}$ can be described by specifying the coordinates (k_x, k_y). Because this frame is orthogonal these coordinates are also the (orthogonal) projection of $\mathbf{k}$ on the basis vectors,

$$\begin{aligned} \mathbf{k} \cdot \mathbf{e}_x &= k_x \\ \mathbf{k} \cdot \mathbf{e}_y &= k_y \end{aligned} \quad \text{or,} \quad \begin{bmatrix} \mathbf{e}_x \\ \mathbf{e}_y \end{bmatrix} \cdot \mathbf{k} = \begin{bmatrix} k_x \\ k_y \end{bmatrix} \tag{6.1}$$

In the primed reference frame $\mathbf{k}$ is described by the coordinates (k'_x, k'_y). Because this reference frame is non-orthogonal, the coordinates are not the same as the (orthogonal) projections. Instead of coordinates $\mathbf{k}$ can also (uniquely) be described by specifying it's *projections* on the basis vectors,

$$\begin{aligned} \mathbf{k} \cdot \mathbf{e}_{x'} &= k_1 \\ \mathbf{k} \cdot \mathbf{e}_{y'} &= k_2 \end{aligned} \quad \text{or,} \quad \begin{bmatrix} \mathbf{e}_{x'} \\ \mathbf{e}_{y'} \end{bmatrix} \cdot \mathbf{k} = \begin{bmatrix} k_1 \\ k_2 \end{bmatrix} \tag{6.2}$$

In this latter, more general, case $\mathbf{k}$ is found by pre-multiplying both sides of Eq. 6.2 by the inverse of the matrix on the LHS of Eq. 6.2,

$$\mathbf{k} = \begin{bmatrix} \mathbf{e}_{x'} \\ \mathbf{e}_{y'} \end{bmatrix}^{-1} \begin{bmatrix} k_1 \\ k_2 \end{bmatrix} \tag{6.3}$$

In the former case, where the basis of the reference frame is orthogonal, the inversion operator can be replaced by the transpose operator,

$$\mathbf{k} = \begin{bmatrix} \mathbf{e}_{x'} \\ \mathbf{e}_{y'} \end{bmatrix}^{T} \begin{bmatrix} k_1 \\ k_2 \end{bmatrix} \tag{6.4}$$

6.2.2 k Determination

Using the method for dual satellite measurements, but switching between pairs of satellites, the dispersion along each of the three separation vectors $\mathbf{x}_{ij}$ can be found. This results in the determination of the projections of $\mathbf{k}$ on the basis formed by the satellite separation vectors.

It is then a case of transforming these projections to a more suitable reference frame. The GSE coordinate reference frame is chosen, as it is the frame in which the satellite separation vectors are known. From GSE any other coordinate system can be used as long as the appropriate transformation is made. See Hapgood [1992, 1997] for comprehensive descriptions of transforms between other coordinate systems.

Initially the case of three independent separations $(i = 1; j = 1, 2, 3)$ is considered. The case where, with four satellites, the additional three dependent separations $(i = 2, 3; j = 2, 3, 4; i \neq j)$ are included is discussed later.

Three separations

After identifying, from the dispersion plots, the projections of the wave vector of interest, there are the following equations to solve to find $\mathbf{k}$,

$$\begin{aligned} \mathbf{k} \cdot \hat{\mathbf{x}}_{12} &= k_{12} \\ \mathbf{k} \cdot \hat{\mathbf{x}}_{13} &= k_{13} \\ \mathbf{k} \cdot \hat{\mathbf{x}}_{14} &= k_{14} \end{aligned} \quad \text{or,} \quad \begin{bmatrix} \hat{\mathbf{x}}_{12} \\ \hat{\mathbf{x}}_{13} \\ \hat{\mathbf{x}}_{14} \end{bmatrix} \begin{bmatrix} k_x \\ k_y \\ k_z \end{bmatrix} = \begin{bmatrix} k_{12} \\ k_{13} \\ k_{14} \end{bmatrix} \tag{6.5}$$

which can be rewritten,

$$R \cdot \mathbf{k}_{GSE} = \mathbf{k}_{sat} \tag{6.6}$$

where R is a matrix containing, as rows, the satellite separation vectors, $\mathbf{k}_{sat}$ contains the projections of the wave vector on the satellite separation vectors, and $\mathbf{k}_{GSE}$ contains the GSE coordinates of the wave vector.

It is rare to find the satellites in a configuration where three separations are orthogonal. The solution of Eq. 6.6 is found using the general method expressed in Eq. 6.3,

$$\mathbf{k}_{GSE} = R^{-1} \cdot \mathbf{k}_{sat} \tag{6.7}$$

Six separations

Considering all separations possible with four satellites three more (dependent) separations are available. Using the dispersion methods the orthogonal wave vector projections can be found on these separations and all six projections combined can be used to obtain a more robust estimate for $\mathbf{k}$.

These extra separations give rise to three more equations defining $\mathbf{k}$,

$$\begin{aligned} \mathbf{k} \cdot \hat{\mathbf{x}}_{23} &= k_{23} \\ \mathbf{k} \cdot \hat{\mathbf{x}}_{24} &= k_{24} \\ \mathbf{k} \cdot \hat{\mathbf{x}}_{34} &= k_{34} \end{aligned} \quad \text{or,} \quad \begin{bmatrix} \hat{\mathbf{x}}_{23} \\ \hat{\mathbf{x}}_{24} \\ \hat{\mathbf{x}}_{34} \end{bmatrix} \begin{bmatrix} k_x \\ k_y \\ k_z \end{bmatrix} = \begin{bmatrix} k_{23} \\ k_{24} \\ k_{34} \end{bmatrix} \tag{6.8}$$

Adding these to those in Eq. 6.5, they can be written in the same form as Eq. 6.6, where R is now a matrix containing, in rows, the *six* satellite separation vectors, and $\mathbf{k}_{sat}$ contains the *six* projections.

Combined with the equations in Eq. 6.5 there is now an over-determined set of equations which can be solved using Least Squares,

$$\mathbf{k}_{GSE} = (R^T R)^{-1} R^T \mathbf{k}_{sat} \tag{6.9}$$

6.2.3 Notes on Periodic boundaries

Periodic boundaries in the dispersion plots arise due to the wave-vector component being derived from a phase measurement,

$$\Delta\psi_{ij} = \mathbf{k}_{ij} \cdot \mathbf{x}_{ij} \qquad k_{ij} = \frac{\Delta\psi_{ij}}{\Delta|\mathbf{r}_{ij}|}$$

Noting that the phase difference is bounded by π, $-\pi < \Delta\psi_{ij} < \pi$, the position of the periodic boundaries in terms of the wave-vector component are then,

$$-\frac{\pi}{\Delta|\mathbf{r}_{ij}|} < k_{ij} < \frac{\pi}{\Delta|\mathbf{r}_{ij}|}$$

For the cases presented here so far the wave-vectors considered have been in the principal domain, meaning that determination of the wave-vector components has been unambiguous. In the case of the linear dispersive waves the dispersion branch did encounter the periodic boundary, but *a priori* knowledge allowed the artificial unwrapping and the unambiguous wave-vector component determination. In some cases there may not be enough information to choose a wave-vector component unambiguously. This is the manifestation of the limit encountered when considering time series in the frequency domain.

The upper limit in the frequency domain is called the Nyquist frequency limit. When sampling a signal with sampling interval dt the frequencies resolvable are ones observed with at least two sampling points, i.e. the upper frequency limit, the Nyquist frequency, is $f_{\text{Nyquist}} = 1/2dt$. This is the upper limit for resolving frequencies unambiguously.

The upper limit in wave-vector space is accounted for by considering the periodic boundary conditions. When sampling a signal with probes separated by particular distance $\Delta|\mathbf{r}_{ij}|$ only wave-vectors in the range $-\frac{\pi}{\Delta|\mathbf{r}_{ij}|} < k_{ij} < \frac{\pi}{\Delta|\mathbf{r}_{ij}|}$ are resolvable. The Nyquist wavenumber, $k_{\text{Nyquist}} = \frac{\pi}{\Delta|\mathbf{r}|}$, is the upper limit on wave-numbers that can be resolved unambiguously.

Considering wavelengths, this means only waves whose wavelength λ satisfies,

$$1/\lambda_{ij} < 1/2\Delta|\mathbf{r}_{ij}| \quad \equiv \quad \lambda_{ij} > 2\Delta|\mathbf{r}_{ij}|$$

can be resolved. Surprisingly, *only waves with wavelengths larger than the satellite separations can be determined unambiguously.* Smaller separations (larger periodic boundaries) mean larger Nyquist wave numbers, meaning smaller wavelengths are resolvable. Conversely larger separations (smaller periodic boundaries) mean smaller Nyquist wave numbers, meaning only larger wavelengths are resolvable.

6.3 Examples

To test the method, simultaneous four-satellite measurements need to be obtained of a wave-field containing known waves. This can be done by generating an artificial wave-field and simulating the passage of four satellites. A successful test would be one where all the known waves are identified.

This section describes tests for the wave vector determination method. An artificial signal is generated containing signals, similar in nature to those already identified in *CLUSTER* data, and is artificially sampled to resemble *CLUSTER* data. The artificially generated *CLUSTER* data is then analysed by the wave vector determination technique to attempt to reproduce the original signal characteristics.

The following examples are presented to address specific points but also to illustrate the method algorithm,

- The method is shown to identify a simple wave in $(\omega, \mathbf{k})$ space,
- The method is shown to identify two waves, both with different $(\omega, \mathbf{k})$ parameters,
- The method is shown to identify a linearly dispersive wave field,
- The case where identification is attempted when two waves exist at the same frequency but

with different **k** parameters, in general it fails but in a particular case, is shown to work.

6.3.1 Method

- The satellite configuration, positions and velocities are chosen,
- The waves to be present in the wave-field are chosen, i.e. their GSE **k**-vector and frequency. The exact nature of the waves chosen is dependent on the concern to be addressed,
- The above, along with a given time interval, enables the artificial wave-field to be generated, the satellites to be flown through the wave-field, and for them to sample the resulting wave-forms.
- The time series waveforms from the four satellites are analyzed, with the minimum variance free wave vector determination method, in an attempt to reconstruct the virtual wave field parameters.

Assumptions

- the virtual wave-field is stationary on the temporal and spatial scale chosen,
- the virtual satellite separations are constant on the interval chosen,
- the virtual satellite orbit is linear on the interval chosen,
- the virtual measurements are made from a non-rotating source.

These assumptions will not always be valid for real data. The real wave-field may not be stationary on the time scale of the time interval chosen. The real separations change as a function of time. The real orbit is an elliptic arc. The true satellites rotate as they take real measurements which are then de-spun. For example at shock crossings the wave-field is far from stationary, near Earth at perigee separations may change quickly and the orbit is more elliptic on large intervals.

The validity of these assumptions is dependent on the temporal and spatial interval chosen. In general a smaller interval makes the separation and orbit assumptions more valid, also to some extent the stationary nature of the wave-field.

This list is not supposed to be exhaustive, only to serve as a reminder that this is not supposed to be a comprehensive model, simply sufficient for means of illustration.

Virtual Satellite Parameters

The satellite parameters are chosen to be similar to those in the *CLUSTER* magnetosheath crossing on 21/02/2001,

```
RE = 6378 ; %% km


x05 = [ 12*RE 0 0] ; %% km
x06 = [ 12*RE 0 0] + [  200 -500 -300 ] ; %% km
x07 = [ 12*RE 0 0] + [  400   50 -450 ] ; %% km
x08 = [ 12*RE 0 0] + [ -100  -40 -600 ] ; %% km


V5 = [ 2 0 0 ] ; %% km/s
V6 = [ 2 0 0 ] ; %% km/s
V7 = [ 2 0 0 ] ; %% km/s
V8 = [ 2 0 0 ] ; %% km/s
```

The model time t is such that it contains values for the four minute time interval 2001/52 14:38:00 UT to 2001/52 14:42:00 UT every 1/25 seconds,

```
ut_start = [ 2001 52 14 38 0 ] ; %% [ yyyy doy hh mm ss ]
ut_end   = [ 2001 52 14 38 0 ] ; %% [ yyyy doy hh mm ss ]


rate = 25 ; %% Hz
```

The satellite positions are generated simply as $\mathbf{x}_i = \mathbf{x}_{0i} + \mathbf{V}_i t$.

Virtual wave-field parameters

The parameters for the wave-field are specified simply by the wave-vector $\mathbf{k}$ and the frequency ω. For each case presented these parameters will vary, but will always follow this general method. The waveform is generated as,

$$E_j(t) = \sum_{i=1}^{N} \sin(\mathbf{k}_i \cdot \mathbf{x}_j(t) - \omega_i t) \qquad j \in \{1,2,3,4\}$$

where j represents each of the four satellites, and $\mathbf{k}_i, \omega_i$ the specified wave-field parameters, with $i \in \{1,\ldots,N\}$ varying over the number of components present in the virtual wave-field.

A Gaussian noise term is also added,

$$E_j(t) = E_j(t) + \alpha\zeta(t)$$

where α is chosen to give an amplitude ratio of signal-to-noise of snr, for these cases chosen to be 3, i.e. $\alpha = \langle E_j(t)\rangle / snr$.

Comment on the Doppler Shift

The Doppler shift is given by,

$$\omega' = \omega - \mathbf{k} \cdot \mathbf{x}$$

i.e. the observed frequency is increased/decreased according to the relative direction of the wave and the reference frame, by a fractional amount proportional to the product of the magnitudes of the wave-vector and the reference frame velocity.

For these examples, $|\mathbf{k}| \sim 5 \times 10^{-3}$ 1/km, $\mathbf{V} \sim 2 \times 10^{0}$ km/s, giving the Doppler shift $\delta\omega \sim 10^{-2}$ rad/s $\sim 10^{-3}$ Hz. This is negligible compared with the frequency of the waves considered, $\omega \sim 10^{-1}$–10^{-2} Hz.

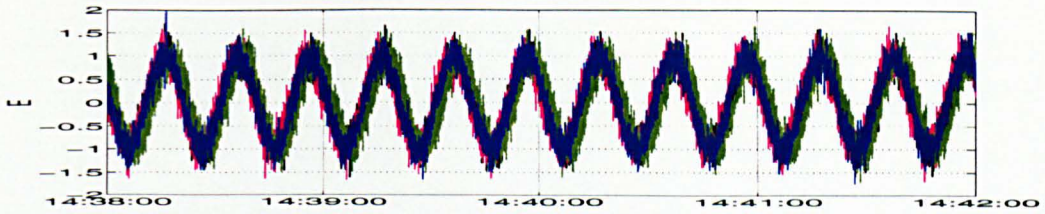

Figure 6.4: One wave present (waveforms). This is the result of sampling the wave-field with four satellites. The main wave can be seen, with offsets between the satellites due to their relative separation. It is this that enables the method to find the wave vector.

6.3.2 One wave present

This example addresses the first concern, that the method works. To test this a single wave will be present in the wave-field. If the method works then the original wave-field parameters, i.e. $\mathbf{k}$ and ω, should be identified.

Wave-field parameters

$$\mathbf{k}_{GSE} = (1, 1, 0) \times 10^{-3} \text{ 1/km} \quad \omega = 2\pi \times 0.05 \text{ rad/s} \tag{6.10}$$

The resulting waveform can be seen in Figure 6.4.

Wave-vector determination

From the dispersion plots (Figure 6.5) the wave is clearly seen. For waves at 50 mHz, the method gives,

```
onewave
ksat=   [  -0.52  +0.87  -0.14  +1.20  +0.16  -0.96 ] * 1e-3
kgse=   [  +1.05  +1.12  -0.11 ] * 1e-3
kgseLS= [  +0.96  +0.94  -0.07 ] * 1e-3
```

where `ksat` are the satellite frame wave vector projections along the satellite separations (an average is shown, taken over two inspections of the dispersion plots), with the respective GSE frame transformations given as `kgse` using the first three projections with the exactly determined case (Eq. 6.7),

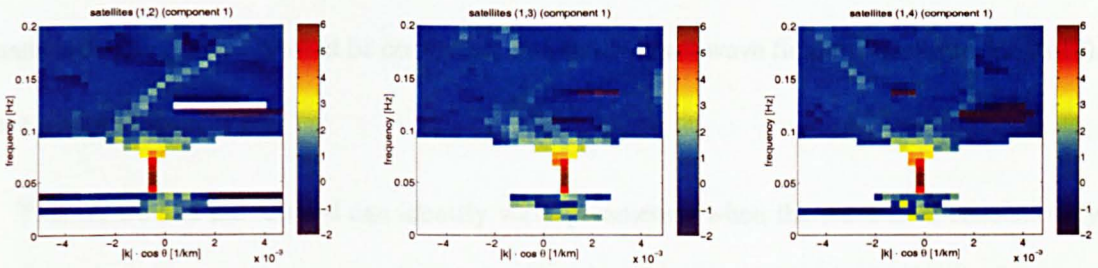

(a) $k_{12} \approx$ -0.5×10^{-3} 1/km. (b) $k_{13} \approx$ 1.0×10^{-3} 1/km. (c) $k_{14} \approx$ -0.2×10^{-3} 1/km.

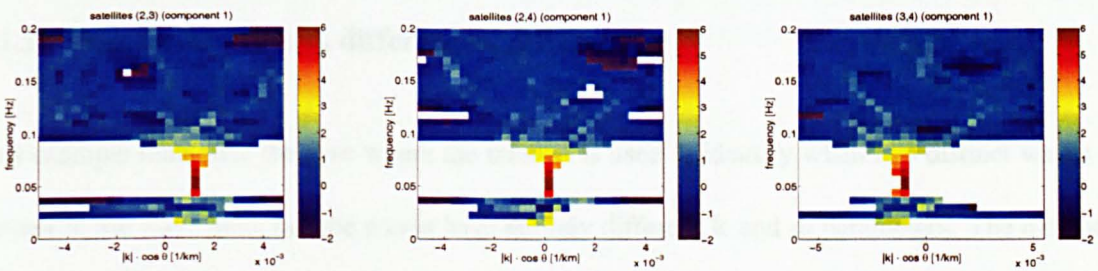

(d) $k_{23} \approx$ 1.5×10^{-3} 1/km. (e) $k_{24} \approx$ -0.2×10^{-3} 1/km. (f) $k_{34} \approx$ -1.0×10^{-3} 1/km.

Figure 6.5: One wave present (dispersions). These are the dispersions between all six of the satellite separations. Each panel shows the satellite frame dispersion, with the projection of the wave vector along the x-axis and the satellite frame frequency along the y-axis. Maxima in the panels indicate where there most of the wave energy is located. In each of the above panels it is clear that there is one wave present. Approximate values for the satellite frame components are given below each panel.

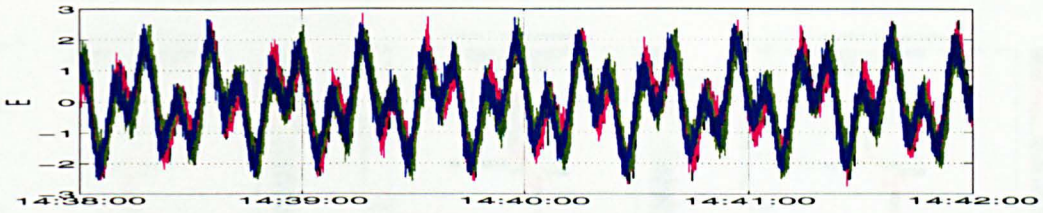

Figure 6.6: Two waves present, different ω, different $\mathbf{k}$ (time series). This shows the waveform resulting from sampling a wave-field containing two waves with different $\mathbf{k}$ and ω (given by Eq. 6.11). Periodic waves can be seen, however the underlying nature of the waves cannot clearly be seen by direct inspection.

and `kgseLS` using all the projections for the over determined case (Eq. 6.8). The GSE frame coordinates calculated above should be compared with the original wave field components (Eq. 6.10). A close match is seen.

This shows that the method can identify wave parameters when the wave field consists only of one wave.

6.3.3 Two waves present, different ω, different $\mathbf{k}$

This example illustrates the case where the method is used to identify when two distinct waves are present in the wave field, i.e. the waves have entirely different $\mathbf{k}$ and ω parameters. The method is applied to identify these known parameters.

Wave-field parameters

$$\begin{aligned} \mathbf{k}_{GSE} &= (1,1,0) \times 10^{-3} \text{ l/km} \quad \omega = 2\pi \times 0.05 \text{ rad/s} \\ \mathbf{k}_{GSE} &= (1,0,1) \times 10^{-3} \text{ l/km} \quad \omega = 2\pi \times 0.12 \text{ rad/s} \end{aligned} \tag{6.11}$$

where the first wave is the same as that present in the first wave field (Section 6.3.2) and the second wave has a different $\mathbf{k}$ and ω. The resulting waveform can be seen in Figure 6.6.

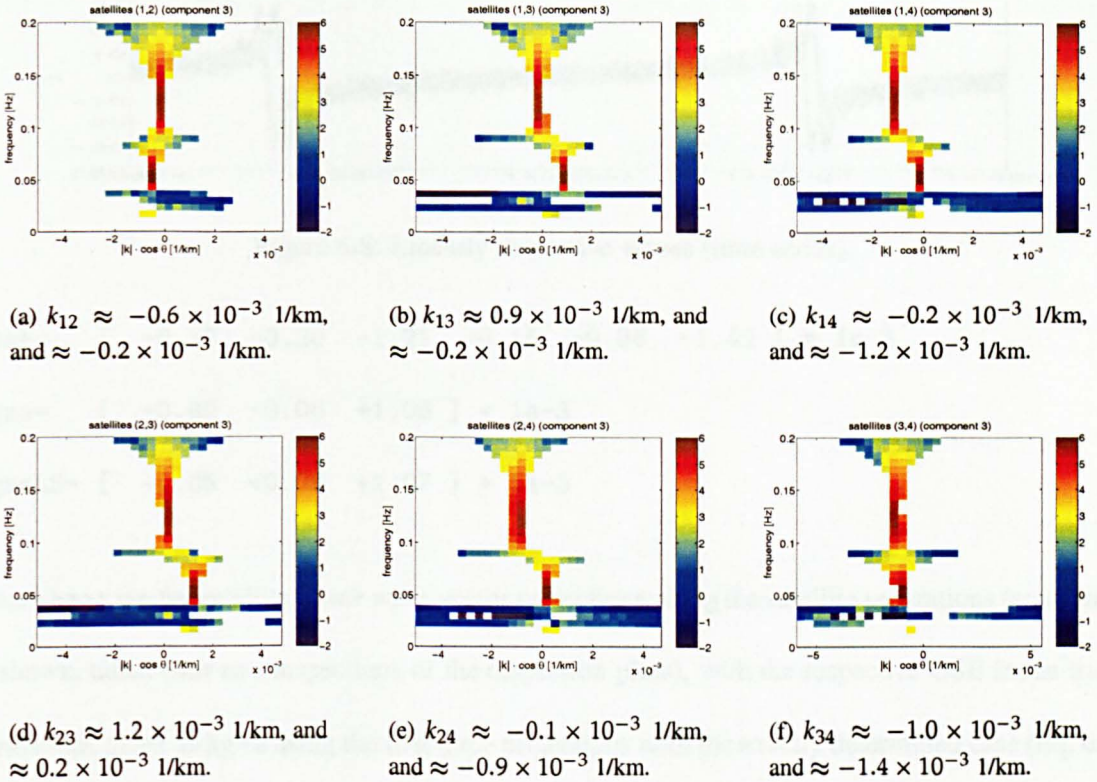

(a) $k_{12} \approx -0.6 \times 10^{-3}$ 1/km, and $\approx -0.2 \times 10^{-3}$ 1/km.

(b) $k_{13} \approx 0.9 \times 10^{-3}$ 1/km, and $\approx -0.2 \times 10^{-3}$ 1/km.

(c) $k_{14} \approx -0.2 \times 10^{-3}$ 1/km, and $\approx -1.2 \times 10^{-3}$ 1/km.

(d) $k_{23} \approx 1.2 \times 10^{-3}$ 1/km, and $\approx 0.2 \times 10^{-3}$ 1/km.

(e) $k_{24} \approx -0.1 \times 10^{-3}$ 1/km, and $\approx -0.9 \times 10^{-3}$ 1/km.

(f) $k_{34} \approx -1.0 \times 10^{-3}$ 1/km, and $\approx -1.4 \times 10^{-3}$ 1/km.

Figure 6.7: Two waves present, different ω, different k (dispersions). Each panel clearly shows the two waves. Below each panel approximate values for the satellite frame components are given.

Wave-vector determination

The two waves can clearly be seen in the dispersion plots (Figure 6.7). For the wave at $\omega = 2\pi \times 0.05$ rad/s (which is the same as the wave in Section 6.3.2),

```
twowaves_dw_dk_loww

ksat=   [  -0.55   +0.85   -0.18   +1.23   +0.11   -1.01 ] * 1e-3

kgse=   [  +1.06   +1.15   -0.07 ] * 1e-3

kgseLS= [  +1.00   +0.96   -0.02 ] * 1e-3
```

These results should be compared with the first wave in Eq. 6.11. A close match can be seen, also in accordance with the previous section (Section 6.3.2).

For the wave at $\omega = 2\pi \times 0.12$ rad/s,

```
twowaves_dw_dk_highw
```

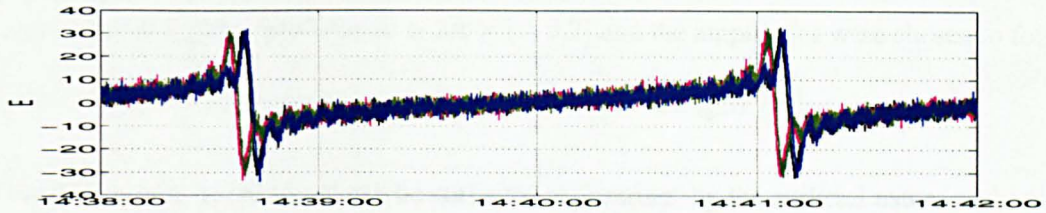

Figure 6.8: Linearly dispersive waves (time series).

```
ksat=   [ -0.17  -0.20  -1.21  +0.15  -0.86  -1.42 ] * 1e-3

kgse=   [ +0.92  -0.08  +1.08 ] * 1e-3

kgseLS= [ +1.05  +0.08  +1.07 ] * 1e-3
```

where `ksat` are the satellite frame wave vector projections along the satellite separations (an average is shown, taken over two inspections of the dispersion plots), with the respective GSE frame transformations given as `kgse` using the first three projections with the exactly determined case (Eq. 6.7), and `kgseLS` using all the projections for the over determined case (Eq. 6.8). These results should be compared with the second of Eq. 6.11. A close match can be seen.

This shows that the method can be used to differentiate and identify waves for the case where the wave field contains two waves with differing $\mathbf{k}$ and ω.

6.3.4 Linearly dispersive waves

This example explores the ability of the method in determining wave vectors for a case found in space plasmas, i.e. of a dispersive wave-field.

Wave-field parameters

For a linearly dispersive wave-field it is enough to specify a phase speed (which for a linear dispersion is also the group speed) and a direction for the waves,

$$\widehat{\mathbf{k}}_{GSE} = \tfrac{1}{\sqrt{5}}\,(-2,1,0) = (-0.89, 0.45, 0)\ \text{1/km} \qquad \left|\frac{\partial\omega}{\partial\mathbf{k}}\right| = 100\ \text{km/s} \tag{6.12}$$

where the frequency range used was $\omega \in 2\pi \times (0, 0.2]$ and the amplitudes were chosen to follow a power law, $A \propto \omega^{-\frac{1}{2}}$. The resulting waveform can be seen in Figure 6.8.

The features seen in the signal can be attributed to 'beating' by the artificial nature of the signal.

For n_ω odd,

$$
\begin{aligned}
y(t) &= \cdots + \sin(\omega t - d\omega t) + \sin(\omega t) + \sin(\omega t + d\omega t) + \cdots \\
&\quad (s_{\alpha\pm\beta} = s_\alpha c_\beta \pm s_\beta c_\alpha) \\
&= \cdots + \sin(\omega t)\cos(d\omega t) - \sin(d\omega t)\cos(\omega t) \\
&\quad + \sin(\omega t) \\
&\quad + \sin(\omega t)\cos(d\omega t) + \sin(\omega t)\cos(d\omega t) + \cdots \\
&= \cdots + \sin(\omega t)\cos(d\omega t) + \sin(\omega t) + \sin(\omega t)\cos(d\omega t) + \cdots \\
&= \cdots + \sin(\omega t)\,(1 + 2\cos(d\omega t)) + \cdots \\
&= \sin(\omega t)\,(1 + 2\cos(d\omega t) + 2\cos(2d\omega t) + \cdots) \\
&= \sin(\omega t)\left(1 + 2\sum_{i=1}^{(n_\omega - 1)/2} \cos(id\omega t)\right)
\end{aligned}
$$

This shows that the signal can be written as a sine wave, with frequency equal to the average all the frequencies present, modulated by an amplitude dependent on the difference between successive frequencies dw.

The lowest frequency term is found when $i = 1, n_\omega = 3$, and is $\cos(d\omega t)$. The magnitude of the resulting signal is proportional to the square of this, giving a beating period of $T_{\text{beat}} = \frac{2\pi}{2d\omega} = \frac{\pi}{d\omega}$.

For n_ω even,

$$
\begin{aligned}
y(t) &= \sin(\omega t) + \sin(\omega t + d\omega t) + \sin(\omega t + 2d\omega t) + \sin(\omega t + 3d\omega t) + \cdots \\
&\left(s_\alpha \pm s_\beta = 2s_{\frac{\alpha \pm \beta}{2}} c_{\frac{\alpha \mp \beta}{2}}\right) \\
&= 2\sin\left(\omega t + \tfrac{1}{2}d\omega t\right)\cos\left(\tfrac{1}{2}d\omega t\right) + 2\sin\left(\omega t + \tfrac{5}{2}d\omega t\right)\cos\left(\tfrac{1}{2}d\omega t\right) + \cdots \\
&= 2\cos\left(\tfrac{1}{2}d\omega t\right)\left(\sin\left(\omega t + \tfrac{1}{2}d\omega t\right) + \sin\left(\omega t + \tfrac{5}{2}d\omega t\right) + \cdots\right) \\
&= 2\cos\left(\tfrac{1}{2}d\omega t\right)\left(\sum_{i=1}^{n_\omega/2} \sin\left(\omega t + \tfrac{4(i-1)+1}{2}d\omega t\right)\right)
\end{aligned}
$$

This shows that the signal can be written as a sum of sine waves, modulated by a cosine wave with frequency half the difference between successive frequencies, $d\omega/2$.

The lowest frequency term, for $\omega = 0$, is found when $i = 1, n_\omega = 2$, and is $2\cos\left(\frac{1}{2}d\omega t\right)\sin\left(\frac{1}{2}d\omega t\right)$. This is the same as $\sin(d\omega t)$. The magnitude is proportional to the square of this term, giving a beating period $T_{\text{beat}} = \frac{2\pi}{2d\omega} = \frac{\pi}{d\omega}$, as for the case where n_ω is odd.

For this example, $d\omega = 2\pi\frac{0.2}{30} = \frac{2\pi}{150}$ rad/s, giving a beating period $T_{\text{beat}} = 150$ s, which is the period observed in Figure 6.8.

Wave-vector determination

The dispersion plots for this wave-field are shown in Figures 6.9, 6.10. The linear dispersion branch is seen in both plots. In Figure 6.9 the principal dispersion branch is shown, i.e. where $-\pi \leq \Delta\psi < \pi$. In these plots the boundaries are periodic, e.g. in Figure 6.9(a) the branch from the top-right edge, $k_{12} \approx 5 \times 10^{-3}$ 1/km, $\omega \approx 2\pi \times 0.15$ rad/s, is a continuation of the branch from the left edge, $k_{12} \approx -5 \times 10^{-3}$ 1/km, $\omega \approx 2\pi \times 0.15$ rad/s. In Figure 6.10 the boundaries have been unwrapped by plotting the principal branch next to itself, making the linear dispersion clearer.

To reconstruct the linear dispersive wave-field parameters, the wave direction $\hat{\mathbf{k}}$ and the wave phase speed $\left|\frac{\partial\omega}{\partial\mathbf{k}}\right|$, waves at particular frequencies are chosen to find particular GSE frame wave-

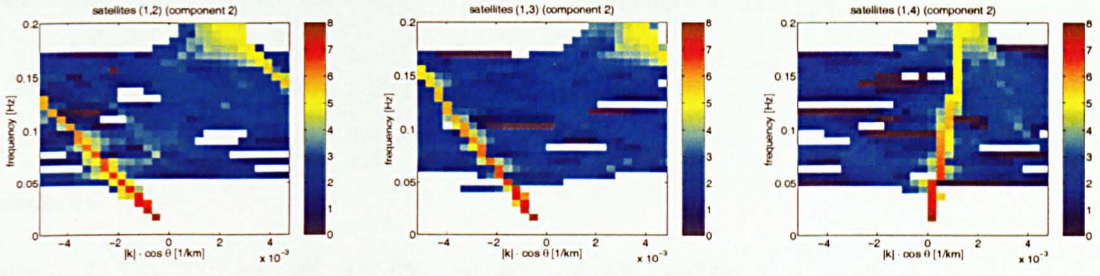

(a) $k_{12} \approx$ -4.0×10^{-3} 1/km. (b) $k_{13} \approx$ -3.5×10^{-3} 1/km. (c) $k_{14} \approx$ -0.5×10^{-3} 1/km.

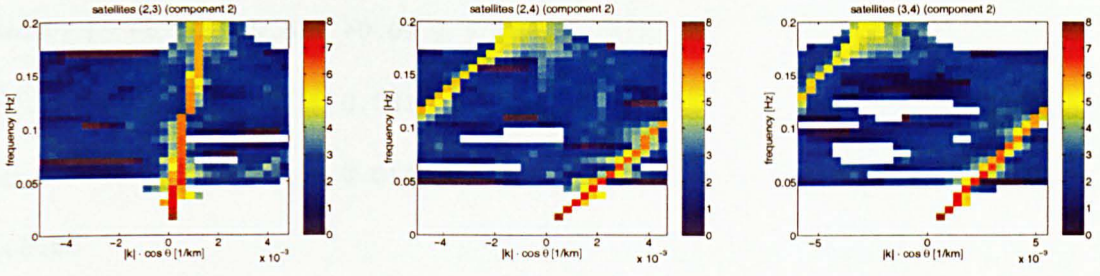

(d) $k_{23} \approx$ 1.0×10^{-3} 1/km. (e) $k_{24} \approx$ 4.5×10^{-3} 1/km. (f) $k_{34} \approx$ 5.0×10^{-3} 1/km.

Figure 6.9: Linearly dispersive waves (dispersions, wrapped). The linear dispersion can be seen in all pairs. The interpretation of these dispersion plots is complicated by the wrapping that occurs at the periodic boundaries. The wave-field parameters, the wave-vector direction $\widehat{\mathbf{k}}$ and phase speed $\left|\frac{\partial\omega}{\partial\mathbf{k}}\right|$, are determined by choosing a particular frequency to find the corresponding GSE frame wave vector, then using the result to calculate directly $\widehat{\mathbf{k}}$ and $\left|\frac{\partial\omega}{\partial\mathbf{k}}\right|$. The satellite frame wave-vector components for waves at $\omega = 2\pi \times 0.1$ rad/s are shown below each panel.

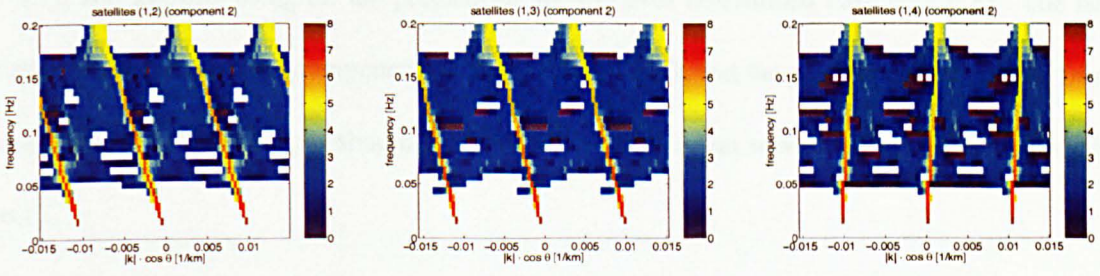

(a) $k_{12} \approx$ 8.0×10^{-3} 1/km. (b) $k_{13} \approx$ -6.5×10^{-3} 1/km. (c) $k_{14} \approx$ 1.0×10^{-3} 1/km.

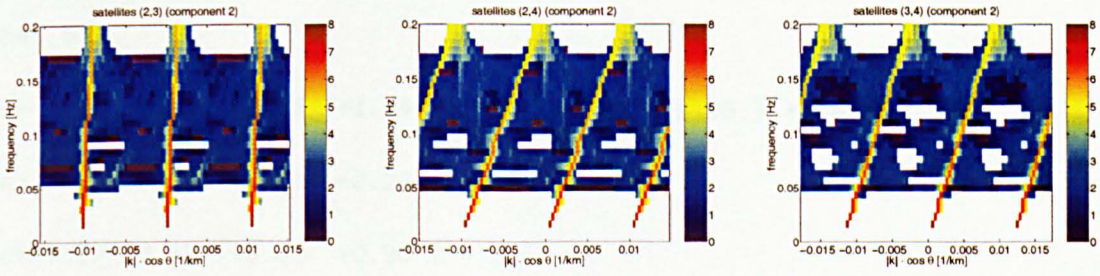

(d) $k_{23} \approx$ 1.5×10^{-3} 1/km. (e) $k_{24} \approx$ 9.0×10^{-3} 1/km. (f) $k_{34} \approx$ 9.0×10^{-3} 1/km.

Figure 6.10: Linearly dispersive waves (dispersions, unwrapped). As the previous figure, but with the principal dispersion artificially unwrapped. Below each panel are the satellite frame wave-vector coordinates for waves at $\omega = 2\pi \times 0.2$ rad/s.

vectors. These are then used the find the wave-field parameters $\widehat{\mathbf{k}}$ and $\left|\frac{\partial\omega}{\partial\mathbf{k}}\right|$.

From Figure 6.9 waves at $\omega = 2\pi \times 0.1$ rad/s give,

```
linear_01
ksat=   [  -3.73  -3.38  +0.52  +0.66  +4.40  +4.60 ] * 1e-3
kgse=   [  -5.20  +2.41  +0.18 ] * 1e-3
kgseLS= [  -5.29  +2.57  +0.09 ] * 1e-3
  -0.906911   0.420157   0.031306
  -0.899419   0.436830   0.014983
  109.65
  106.85
```

where `ksat` are the satellite frame wave vector projections along the satellite separations (an average is shown, taken over two inspections of the dispersion plots), with the respective GSE frame transformations given as `kgse` using the first three projections with the exactly determined case (Eq. 6.7), and `kgseLS` using all the projections for the over determined case (Eq. 6.8). The last four rows show the direction components of `kgse` and `kgseLS`, and the phase speed calculated from `kgse` and `kgseLS`. These results should be compared to the original wave-field parameters shown in Eq. 6.12.

From Figure 6.10 waves at $\omega = 2\pi \times 0.2$ rad/s give,

```
linear_02
ksat=   [  -7.89  -6.64  +1.14  +1.39  +8.98  +8.95 ] * 1e-3
kgse=   [ -10.45  +5.41  +0.23 ] * 1e-3
kgseLS= [ -10.52  +5.43  +0.20 ] * 1e-3
  -0.887751   0.459925   0.019184
  -0.888569   0.458445   0.016516
  106.77
```

```
106.18
```

where `ksat` are the satellite frame wave vector projections along the satellite separations (an average is shown, taken over two inspections of the dispersion plots), with the respective GSE frame transformations given as `kgse` using the first three projections with the exactly determined case (Eq. 6.7), and `kgseLS` using all the projections for the over determined case (Eq. 6.8). The last four rows show the direction components of `kgse` and `kgseLS`, and the phase speed calculated from `kgse` and `kgseLS`.

Both `linear_01` and `linear_02` give similar results, those for `linear_02` should be better as the relative accuracy of reading measurements for $\omega = 2\pi \times 0.2$ rad/s should be better than for $\omega = 2\pi \times 0.1$ rad/s, The results for all measurements and calculations show good agreement with Eq. 6.12.

This shows that the method can be used to identify waves in a linearly dispersive wave-field.

6.3.5 Two waves present, same ω, different k

These next two examples highlight a case where the method does not perform so well. This case is the Achilles Heel of the method.

This example is an extension of the case presented in Section 6.3.3. It is shown here to assess the ability of the method to determine wave properties for the case of two waves at the same frequency propagating in different directions simultaneously.

Wave-field parameters

$$\begin{aligned} \mathbf{k}_{GSE} &= (1,1,0) \times 10^{-3} \text{ 1/km} \quad \omega = 2\pi \times 0.05 \text{ rad/s} \\ \mathbf{k}_{GSE} &= (2,-2,3) \times 10^{-3} \text{ 1/km} \quad \omega = 2\pi \times 0.05 \text{ rad/s} \end{aligned} \tag{6.13}$$

The resulting waveform can be seen in Figure 6.11. From this figure a wave at the common frequency can be seen.

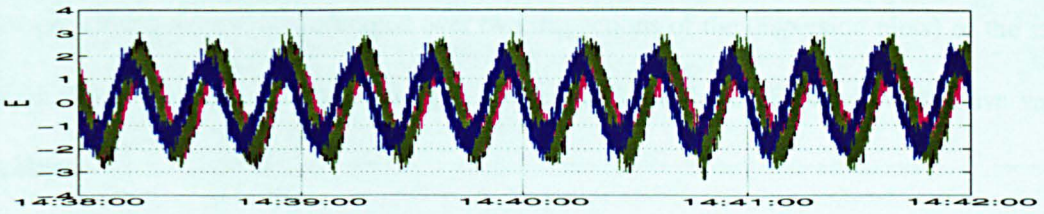

Figure 6.11: Two waves present, same ω, different k (time series).

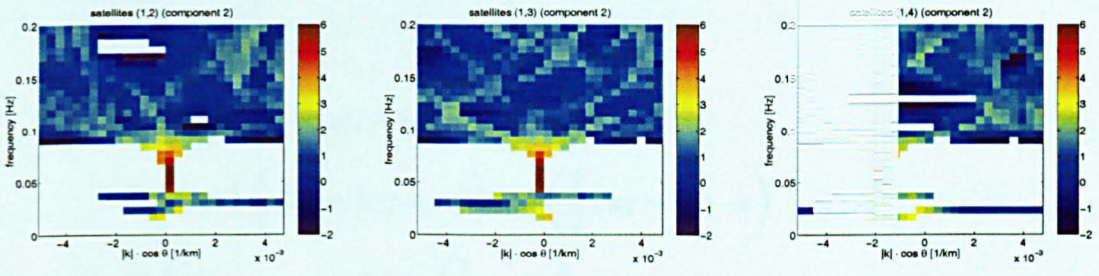

(a) $k_{12} \approx 0.1 \times 10^{-3}$ 1/km. (b) $k_{13} \approx$ -0.2$\times 10^{-3}$ 1/km. (c) $k_{14} \approx$ -1.7$\times 10^{-3}$ 1/km.

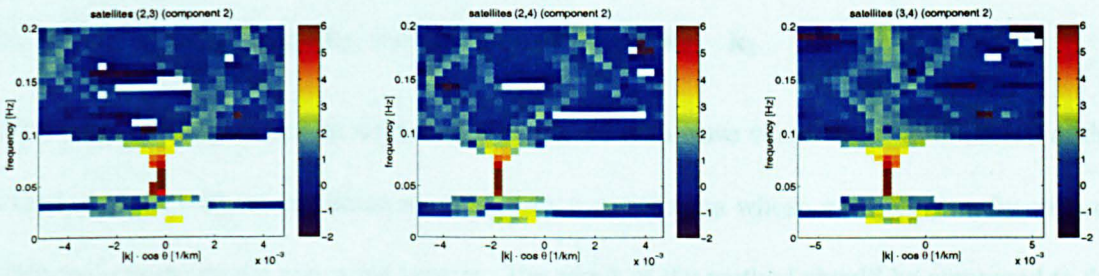

(d) $k_{23} \approx$ -0.2$\times 10^{-3}$ 1/km. (e) $k_{24} \approx$ -1.9$\times 10^{-3}$ 1/km. (f) $k_{34} \approx$ -1.8$\times 10^{-3}$ 1/km.

Figure 6.12: Two waves present, same ω, different k (dispersions)

Wave-vector determination

The dispersion plots are shown if Figure 6.12. There appears only one significant wave component present between each pair. From this it appears that it is not possible for the method to resolve the two different directions. However proceeding for this one wave gives,

```
twowaves_sw_dk_st

ksat=   [  +0.13  -0.22  -1.72  -0.24  -1.87  -1.78 ] * 1e-3

kgse=   [  +1.46  -0.51  +1.54 ] * 1e-3

kgseLS= [  +1.52  -0.47  +1.55 ] * 1e-3
```

where `ksat` are measurements (averaged over two inspections of the dispersion plots) of the satellite frame wave vector projections, and `kgse` and `kgseLS` are the GSE transformed wave vector components.

The method has found only one wave. This can be explained by considering how the artificial signal is generated,

$$\begin{aligned} E(\mathbf{x},t) &= \sin(\mathbf{k}_1\cdot\mathbf{x}-\omega t)+\sin(\mathbf{k}_2\cdot\mathbf{x}-\omega t) \\ &= \frac{1}{2}\sin\left(\frac{1}{2}(\mathbf{k}_1+\mathbf{k}_2)-\omega t\right)\cos\left(\frac{1}{2}(\mathbf{k}_2-\mathbf{k}_1)\cdot\mathbf{x}\right) \\ &= \frac{1}{2}\sin(\mathbf{k}\cdot\mathbf{x}-\omega t)\cos\left(\frac{1}{2}\Delta\mathbf{k}\cdot\mathbf{x}\right) \end{aligned}$$

where $\mathbf{k}$ is the mean of $\mathbf{k}_1$ and $\mathbf{k}_2$, and $\Delta\mathbf{k}$ is the difference $\mathbf{k}_2-\mathbf{k}_1$.

This shows the signal can be written as a sine wave with wave vector equal to the mean of the two wave vectors, with an amplitude modulated by a cosine term whose argument is a function of the difference between the two wave vectors. The result of the method should be compared to the mean of the artificial wave vector,

$$\mathbf{k}_{mean} = (1.5,-0.5,1.5)\times 10^{-3}\ \text{1/km} \qquad \omega = 2\pi\times 0.05\ \text{rad/s}$$

where a close match is seen.

By considering only the phase information in the signal this method cannot distinguish the two wave vectors in this case. Extra information may enable the resolution of the two wave-vectors. For instance it may be possible to consider the amplitude modifications between the four satellite field measurements, but knowing when it is possible to do this is also a problem.

The method cannot determine wave field parameters for the case where two waves of the same frequency are propagating in different directions.

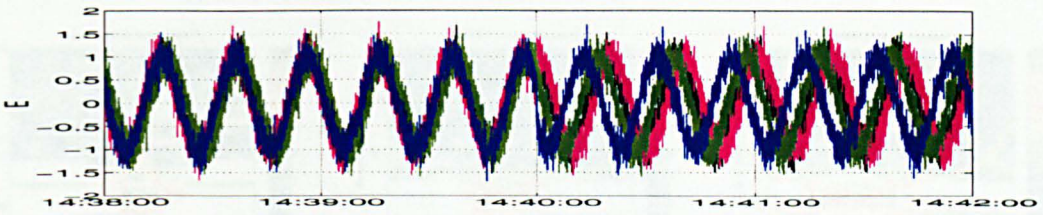

Figure 6.13: Two waves present, same ω, different $\mathbf{k}$, present at different times (time series).

6.3.6 Two waves present, same ω, different $\mathbf{k}$, present at different times

This example is similar to the previous example except instead of present simultaneously the waves appear one after the other. They are both present over the whole interval, but at no time are they present simultaneously.

Wave-field parameters

$$\begin{aligned} \mathbf{k}_{GSE} &= (1,1,0) \times 10^{-3} \text{ 1/km} \quad \omega = 2\pi \times 0.05 \text{ rad/s} \quad t < 14:40:00 \\ \mathbf{k}_{GSE} &= (2,-2,3) \times 10^{-3} \text{ 1/km} \quad \omega = 2\pi \times 0.05 \text{ rad/s} \quad t > 14:40:00 \end{aligned} \tag{6.14}$$

These parameters are the same as the previous example, only the waves described are present at different times, *not* simultaneously. The waveform can be seen in Figure 6.13.

Wave-vector determination

The dispersion plots are shown in Figure 6.14. Although not clear two areas can be made out in each dispersion plot.

It is expected that two distinct waves are seen. However the positive identification from these plots is difficult if nothing is known initially about the wave field.

There is also the problem of matching the projections between plots, e.g. does the LH area in Figure 6.14(a) correspond to the LH or the RH area in Figure 6.14(b)? Because one of the waves known to be present has already been used in a previous example (Section 6.3.2) it is possible to ignore the projections associated with this wave to find the projections of the second wave,

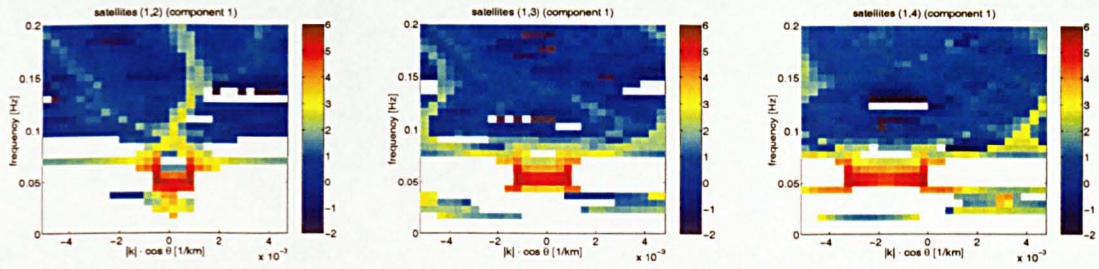

(a) $k_{12} \approx -0.5 \times 10^{-3}$ 1/km, and $\approx 0.8 \times 10^{-3}$ 1/km.

(b) $k_{13} \approx -1.3 \times 10^{-3}$ 1/km, and $\approx 0.9 \times 10^{-3}$ 1/km.

(c) $k_{14} \approx -3.3 \times 10^{-3}$ 1/km, and $\approx -0.2 \times 10^{-3}$ 1/km.

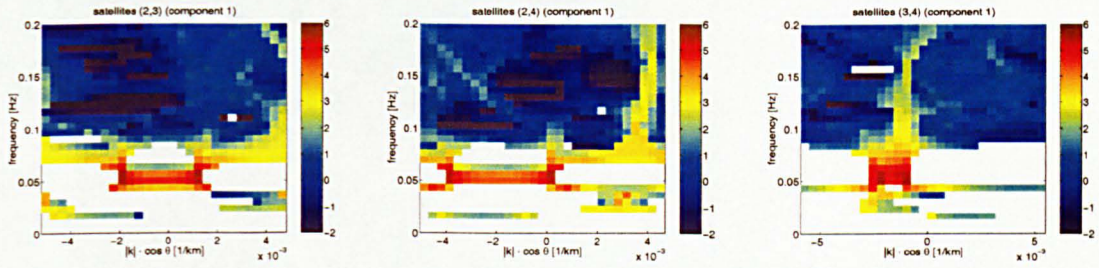

(d) $k_{23} \approx -1.9 \times 10^{-3}$ 1/km, and $\approx 1.2 \times 10^{-3}$ 1/km.

(e) $k_{24} \approx -3.8 \times 10^{-3}$ 1/km, and $\approx 0.2 \times 10^{-3}$ 1/km.

(f) $k_{34} \approx -2.2 \times 10^{-3}$ 1/km, and $\approx -1.0 \times 10^{-3}$ 1/km.

Figure 6.14: Two waves present, same ω, different $\mathbf{k}$, but present at different times (dispersions).

```
twowaves_sw_dk_dt_w1

ksat=   [  -0.53  +0.88  -0.19  +1.24  +0.15  -1.00 ] * 1e-3

kgse=   [  +1.10  +1.14  -0.07 ] * 1e-3

kgseLS= [  +1.00  +0.97  -0.05 ] * 1e-3


twowaves_sw_dk_dt_w2

ksat=   [  +0.82  -1.29  -3.28  -1.94  -3.84  -2.23 ] * 1e-3

kgse=   [  +1.88  -2.16  +3.16 ] * 1e-3

kgseLS= [  +1.83  -2.03  +3.10 ] * 1e-3
```

where `ksat` are measurements (averaged over two inspections of the dispersion plots) of the satellite frame wave vector projections, `kgse` and `kgseLS` are the GSE transformed wave vector components, and `twowaves_sw_dk_dt_w1`, 2 are the particular grouping of components resulting from matching the projections, as described above. These agree with the expected values (Eq. 6.14).

If it is not known how to match projections between separations, incorrect waves can be identified. For example taking all the LH areas to correspond to one wave and taking all the RH areas to corresponding the second gives spurious wave vectors,

```
twowaves_sw_dk_dt_left
ksat=   [  -0.53  -1.29  -3.28  -1.94  -3.84  -2.23 ] * 1e-3
kgse=   [  +1.61  -0.56  +3.10 ] * 1e-3
kgseLS= [  +1.63  -1.49  +3.43 ] * 1e-3

twowaves_sw_dk_dt_right
ksat=   [  +0.82  +0.88  -0.19  +1.24  +0.15  -1.00 ] * 1e-3
kgse=   [  +1.37  -0.46  -0.01 ] * 1e-3
kgseLS= [  +1.20  +0.43  -0.39 ] * 1e-3
```

where `ksat` are measurements (averaged over two inspections of the dispersion plots) of the satellite frame wave vector projections, `kgse` and `kgseLS` are the GSE transformed wave vector components, and `twowaves_sw_dk_dt_left, right` are the particular grouping of components resulting from matching the projections by LH and RH side. These are in disagreement with the expected values (Eq. 6.14).

6.4 Results

For the purpose of illustrating this MVA-free method for determining wave vectors actual *CLUSTER* electric field measurements are taken and the wave vectors are found for the waves observed. Data from orbit 102 (which started on 21/02/2001) is used. The interval, of a few minutes, centered around 14:40:00 UT on 21/02/2001 is considered. This corresponds to the satellites being roughly midway between the Bowshock and the Magnetopause.

6.4.1 Overview of Satellite Environment

Figure 6.15 shows an overview of the satellite environment for this orbit. The *CLUSTER* satellites cross the magnetosheath considered here after first encountering the magnetopause near 12:00 UT and then crossing the bow shock near 18:00 UT. This time interval clearly includes the magnetosheath crossing as there are magnetic field discontinuities (FGM) and increased magnetic field wave activity (STAFF) at the boundaries along with enhancement of electrons at higher energies (PEACE) inside the interval. The magnetosheath is also expected in this interval from inspection of the orbits of the satellites.

6.4.2 Satellite positions and velocities

The *CLUSTER* satellites are on an outward bound crossing of the magnetosheath. Looking towards the Earth from the Sun they are located above the ecliptic, just on the dusk flank (Figure 6.15(b)). They are gradually increasing their relative separations as well as slowing down as they approach earth apogee.

The *CLUSTER* spacecraft are spin-stabilised at a rotation frequency of 0.25 Hz. This may have observable effects on the measured data at the spin frequency and it's harmonics. No spin effects will be apparent in the data at frequencies below the spin frequency. In the following frequencies below 0.2 Hz are studied.

Full hi-resolution (25 Hz) samples of the electric field are available for this magnetosheath crossing. The interval from 14:38 to 14:42 UT is chosen for study.

6.4.3 Wave vector determination

The electric field components measured by satellite 1 are shown in Figure 6.17. The electric field can be seen to be steady with $\sim$ 1 mV/m oscillations about a slowly varying mean. Although not shown there are visible correlations with electric field measurements from the three other satellites.

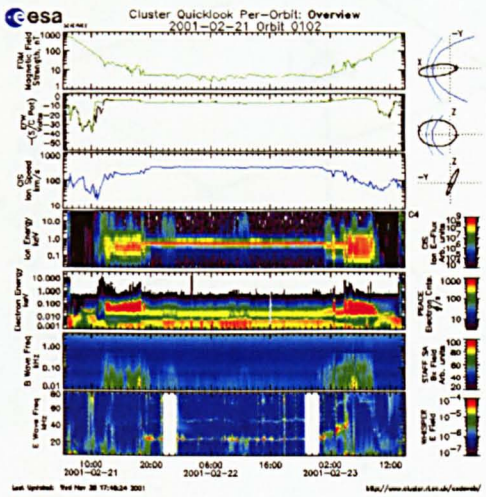

(a) Quicklook per-orbit overview plot for orbit 102 covering the time 21/02/2001 05:00 to 23/02/2001 14:00 UT.

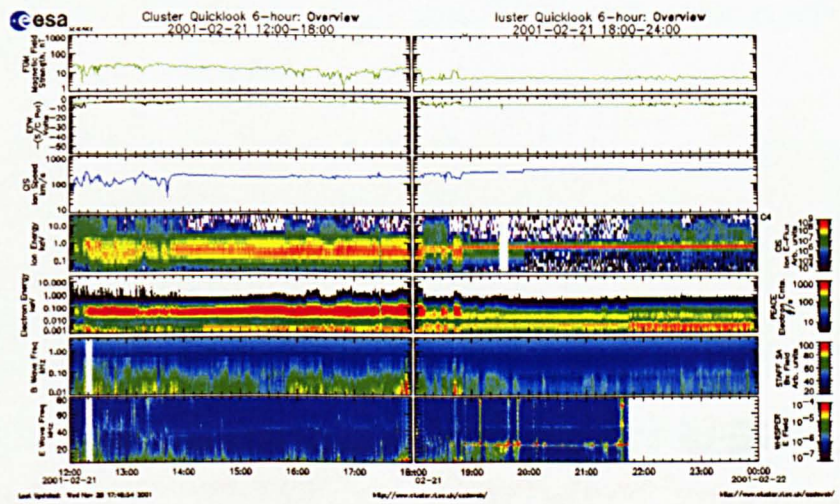

(b) Quicklook 2 × 6-hour overview plot for the interval 21/02/2001 12:00 to 24:00 UT.

Figure 6.15: *CLUSTER* Quicklook overview plots for orbit 102. Shown in the panels, from the top in each plot, are FGM magnetic field magnitude, EFW -(spacecraft potential), CIS ion speed, CIS ion counts/s, PEACE electron counts/s, STAFF magnetic field spectrum and the WHISPER electric field spectrum. The full satellite orbit can be seen to the upper right in each plot. Plots taken from the CSDS website http://www.cluster.rl.ac.uk/csdsweb/.

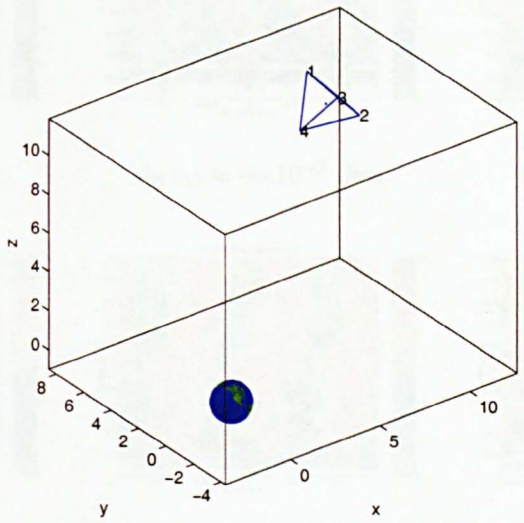

Figure 6.16: Satellite position relative to the Earth.

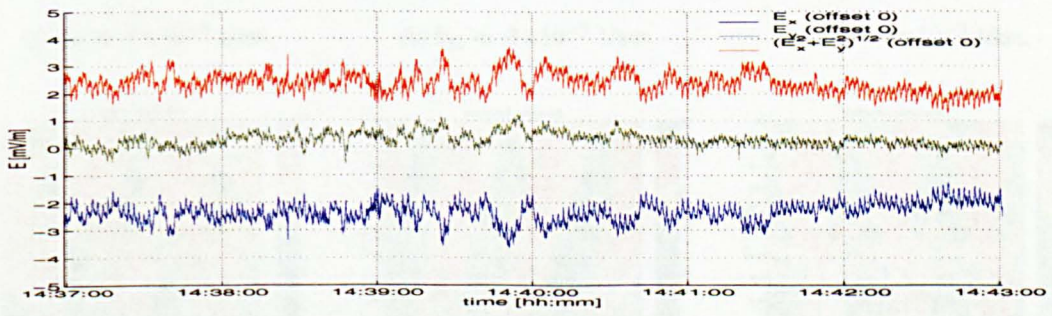

Figure 6.17: *CLUSTER* electric field measured by satellite 1 over interval I. From the top, $(E_x^2 + E_y^2)^{1/2}$, E_y then E_x are plotted. Sampling rate 25 Hz.

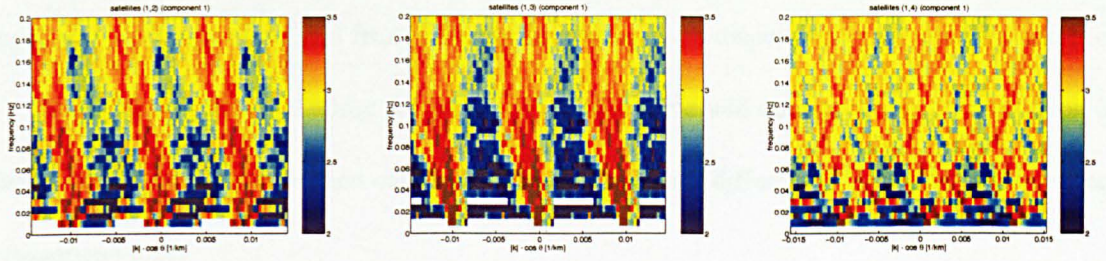

(a) $k_{12} \approx$ -5×10^{-3} 1/km. (b) $k_{13} \approx$ -4×10^{-3} 1/km. (c) $k_{14} \approx$ 1×10^{-3} 1/km.

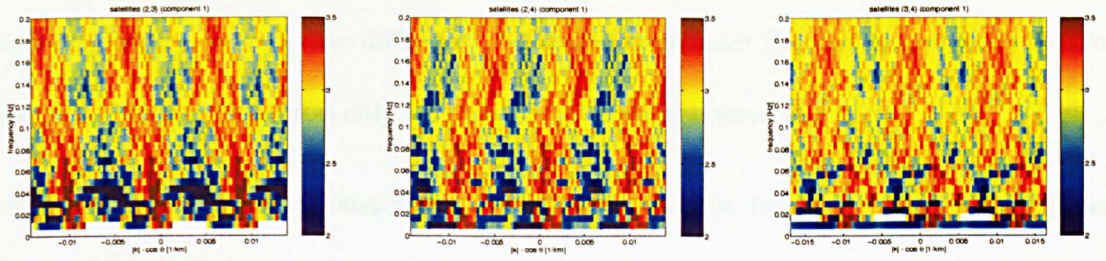

(d) $k_{23} \approx$ -3×10^{-3} 1/km. (e) $k_{24} \approx$ 5×10^{-3} 1/km. (f) $k_{34} \approx$ 9×10^{-3} 1/km.

Figure 6.18: Dispersions for the GSE_X component of the observed electric field. Shown between all six of the satellite separations. Approximate values for the satellite frame components are given below each panel.

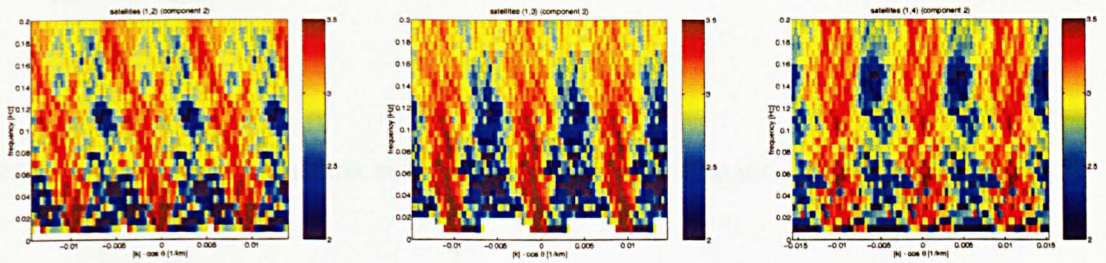

(a) $k_{12} \approx$ -4×10^{-3} 1/km. (b) $k_{13} \approx$ -3×10^{-3} 1/km. (c) $k_{14} \approx$ 2×10^{-3} 1/km.

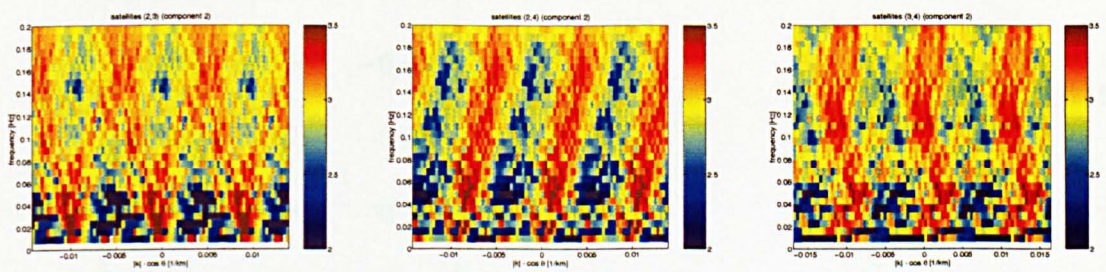

(d) $k_{23} \approx$ -4×10^{-3} 1/km. (e) $k_{24} \approx$ 4×10^{-3} 1/km. (f) $k_{34} \approx$ -1×10^{-3} 1/km.

Figure 6.19: Dispersions for the GSE_Y component of the observed electric field. Shown between all six of the satellite separations. Approximate values for the satellite frame components are given below each panel.

Figure 6.18 shows the dispersions calculated from the GSE_X component of the electric field data between all six pairs of satellites. Figure 6.19 shows the dispersions calculated from the GSE_Y component. Although calculated from different components the dispersion in Figure 6.18 and Figure 6.19 should be the same. Only the phase offset of a wave will change when it is observed in different directions. The dispersion calculation is based on phase differencing, so this does not effect the dispersion plots.

The dispersion can be seen to be linear. The phase velocity for all waves is constant, waves of differing frequencies will have differing wave vector magnitudes $|\mathbf{k}|$, but the same wave vector direction $\widehat{\mathbf{k}}$. Because of this it is only necessary to calculate one wave vector.

Examining the dispersions observed in the GSE_X component, for waves at 0.13 Hz, between the satellite pairs (1,2), (1,3) and (1,4) (i.e in Figure 6.18(a), Figure 6.18(b) and Figure 6.18(c)) the projections are,

$$\mathbf{k}_{sat} = \begin{bmatrix} -4.5 \\ -4.0 \\ 1.0 \end{bmatrix} \times 10^{-3} \text{1/km} \tag{6.15}$$

and with the transformation matrix consisting of the satellite separations shown below,

$$R = \begin{bmatrix} 0.333 & -0.817 & -0.471 \\ 0.660 & 0.116 & -0.742 \\ -0.192 & -0.065 & -0.979 \\ 0.304 & 0.921 & -0.245 \\ -0.505 & 0.751 & -0.425 \\ -0.956 & -0.202 & -0.212 \end{bmatrix} \tag{6.16}$$

the $\mathbf{k}_{GSE}$ estimate for the wave vector (from Eq. 6.9), for waves at 0.13 Hz, is found to be,

$$\mathbf{k}_{GSE} = \begin{bmatrix} -6.5 \\ 2.8 \\ 0.1 \end{bmatrix} \times 10^{-3}\,\text{1/km} \qquad = 7.1 \times (-0.92, 0.40, 0.01) \times 10^{-3}\ \text{1/km} \tag{6.17}$$

To identify the observed wave it is useful to estimate the wave phase velocity in the plasma rest frame, v_{pf}. This is calculated by subtracting, from the satellite frame phase speed $\left(v_{\text{sat}} = \frac{\omega}{|\mathbf{k}|}\right)$, the projection of the plasma bulk velocity $\mathbf{V}_i$ along the wave propagation direction. So with,

$$\omega_{\text{sat}} = 2\pi \times 0.13 = 0.82 \text{ rad/s}$$

$$v_{\text{sat}} = \frac{\omega_{\text{sat}}}{|\mathbf{k}_{GSE}|} = 115 \text{ km/s}$$

$$\mathbf{V}_i = 132 \times (-0.90, 0.21, 0.39) \text{ km/s} = (-119, 27.7, 51.5) \text{ km/s}.$$

the projection of $\mathbf{V}_i$ on the propagation direction is,

$$\mathbf{V}_i \cdot \widehat{\mathbf{k}}_{GSE} = 120.4 \text{ km/s}$$

resulting in a plasma frame phase velocity,

$$v_{\text{plasma}} = v_{\text{sat}} - \mathbf{V}_i \cdot \widehat{\mathbf{k}}_{GSE} = -5.0 \text{ km/s}$$

$$\omega_{plasma} = v_{\text{plasma}} |\mathbf{k}_{GSE}| = -0.035 \text{ rad/s}$$

It is directed opposite to the wave velocity in the satellite frame, implying that the waves are virtually non-propagating in the plasma rest frame. The discrepancy between v_{sat} and the projection of $\mathbf{V}_i$ can be explained by the errors related to the width of the "ridges" in Figure 6.18 and Figure 6.19.

The results are similar when considering the remaining three projections, in Figure 6.18(d), Figure 6.18(e) and Figure 6.18(f), with $\mathbf{k}_{GSE}$ resulting from the LS solution (Eq. 6.9) comparable

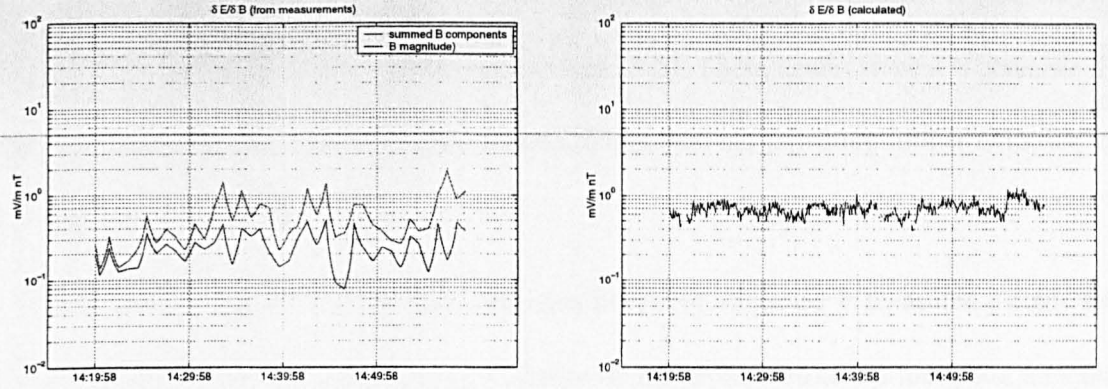

(a) Actual $\delta E/\delta B$ fluctuations. Taken from the observed **E** field and **B** fields.

(b) $\delta E/\delta B$ calculated using Eq. 6.18.

Figure 6.20: $\delta E/\delta B$ ratio, from measured field fluctuations and from the formula expressed in the text [Pokhotelov et al., 2000].

with the result in Eq. 6.17, and as a self-consistency check the observed projections, $\mathbf{k}_{sat}$, can be compared to the projections resulting from ${\mathbf{k}_{GSE}}^{\mathrm{LS}}$ (using Eq. 6.6) with good agreement, within acceptable errors related to the width of the ridges.

The absence of propagation in the plasma rest frame indicates non-propagating mirror structures convected by the plasma flow. Mirror wave structures are often observed in the magnetosheath, but usually in the magnetic field components. Their physics is related to the mirror force effect on ion motion. The question is can mirror wave structures have a significant electric field component, which will make them observable in the electric field. The E/B ratio was calculated in Pokhotelov et al. [2000] and is given by,

$$\frac{\delta E}{\delta B_{||}} = i|\mathbf{k}|\rho_{i_{||}} \frac{T_{i_\perp}/T_{i_{||}} - T_{e_\perp}/T_{e_{||}}}{1 + T_{i_{||}}/T_{e_{||}}} \upsilon_{T_{i_{||}}} \tag{6.18}$$

where,

$$\upsilon_{T_{i_{||}}} = \left(T_{i_{||}}/m_i\right)^{\frac{1}{2}}$$

$$\rho_{i_{||}} = \upsilon_{T_{i_{||}}}/\omega_{ci}$$

Values for the ion and electron temperatures were taken from the *CLUSTER II* summary parameters. The resulting estimation can be seen in Figure 6.20. These figures show it is plausible that mirror wave structures exist in the magnetosheath in this interval, providing further evidence that mirror waves are observed.

This is the first time that mirror wave structures have been observed in measured electric field components. Electric field measurements are suitable for the application of this four-point minimum variance free method.

6.5 Summary

CLUSTER II is the first satellite mission that enables the identification of the dispersion of plasma waves observed in the electric field component. WEC data are self-sufficient for this identification (acknowledging the inclusion of auxilliary data for the satellite positions). FGM data and basic plasma parameters are still needed to form a more meaningful physical interpretation.

Future work will involve a comprehensive study of waves observed in the magnetosheath. The wave vector and it's variations can be found for each magnetosheath crossing of the *CLUSTER II* satellites. Combining these observations for many such crossings will allow an experimentally derived understanding of the plasma waves present.

6.5.1 Note on Separation Vectors

Only three independent spatial vectors are required to define a full coordinate system in 3D space. With four satellites (as in the *CLUSTER* mission) there are six relative separation vectors, three being independent and the other three a linear combination of the first three. Using wave vector projections on three of these six possible separations to find $\mathbf{k}$ provides a minimal solution. However the extra information that knowledge of the wave vector projection on the other three dependent separation vectors can be used to increase the accuracy and precision of the wave vector determination.

The six independent measurements along the three independent and the three dependent separation vectors form an over-determined system, the solution of which is the wave vector. This way the full information contained in the *CLUSTER* satellite measurements is utilised.

The satellite configuration has a bearing on this wave vector determination, as the separation vectors are used as a basis to measure the wave vector components. For a given wave propagating in a given direction there are obviously preferential directions for measuring the wave. The projection of $\mathbf{k}$ will be maximised for directions $\hat{\mathbf{x}}_{ij}$ near-parallel to $\hat{\mathbf{k}}$ and will be virtually zero for directions $\hat{\mathbf{x}}_{ij}$ near-perpendicular to $\hat{\mathbf{k}}$. An ideal situation (not only for this analysis but more generally) is the case when the satellite separations $\hat{\mathbf{x}}_{ij}$ form a mutually orthogonal basis. For the *CLUSTER* mission this is not always the case for all the time. The satellite configuration varies considerably over the full orbit, generally forming a tight configuration at perigee and evolving to a looser configuration at apogee.

Each successive orbit precesses about the Earth thus rotating apogee from out in the solar wind to inside the magnetotail. The *CLUSTER* Master Science Plan (MSP), which determines when to measure what, is strongly influenced by the satellite configuration. The magnetosheath is included in the MSP and will be crossed in successive orbits at varying stages in the full orbit and hence with a variety of satellite configurations. In summary ideal configurations are not necessary; but some days *are* better than others.

6.5.2 Note on Doppler shift

Care should be taken when transforming frequencies between reference frames. The frequency observed in the satellite frame will be Doppler-shifted when observed in another frame.

$$\begin{aligned} \mathbf{k} &= \mathbf{k}' \\ \omega &= \omega' - \mathbf{k} \cdot \mathbf{V} \end{aligned} \tag{6.19}$$

Eq. 6.19 gives the Doppler shift formula when transforming waves between reference frames. The wave vector $\mathbf{k}$ is unchanged between reference frames; however the measured frequency ω' is different from rest frame frequency ω by an amount according to $\mathbf{k}$ and the relative velocity $\mathbf{V}$. The measured frequency is less (greater) than the rest frame frequency when the satellites are moving in the same (opposite) direction to the waves, and is not shifted when the satellites are moving perfectly perpendicular to them.

For the intervals presented here the Doppler shift is small. $|\mathbf{k}| \sim 10^{-3}$ km^{-1}, $|\mathbf{V}| \sim 10^{0}$ km/s, so $\mathbf{k} \cdot \mathbf{V} \sim 10^{-3}$ Hz or less. However for larger $|\mathbf{k}|$ and greater relative velocities it will become significant.

Chapter 7

Conclusions

Frequency domain analysis tools have been developed to analyse simultaneous multi-point measurements of developed space plasma turbulence.

- A technique for determining the coherence length from single, dual or multiple satellite measurements has been found and developed.

  The Coherence Length technique enables the scale length for plasma wave structures to be measured from magnetic field measurements. The coherence length defines a length scale for the measurement of wave phenomena. Single satellite measurements can be used, the technique becoming more reliable with higher numbers of satellites.

  The technique is used to identify coherence lengths for waves observed in the magnetic field near the bow shock by the dual *AMPTE-UKS/AMPTE-IRM* satellites, and for mirror wave structures observed in the magnetic field in the magnetosheath by the dual *ISEE-1/ISEE-2* satellites.

- A Transfer Function Estimation technique has been developed for plasmas containing dispersive waves, with the addition of an improved inversion technique,

  The Transfer Function Estimation technique enables the transfer of energy between plasma waves to be measured, from simultaneous dual-point measurements, resulting in linear growth

/ damping rates and second-order wave coupling. The technique is improved by replacing the LS method for inversion with Regularisation.

The technique is applied to simultaneous magnetic field measurements near the bow shock by the *AMPTE-UKS/AMPTE-IRM* satellites, where a linear instability in the wave field is identified, which is attributed to an ion anisotropy instability, and accompanying sequence of second-order three-wave coupling processes is also identified, which dissipates the energy from the linear instability.

- A wave vector propagation determination technique has been developed, by extending the method available for dual satellites, and found to be successful.

  The Wave vector Determination technique enables the identification of wave vectors from simultaneous four-point measurements. The availability of four-point measurements means that the reliance on Minimum Variance Analysis, and that of only being able to use magnetic field measurements, is removed, the wave vector can be determined unambiguously directly from the magnetic field measurements. The technique can identify between waves of different frequency, and waves at the same frequency but propagating in different directions.

  The technique is applied to simultaneous observations of the electric field by the four-point *CLUSTER II* satellites, enabling the determination of the wave vector and the identification of a mirror mode structure, solely from the electric field measurements.

7.1 Final Remarks

Single-satellite multi-instrument observations have been available for a long time, their analysis methods mature and interpretation well understood. Multi-satellite multi-instrument observations, analysis, and interpretation can build from this healthy start but are still to be considered in development.

Bibliography

A. N. Akanso. *Multiresolution signal decomposition : transforms, subbands, and wavelets.* Academic Press, 1992.

M. A. Balikhin, I. Bates, and S. Walker. Identification of linear and nonlinear processes in space plasma turbulence data. *Advances in Space Research*, 28(5):787–800, 2001a.

M. A. Balikhin, T. D. deWit, H. St. C. K. Alleyne, L. J. C. Woolliscroft, S. N. Walker, V. Krasnoselskikh, W. A. C. MierJedrzejeowicz, and W. Baumjohann. Experimental determination of the dispersion of waves observed upstream of a quasi-perpendicular shock. *Geophys. Res. Lett.*, 24(7):787–790, APR 1 1997a.

M. A. Balikhin and M. E. Gedalin. Comparative analysis of different methods for distinguishing temporal and spatial variations. In *SP-183 START Conference, Aussois, France, Jan.31-Feb.5*, volume ESA WP-047. European Space Agency, 1993.

M. A. Balikhin, S. Schwartz, S. N. Walker, H. St. C. K. Alleyne, M. Dunlop, and H. Lühr. Dual-spacecraft observations of standing waves in the magnetosheath. *J. Geophys. Res-Space Phys.*, 106(A11):25395–25408, NOV 1 2001b.

M. A. Balikhin, L. J. C. Woolliscroft, H. St. C. K. Alleyne, M. Dunlop, and M. A. Gedalin. Determination of the dispersion of low frequency waves downstream of a quasiperpendicular bow shock. *Annales Geophysicae*, 15:143–151, 1997b.

I. Bates, M. A. Balikhin, H. St. C. K. Alleyne, and M. Andre. Minimum-variance free determination of magnetosheath wave propagation vectors. In *Sheffield Space Plasma Meeting: Multi-point measurements versus theory*, volume SP-492, pages 133–140. ESA, July 2001.

I. Bates, M. A. Balikhin, H. St. C. K. Alleyne, M. Dunlop, and H. Lühr. Coherence lengths of low frequency turbulence at the bow shock and in the magnetosheath. In *Proceedings of the Cluster II Workshop on Multi-scale/Multi-point Plasma Measurements*, volume ESA SP-449, pages 283–286. European Space Agency, 2000.

N. Beloff, P. Denisenko, and M. P. Gough. Using the regularisation technique for the reconstruction of non-monochromatic n(h) profiles from vertical sounding ionograms. In *Sheffield Space Plasma Meeting: Multi-point measurements versus theory*, volume SP-492, pages 147–150. ESA, July 2001.

J. S. Bendat and A. G. Piersol. *Random data - analysis and measurement procedures.* John Wiley and sons, second edition, 1986.

C. S. Burrus. *Introduction to wavelets and wavelet transforms : a primer.* Prentice Hall, 1998.

S. C. Chapman and M. W. Dunlop. Some consequences of the shift theorem for multispacecraft measurements. *Geophys. Res. Lett.*, 20(19):2023–2026, OCT 8 1993.

I. Daubechies. *10 lectures on Wavelets.* Society for Industrial and Applied Mathematics, 1992.

T. D. deWit and V. V. Krasnoselskikh. Wavelet bicoherence analysis of strong plasma turbulence at the earths quasiparallel bow shock. *Phys. Plasmas*, 2(11):4307–4311, NOV 1995.

T. D. deWit, V. V. Krasnoselskikh, S. D. Bale, M. W. Dunlop, H. Lühr, S. J. Schwartz, and L. J. C. Woolliscroft. Determination of dispersion-relations in quasi-stationary plasma turbulence using dual satellite data. *Geophys. Res. Lett.*, 22(19):2653–2656, OCT 1 1995.

T. D. deWit, V. V. Krasnosel'skikh, M. Dunlop, and H. Lühr. Identifying nonlinear wave interactions in plasmas using two-point measurements: A case study of short large amplitude magnetic structures (slams). *Journal of Geophysical Research - Space Science*, 104(A8):17079–17090, 1999.

M. W. Dunlop and A. Balogh. On the analysis and interpretation of four-spaecraft magnetic field measurements in terms of small scale plasma processes. In *Proc. Int. Conf. "Spatio-temporal Analysis for Resolving Plasma Turbulence (START)", Aussios, 31 Jan.–5 Feb.*, volume ESA WPP-047, Paris, France, 1993. European Space Agency.

M. W. Dunlop, T. M. Bauer, B. U. O. Sonnerup, N. Schopke, A. V. Khrabrov, T. Woodward, and A. N. Fazakerley. Dual spacecraft verification of magnetopause orientation and motion: Preliminary results. In *Proceedings of the Cluster II Workshop on Multiscale/Multipoint Plasma Measurements*, volume ESA SP-449, pages 103–110. European Space Agency, 2000.

M. W. Dunlop and T. I. Woodward. Multi-spacecraft discontinuity analysis: Orientation and motion. In Götz Paschmann and Patrick W. Daly, editors, *Analysis Methods for Multi-Spacecraft Data*, chapter 11. International Space Science Institute, 1998.

M. W. Dunlop and T. I. Woodward. Analysis of thick, non-planar boundaries using the discontinuity analyser. *Ann. Geophys.-Atmos. Hydrospheres Space Sci.*, 17(8):984–995, AUG 1999.

M. W. Dunlop, T. I. Woodward, and C. J. Farrugia. Minimum variance analysis: Cluster themes. In *Proceedings of the Cluster Workshops*, volume SP-371, pages 33–42. ESA, June 1995a.

M. W. Dunlop, T. I. Woodward, U. Motschmann, D. J. Southwood, and A. Balogh. Analysis of non-planar structures with multipoint measurements. *Advances in Space Research*, 18(8):309–314, 1995b.

M. W. Dunlop, T. I. Woodward, D. J. Southwood, K. H. Glassmeier, and R. Elphic. Merging 4 spacecraft data: Concepts used for analysing discontinuities. *Advances in Space Research*, 20 (4-5):1101–1106, 1997.

A. Fazakerley and D. Southwood. Theory and observation of magnetosheath waves. In *Geophysical Monograph*, volume 81. AGU, 1994.

K. H Glassmeier, U. Motschmann, M. Dunlop, A. Balogh, M. Acuna, C. Carr, G. Musmann, K. H. Fornacon, K. Schweda, J. Vogt, E. Georgescu, and S. Buchert. Cluster as a wave telescope - first results from the fluxgate magnetometer. *Annales Geophysicae*, 19:1439–1447, 2001.

M. A. Hapgood. Space physics coordinate transformations - a user guide. *Planet Space Sci*, 40(5): 711–717, 1992.

M. A. Hapgood. Space physics coordinate transformations: A user guide (vol 40, pg 711, 1992). *Planet Space Sci.*, 45(8):1047, 1997.

Øivin Holter. Wavelet analysis of time series. In *Proceedings of the Cluster Workshops*, volume SP-371, pages 43–50. ESA, June 1995.

T. Horbury, P. Cargill, E. Lucek, A. Balogh, M. Dunlop, T. Oddy, C. Carr, P. Brown, A. Szabo, and K. Fornacon. Cluster magnetic field observations of the bowshock: Orientation, motion and structure. *Annales Geophysicae*, 19:1399–1409, 2001.

IEEE85. *Special issue on Active Magnetospheric Partial Tracer Explorer (AMPTE)*, volume GE-23, May 1985.

K. I. Kim and E. J. Powers. A digital method of modelling quadratically nonlinear systems with a general random input. *IEEE Transactions on Acoustics, Speech and Signal Processing*, 36(11): 1758–1769, November 1988.

N. A. Krall and A. W. Trivelpiece. *Principles of Plasma Physics*. McGraw-Hill, 1973.

Kravtchenko-Berejnoi, Krasnoselskikh V., Mourenas D., and Lefeuvre F. Higher-order spectra and analysis of a non-linear dynamic model. In *Proceedings of the Cluster Workshops*, volume SP-371, pages 61–67. ESA, June 1995.

G. Le, C. T. Russell, and D. S. Orlowski. Coherence lengths of upstream ulf waves - dual isee observations. *Geophys. Res. Lett.*, 20(17):1755–1758, SEP 3 1993.

D. McCaffrey, I. Bates, M. A. Balikhin, H. St. C. K. Alleyne, M. Dunlop, and W. Baumjohann. Experimental method for the identification of dispersive three-wave coupling in space plasma. *Advances in Space Research*, 25(7/8):1571–1577, 1999.

U. Motschmann and K. H. Glassmeier. Mode recognition of mhd wave fields. In *Proceedings of the Cluster Workshops*, volume SP-371, pages 103–106. ESA, June 1995.

U. Motschmann, K. H. Glassmeier, and J. L. Pinçon. Filtering: Plasma mode recognition. In Götz Paschmann and Patrick W. Daly, editors, *Analysis Methods for Multi-Spacecraft Data*, chapter 4, pages 79–90. International Space Science Institute, 1998.

U. Motschmann, T. I. Woodward, K. H. Glassmeier, D. J. Southwood, and J. L. Pincon. Wavelength and direction filtering by magnetic measurements at satellite arrays: Generalized minimum variance analysis. *J. Geophys. Res-Space Phys.*, 101(A3):4961–4965, MAR 1 1996.

N. Nastasyina-Beloff, M. Balikhin, I. Bates, and M. P. Gough. Regularisation methods for ill-posed problems in the identification of non-linear processes in plasma turbulence. In *EOS trans. AGU*, volume 81(40), November 28 2000. Fall Meeting.

F. M. Neubauer and K. H. Glassmeier. Use of an array of satellites as a wave telescope. *J. Geophys. Res-Space Phys.*, 95(A11):19115–19122, NOV 1 1990.

J. A. Newbury and C. T. Russell. Observations of a very thin collisionless shock. *Geophys. Res. Lett.*, 23(7):781–784, APR 1 1996.

J. L. Pinçon. Cluster and the k-filtering. In *Proceedings of the Cluster Workshops*, volume SP-371, pages 87–94. ESA, June 1995.

O. A. Pokhotelov, M. A. Balikhin, H. St. C. K. Alleyne, and O. G. Onishchenko. Mirror instability with finite electron temperature effects. *J. Geophys. Res-Space Phys.*, 105(A2):2393–2401, FEB 2000.

W. Press, S. Teukolsky, W. Vetterling, and B. Flannery. *Numerical Recipes in C*, chapter 8. Cambridge University Press, 1992.

C. P. Ritz and E. J. Powers. Estimation of nonlinear transfer-functions for fully-developed turbulence. *Physica D*, 20(2-3):320–334, JUN-JUL 1986.

C. P. Ritz, E. J. Powers, and R. D. Bengtson. Experimental-measurement of 3-wave coupling and energy cascading. *Phys. Fluids B*, 1(1):153–163, JAN 1989.

P. Robert, M. W. Dunlop, A. Roux, and G. Chanteur. Accuracy of current density determination. In Götz Paschmann and Patrick W. Daly, editors, *Analysis Methods for Multi-Spacecraft Data*, chapter 16. International Space Science Institute, 1998.

P. Robert and A. Roux. Accuracy of the estimate of j via multi-point measurements. In *Proceedings of the International Workshop on "Space Plasma Physics Investigations by Cluster and Regatta"*, volume ESA SP-306, Paris, France, 1990. European Space Agency.

P. Robert and A. Roux. Dependenace of the shape of the tetrahedron on the accuracy of the estimate of the current density. In *Proc. Int. Conf. "Spatio-temporal Analysis for Resolving Plasma Turbulence (START)", Aussios, 31 Jan.–5 Feb.*, volume ESA WPP-047, Paris, France, 1993. European Space Agency.

W. J. Rugh. *Nonlinear Systems Theory: the Volterra/Wiener approach.* John Hopkins Press, Baltimore, Maryland, 1981.

R. Sagdeev and A Galeev. *Nonlinear Plasma Theory.* W. A. Benjamin, 1969. rev.

S. J. Schwartz, D. Burgess, W. P. Wilkinson, R. L. Kessel, M. Dunlop, and H. LÜHR. Observations of short large-amplitude magnetic-structures at a quasi-parallel shock. *J. Geophys. Res-Space Phys.*, 97(A4):4209–4227, APR 1 1992.

B. U. O. Sonnerup and L. J. Cahill. Magnetopause structure and attitude from explorer 12 observations. *Journal of Geophysical Research - Space Physics*, 72:171–183, 1967.

B. U. Ö. Sonnerup and M. Schieble. Minimum and maximum variance analysis. In Götz Paschmann and Patrick W. Daly, editors, *Analysis Methods for Multi-Spacecraft Data*, chapter 8, pages 185–220. International Space Science Institute, 1998.

M. Vettereli. *Wavelets and subband coding.* Prentice Hall, 1995.

S. N. Walker, R. Huff, and M. A. Balikhin. An investigation into instrumental nonlinear effects. In *Proceedings of the Cluster II Workshop on Multiscale/Multipoint Plasma Measurements*, volume ESA SP-449, pages 279–282. European Space Agency, 2000.

Appendix A

Coherence Lengths of the Low Frequency Turbulence at the Bow Shock and in the Magnetosheath

(Reprint of Bates et al. [2000]).

I. Bates[1], M. Balikhin[1], H. St. C. K. Alleyne[1], M. Dunlop[2], and H. Lühr[3]

[1]*ACSE, University of Sheffield, England*
[2]*Imperial College, London, England*
[3]*Geoforschungszentrum Potsdam, Germany*

ABSTRACT

The coherence length of turbulence is an important parameter which limits the ability of a multi-satellite study of waves in space plasma. Multi-satellite measurements cannot be used to identify the composition of observed turbulence and its dynamics if the satellite separation exceeds this coherence length. *AMPTE UKS* and *AMPTE IRM* data were used to find the coherence lengths for low frequency turbulence in the Magnetosheath and the Bow Shock.

Key words: coherence length; magnetic field measurements; multi-satellite measurements; waves.

INTRODUCTION

There have been many measurements of space plasma turbulence by single satellites, these measurements revealing many processes in various space regions. However single satellite measurements are not able to separate between spatial and temporal variations, so not revealing the full composition of linear and nonlinear processes taking place. For these reasons multipoint measurements are required. Studies of mutual phase relations are then usually carried out to find the composition of and identify dynamical processes in the plasma turbulence.

If the distance between the satellites is larger than a certain scale length (or coherence length) the mutual phase information is lost in the sense that the measurements become effectively independent. The study of coherence lengths is crucial to understand, for given separations, which waves will carry mutual phase information and will be possible to compare with multipoint measurements.

One of the scientific objectives of *CLUSTER II* is to distinguish between variations in space and time. We use previous experiments to study the coherence lengths in magnetosheath and parallel

shock turbulence, to find the inherent limitations imposed by the *CLUSTER* separation strategy for observing wave phenomena in those regions. Turbulence in quasi-perpendicular shock has been explored by Le et al. (1993) and their results showed that the *CLUSTER* separation will be too large to apply multipoint measurements to some of the smaller scale phenomena.

This paper presents a method to find these coherence lengths using dual satellite measurements, and results obtained from those measurements in the magnetosheath.

METHOD

The assumption is that the wave field is a composition of plane waves:

$$\vec{B}(\vec{r},t) = \sum_{\omega_j} \vec{B}(\omega_j) \exp\, i(\vec{k_j}\cdot\vec{r} - \omega_j t) + \text{c.c.}, \tag{A.1}$$

(where c.c. denote complex conjugate terms).

The argument is that introducing a time delay into one of the datasets is equivalent to a spatial shift along the satellite separation direction (with dual satellite data only information about the projection of the wave vector on the satellite separation vector, $k_{\text{proj}} = \vec{k}.\vec{r}/|\vec{r}|$, is known).

$$\begin{aligned}
\psi(|\vec{r}|, t-\Delta t) &= k_{\text{proj}}.|\vec{r}| - \omega.(t-\Delta t) \\
&= k_{\text{proj}}.|\vec{r}| - \omega.t + \omega.\Delta t \\
&= k_{\text{proj}}.(|\vec{r}| + \tfrac{\omega}{k_{\text{proj}}}\Delta t) - \omega t \\
&= \psi(|\vec{r}| + \tfrac{\omega}{k_{\text{proj}}}.\Delta t, t) \\
&= \psi(|\vec{r}| + \Delta r, t)
\end{aligned} \tag{A.2}$$

The coherence function is used to find the coherence between the original and the time delayed datasets. This results in a quantitative measure of the coherence of frequency components in the datasets (Bendat & Piersol, 1986).

$$\gamma^2(\omega) = \frac{|G_{xy}(\omega)|^2}{G_{xx}(\omega)G_{yy}(\omega)} \tag{A.3}$$

(where $G_{xy}(\omega)$ is the spectral density function, calculated using wavelet transforms).

Equation A.3 is bounded between 0 and 1, with $\gamma(\omega) = 1$ meaning the waves at frequency ω essentially carry mutual phase information and $\gamma(\omega) = 0$ meaning they don't.

A coherence cut-off is defined to distinguish between coherent and non-coherent waves. This is applied to the coherence plot to find the maximum coherent frequency for the time delay.

The dispersion relation (Balikhin et al., 1997) is used to find $\frac{\omega}{k_{\text{proj}}}$, hence using Equation A.2 enables Δr to be found for the given frequency. This constitutes part of the Coherence Length (km) Vs frequency plot.

Calculating $n = \Delta r/\lambda = \frac{\omega}{2\pi}\Delta t$ (as $k_{\text{proj}} = 2\pi/\lambda_{\text{proj}}$) gives the number of wavelengths at the given frequency that fit into the coherence length Δr. This constitutes part of the Coherence Length ($n\lambda$) Vs frequency plot.

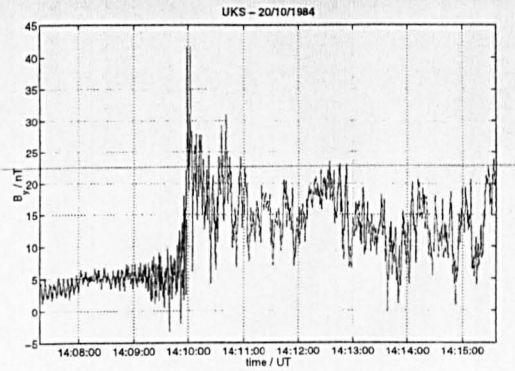

Figure A.1: Magnetic field magnitude plot for 20/10/1984 around 14:11:00 to 14:14:00 UT (*UKS* satellite shown, *IRM* not shown for clarity).

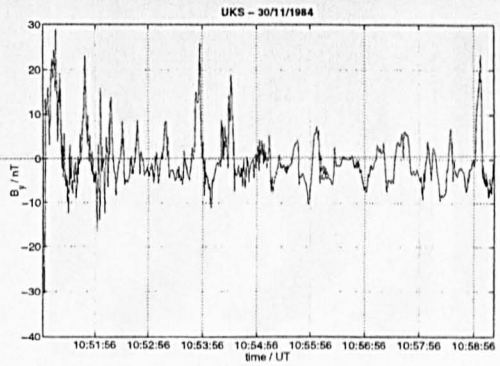

Figure A.2: Magnetic field magnitude plot for 30/11/1984 10:55:00 to 10:58:00 UT (*UKS* satellite shown, *IRM* not shown for clarity).

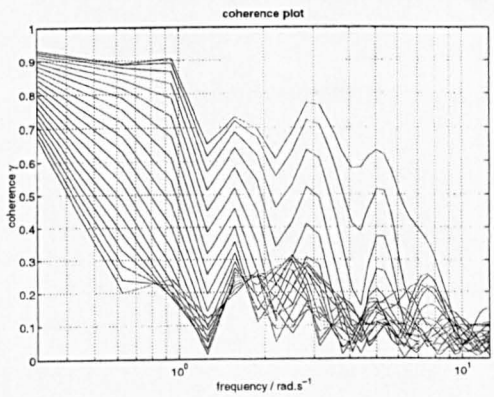

Figure A.3: Coherence plots for 20/10/1984. 20 incremental time delays of 1 s are shown. As the time delay increases the maximum coherent frequency (defined by an arbitrary cut-off value) decreases.

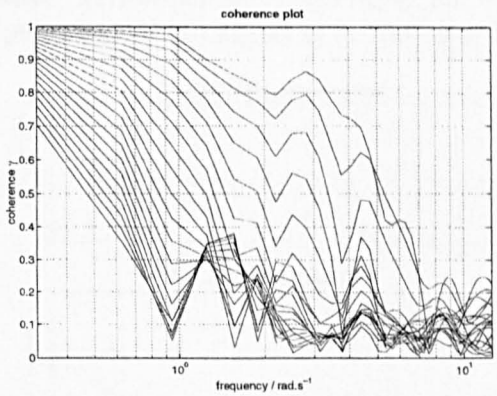

Figure A.4: Coherence plots for 30/11/1984. 20 incremental time delays of 1 s are shown. Again, as the time delay increases the maximum coherent frequency (defined by an arbitrary cut-off value) decreases.

This process is then repeated for various time delays to build up the coherence length plots.

RESULTS

Experimental Data

Two datasets are used. Both are magnetic field measurements made by *AMPTE UKS/IRM*. The first dataset used was from 20/10/1984 around 14:11:00 to 14:14:00 UT, where the satellite separation was 60 km and they were in the magnetosheath in the vicinity of a quasi-parallel Bow Shock. The second dataset was from 30/11/1984 around 10:55:00 to 10:58:00 UT, where the satellite separation was 145 km and they were in the magnetosheath. The *UKS* magnetic field measurements for the B_y component are shown in Figures A.1 and A.2 respectively.

Coherence calculations

Coherence functions were calculated for 20 artificial time delays in increments of 1 s. They can be seen in Figures A.3 and A.4. The general trend is for the tail end of the coherence function to move

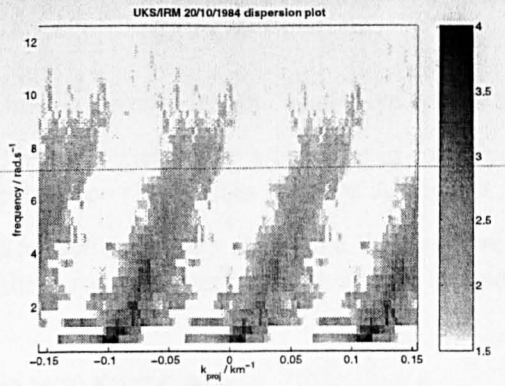

Figure A.5: Initial dispersion plot for 20/10/1984. Satellite separation distance of 60 km. ω plotted against k_{proj}, the projection of the wave vector on the satellite separation vector. This dispersion is linear, with a phase and group velocity of $\approx 100\ km\ s^{-1}$

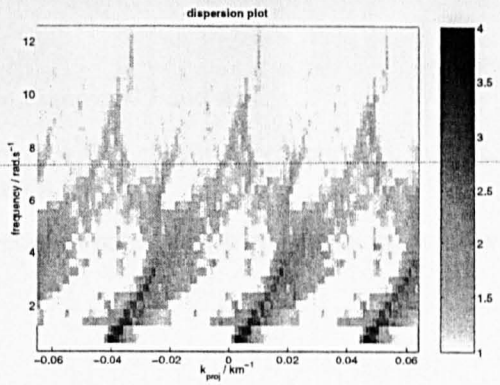

Figure A.6: Initial dispersion plot for 20/10/1984. Satellite separation distance of 145 km. ω plotted against k_{proj}, the projection of the wave vector on the satellite separation vector. This dispersion is also linear, but with a phase and group velocity of $\approx 200\ km\ s^{-1}$

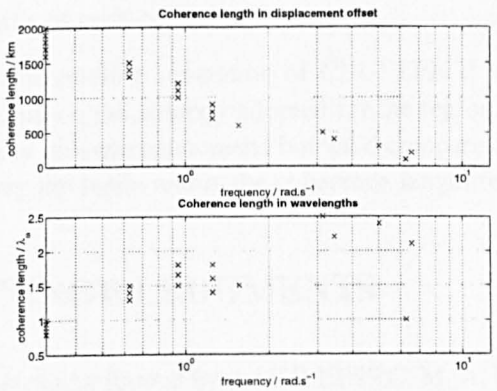

Figure A.7: Coherence lengths for 20/10/1984. Shown against satellite separation in km (top panel) and against number of wavelengths (bottom panel).

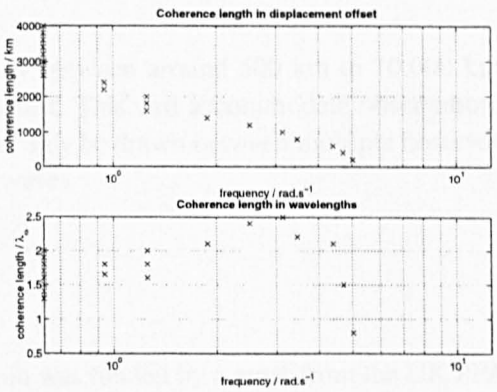

Figure A.8: Coherence lengths for 30/11/1984. Shown against satellite separation in km (top panel) and against number of wavelengths (bottom panel).

closer to lower frequencies as the time delay gets larger. This indicates that lower frequency waves stay coherent over longer temporal distances, and hence over larger spatial distances.

Dispersion calculations

The dispersion relation for the waves need to calculated to find the coherence length in km. These dispersion plots can be seen in Figures A.5 and A.6. Both dispersions are seen to be linear. The dispersion in Figure A.5 has a group and phase velocity of $\approx 100\ km\ s^{-1}$. The corresponding value in Figure A.6 is $\approx 200\ km\ s^{-1}$. These calculated values are higher than they are in reality as they are based on a projection of the wave vector which will never be greater than the true magnitude. This is an ambiguity in the wave vector determination which is inherent with dual satellite measurements. *CLUSTER II* if successfully launched will allow this ambiguity to be removed (Dunlop et al., 1997, Balikhin et al., 1999).

Coherence Length calculations

The final coherence length calculations can be seen in Figures A.7 and A.8.

The top panels show a decrease in coherence length with increasing frequency, as indicated in the coherence calculations (Section A, Figures A.7 and A.8).

The bottom panels show that the comparison between coherence length in number of wavelengths is roughly constant, with a value around 2.

CONCLUSIONS

Low frequency waves in the magnetosheath have finite coherence lengths. It is found that this length depends on the frequency of the waves being observed, with lower frequency waves having longer coherence lengths.

It is found that the ratio of coherence length to wavelength $n \approx 2$, giving a rule-of-thumb estimate that to observe waves coherently, the measurements must be made within about two wavelengths of each other.

The satellite separation of *CLUSTER II* will vary between around 500 km to 10,000 km depending on the strategy adopted for the region of interest. This will accommodate observation of a variety of wave phenomena but valid comparisons can only be drawn between multiple observations if they are made within the coherence length for the waves.

ACKNOWLEDGMENTS

I. Bates was funded by the UK EPSRC. M. A. Balikhin was funded by a grant from the UK PPARC.

REFERENCES

Balikhin, M. A., Bates, I., Minimum Variance free identification of the composition of space plasma turbulence and nonlinear processes in it, these proceedings

Balikhin, M. A., Woolliscroft, L. J. C., Alleyne, H. S. C., Dunlop, M., Gedalin, M. A., 1997, Determination of the dispersion of low frequency waves downstream of a quasiperpendicular collisionless shock, Annales Geophysicae, Vol. 15, pp. 143-151

Dunlop, M. W., Woodward, T.I., Southwood, D.J., Glassmeier, K. H., Elphic, R., 1997, Merging 4 spacecraft data: Concepts used for analysing discontinuities, Advances in Space Research, Vol. 20, No. 4-5, pp. 1101-1106

Bendat, J. S., Piersol, A. G. 1986, Random Data - Analysis and Measurement Procedures (2nd ed.), John Wiley & Sons

Le, G., Russell, C. T., Orlowski, D. S. 1993, Coherence Lengths of upstream ULF waves: Dual ISEE observations, Geophysical Research Letters, Vol. 20, No. 17, pp. 1755-1758

Le, G., Russell, C. T. 1990, A study of the coherence length of ULF waves in the Earth's foreshock, Journal Geophysical Research, Vol. 95, pp. 10,703

Appendix B

Experimental Method for Identification of Dispersive Three-Wave Coupling in Space Plasma

(Reprint of McCaffrey et al. [1999]).

D. McCaffrey[1], I. Bates[1], M. A. Balikhin[1], H. St. C. K. Alleyne[1], M. Dunlop[2], and W. Baumjohann[3]

[1]*ACSE Department, University of Sheffield, UK.*
[2]*Department of Physics, Imperial College, London, UK.*
[3]*Max Planck Institut fur Extraterrestische Physik, Garching bei Munchen, Germany*

ABSTRACT

A statistical method used for estimating the linear and quadratic processes in laboratory plasma is adapted for dispersive waves in space plasma turbulence. This method is applied to magnetic field data obtained from *AMPTE IRM* and *AMPTE UKS* satellites in the magnetosheath just downstream of the Earth's bow shock. The results show the presence of two instabilities, presumably related to the distribution of ions.

INTRODUCTION

In this paper we describe a statistical method for estimating the strength of three wave coupling in space plasma using data from two satellites. The method was originally proposed by Ritz, Powers and their co-workers (see Ritz and Powers, 1985; Ritz *et al.*, 1989 and the references therein) and applied to the study of turbulence in a tokamak. Recently it has been applied in de Wit *et al.* (1999) to study turbulence in the vicinity of the Earth's bow shock. However, this application assumed that the plasma was non-dispersive in order to apply the Ritz and Powers method. We therefore describe in this paper how to modify their method to estimate three-wave coupling in the presence of dispersion. The results are then applied to study nonlinear wave interactions in data obtained from the *AMPTE UKS* and *IRM* satellites in the Earth's magnetosheath.

We begin with a brief review of how the evolution of turbulence between two points in time can be modelled as an input-output system. Following de Wit (1999), we consider a wave-field $B(x,t)$ depending on one spatial coordinate and on time and assume it is statistically stationary with a zero mean. The dynamics of this wave-field can then generally be described by the following equation:

$$\frac{\partial B(x,t)}{\partial t} = F(B(x,t)) \tag{B.1}$$

Here $F(B)$ is a nonlinear time-invariant operator which can be expanded as a Volterra series of convolution type operators on powers of B (Rugh, 1981). Taking Fourier transforms of this expansion for discrete measurements and truncating to second order we get

$$\frac{\partial B(k,t)}{\partial t} = \Gamma_1(k)B(k,t) + \frac{1}{2}\sum_{\substack{k_1,k_2 \\ k=k_1+k_2}} \Gamma_2(k_1,k_2)B(k_1,t)B(k_2,t) \tag{B.2}$$

The first kernel $\Gamma_1(k) = \gamma(k) + i\bar{\omega}(k)$ contains the linear growth (damping) rate and the dispersion. The second kernel $\Gamma_2(k_1,k_2)$ is called the quadratic interaction term and describes the strength of three-wave coupling for those waves that satisfy the resonance condition $k_1 + k_2 = k$. This resonance condition for wave vectors is a result of the conservation of momentum in three-wave processes. The conservation of energy in such processes leads to the resonance condition for frequency $\omega_1 + \omega_2 = \omega$. If included in Eq. B.2 the third order term, $\Gamma_3(k_1,k_2,k_3)$, would describe four-wave interactions, etc. The above Fourier space model arises naturally in the study of plasma turbulence. For instance, Zakharov's Hamiltonian formulation of plasma turbulence (Zakharov, 1985) leads to explicit formulae for the kernels Γ_2 and Γ_3.

The efficiency of three-wave processes in plasma turbulence is proportional to the product of the amplitudes of the three waves involved, measured relative to the background field. Similarly the efficiency of four-wave processes is proportional to the product of the amplitudes of the four waves involved. When the magnitudes of the waves are less than the background field, it follows that the three-wave processes will be more significant for the evolution of the wave field than four-wave processes which in turn will be more significant than processes involving higher numbers of waves. Sometimes resonance conditions for both frequencies and wave vectors cannot be satisfied simultaneously due to the particular dispersion relation. In that case three-wave processes will be forbidden, and four-wave processes will play the significant role in the evolution of the turbulence. In the present paper we are limited to the case in which three-wave processes are not forbidden and so we disregard higher order nonlinear processes.

The method described in Ritz *et al.* (1989) then involves taking spatial measurements of $B(x,t)$ and $B(x,t+\tau)$ at two fixed times t and $t+\tau$. From these the wavenumber spectra $B(k,t)$ and $B(k,t+\tau)$ can be computed. The complex spectrum $B(k,t)$ is then represented by an amplitude and phase $|B(k,t)|e^{i\Phi(k,t)}$ where the amplitude varies slowly with respect to the phase. Then, estimating the time derivative in Eq. B.2 as a finite difference $(B(k,t+\tau) - B(k,t))/\tau$, Ritz *et al.* (1989) show that for small τ Eq. B.2 can be re-arranged in the form of an input-output system,

$$Y_k = L_k X_k + \frac{1}{2}\sum_{\substack{k_1,k_2 \\ k=k_1+k_2}} Q_k^{k_1,k_2} X_{k_1} X_{k_2} \tag{B.3}$$

where

$$\begin{aligned} X_k &= B(k,t) \\ Y_k &= B(k,t+\tau) \\ L_k &= (\Gamma_1(k)\tau + 1 - i\delta\Phi(k))e^{i\delta\Phi(k)} \\ Q_k^{k_1,k_2} &= \Gamma_2(k_1,k_2)\tau e^{i\delta\Phi(k)} \\ \delta\Phi(k) &= \Phi(k,t+\tau) - \Phi(k,t) \end{aligned}$$

Thus Eq. B.2 is represented by a system with input X_k, output Y_k and transfer functions L_k and $Q_k^{k_1,k_2}$ describing the linear and quadratic responses of the system to the input signal X_k. This now becomes a System Identification problem. Some data analysis is performed to obtain estimates of L_k and $Q_k^{k_1,k_2}$ and thus of Γ_1 and Γ_2. This gives in particular the linear growth rate and the strength of three-wave coupling for triples of wave numbers satisfying $k = k_1 + k_2$.

In practice it is generally difficult to obtain a spatially resolved measurement of $B(x,t)$ as required for calculating $B(k,t)$. The approach taken in Ritz *et al.* (1989) in studying the edge plasma in a tokamak is to take temporally resolved measurements at two fixed points x and $x + \delta x$, where x is the poloidal angle, and then calculate the frequency spectra $B(x,\omega)$ and $B(x+\delta x,\omega)$. The above analysis is then repeated with $B(k,t)$ replaced by $B(x,\omega)$. This leads to an estimate of the spatial growth rate and the strength of the wave coupling during propagation in space rather than the corresponding quantities with respect to time. Physical interpretation is obtained by considering the linear dispersion relation which is observed to hold for the dominant low frequency components. So since all the spectral components are propagating with the same velocity, the measured spatial change in the wave structure can be interpreted as a temporal change.

Similarly, in De Wit *et al.* (1999) three-wave coupling is measured in the vicinity of the Earth's quasi-parallel bow shock using data from two satellites. In this case the analysis takes place in the satellite frame where the satellites are at fixed positions x and $x + \delta x$ and Doppler shifted frequency spectra $B(x,\omega)$ and $B(x+\delta x,\omega)$ are obtained. An analysis similar to that for the tokamak is performed and again a linear dispersion relation holding for lower frequency components is required in order to interpret the measured spatial change as a change in time.

In the next section we describe how to modify the Ritz-Powers method to estimate three-wave coupling using data from two satellites where a nonlinear dispersion relation holds, by taking into account the different propagation velocities of each spectral component.

METHOD

We consider two satellites following similar trajectories and separated by a distance δx. We assume that the wave field is a superposition of plane waves so that the wave propagation direction for each frequency is the same at each satellite. All frequencies are expressed in the satellite frame, in which they are Doppler shifted. It is worth noting that the frequency resonance condition is valid in any inertial frame.

The measurements of one component of the magnetic field will result in two time series, $B_1(t)$ from satellite 1 and $B_2(t)$ from satellite 2. Let us denote the corresponding frequency spectra by $B_1(\omega)$ and $B_2(\omega)$. After encountering the first satellite the wave propagates through the plasma before encountering the second satellite. During this passage the wave is modified by linear and three-wave processes. This can be considered as an input-output system for which the measurements from the first satellite can be regarded as the 'input' into the system and measurements from the second satellite as its 'output'. As only linear and three-wave processes are taking place in that system, Eq. B.1, which describes the wavefield evolution, can be rewritten as:

$$\frac{\partial B_1(\omega)}{\partial t} = \Gamma_1(\omega)B_1(\omega) + \frac{1}{2}\sum_{\substack{\omega_1,\omega_2 \\ \omega=\omega_1+\omega_2}} \Gamma_2(\omega_1,\omega_2)B_1(\omega_1)B_1(\omega_2) \tag{B.4}$$

As above we represent $B_1(\omega)$ by a phase and a slowly varying amplitude $|B_1(\omega)|e^{i\Phi_1(\omega)}$. We also note that the dispersion relation $\omega = c_\omega k_\omega$ can be estimated from two-point measurements (Balikhin *et al.*, 1997; Balikhin and Gedalin, 1993). Thus the phase speed in the satellite frame can be calculated for each spectral component. So we know that the time for each spectral component to pass between satellite 1 and satellite 2 is $\delta x \cos\theta/c_\omega$, where θ is the angle between the x-axis and the wave vector. The derivative in Eq. B.4 can then be estimated as follows:

$$\frac{\partial B_1(\omega)}{\partial t} = \lim_{\delta x \to 0}\left(\frac{|B_2(\omega)| - |B_1(\omega)|}{|B_1(\omega)|\delta x\cos\theta/c_\omega} + i\frac{\Phi_2(\omega) - \Phi_1(\omega)}{\delta x\cos\theta/c_\omega}\right)_{B_1(\omega)} \tag{B.5}$$

Substituting Eq. B.5 into Eq. B.4 and solving for $B_2(\omega)$ with δx very small, we obtain the following modification of the input-output system described in Ritz *et al.* (1989),

$$Y_\omega = L_\omega X_\omega + \frac{1}{2}\sum_{\substack{\omega_1,\omega_2 \\ \omega=\omega_1+\omega_2}} Q_\omega^{\omega_1,\omega_2} X_{\omega_1} X_{\omega_2} \tag{B.6}$$

where

$$\begin{aligned} X_\omega &= B_1(\omega) \\ Y_\omega &= B_2(\omega) \\ L_\omega &= (\Gamma_1(\omega)(\delta x\cos\theta/c_\omega) + 1 - i\delta\Phi(\omega))e^{i\delta\Phi(\omega)} \\ Q_\omega^{\omega_1,\omega_2} &= \Gamma_2(\omega_1,\omega_2)(\delta x\cos\theta/c_\omega)e^{i\delta\Phi(\omega)} \\ \delta\Phi(\omega) &= \Phi_2(\omega) - \Phi_1(\omega) \end{aligned}$$

The technique described in Kim and Powers (1988) can now be used to estimate the linear and quadratic transfer functions and thus the linear growth rate and the quadratic interaction term. We outline this briefly and refer the reader to the cited reference for more details.

For each frequency ω the summation in Eq. B.7 can be expanded to form

$$\begin{bmatrix} U_\omega & U_{\omega_1}U_{\omega_2} & U_{\omega_1'}U_{\omega_2'} & \cdots \end{bmatrix} \begin{bmatrix} L_\omega \\ Q_\omega^{\omega_1,\omega_2} \\ Q_\omega^{\omega_1',\omega_2'} \\ \vdots \end{bmatrix} = [\, Y_\omega \,] \tag{B.7}$$

where the rows in the first term on the LHS and in the term on the RHS contain the n_{ens} ensemble measurements and the remaining term contains the n_{coeff} model coefficients. These coefficients are found by solving Eq. B.7 as a Least Squares problem. The spectral representation of $B(\omega)$ is carried out using Morlet wavelet transforms. Each ensemble in Eq. B.7 can then be taken as one of the sample points over which the wavelet transform is taken.

It has been found by de Wit *et al.* (1999) that the frequency range and the number of frequencies (the mesh size n_ω) to divide the range into must be chosen carefully to get statistically reliable

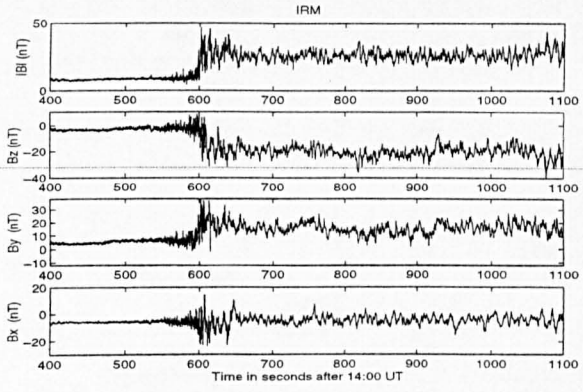

Figure B.1: Absolute value and three components of the magnetic field measured by *AMPTE IRM* during the bow shock crossing which occurred at about 14:10:00 UT on 20.10.1984. Time scale is in seconds after 14:00:00.

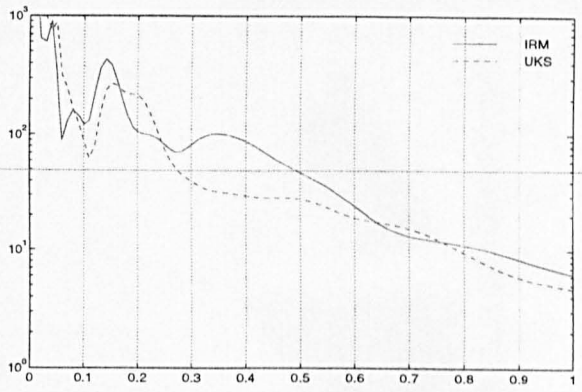

Figure B.2: Auto power spectra plot of the B_y components measured by *AMPTE UKS* and *IRM*. Morlet wavelet transforms were used.

results. The Nyquist frequency and a decreasing signal to noise ratio at higher frequencies limits the frequency range. A good indicator is the range over which the system coherence $\gamma^2(\omega)$ remains near unity. The choice of n_ω is limited by the necessity of a matrix inversion to solve Eq. B.7, as a high value of n_ω, which can introduce similar and therefore linearly dependent ensemble measurements in the first term on the LHS of Eq. B.7, making it difficult to invert. Evaluating the matrix condition number for this term over different mesh sizes gives an indication of the appropriate mesh size to use. Based on calculations similar to those in de Wit et al (1999) the frequency range was chosen as $0 \leq f \leq 1$ Hz and the mesh size n_ω as 20.

BOW SHOCK CROSSING ON 20 OCTOBER 1984 AT ABOUT 14:10 UT

We consider the Earth's bow shock which was measured by *AMPTE UKS* and *IRM* at about 14:10 UT on 20 October 1984. The position of *AMPTE UKS* at 14:10 UT was $(12.19, 0.77, -0.40)$ R_e (GSE). The bow shock was crossed first by *AMPTE UKS* and then by *AMPTE IRM*. The separation vector between the two satellites during the crossing was $\vec{R} = (-50.5, -24.6, 18.2)$ km (GSE).

Three components and the absolute values of the magnetic field measured by *AMPTE IRM* are shown in Figure B.1. The time scale on these figures is seconds after 14:00:00 UT. In the downstream region, waves observed from 650 sec to 1100 sec are studied. The angle between the upstream magnetic field and the normal to shock front, estimated on the basis of the co-planarity theorem, was $\approx 50°$. Features of the turbulence are usual for the quasiperpendicular shocks. In the foot the main part of the wave energy resides in the frequency range from about one to a few Hz. In this frequency range the waves are whistlers. As the satellite approaches the downstream region, the wave frequency drops. The main energy of the turbulence is present in the downstream region in the frequency range 0–1.5 Hz. These are the waves that are studied in the present paper. The dispersion relation of these waves in the plasma rest frame is obtained by Balikhin *et al.* (1997). These waves are convected by the solar wind flow from *AMPTE IRM* towards *AMPTE UKS*. Thus the data set (B_y^{IRM}) was considered as the input and data set (B_y^{UKS}) as the output.

The B_y^{IRM} and B_y^{UKS} measurements are used to calculate the power spectra (shown in Figure B.2). The spectra are not smooth but have a number of local maxima. There are regions where the *IRM* spectrum is greater than the *UKS* spectrum, indicating there is a decrease of energy contained in

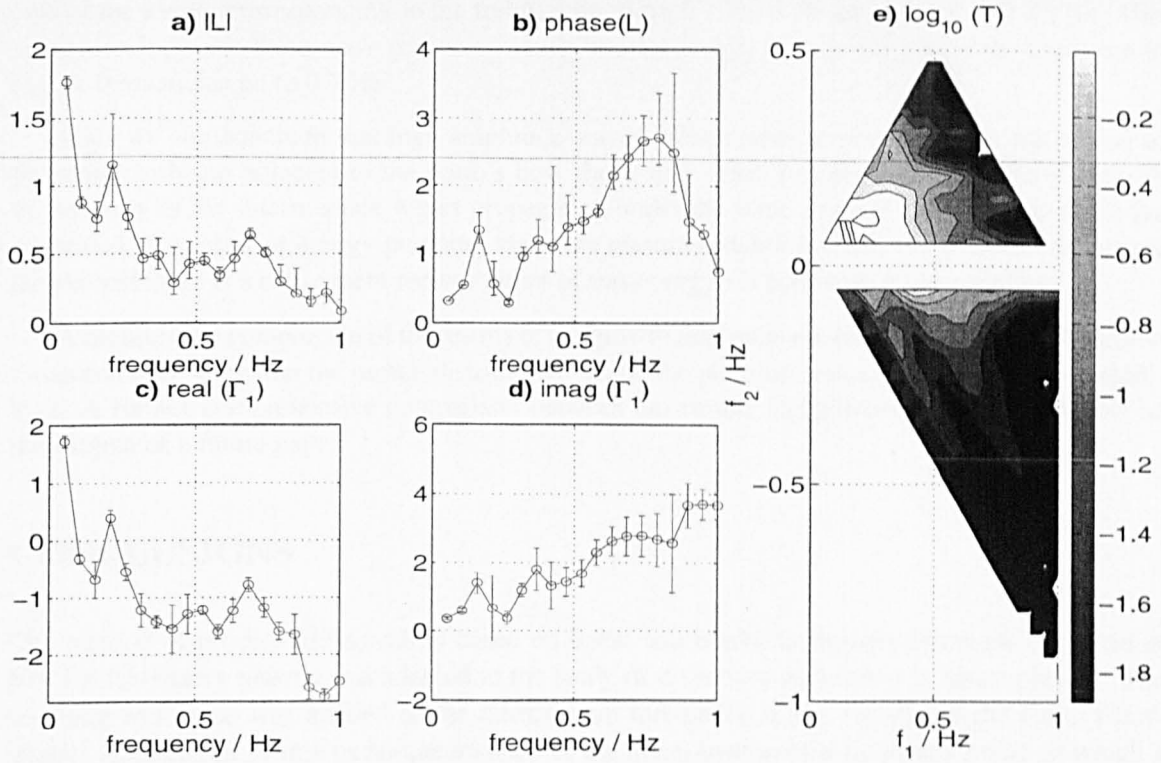

Figure B.3: The estimated quantities calculated from the *AMPTE UKS* and *IRM* measurements: a) Magnitude of the linear transfer function (vertical lines correspond to the error bars), b) Phase of the linear transfer function, c) Real part of Γ_1, corresponding to the growth rate, d) Imaginary part of Γ_1, corresponding to the dispersion $\omega(k)$ and e) Magnitude of the spectral energy transfer rate (arbitrary units)

those regions as the waves propagate between the satellites. The reverse is true in regions where the *UKS* spectrum is greater than the *IRM* spectrum, i.e. there is an increase of energy contained in those regions. This figure cannot however say anything of the mechanisms involved.

The estimates obtained from the B_y^{IRM} and B_y^{UKS} measurements are shown in Figure B.3. The magnitude $|L|$ in Figure B.3a gives the change of the signal level between the input B_y^{IRM} and the output B_y^{UKS} due to linear growth (damping) of the waves. $|L| > 1$ indicates a positive growth rate for the wave while it propagates between the satellites (Ritz and Powers, 1985). A magnitude less than one indicates linear damping of the wave due to interactions with plasma particles. The actual growth rate (the real part of the first Volterra kernel Γ_1) is also calculated and plotted in Figure B.3c. We can observe in Figure B.3a, c that $|L| > 1$ and a positive growth rate exist only for very low frequencies $f < 0.15$ Hz and near $f \approx 0.25$ Hz. This corresponds with the regions mentioned in the power spectra in Figure B.2. There is now evidence that the earlier indication is justified and that a linear instability pumps energy from the plasma to the turbulence in these frequency intervals.

The phase of the linear transfer function (Figure B.3b) should correspond to the phase shift undergone by the wave packets as they move between spacecraft. Thus the phase of the linear transfer function determines the dispersion of the observed turbulence. This phase on the interval $0 - 1$ Hz is similar to the phase of cross-coherence function between the B_y^{IRM} and B_y^{UKS} data sets calculated in Balikhin *et al.* (1997). So the estimation of the dispersion of the observed waves from the present model is close to the dispersion calculated making use of the coherence function.

The spectral energy transfer function which quantifies the energy transfer between various scales of turbulence (De Wit *et al.*, 1999) due to three-wave processes is plotted in Figure B.3e. The upper part of this figure corresponds to processes of the form $|f_1| + |f_2| \Rightarrow |f|$. The lower part of the figure corresponds to processes of the form $|f_1| \Rightarrow |f_2| + |f|$. There is prominent maximum in the upper

part of the figure, corresponding to the frequencies $f_1 \approx 0 - 0.45$ Hz and $f_2 \approx 0 - 0.25$ Hz. This maximum indicates three-wave processes which transfer energy from lower part of the spectrum to higher frequencies up to 0.7 Hz.

Thus we can conclude that high amplitude waves, which have been observed in the region of the magnetosheath adjacent to the Earth's bow shock and which possess a phase velocity close to the velocity of the intermediate waves propagating under the same angle to the magnetic field, are generated as a result of energy pumping via some plasma instabilities into two unstable frequency ranges and there is a subsequent redistribution of this energy via nonlinear wave coupling.

A preliminary comparison of the results of the growth rate value estimation with *AMPTE* plasma measurements show that the proton distribution can be the possible source of the observed instabilities. A further comprehensive comparison between our results and plasma measurements will be the subject of a future paper.

CONCLUSIONS

The method of process identification based on linear and nonlinear transfer functions proposed at first for laboratory plasma was adapted to the study of dispersive turbulence in space plasma. The resulting technique was applied to the downstream turbulence in the vicinity of the Earth's bow shock. Application of this technique resulted in the identification of a frequency range in which a pumping of energy to the turbulence from the plasma via a linear instability occurs. It was shown that this energy later is transferred to other scales through nonlinear wave coupling.

ACKNOWLEDGMENTS

M. Balikhin and M. Dunlop acknowledge ISSI for providing the possibility for meetings. I. Bates was funded by EPSRC, U.K. M. Balikhin was funded by PPARC, U.K.

REFERENCES

Balikhin, M. A. and Gedalin, M. E., Comparative Analysis of Different Methods for Distinguishing Temporal and Spatial Variations, Proceedings of START Conference, Aussois, France, Jan.31-Feb.5, ESA **SP-183**, 1993.

Balikhin, M. A., Woolliscroft, L. J. C., Alleyne, H. S. C. K., Dunlop, M., and Gedalin, M. A., Determination of the Dispersion of Low Frequency Waves Downstream of a Quasiperpendicular Bow Shock, *Annales Geophysicae*, **15**:143–151, 1997.

de Wit, T. D., Krasnosel'skikh, V. V., Dunlop, M., and Lühr, H., Identifying Nonlinear Wave Interactions in Plasmas using Two-point Measurements: A Case Study of Short Large Amplitude Magnetic Structures, *J. Geophys. Res.*, **104(A8)**:17079–17090, 1999.

Kim, K. I. and Powers, E. J., A Digital Method of Modelling Quadratically Nonlinear Systems with a General Random Input, *IEEE Transactions of Acoustics, Speech and Signal Processing*, **36(11)**:1758–1769, 1988.

Ritz, C. P., Powers, E. J., and Bengston, R. D., Experimental Measurement of Three-Wave Coupling and Energy Cascading, *Phys. Fluids B*, **1(1)**:153–163, 1989.

Rugh, W. J., Nonlinear Systems Theory: the Volterra/Wiener approach, John Hopkins Press, Baltimore, Maryland, 1981.

Zakharov, V. E., Musher, S. L., and Rubenchik, A. M. , Hamiltonian Approach to the Description of Nonlinear Plasma Phenomena, *Phys. Reports*, **129**(**5**):285–366, 1985.

Appendix C

Minimum-Variance free determination of Magnetosheath Wave Propagation Vectors

(Reprint of Bates et al. [2001]).

I. Bates[1], M. Balikhin[1], H. St. C. K. Alleyne[1], and M. Andre[2]

[1]*Department of Automatic Control and Systems Engineering, University of Sheffield, U.K.*
[2]*Swedish Institute of Space Physics, Uppsala Division, Sweden*

ABSTRACT

The direction of propagation of waves in the plasma is important when studying space plasma turbulence and the linear and nonlinear processes that occur.

The usual procedure of determining this propagation direction involves minimum variance analysis. This technique has many limitations, such as not being suitable for plane-polarised waves or for multiple waves at the same frequency, but is the only way of finding the propagation direction from dual satellite measurements. With *CLUSTER II* affording simultaneous four-point measurements the reliance on minimum variance analysis is removed and for the first time the determination of wave propagation directions directly from the instrument measurements is possible.

The propagation directions of magnetosheath waves measured by EFW on *CLUSTER II* are determined using this minimum variance analysis-free method. Further information, such as FGM measurements and the basic plasma parameters, are needed to make a full physical interpretation of these results.

wave vector; multi-satellite multi-point measurements; dispersion; magnetosheath

INTRODUCTION

Measuring wave phenomena with simultaneous multi-point satellite instruments enables, through phase differencing, the wave vector to be completely determined. The magnitude of the wave vector $|\mathbf{k}|$ gives information about the wavelength of the wave (as $|\mathbf{k}| = 2\pi/\lambda$). The wave propagates in the direction given by the vector $\widehat{\mathbf{k}}$.

Phase Differencing

Phase differencing is a useful technique, and has been applied to plasma wave observations previously, e.g. Balikhin et al. [1997a], Balikhin and Gedalin [1993], Balikhin et al. [1997b], deWit et al. [1995].

Assuming the wave-field is composed of plane waves, it can be expressed as

$$\vec{B}(\mathbf{k},t) = \sum_{\omega_i} \alpha(\omega_i) e^{i(\mathbf{k}_i \cdot \mathbf{x} - \omega_i t)} \tag{C.1}$$

where $\alpha(\omega_i)$ is the amplitude of the ω_i component and the dispersion relation is given by $\omega_i = \omega(|\mathbf{k}_i|)$ (the phase speed is $\omega_i/|\mathbf{k}_i|$ and the group speed is $\partial\omega/\partial|\mathbf{k}_i|$).

Writing the phase as $\psi(\mathbf{x},t) = \mathbf{k}.\mathbf{x} - \omega t$ and the phase at the i^{th} satellite as $\psi_i = \psi(\mathbf{x}_i, t)$, it can be shown that the phase difference between the two satellites ψ_{ij} contains information about the projection of $\mathbf{k}$ on the separation vector $\mathbf{x}_{ij}$:

$$\begin{aligned}
\psi_{ij} &= \psi_j - \psi_i \\
&= \psi(\mathbf{x}_j, t) - \psi(\mathbf{x}_i, t) \\
&= (\mathbf{k} \cdot \mathbf{x}_j - \omega t) - (\mathbf{k} \cdot \mathbf{x}_i - \omega t) \\
&= \mathbf{k} \cdot (\mathbf{x}_j - \mathbf{x}_i) \\
&= \mathbf{k} \cdot \mathbf{x}_{ij} \\
&= |\mathbf{x}_{ij}|\, k_{ij}
\end{aligned} \tag{C.2}$$

where $k_{ij} = |\mathbf{k}| \cos\theta_{ij}$ is the projection of the wave vector $\mathbf{k}$ along the satellite separation vector $\mathbf{x}_{ij}$.

Finding the projection of $\mathbf{k}$ on the separation vector between the two satellites places a lower limit on $|\mathbf{k}|$: $-1 \leq \cos\theta < 1$, therefore $-|\mathbf{k}| \leq |\mathbf{k}| \cos\theta < |\mathbf{k}|$. So k_{ij} is a lower limit for $|\mathbf{k}|$.

Eq. C.2 shows how the wave vector projection k_{ij} is related to the phase difference ψ_{ij}. The phase difference between dual satellite measurements can be determined by one of two methods.

The first method involves taking Fast Fourier Transforms (FFTs) of the time series and finding the spectral coherence [Bendat and Piersol, 1986]. The phase difference ψ_{ij} is then taken as the phase of the coherence function. Usual windowing and averaging techniques are employed in calculating the coherence.

The second method involves using Wavelet Transforms (WTs). The phase difference is calculated in a similar manner as above except that the extra information that WTs provide allow a phase difference histogram to be constructed. Inspection of the histogram reveals the phase difference.

Single-satellite measurements

Single satellite measurements are the least useful for determining the wave vector. But even from these measurements an method exists that at least enables an estimate of the wave direction vector $\widehat{\mathbf{k}}$.

The method for determining the wave propagation direction from single satellite measurements involves use of Minimum Variance Analysis (MVA), introduced by Sonnerup and Cahill [1967]. The method requires three-dimensional vector time series measurements and results in a coordinate transformation matrix M whose eigenvectors define a reference frame in which the principal axes correspond to directions of 'Maximum', 'Intermediate' and 'Minimum' variance of vector measurements. The associated eigenvalues indicate how well those directions are defined. Knowledge of the

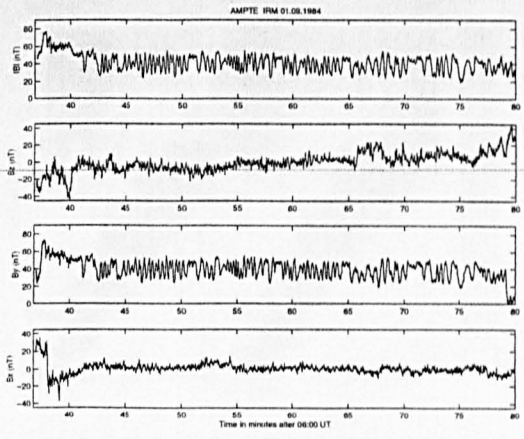

Figure C.1: *IRM* magnetic field measurements 01/09/1984. The plot shows the time interval 06:35 to 07:35 UT. The *AMPTE* satellites were in the magnetosheath in this time interval. *UKS* magnetic field measurements are also available for this time interval. The magnetic field was sampled at a rate of 8 Hz.

eigenvalues and eigenvectors allow the nature of the measured wave to be deduced.

The requirement for having three-dimensional vector measurements means MVA is suitable for magnetic field measurements (flux-gate magnetometers are more than capable to measure the three components of the magnetic field vector) but is not suitable for electric field measurements which generally only consist of the two components of the electric field lying in the satellite spin plane (as extending a boom to measure the third component of the electric field vector perpendicular to the spin-plane of a spin-stabilised satellite causes it to become attitude unstable and so is generally not done).

When it is possible to use MVA there is still the possibility of degeneracy (when some or all the eigenvalues are similar) which compromises the definite determination of the propagation direction [Sonnerup and Schieble, 1998]. This can be dealt with by combining MVA with other complementary analysis techniques [Dunlop et al., 2000, 1995a] but this requires more thought and can be problematic too. Another problem is when waves are propagating in different directions at the same frequency. MVA is unable to distinguish between these directions.

Dual-satellite measurements

Treating each satellite individually the wave direction $\widehat{\mathbf{k}}$ can be estimated using the analysis described above for single satellites, with the enhancement that the $\widehat{\mathbf{k}}$ resulting from MVA on each satellite can be compared to improve (slightly; use of MVA is still suspect) the estimate.

However the main advantage dual satellite measurements have over single satellite measurements is that information about the magnitude of the wave vector, $|\mathbf{k}|$, can be found using the phase differencing technique.

The *AMPTE* satellite mission consisted of dual satellites, *IRM* and *UKS*. Simultaneous magnetic field measurements were taken by each spacecraft. *IRM* measurements of the magnetic field in the magnetosheath on 01/09/1984 are shown in Figure C.1.

Figure C.2 shows the wave dispersion in the magnetic field measured by *IRM*. The figure shows a clear dispersion branch starting from (0,0) and continuing with a phase speed of just under 1 km/s.

There is a $2\pi n$ ambiguity in the phase difference ψ_{ij}, i.e. Eq. C.2 really is $\psi_{ij} = |\mathbf{x}_{ij}|\, k_{ij}/ + 2\pi n$, and this has to be accounted for in determining k_{ij}. The ambiguity can be resolved when using the second WT-based method by plotting the main branch $n = 0$ plus the additional ($n =$

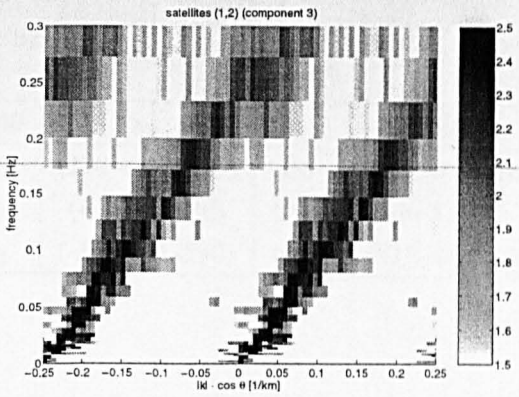

Figure C.2: *IRM* magnetic field wave dispersion 01/09/1984. The time interval 07:05 to 07:15 UT is used for the dispersion calculation.

$\cdots, -2, -1, 1, 2, \cdots$) branches, inspecting the plot, and choosing the main dispersion branch. This is done in Figure C.2. The true dispersion branch is obviously apparent (starting at $k_{ij} = 0$), but the branch apparently starting at k_{ij} = -0.25 km^{-1} is not physical but a manifestation of this phase ambiguity. This advantage over the FFT-based method is the reason for this to be the method of choice in this paper.

Considering the waves at 0.05 Hz the projection on the satellite separation vector can be seen to be $k_{ij} \approx 0.075$ km^{-1}. So for these waves the lower bound on $|\mathbf{k}|$ is 0.075 km^{-1}. This also places an upper bound on the phase velocity for these waves:

$$\begin{aligned} V_{\text{phase}} &= \omega/|\mathbf{k}| = 2\pi f/|\mathbf{k}| \\ &\leq \omega/k_{ij} \\ &\leq 2\pi \cdot 0.05/0.075 \\ &\leq 4.2\text{km/s} \end{aligned}$$

This example uses magnetic field measurements so it is possible to apply MVA to the measurements. The analysis reveals the wave propagation direction $\widehat{\mathbf{k}}$. The scalar product of $\widehat{\mathbf{k}}$ and the known satellite separation direction $\widehat{\mathbf{x}}_{ij}$ gives the cosine of the angle between the two directions $\widehat{\mathbf{k}} \cdot \widehat{\mathbf{x}}_{ij} = \cos\theta_{ij}$. From this the magnitude of the wave vector is determined:

$$|\mathbf{k}| = k_{ij}/\widehat{\mathbf{k}} \cdot \widehat{\mathbf{x}}_{ij}$$

Hence $\mathbf{k}$ is fully determined. It must be again noted that this method for determining the full wave vector has uncertainties involved due to the use of MVA, and that MVA can only be used with three-dimensional vector measurements, which generally excludes electric field measurements.

Multi-satellite measurements

Following the successful launch of the four *CLUSTER II* satellites simultaneous four-point measurements are available enabling, unambiguously, the complete direct determination of the wave propagation direction.

The method is an extension of the dual-satellite method. With four satellites the projection of the wave propagation direction can be found on three independent satellite separation vectors and hence can be completely determined without using MVA. This lifts the restriction that three-dimensional vector measurements are needed; the method can be used with three-component magnetic field measurements and two-component electric field measurements.

Table C.1: *CLUSTER* satellite separations at 14:40 UT. Relative to satellite 1. $\mathbf{x}$ and $|\mathbf{x}|$ are km in GSE coordinates.

14:40	$\mathbf{x}_{ij}$	$\lvert\mathbf{x}_{ij}\rvert$	$\hat{\mathbf{x}}_{ij}$
$\mathbf{x}_{12}$	(200 -540 -305)	650	(0.31 -0.83 -0.47)
$\mathbf{x}_{13}$	(415 60 -470)	630	(0.66 0.10 -0.75)
$\mathbf{x}_{14}$	(-105 -40 -590)	600	(-0.18 -0.07 -0.98)

METHOD

Using the method for dual satellite measurement the dispersion along each of the three separation vectors $\mathbf{x}_{ij}$ (i=1; j=2,3,4) can be calculated. This results in the determination of the projection of $|\mathbf{k}|$ on the basis formed by the satellite separation vectors. It is then a case of transforming these projections to another suitable reference frame.

The GSE coordinate reference frame is chosen. The choice of GSE as a coordinate reference frame for the wave vectors is made arbitrarily. Any other coordinate system could be used, e.g. GSM, as long as the appropriate transformation is made. See Hapgood [1992, 1997] for comprehensive descriptions of transforms between other coordinate systems. The equation relating measurements in the satellite frame to those in the GSE frame for this case is simply a rotation:

$$\mathbf{k}_{\mathrm{GSE}} = R \cdot \mathbf{k}_{\mathrm{sat}} \tag{C.3}$$

$$\mathbf{k}_{\mathrm{sat}} = \begin{bmatrix} k_{12} \\ k_{13} \\ k_{14} \end{bmatrix}$$

$$R = \left[\hat{\mathbf{x}}_{12} | \hat{\mathbf{x}}_{13} | \hat{\mathbf{x}}_{14}\right]$$

where $\mathbf{k}_{\mathrm{sat}}$ is the wave vector in the satellite array reference frame and R represents the transformation from the satellite reference frame to the GSE reference frame, and is simply a matrix with the satellite separation directions as it's columns.

RESULTS

For the purpose of illustrating this MVA-free method for determining wave vectors actual *CLUSTER* electric field measurements are taken and the wave vectors are found for the waves observed. Data for orbit 102 from 21/02/2001 is used.

Overview of Satellite Environment

Figure C.3 shows an overview of the satellite environment for this orbit. The *CLUSTER* satellites cross the magnetosheath considered here after first encountering the magnetopause near 12:00 UT and then crossing the bow shock near 18:00 UT. This time interval clearly includes the magnetosheath crossing as there are magnetic field discontinuities (FGM) and increased magnetic field wave activity (STAFF) at the boundaries along with enhancement of electrons at higher energies (PEACE) inside the interval. The magnetosheath is also expected in this interval from inspection of the orbits of the satellites.

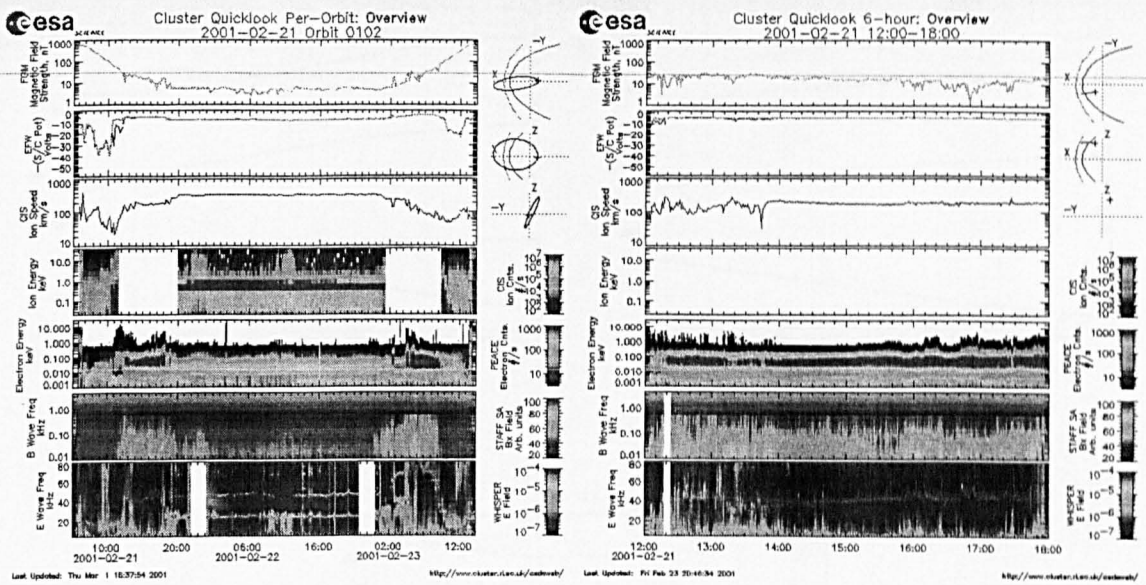

(a) Quicklook per-orbit overview plot for orbit 102 covering the time 21/02/2001 05:00 to 23/02/2001 14:00 UT.

(b) Quicklook 6-hour overview plot for the interval 21/02/2001 12:00 to 18:00 UT.

Figure C.3: *CLUSTER* Quicklook overview plots for orbit 102. Shown in the panels, from the top in each plot, are FGM magnetic field magnitude, EFW -(spacecraft potential), CIS ion speed, CIS ion counts/s, PEACE electron counts/s, STAFF magnetic field spectrum and the WHISPER electric field spectrum. The full satellite orbit can be seen to the upper right in each plot. Plots taken from the CSDS website http://www.cluster.rl.ac.uk/csdsweb/.

Table C.2: *CLUSTER* satellite separations at 15:30 UT. Relative to satellite 1. $\mathbf{x}$ and $|\mathbf{x}|$ are km in GSE coordinates.

15:30	$\mathbf{x}_{ij}$	$\lvert\mathbf{x}_{ij}\rvert$	$\hat{\mathbf{x}}_{ij}$
$\mathbf{x}_{12}$	(225,-580,-310)	695	(0.32,-0.84,-0.45)
$\mathbf{x}_{13}$	(425,80,-500)	660	(0.64,0.12,-0.76)
$\mathbf{x}_{14}$	(-75,-20,-610)	615	(-0.12,-0.03,-0.99)

Table C.3: *CLUSTER* satellite 1 velocity. $\mathbf{V}$ and $|\mathbf{V}|$ are in km/s.

	$\mathbf{V}$	$\lvert\mathbf{V}\rvert$
14:40	(2.1, 0.3, 0.1)	2.1
15:30	(2.0, 0.2, -0.1)	2.0

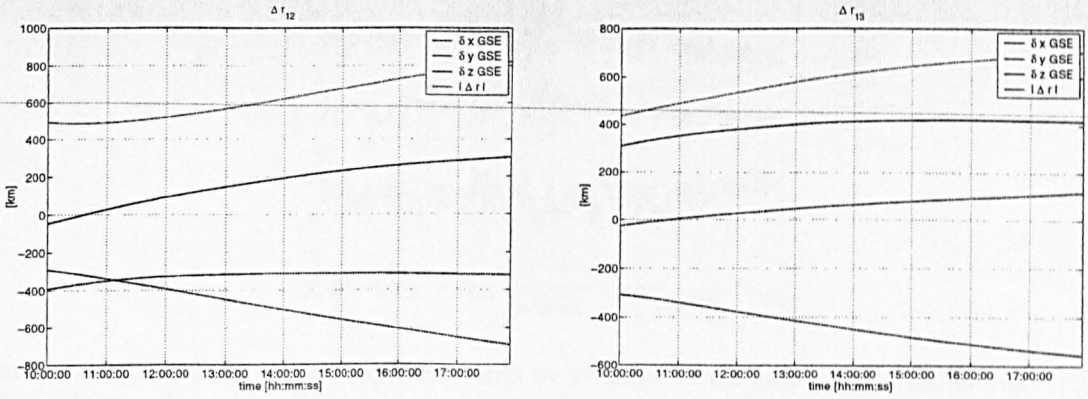

(a) Satellites 1 and 2

(b) Satellites 1 and 3

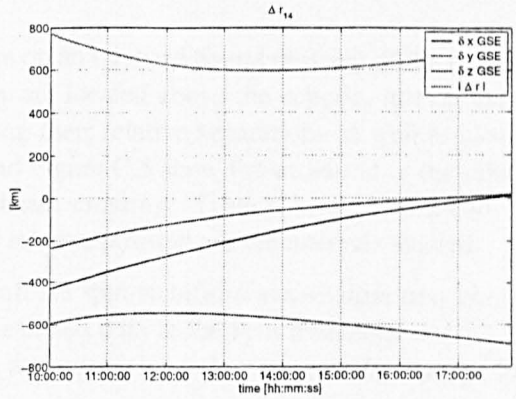

(c) Satellites 1 and 4

Figure C.4: Relative positions of the *CLUSTER* satellites for the interval 10:00 to 18:00 UT on 21/02/2001. The magnitude of the separation is given by the top line. In the first two plots the $\delta x, \delta y, \delta z$ components are (initially) directly below the magnitude, in that order. In the final plot the order is $\delta y, \delta x, \delta z$. Table C.1 and Table C.2 contain details of the intervals studied.

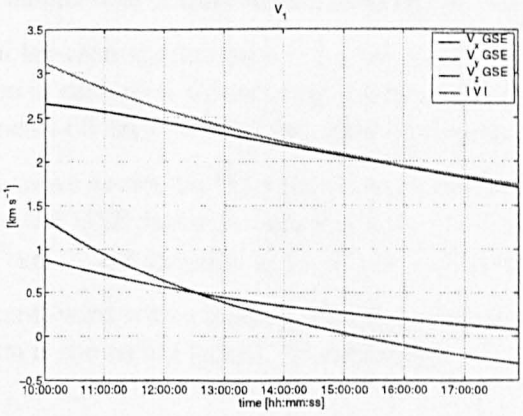

Figure C.5: *CLUSTER* satellite 1 velocity for the interval 10:00 to 18:00 UT on 21/02/2001. The top line is the magnitude of the velocity, followed by (initially) the components V_x, V_z, V_y in that order. Units are km/s. The other satellites will be travelling with very similar velocities which for this interval con be considered the same. Table C.3 contain details of the intervals studied.

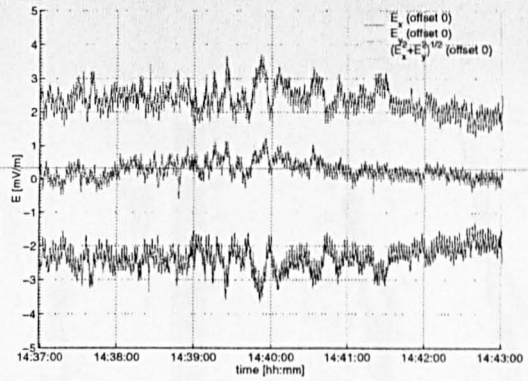

Figure C.6: *CLUSTER* electric field measured by satellite 1 over interval I. From the top, $(E_x^2 + E_y^2)^{1/2}$, E_y then E_x are plotted. Sampling rate 25 Hz.

Satellite positions and velocities

The *CLUSTER* satellites are on an outward bound crossing of the magnetosheath. Looking towards the Earth from the Sun they are located above the ecliptic, just on the dusk flank (Figure C.3(b)). They are gradually increasing their relative separations as well as slowing down as they approach earth apogee. Figure C.4 and Figure C.5 show the evolution of the relative positions and collective velocity over the magnetosheath crossing. Table C.1, Table C.2 and Table C.3 contain details of their collective velocity and relative positions in the intervals studied.

The *CLUSTER* spacecraft are spin-stabilised at a rotation frequency of 0.25 Hz. This may have observable effects on the measured data at the spin frequency and it's harmonics. No spin effects will be apparent in the data at frequencies below the spin frequency. In the following frequencies below 0.2 Hz are studied.

Full hi-resolution (25 Hz) samples of the electric field are available for this magnetosheath crossing. Two specific intervals of electric field measurements are considered.

Interval I: 14:38 to 14:42 UT

The electric field components measured by satellite 1 are shown in Figure C.6. The electric field can be seen to be steady with $\sim$ 1 mV/m oscillations about a slowly varying mean. Although not shown there are visible correlations with electric field measurements from the three other satellites.

The calculated dispersion between satellite pairs ij for i=1; j=1,2,3 are shown in Figure C.7. A dispersion branch can be seen in each plot. Considering waves at 0.13 Hz, the wave vector can be found by reading the components off each plot and then transforming using Eq. C.2.

In the satellite frame the wave vector for 0.13 Hz waves is given by $\mathbf{k}_{\text{sat}} = (-5, -4, 1) \times 10^{-3}$ km^{-1}. Transformed to the GSE frame $\mathbf{k}$ becomes $\mathbf{k}_{\text{GSE}} = (-4.0, 3.7, 3.9)$ km^{-1}, with magnitude $|\mathbf{k}| = 6.2 \times 10^{-3}$ km^{-1} and direction $\widehat{\mathbf{k}} = (-0.81, -0.57, 0.16)$.

This wave is travelling Earth-ward with a dawn-ward and up-out-of-the-ecliptic motion, taking it over the Earth. The direction is shown in Figure C.10 (labelled $\mathbf{k}_{\text{I}}$).

Interval II: 15:28 to 15:32 UT

The electric field components measured by satellite 1 for this second interval are shown in Figure C.8. This interval is 50 minutes later into the orbit where the satellites have moved further through the magnetosheath and are now closer to the bow shock region. In appearance the electric

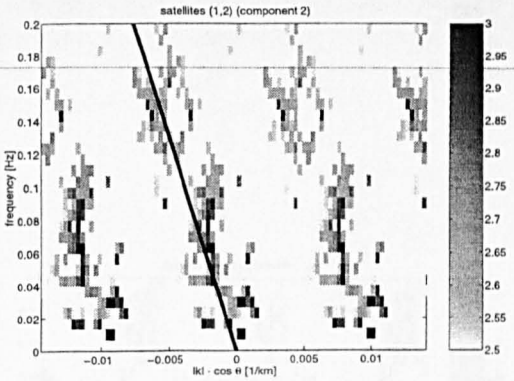

(a) Dispersion along $\mathbf{x}_{12}$. $k_{12} \approx -5 \times 10^{-3}$ km^{-1}.

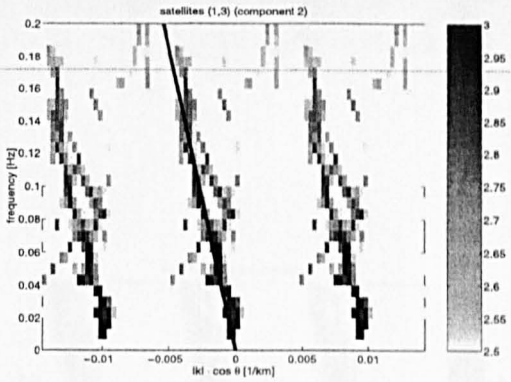

(b) Dispersion along $\mathbf{x}_{13}$. $k_{13} \approx -4 \times 10^{-3}$ km^{-1}.

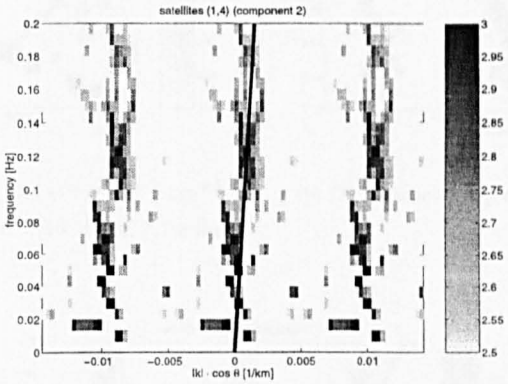

(c) Dispersion along $\mathbf{x}_{14}$. $k_{14} \approx 1 \times 10^{-3}$ km^{-1}.

Figure C.7: Dispersions calculated for interval I. There is one distinctive branch in each of the dispersion plots, indicating the presence of one wave mode. Waves at 0.13 Hz have $\mathbf{k}_{\text{sat}} \approx (-5, -4, 1) \times 10^{-3}$ km^{-1}.

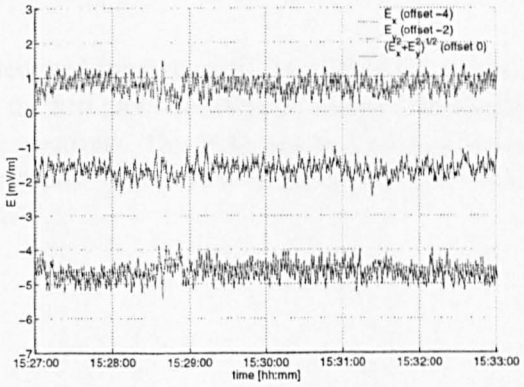

Figure C.8: *CLUSTER* electric field measured by satellite 1 over interval II. From the top, $(E_x^2 + E_y^2)^{1/2}$, E_y then E_x are plotted. Sampling rate 25 Hz.

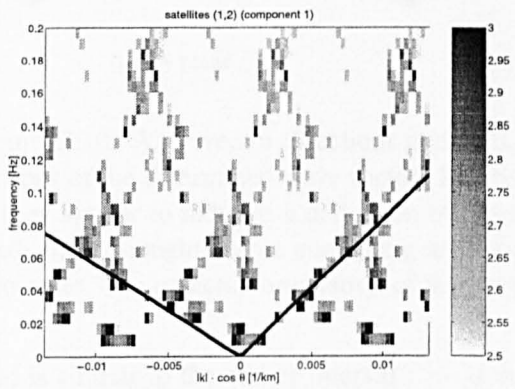

(a) Dispersion along $\mathbf{x}_{12}$. $k_{12} \approx -9 \times 10^{-3}$ km^{-1} for the first branch, and $k_{12} \approx 6 \times 10^{-3}$ km^{-1} for the second branch.

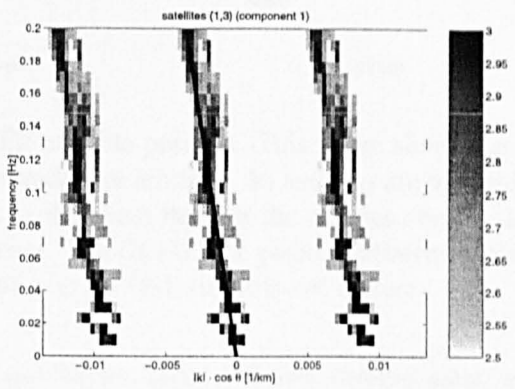

(b) Dispersion along $\mathbf{x}_{13}$. $k_{13} \approx -1 \times 10^{-3}$ km^{-1}.

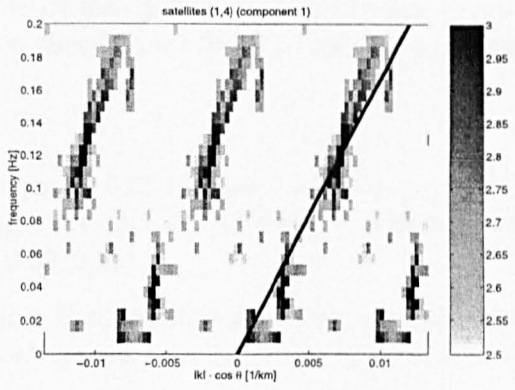

(c) Dispersion along $\mathbf{x}_{14}$. $k_{14} \approx 3 \times 10^{-3}$ km^{-1}.

Figure C.9: Dispersions calculated for interval II. In each of the last two plots there is a clear dispersion branch. However in the first plot two branches can be distinguished, having phase velocities ≈ -5 km/s and ≈ 8 km/s respectively. This indicates the presence of wave modes where waves are propagating in different directions. Waves at 0.05 Hz have $\mathbf{k}_{\text{sat}} \approx (-9, -1, 3) \times 10^{-3}$ km^{-1} and $\mathbf{k}_{\text{sat}} \approx (6, -1, 3) \times 10^{-3}$ km^{-1}.

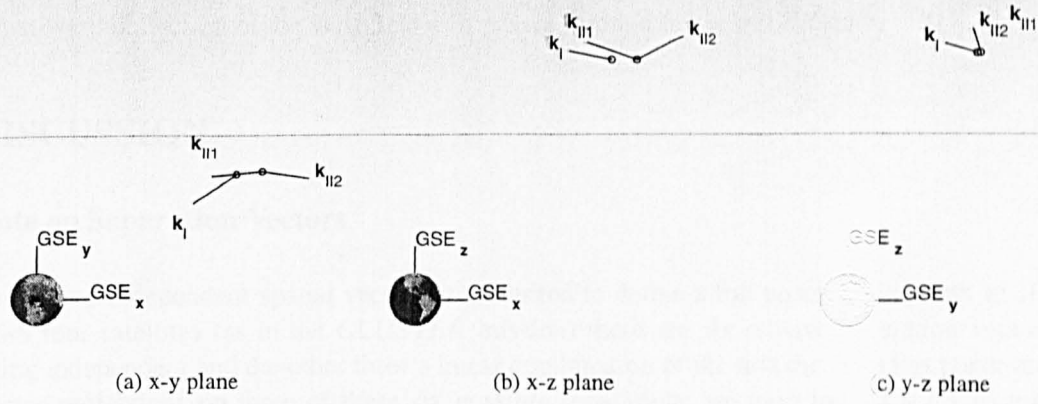

(a) x-y plane (b) x-z plane c) y-z plane

Figure C.10: Wave vector directions at the *CLUSTER* satellite position. This figure shows the directions of the determined wave vectors $\mathbf{k}$. The magnitudes are arbitrary. $\widehat{\mathbf{k}}_I$ and $\widehat{\mathbf{k}}_{II1}$ are interesting as they appear to indicate a deflection of the waves as they pass through the magnetosheath. $\widehat{\mathbf{k}}_{II2}$ needs more thought before attempting an interpretation. The *CLUSTER* position relative to Earth is to scale. The depicted orientation of the Earth relative to the GSE frame is not correct.

field is similar to the earlier interval : $\sim$ 1 mV/m oscillations about a slowly varying mean with visible correlations (not shown) with electric field measurements from the other three satellites.

The calculated dispersions for this interval are shown in Figure C.9. Figure C.9(b) has a clear dispersion branch. Figure C.9(c) also shows a dispersion branch, but with a break near 0.07 Hz. However Figure C.9(a) is more interesting as two branches can be made out, both branches starting at the origin, and identifiable by their phase speeds along this separation as 8 km/s and -5 km/s respectively. The propagation directions are found by considering waves at 0.05 Hz.

First Branch

The satellite frame wave vector for 0.05 Hz waves is $\mathbf{k}_{sat} = (-9, -1, 3) \times 10^{-3}$ km^{-1}. In GSE coordinates this becomes $\mathbf{k}_{GSE} = (-3.9, 7.3, 1.7)$ km^{-1}, with magnitude $|\mathbf{k}| = 9.5 \times 10^{-3}$ km^{-1} and direction $\widehat{\mathbf{k}} = (-0.94, 0.09, 0.31)$.

These waves are travelling Earth-ward, with a dawn-ward and up-out-of-the-ecliptic motion, but less dawn-ward and more upward than the waves in Interval I. The directions are shown in Figure C.10 (labelled $\mathbf{k}_{II1}$).

Second Branch

The satellite frame the wave vector for 0.05 Hz waves is $\mathbf{k}_{sat} = (6, -1, 3) \times 10^{-3}$ km^{-1} . When transformed to GSE coordinates it becomes $\mathbf{k}_{GSE} = (1.0, -5.2, -5.0)$ km^{-1}, with magnitude $|\mathbf{k}| = 6.8 \times 10^{-3}$ km^{-1} and direction $\widehat{\mathbf{k}} = (0.89, -0.13, -0.44)$.

These waves differ significantly from those described previously as they are propagating Sun-ward, but they also posses up-out-of-the-ecliptic and dawn-ward components. The directions are shown in Figure C.10 (labelled $\mathbf{k}_{II2}$).

Summary

A comprehensive interpretation is not possible without knowing in detail other plasma parameters, e.g. the magnetic field and plasma bulk velocity, and is not presented here. however it is interesting to briefly compare the wave directions found in these two intervals. The wave propagation directions

are shown in Figure C.10. $\widehat{\mathbf{k}}_{\perp}$ and $\widehat{\mathbf{k}}_{\parallel\perp}$ are interesting in that they appear to indicate a predominantly dawn-ward deflection of the wavefield as it passes through the magnetosheath.

DISCUSSION

Note on Separation Vectors

Only three independent spatial vectors are required to define a full coordinate system in 3D space. With four satellites (as in the *CLUSTER* mission) there are six relative separation vectors, three being independent and the other three a linear combination of the first three. In this paper only wave vector projections on three of these six possible separations are used to find $\mathbf{k}$. This provides a minimal solution. However the extra information that knowledge of the wave vector projection on the other three dependent separation vectors can be used to increase the accuracy and precision of the wave vector determination. The six independent measurements along the three independent and the three dependent separation vectors form an over-determined system, the solution of which is the wave vector. This way the full information contained in the *CLUSTER* satellite measurements is utilised.

The satellite configuration has a bearing on this wave vector determination, as the separation vectors are used as a basis to measure the wave vector components. For a given wave propagating in a given direction there are obviously preferential directions for measuring the wave. The projection of $\mathbf{k}$ will be maximised for directions $\widehat{\mathbf{x}}_{ij}$ near-parallel to $\widehat{\mathbf{k}}$ and will be virtually zero for directions $\widehat{\mathbf{x}}_{ij}$ near-perpendicular to $\widehat{\mathbf{k}}$. An ideal situation (not only for this analysis but more generally) is the case when the satellite separations $\widehat{\mathbf{x}}_{ij}$ form a mutually orthogonal basis. For the *CLUSTER* mission this is not always the case for all the time. The satellite configuration varies considerably over the full orbit, generally forming a tight configuration at perigee and evolving to a looser configuration at apogee. Each successive orbit precesses about the Earth thus rotating apogee from out in the solar wind to inside the magnetotail. The *CLUSTER* Master Science Plan (MSP), which determines when to measure what, is strongly influenced by the satellite configuration. The magnetosheath is included in the MSP and will be crossed in successive orbits at varying stages in the full orbit and hence with a variety of satellite configurations. In summary ideal configurations are not necessary; but some days *are* better than others.

Note on Doppler shift

Care should be taken when transforming frequencies between reference frames. The frequency observed in the satellite frame will be doppler-shifted when observed in another frame.

$$\begin{aligned} \mathbf{k} &= \mathbf{k}' \\ \omega &= \omega' - \mathbf{k} \cdot \mathbf{V} \end{aligned} \tag{C.4}$$

Eq. C.4 gives the doppler shift formula when transforming waves between reference frames. The wave vector $\mathbf{k}$ is unchanged between reference frames; however the measured frequency ω' is different from rest frame frequency ω by an amount according to $\mathbf{k}$ and the relative velocity $\mathbf{V}$. The measured frequency is less (greater) than the rest frame frequency when the satellites are moving in the same (opposite) direction to the waves, and is not shifted when the satellites are moving perfectly perpendicular to them.

For the intervals presented here the doppler shift is small. $|\mathbf{k}| \sim 10^{-3}$ km^{-1}, $|\mathbf{V}| \sim 10^{0}$ km/s, so $\mathbf{k} \cdot \mathbf{V} \sim 10^{-3}$ Hz or less. However for larger $|\mathbf{k}|$ and greater relative velocities it will become significant.

CONCLUSIONS AND FURTHER WORK

CLUSTER II is the first satellite mission that enables the identification of the dispersion of plasma waves observed in the electric field component. WEC data are self-sufficient for this identification (acknowledging the inclusion of auxilliary data for the satellite positions). FGM data and basic plasma parameters are still needed to form a more meaningful physical interpretation.

Future work will involve a comprehensive study of waves observed in the magnetosheath. The wave vector and it's variations can be found for each magnetosheath crossing of the *CLUSTER II* satellites. Combining these observations for many such crossings will allow an experimentally derived understanding of the plasma waves present.

ACKNOWLEDGEMENTS

I. Bates was funded by EPSRC U.K.

REFERENCES

M. A. Balikhin, T. D. deWit, H. St. C. K. Alleyne, L. J. C. Woolliscroft, S. N. Walker, V. Krasnoselskikh, W. A. C. MierJedrzejeowicz, and W. Baumjohann. Experimental determination of the dispersion of waves observed upstream of a quasi-perpendicular shock. *Geophys. Res. Lett.*, 24(7):787–790, APR 1 1997.

M. A. Balikhin and M. E. Gedalin. Comparative analysis of different methods for distinguishing temporal and spatial variations. In *SP-183 START Conference, Aussois, France, Jan.31-Feb.5*, volume ESA WP-047. European Space Agency, 1993.

M. A. Balikhin, L. J. C. Woolliscroft, H. St. C. K. Alleyne, M. Dunlop, and M. A. Gedalin. Determination of the dispersion of low frequency waves downstream of a quasiperpendicular bow shock. *Annales Geophysicae*, 15:143–151, 1997b.

J. S. Bendat and A. G. Piersol. *Random data - analysis and measurement procedures.* John Wiley and sons, second edition, 1986.

T. D. deWit, V. V. Krasnoselskikh, S. D. Bale, M. W. Dunlop, H. Lühr, S. J. Schwartz, and L. J. C. Woolliscroft. Determination of dispersion-relations in quasi-stationary plasma turbulence using dual satellite data. *Geophys. Res. Lett.*, 22(19):2653–2656, OCT 1 1995.

M. W. Dunlop, T. M. Bauer, B. U. O. Sonnerup, N. Schopke, A. V. Khrabrov, T. Woodward, and A. N. Fazakerley. Dual spacecraft verification of magnetopause orientation and motion: Preliminary results. In *Proceedings of the CLUSTER II Workshop on Multiscale/Multipoint Plasma Measurements*, volume ESA SP-449, pages 103–110. European Space Agency, 2000.

M. W. Dunlop, T. I. Woodward, and C. J. Farrugia. Minimum variance analysis: *CLUSTER* themes. In *Proceedings of the CLUSTER Workshops*, volume SP-371, pages 33–42. ESA, June 1995.

M. A. Hapgood. Space physics coordinate transformations - a user guide. *Planet Space Sci*, 40(5): 711–717, 1992.

M. A. Hapgood. Space physics coordinate transformations: A user guide (vol 40, pg 711, 1992). *Planet Space Sci.*, 45(8):1047, 1997.

B. U. O. Sonnerup and L. J. Cahill. Magnetopause structure and attitude from explorer 12 observations. *Journal of Geophysical Research - Space Physics*, 72:171–183, 1967.

B. U. Ö. Sonnerup and M. Schieble. Minimum and maximum variance analysis. In Götz Paschmann and Patrick W. Daly, editors, *Analysis Methods for Multi-Spacecraft Data*, chapter 8, pages 185–220. International Space Science Institute, 1998.

Appendix D

Identification of Linear and Nonlinear Processes in Space Plasma Turbulence data

(Reprint of Balikhin et al. [2001a]).

M. A. Balikhin, I. Bates, and S. Walker

Department of Automatic Control and Systems Engineering, University of Sheffield, U.K.

ABSTRACT

Experimental data acquired using multi-point measurements of space plasma turbulence enables not only the determination of the composition of the plasma turbulence but also the identification of quantitative characteristics of processes involved in the dynamics of the turbulence. Various data analysis methods that have been developed to extract such information from multi-satellite missions are compared. The advantages and pitfalls of these are discussed.

INTRODUCTION

The ultimate goal of any experimental study of plasma turbulence is to deduce a complete description of the observed turbulence. This includes the composition of the turbulence (i.e. energy distribution among various plasma wave modes), and the identification of linear and nonlinear processes involving energy transfer within the turbulence itself as well as between the turbulence and plasma particles. The development of experimental techniques and data analysis methods, ever since the very first in-situ measurements of space plasma turbulence, are gradually approaching this ultimate goal.

In the beginning, the primary "product" of measurements in space plasma turbulence were power spectra, i.e. energy distribution versus observed frequency. It is impossible to distinguish between spatial and temporal variations using these early single satellite measurements. The inability to determine the Doppler shift means the transformation of the spectra obtained from the satellite frame to the plasma rest frame is not possible. As usual the lack of experimental information stimulated imagination in theoretical studies. In many cases, the observed waves were attributed to various incompatible plasma modes, and were explained by conflicting generation mechanisms proposed in competing theories. For example, the low frequency fluctuations observed in the foot of a supercrit-

ical quasi-perpendicular shock were considered to be either oblique whistler waves (Fairfield, 1974; Balikhin *et al.*, 1987) or lower hybrid waves (Vaisberg *et al.*, 1982). Their generation has been explained by many models including the two-stream instability, the kinetic cross-field instability, nonlinear processes at the shock front, temperature anisotropy and an instability of non-gyrotropic distributions (Tidman and Northrop, 1968; Bertotti and Biskamp, 1969; Sentman *et al.*, 1983; Krasnosel'skikh, 1985; Galeev *et al.*, 1988; Wong and Goldstein, 1988).

The availability of dual satellite observations from the *ISEE* and later *AMPTE* missions enabled the separation of spatial and temporal variations. Using these data sets it is possible to determine not only the frequency of the observed waves in the satellite frame but also the wave vector and frequency in the plasma frame (Hoppe *et al.*, 1982; Balikhin and Gedalin, 1993; Balikhin *et al.*, 1997a, 1997b). Therefore this important ambiguity in the interpretation of experimental data has been removed. A comparison of the dispersion relation of the observed waves and those predicted by the various theoretical models enables us to filter out those models which result in incorrect wave modes. In the particular case of low frequency waves at the foot of a quasi-perpendicular shock the experimentally determined dispersion relation enabled us to exclude various theoretical models, e.g. plasma instability in the ramp (Orlowskii *et al.*, 1995), instability related to a peculiar electron distribution (Sentman *et al.*, 1983), non-gyrotropic proton distribution (Wong and Goldstein, 1988), high electron temperature anisotropy (Wu *et al.*, 1984) and kinetic cross field streaming instability (Wu *et al.*, 1984). It was shown that the only mechanism which does not contradict the observed joint wave vector-frequency spectrum are the models which relate these waves to the nonlinear dynamics of the shock ramp (Tidman and Northrop, 1968; Krasnosel'skikh, 1985). In many cases the choice between competing theories is not so simple and the determination of the dispersion relation does not provide enough information to eliminate all but one of the theories.

For some space plasma regions comprehensive theories of the observed plasma wave turbulence have not, as yet, been elaborated. For these more complex cases a complete model of the turbulence needs to be determined directly from experimental data. This implies that, in addition to the dispersion relations, unstable frequency ranges at which energy is supplied to turbulence via plasma instabilities and quantitative characteristics of wave-wave interactions that re-distribute this energy among various scales of turbulence need to be determined. Multi-point measurements enable the identification of all of these characteristics directly from data.

A review of these data analysis methods is given in the present paper.

DETERMINATION OF WAVE DISPERSION RELATION

A technique to determine the dispersion relation of waves observed in space plasma was proposed by Balikhin and Gedalin (1993). Technical details of this method may be found in Balikhin *et al.* (1997a,b), Chisham *et al.* (1999) and Balikhin *et al.* (2000a).

The basic assumption of this method is that in the plasma rest frame, a wave field can be described as a superposition of plane waves:

$$\vec{B}(\vec{r},t) = \sum_{\omega_{p.f.}} \vec{B}(\omega_{p.f.}) \exp i(\vec{k}\cdot\vec{r} - \omega_{p.f.}t) + C.C., \tag{D.1}$$

where $\vec{B}(\omega_{p.f.})$ is a complex amplitude and $C.C.$ is the complex conjugate term. The plasma frame frequency $\omega_{p.f.}$ and the wave vector $\vec{k}$ are related by the dispersion relation:

$$\vec{k} = \vec{k}(\omega_{p.f.}) \tag{D.2}$$

If two satellites are separated by a vector $\vec{R}$, the phase shift $\Delta\psi$ between the two simultaneously measured time series at an observed frequency ω can be estimated as

$$\Delta\psi(\omega) = \vec{k}(\omega) \cdot \vec{R} = |\vec{k}||\vec{R}| \cos\theta_{\vec{k},\vec{R}} \tag{D.3}$$

Thus the projection of $\vec{k}$ on $\vec{R}$ can be studied by determining the phase shift. In the situation when simultaneous data are available from four satellites and the satellites are in a non-planar configuration it is possible to compute projections of the wave vector onto three independent directions which, when combined, enable the construction of the complete three dimensional wave vector for waves observed in either the magnetic or electric field (Balikhin *et al.*, 2000b). When the magnetic field is observed by a pair of satellites, there are a number of methods that can be used to determine the direction of the wave vector for each spectral component. For an elliptically polarised wave, the most commonly used is the minimum variance method. For linearly polarised waves other methods can be used.

Knowledge of the phase difference together with the direction of the wave vector and the satellite separation vector provides enough information to calculate the wave vector for a particular frequency using Eq. D.3. Morlet wavelet decomposition of both signals can be used to calculate $\Delta\psi(\omega)$ at each data point during the observation interval. The joint spectrum of the observed frequency (ω) and the projection of the wave vector on the satellite separation direction k_R $(= \Delta\psi/|R|$ by Eq. D.3) can then be constructed from the distribution of energy versus frequency and $\Delta\psi$ (which is proportional to k_R). The observed frequency ω, the plasma rest frame frequency $\omega_{p.f.}$ and the wave vector are related by the Doppler equation.

$$\omega = \omega_{p.f.} + \vec{k} \cdot \vec{v_0} \tag{D.4}$$

Eq. D.4 can be used to calculate $\omega_{p.f.}$ and hence the dispersion relations of the observed waves in the plasma rest frame.

Identification of dispersion relations has been performed using this method for waves observed in various regions of space plasma, e.g. at the foot of the quasi-perpendicular shock, downstream of the bow shock, in the inner magnetosheath and elsewhere. We will use the region of the magnetosheath adjacent to the magnetopause studied in Balikhin *et al.* (2000a) (hereafter referred to as B2000) to illustrate the above method. Magnetic field data measured by the *AMPTE* satellites *UKS* and *IRM* in the vicinity of the magnetopause on September 1st, 1984 were used in B2000 to identify the dispersion relation of waves in that region. The three components of the magnetic field together with its magnitude as measured by *IRM* are shown in Figure D.1. The dispersion relation was determined using data from the time interval 7:03:24.5–7:15:00 UT for which simultaneous data from both *UKS* and *IRM* were available. The joint $(\omega, \mathbf{k}_R)$ spectrum of the B_y component is shown in Figure D.2 (k_R is the projection of wave vector on the satellite separation direction). For each frequency, the joint $(\omega, \mathbf{k}_R)$ spectrum shows the distribution of energy as a function of k_R. By using 2-point measurements, we are limited to the determination of the component of the wave vector along the satellite separation vector.

As described above, the knowledge of the propagation direction enables the determination of the magnitude of complete wave vector $|K| = k_R/\cos\theta_{\vec{k},\vec{R}}$. Therefore the dispersion relation for the observed waves in the plasma rest frame using the joint $(\omega, \mathbf{k}_R)$ spectrum can be determined. For that particular case it was shown in B2000 that these waves are almost standing in the magnetopause frame, similar to the MIAOW waves (MIrror And slOW) observed in the results of hybrid simulations (particle ions and fluid electrons) by Omidi and Winske (1995) and the almost standing waves observed in the vicinity of the magnetopause reported by Song *et al.* (1994).

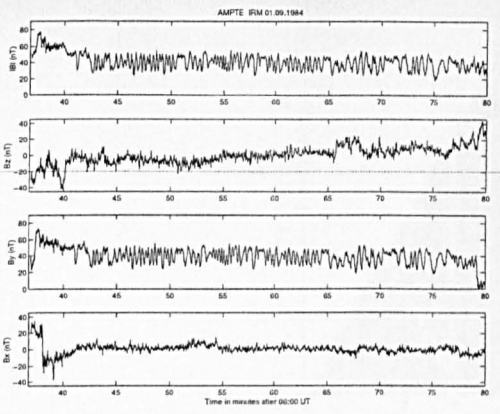

Figure D.1: The magnitude and GSE components of the magnetic field measured by *AMPTE IRM* during the period 06:36-07:20 UT on 1st September 1984.

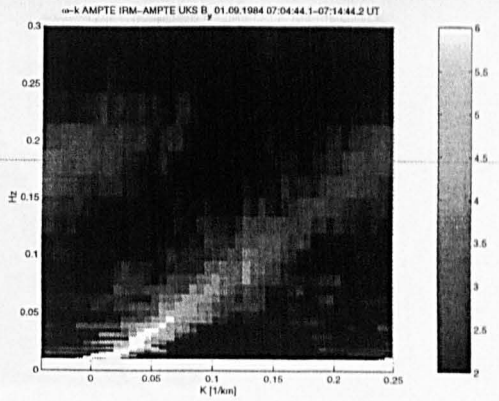

Figure D.2: The joint $(\omega, \mathbf{k}_R)$ spectrum of the B_y component of the magnetic field projected on the maximum variance direction. The spectral magnitude is in arbitrary units plotted on a logarithmic scale. The ridge-like maximum corresponds to the dominant component of the turbulence. The slope of this ridge represents the velocity of the observed wave along the satellite separation direction.

HIGH ORDER COHERENCE BASED METHODS OF NONLINEAR PROCESSES IDENTIFICATION IN SPACE PLASMA TURBULENCE

Techniques based on the estimation of the bi- and tri- coherence have been the main tool for the identification of nonlinear processes in space plasma turbulence. The bicoherence method is based on the resonance conditions for three wave interactions (or for four wave interaction in the tricoherence case). The frequencies and the corresponding wave vectors of waves involved in such an interaction must satisfy resonance conditions in any frame of reference (Sagdeev and Galeev, 1969):

$$\begin{array}{ccccc} \omega_1 & + & \omega_2 & = & \omega_3 \\ \vec{k}_1 & + & \vec{k}_2 & = & \vec{k}_3 \end{array} \tag{D.5}$$

The phases of the interacting waves (denoted by ϕ_i) should also be related:

$$\phi_1 + \phi_2 - \phi_3 = \text{const.} \tag{D.6}$$

If such a phase relation is statistically established then this can be considered an indicator of a nonlinear interaction between the corresponding waves.

The bicoherence function is a tool to validate the phase relation Eq. D.6. Let us consider a real, stationary signal $X(t)$. The bi-spectrum $\mathcal{B}(f_1, f_2)$ of $X(t)$ is defined as:

$$\mathcal{B}(f_1, f_2) = \langle X(f_1) X(f_2) X^*(f_1 + f_2) \rangle$$

where $X(f_i)$ is the Fourier component at frequency f_i; * denotes complex conjugation and brackets denote ensemble averaging. The bicoherence function $b(f_1, f_2)$ is the normalised bi-spectrum (Kim

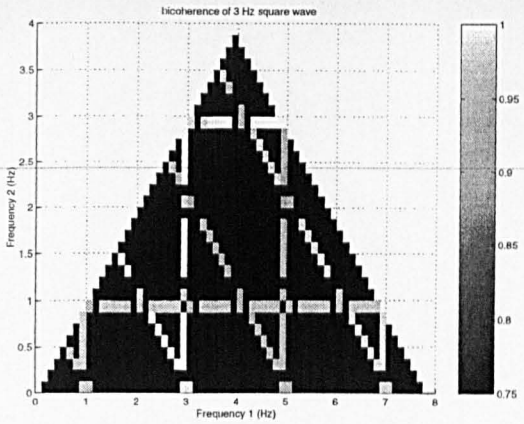

Figure D.3: Bicoherence of a simulated signal $S(t)$ given by $S(t) = 1$ if $2kT < t < (2k+1)T$ and $S(t) = 0$ for all other values of t.

and Powers, 1979):

$$b^2(f_1, f_2) = \frac{|\mathcal{B}(f_1, f_2)|^2}{\langle |X(f_1)X(f_1)X^*(f_1+f_2)| \rangle^2}$$

The normalisation factor used is that of Kravtchenko-Berejnoi *et al.* (1995). The value of the bicoherence function lies between 0 and 1. Values of the bicoherence close to 1 indicate that Eq. D.6 is statistically valid. Values of the bicoherence close to 0 indicate statistical independence of the wave phases and hence absence of any nonlinear interaction between the waves.

In spite of the numerous applications of the bicoherence method to the identification of nonlinear processes in various space plasma regions it has significant disadvantages. One of the effects is related to so called *historical nonlinearities*. Let us assume that as the result of some space plasma process a variation in the electro-magnetic field is generated with a shape that differs from an ideal sine wave, and propagates as a stable wave, without any energy transfer between plasma modes. The phases of the various spectral components which compose such a structure are not independent. Therefore the application of the bicoherence will indicate numerous multi-wave coupling processes which do not take place in reality. It will instead identify the nonlinear process which took place in the past when the wave was generated. The bicoherence is not able to distinguish between this case and processes of energy transfer between scales of turbulence. This was illustrated by Walker *et al.* (2000) (hereafter referred to as W2000) where the application of bicoherence to periodic stationary non-sinusoidal waves has been investigated. Figure D.3 represents a bicoherence calculation for a quasi-periodic square wave $S(t)$ ($S(t) = 1$ if $2kT < t < (2k+1)T$ and $S(t) = 0$ for all other values of t). In such a wave the phases of various spectral harmonics are strongly correlated. This leads to the numerous maxima in the bicoherence which are not related to any energy transfer between scales (see Figure 2 in W2000).

The importance of this effect on the reliability of the results obtained from the application of the bicoherence to space plasma measurements is related to basic satellite on board operations such as the digitisation of signals. Digitisation is itself a nonlinear process which modifies the shape of signals due to the use of finite levels of quantisation. This was tested using as an example the Wide-Band Data (WBD) instrument for *CLUSTER*. The digital output of the analogue waveform is produced by an 8-bit Analogue to Digital Converter (ADC). Within the ADC the main source occurs as a result of the conversion of the continuous analogue signal into a sampled, digitally quantised waveform, essentially generating a composition of various square waves.

To study the effect of digitisation a few independent monochromatic waves were applied as

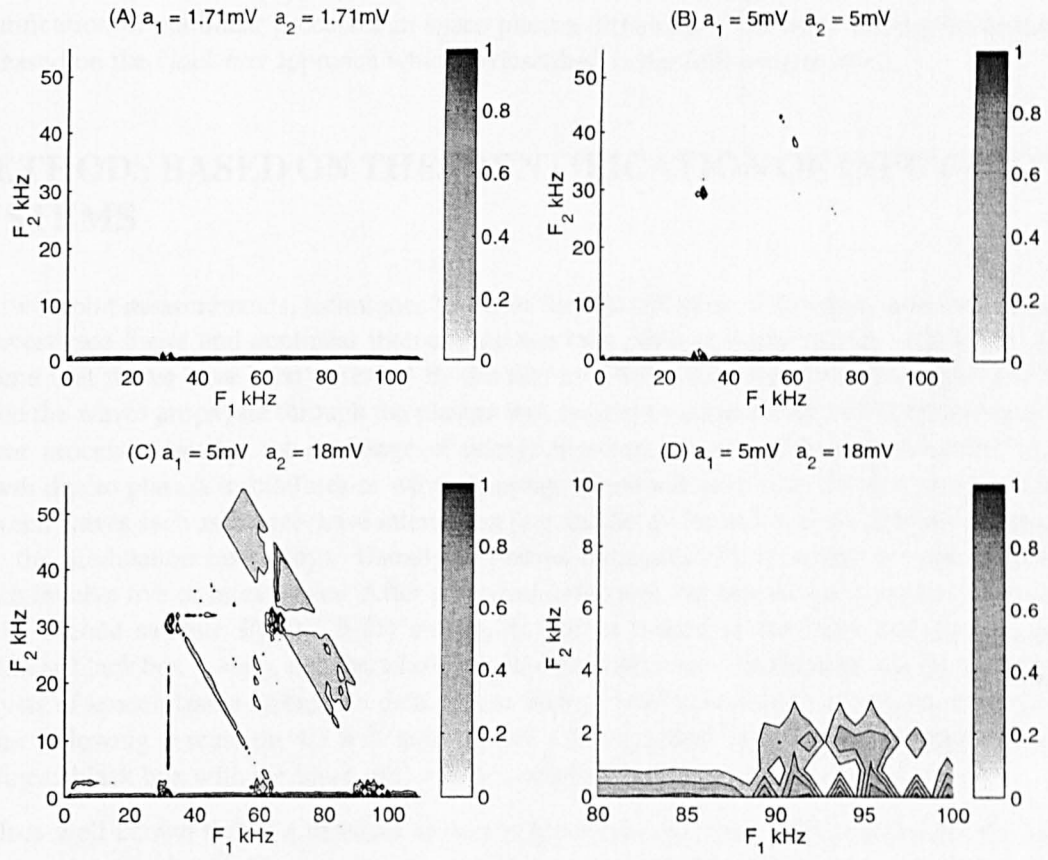

Figure D.4: Bicoherence of the response of the WBD instrument to independent input signals of 30 and 32 kHz with varying amplitudes.

input signals to the WBD electronic unit. The WBD output was analysed using the bicoherence function. Finite quantisation in the ADC led to various artificial maxima on numerous harmonics and beating frequencies, which were absent in the input test signal (W2000). The results of the bicoherence analysis performed by W2000 are shown in Figure D.4. Two monochromatic spectral harmonics at 30 and 32 kHz were applied as input signals to the WBD electronic unit. When both input signal amplitudes are 5 mV, the bicoherence confirms the fact that there is an interaction between the input signals, either generation of the second harmonic or their summation resulting in the frequency peak observed at around 60 kHz (Panel B). Panel C shows the effect when the second input signal amplitude is increased to 18 mV. The higher amplitude makes the evidence for the nonlinear interactions more pronounced. The diagonal structures in these panels represent lines of constant frequency i.e. $f_1 + f_2 \approx 60$ and 90 kHz, corresponding to the interaction of waves with the 2^{nd} and 3^{rd} harmonics of the input frequencies.

In conclusion methods based on the bi- or tri- coherence can not provide reliable results in the identification of nonlinear processes in space plasma turbulence. The other more reliable methods are based on the *black box* approach which is described in the following section.

METHODS BASED ON THE IDENTIFICATION OF INPUT-OUTPUT SYSTEMS

For two-point measurements, techniques based on the identification of dynamic systems can be used to investigate linear and nonlinear interactions that take place in space plasma turbulence. Let us assume that waves have been observed by the first satellite, which measured the waveform $B_1(t)$. While the waves propagate through the plasma they undergo various linear and nonlinear processes. Linear processes involve the exchange of energy between waves and particles resulting in wave growth due to plasma instabilities or wave damping. Nonlinear processes involve energy exchange between waves such as a three wave interaction (e.g. the decay instability) or a four wave interaction (e.g. the modulation instability). Usually in plasma turbulence it is possible to neglect processes which involve five or more waves. After propagation through the plasma the wave field is measured by the second satellite $B_2(t)$. $B_1(t)$ and $B_2(t)$ can be treated as the input and the output of a nonlinear black box system, and the whole machinery of process identification can be applied to the analysis of space plasma turbulence data. Let us make a brief introduction to process identification. In the following discussion we will assume that some physical system can be represented by a nonlinear black box with the input $u(t)$ and output $y(t)$.

It is well known that if a physical system is linear, its evolution is determined by *the impulse response function* $h_1(t)$. The output is thus related to the input through the convolution integral:

$$y(t) = \int_0^\infty h_1(\tau)u(t-\tau)d\tau.$$

The Fourier transform of $h_1(t)$ is *the linear frequency response function* $H_1(f)$ and if $U(f)$ and $Y(f)$ are the Fourier transforms of the input and the output then $Y(f) = H_1(f)U(f)$. Thus the absolute value and the phase of $H_1(f)$ determine the amplification and phase delay of a spectral component at frequency f. Both descriptions, the impulse response function in the time domain and the linear frequency response function in the frequency domain, are equivalent. Thus the output of linear systems is fully determined by the input and either the impulse response function $h_1(t)$ or the linear frequency response function $H_1(f)$.

Volterra decomposition is a generalisation of the convolution integral to nonlinear systems. The Volterra series is given by:

$$\begin{aligned} y(t) &= \int_0^\infty h_1(\tau)u(t-\tau)d\tau \\ &+ \int_0^\infty \int_0^\infty h_2(\tau_1,\tau_2)u(t-\tau_1)u(t-\tau_2)d\tau_1 d\tau_2 + \ldots \\ &+ \int_0^\infty \ldots \int_0^\infty h_i(\tau_1,\ldots,\tau_i)u(t-\tau_1)\ldots u(t-\tau_i)d\tau_1 \ldots d\tau_i + \ldots \end{aligned} \tag{D.7}$$

where each term $h_i(\tau_1,\ldots,\tau_i)$ is referred to as the ith order Volterra kernel. Once all the kernels are known the output of the system is determined and all properties of the system can be investigated analytically. The set of kernels determines the system completely.

For discrete measurements Eq. D.7 takes the form

$$\begin{aligned} y(k) &= \sum_{n_1} h_1(n_1)u_{k-n_1} \\ &+ \sum_{n_1,n_2} h_2(n_1,n_2)u_{k-n_1}u_{k-n_2} + \cdots \\ &+ \sum_{n_1,n_2,\ldots,n_i} h_i(n_1,n_2,\ldots,n_i)u_{k-n_1}u_{k-n_2}\ldots u_{k-n_i} + \cdots \end{aligned} \tag{D.8}$$

The Fourier Transform of Eq. D.8 leads to the equivalent frequency domain representation:

$$Y(f) = H_1(f)U(f) + \sum_{f_1,f_2;f_1+f_2=f} H_2(f_1,f_2)U(f_1)U(f_2) + \cdots \tag{D.9}$$

where $H_l(f_1,f_2,\ldots,f_l)$ are referred to as higher order terms, nonlinear terms or more commonly Generalised Frequency Response Functions (GFRFs). In weak space plasma turbulence this expansion can be truncated after the third term, because nonlinear processes involving five or more waves can be disregarded. $H_1(f)$ is equivalent to the linear frequency response function. The absolute value and phase of $H_1(f)$ determines the amplification and phase delay for each spectral component of the output. The second order kernel $H_2(f_1,f_2)$ is often called the quadratic interaction term and describes the strength of three-wave coupling processes for those waves that satisfy the resonance condition $f_1 + f_2 = f$. Similarly H_3 describe four-wave interactions, etc. The set of all GFRFs completely determine the system.

Both representations of the nonlinear system (Eq. D.7 and Eq. D.8 in the time domain and Eq. D.9 in the frequency domain) are equivalent. Methods for nonlinear system identification can also be subdivided into the frequency and time domains, depending on whether they operate in time space in order to identify the kernels in Eq. D.8 or in frequency space in order to estimate the GFRFs.

It is worth noting that Eq. D.9 also arises naturally in the Hamiltonian formulation of the theory of plasma turbulence. In the framework of the canonical approach, Zakharov (1985) derived explicit expressions for the kernels H_2 and H_3. Such a compatibility between mathematical formulation of plasma turbulence theory and frequency domain Volterra modelling is an important advantage for the application of the latter to the analysis of the experimental measurements of plasma turbulence.

FREQUENCY DOMAIN IDENTIFICATION OF NONLINEAR PROCESSES IN SPACE PLASMA TURBULENCE

The efficiency of three-wave processes in plasma turbulence is proportional to the product of the amplitudes of three waves involved, measured relative to the background field. Similarly the efficiency of four-wave processes is proportional to the product of amplitudes of the four waves involved. When the magnitudes of the waves are less than the background field, it follows that the three-wave processes will be more significant for the evolution of the wave field than four-wave processes which in turn will be more significant than processes involving higher numbers of waves. The resonance

condition for frequencies (Eq. D.5) results from the conservation of energy in the processes of wave coupling. The conservation of momentum in such processes leads to the resonance condition for wave vectors (Eq. D.5). Sometimes resonance conditions for both frequencies and wave vectors cannot be satisfied simultaneously due to the particular dispersion relation. In that case three-wave processes will be forbidden, and four-wave processes will dominate the nonlinear dynamics of the turbulence.

If the turbulent wave field is measured by a pair of satellites ($b_1(t)$ and $b_2(t)$), these measurements can be treated as the input and the output of a dynamic system. The frequency domain relation Eq. D.9 can be applied to the system:

$$\begin{aligned} B_2(f) &= H_1(f)B_1(f) \\ &+ \textstyle\sum_{f_1,f_2;f_1+f_2=f} H_2(f_1,f_2)B_1(f_1)B_1(f_2) \\ &+ \textstyle\sum_{f_1,f_2,f_3;f_1+f_2+f_3=f} H_3(f_1,f_2,f_3)B_1(f_1)B_1(f_2)B_1(f_3) + \cdots \end{aligned} \tag{D.10}$$

where $B_i(f)$ denotes the spectral component of the signal b_i at frequency f. The knowledge of $H_1(f)$ for every observed spectral component, $H_2(f_1,f_2)$ for every possible pair of observed spectral components and $H_3(f_1,f_2,f_3)$ for every triad of observed spectral components determines the quantitative characteristics of all the possible processes which can take place in space plasma turbulence.

If the number of spectral components observed in the signal is N, it is possible to write Eq. D.10 for each spectral component f_i, resulting in a system of N equations for any subinterval of data. $B_k(f_i)$ can be estimated from a spectral transform of the signal b_k. The number of unknown parameters is equal to the number of unknown values for $\{H_j\}$ e.g. for the case where $j = 3$ the unknown GFRFs are H_1, H_2, H_3 and the number of unknown parameters $\approx N + N^2 + N^3 \sim N^3$. Therefore subdividing the whole interval of observations into $\sim N^2$ subintervals and for each subinterval writing a system of N Eq. D.10's allows all the unknown parameters to be found from this huge set of equations. In reality this system possesses a property common to all high dimension linear systems, namely that the solution of such a system is usually an ill-posed problem. Regularisation techniques to find a correct solution require the system to be over-determined, i.e. the necessary number of subintervals should be even larger. To implement such a method in full (i.e with an arbitrary high value for j) the stationary interval of data should be very long to accommodate the high degree of freedom for the unknown parameters. According to my knowledge there is no single example of an application of this method in full to satellite data. However, a simplified truncated version of this approach can be employed in cases where it is possible to neglect the effects of four wave processes on the dynamics of space plasma turbulence i.e. if three wave processes are not forbidden. Neglecting four wave coupling leads to the simplified version of Eq. D.10:

$$B_2(f) = H_1(f)B_1(f) + \sum_{f_1,f_2;f_1+f_2=f} H_2(f_1,f_2)B_1(f_1)B_1(f_2). \tag{D.11}$$

The number of unknown parameters in this model is $\sim N^2$. As a result, only $\sim N$ subintervals of data are required to implement this method to determine H_1 and H_2. There are many regions in space plasma when finding of such an interval of stationary turbulence is not very difficult: magnetosheath, foreshock, magnetotail etc.

Application of frequency domain modelling can be illustrated using an example of *AMPTE UKS* and *AMPTE IRM* data obtained around 14:10 UT on 20th October 1984. The satellites were situated just downstream of the terrestrial bow shock. Three components and the absolute values of the magnetic field measured by *AMPTE IRM* are shown in Figure D.5. The time scale on these figures is seconds after 14:00:00 UT. In the downstream region, the plasma waves observed during

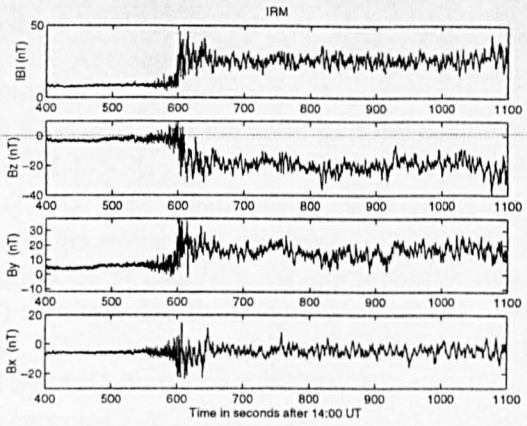

Figure D.5: Magnetic field components and magnitude measured by *AMPTE IRM* on 20th October 1984, from 14:00 UT. The satellite leaves the IMF and crosses the bow shock around 14:10 UT before entering the Earth's magnetosheath.

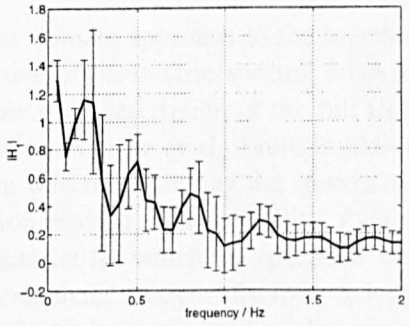

(a) Estimate of the linear GFRF H_1. Frequency regions where $|H_1(f)| > 1$ indicate that the waves are gaining energy by excitation through a plasma instability. Waves with frequencies in the regions where $|H_1(f)| < 1$ are damped and energy is being transferred from the waves to the plasma particles through a plasma instability. From this figure the observed waves are in general damped over all frequencies, exceptions being ranges where $f < 0.1$ Hz and $f \approx 0.25$ Hz.

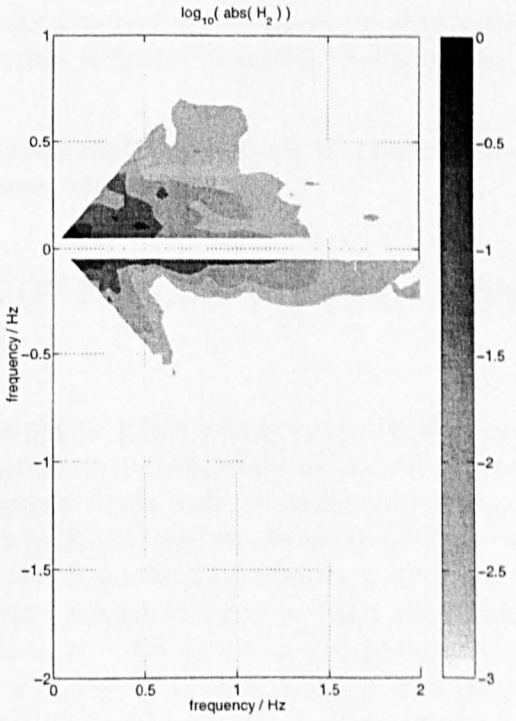

(b) Estimate of the second order GFRF H_2. $|H_2(f_1, f_2)|$ corresponds to the strength of the nonlinear wave coupling between waves f_1, f_2 and their summation frequency $f_1 + f_2$. Frequency regions where $|H_2(f_1, f_2)| > 1$ indicate a strong coupling and that energy is transferred to the summation frequency. Waves in regions where $|H_2(f_1, f_2)| < 1$ are weakly coupled and where $|H_2(f_1, f_2)| \ll 1$ the coupling is not significant. It can be seen that there is strong coupling between low frequency waves up to 0.5 Hz and coupling in other regions is not significant.

Figure D.6: Estimates of GFRF's H_1 (D.6(a)) and H_2 (D.6(b)) using *IRM* data from 20th October 1984 (shown in Figure D.5).

the time interval 650-1100 s have been studied by McCaffrey *et al.* (2000) using frequency domain modelling. The results obtained by these authors are illustrated in Figure D.6. The magnitude of $|H_1|$ is plotted in Figure D.6(a). At frequencies which the waves are unstable, energy is transferred from the plasma to the waves and the magnitude of H_1 will exceed 1. Values of $|H_1|$ less than 1 indicate that linear damping takes place and the turbulence transfers its energy to the plasma. There are frequency ranges where $|H_1| > 1$. The first is at very low frequencies at $f < 0.1$ Hz, and the second around $f \approx 0.25$ Hz. The magnitude of H_2 is plotted in Figure D.6(b). The value of $|H_2(f_1, f_2)|$ corresponds to the strength of nonlinear coupling which transfers energy from the spectral components at frequencies f_1 and f_2 to the summation frequency $f_1 + f_2$. The values of H_2 plotted in Figure D.6(b) correspond to the numerous processes which transfer energy to higher frequencies of up to 0.5 Hz. Thus the physical model of dynamics of this particular interval of plasma turbulence obtained by McCaffrey *et al.* (2000) is that energy is pumped into the plasma due to plasma instabilities at frequencies $f < 0.1$ Hz and $f \approx 0.25$ Hz. This energy is redistributed by three wave processes towards higher frequencies of up to 0.5 Hz.

It is worth noting that truncating the frequency domain Volterra model is only possible when the magnitude of the turbulence is lower than background field, i.e. $\delta B/B_0 < 1$. Only in that case the above considerations for higher efficiency of low order nonlinear processes is valid. As seen in Figure D.5 this is the case for the interval studied by McCaffrey *et al.* (2000). Three components and the magnitude of the magnetic field measured by *AMPTE IRM* on October 30th 1984 in the foreshock are shown in Figure D.7. It can be seen that the amplitude of the waves often exceeds the background field, therefore application of the truncated frequency domain method as used by de Wit *et al.* (1999) is not justified.

If orders of nonlinearity higher than 2 cannot be disregarded then methods of nonlinear process identification which operate in the time domain are more suitable.

TIME DOMAIN IDENTIFICATION OF NONLINEAR PROCESSES IN SPACE PLASMA TURBULENCE

The time domain approach to the identification of nonlinear processes can be described from the perspective of parametric spectral analysis. In this short review paper it is not possible to give a comprehensive description of the full technical intricacies of this method. Such a description can be found in (Boaghe *et al.*, 1999, Balikhin *et al.*, 2001). The discrete Fourier transform is the most common way of estimating the spectra of signals. Often however, parametric methods of spectral estimation provide more reliability. Parametric spectral estimation is based on fitting linear models to the data set for which the spectrum should be estimated. Once the model is fitted the spectrum can be calculated analytically from that model. For example if $y(t_n)$ is a data set representing the output of a linear system with unknown spectra and $u(t_n)$ is the input data set with spectra $U(f)$, the linear Autoregressive Moving Average (ARMA) model can be used to relate these two data sets such that:

$$y(t_n) = \sum_{k=0} A_k u(t_n - k\Delta t) + \sum_{k=1} C_k y(t_n - k\Delta t)$$

The spectrum $Y(f)$ can easily be calculated from the coefficients C_k, A_k and $U(f)$:

$$Y(f) = \frac{\sum_{k=0} A_k e^{-ifk\Delta t}}{1 - \sum_{k=1} C_k e^{-ifk\Delta t}} U(f)$$

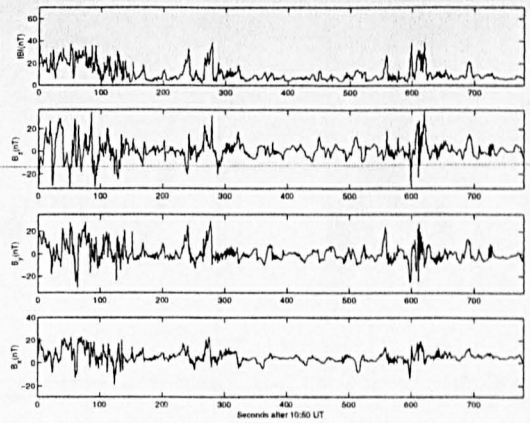

Figure D.7: The magnitude and three GSE components of the magnetic field measured by *AMPTE IRM* during the crossing quasi-parallel part of terrestrial bow shock 30th October 1984 (from Coca *et al.* (2000)).

In practical applications, the Volterra decomposition Eq. D.8 must be truncated to a finite number of terms. Boyd and Chua (1985) concluded that only systems with *fading memory* may be approximated arbitrarily well by truncated Volterra series (see Boyd and Chua (1985) for a precise definition of fading memory systems). Generally speaking, a fading memory system is one in which the dependence on the input decreases rapidly enough with time. The NARMAX (Nonlinear Auto-Regressive Moving Average models with eXogenous inputs) representation is a further generalisation proposed by Leontaritis and Billings (1985a,b):

$$y(k) = F[y(k-1),\ldots,y(k-n_y),u(k-1),\ldots,u(k-n_u),\xi(k-1),\ldots,\xi(k-n_\xi)] + \xi(k) \tag{D.12}$$

where $F[\cdot]$ denotes a nonlinear function and u, y the discrete-time input and output signals. The quantity $\xi(k)$ accounts for possible noise, and uncertainties. The nonlinear function F can be a polynomial, rational function, a set of radial basis functions, wavelet decomposition or any other function. NARMAX models with a finite number of terms can represent a wider class of nonlinear systems than truncated Volterra series. GFRF can be analytically calculated from the NARMAX representation as well as being calculated from the Volterra series. The NARMAX representation of nonlinear systems has sound theoretical foundations (Leontaritis and Billings, 1985a, 1985b, 1987).

Linear models can be fitted using the Least Square Method (LSM) i.e. by minimising the square of the residuals. This approach is not suitable for fitting nonlinear systems, because the number of terms to be fitted grows exponentially with the order of nonlinearity. Instead of LSM so called structure detection and parameter estimation procedures are used to fit Volterra and NARMAX models. Numerous algorithms for structure detection and parameter estimation have been developed (Billings and Chen, 1989; Billings and Voon, 1983; Billings and Zhu, 1994). The structure and parameters in the NARMAX mathematical model can be identified using an orthogonal least-squares algorithm, which searches through all potential model terms and selects the final terms according to the contribution that they make to the variance of the system output. This allows the user to build the simplest possible model using the most significant terms. Model validation techniques are then applied to confirm that the model is adequate. These involve high order correlations which ensure that the residuals are unpredictable from all past values of the input and output (Billings and Zhu, 1994). Once it is proven that the residuals are unpredictable, the time domain model can be used for physical analysis.

This can be illustrated using the example of Coca *et al.* (2000) (hereafter we will refer to this paper as Coca2000). In this paper Volterra models are applied to the analysis of developed turbulence in the terrestrial foreshock as measured by *AMPTE UKS* and *AMPTE IRM* on 30th October 1984.

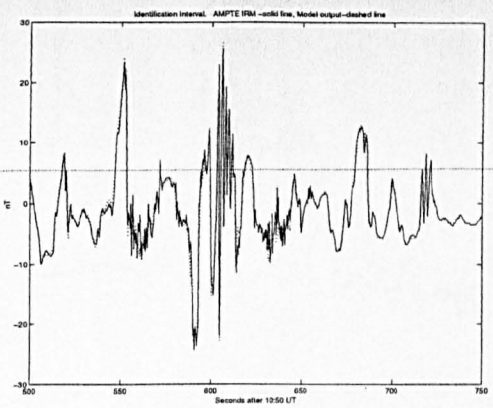

Figure D.8:

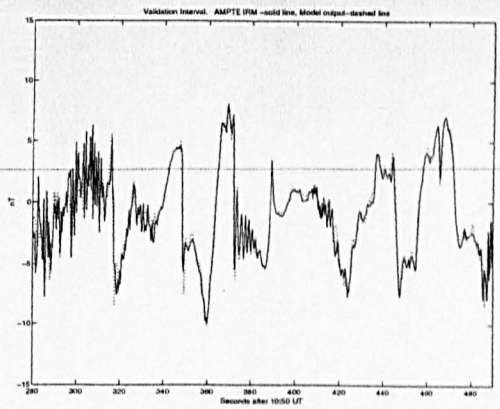

Figure D.9:

The magnitude and three components of the magnetic field measured by the *AMPTE IRM* magnetometer are shown in Figure D.7 (from Coca2000). The two main components of the turbulence in this interval are nonlinear waves known as Short Large Amplitude Magnetic Structures (SLAMS) and smaller amplitude ULF waves (Schwartz *et al.*, 1992). Wave-trains are often observed to be attached to SLAMS. As the convected waves were first encountered by *AMPTE UKS* and then by *AMPTE IRM*, *AMPTE UKS* data were considered to be the input and *AMPTE IRM* data the output of the system, respectively. Only 1000 pairs data points were used to identify the model. The possibility of applying this method of identification to such short data intervals represents the greatest advantage of the time domain technique in comparison with frequency domain methods.

In addition to the nonlinear correlations tests, model validation also can be done by considering the performance of the identified model as a predictor. This complementary type of validation was used by Coca2000. The idea of this method is to "fit" the identified model to the input data (i.e. *AMPTE UKS* measurements of the B_y component) and to compare the output of the model with the measured values of the real output (i.e. *AMPTE IRM* measurements of B_y component).

Such a comparison is shown in Figure D.8 and Figure D.9 from Coca2000 both for the data interval which was used to identify the model (Figure D.8) and outside this interval (Figure D.9). In these figures B_y measured by *AMPTE IRM* is plotted as solid line and output of identified model is plotted as a dotted line. Good performance of the identified model outside of the identification interval was used by Coca2000 as additional validation of the model.

Their model can be expressed as a superposition of linear y_l, quadratic y_q, cubic y_c etc. terms i.e.:

$$y(t) = y_l(t) + y_q(t) + y_c(t) + \cdots$$

therefore the contribution of each term can be assessed separately, to analyse the processes involved in the dynamics of nonlinear waves in more detail.

The superposition of different terms for one of the SLAMS studied by Coca2000 is plotted in Figure D.10. The B_y component (GSE) of the magnetic field measured by *AMPTE IRM* (solid line), the output of the identified model (dotted line), and the output of the linear (dashed-dotted line) and nonlinear (dashed line) contributions of the model derived for one of the the SLAMS are shown. It can be seen from Figure D.10 that the dynamics of SLAMS can be represented by the linear part of the model everywhere except at the upstream edge where the contribution from nonlinear processes is important. This conclusion is in accordance with the common point of view that nonlinear processes of multi-wave coupling are involved in the steepening of waves of finite amplitude.

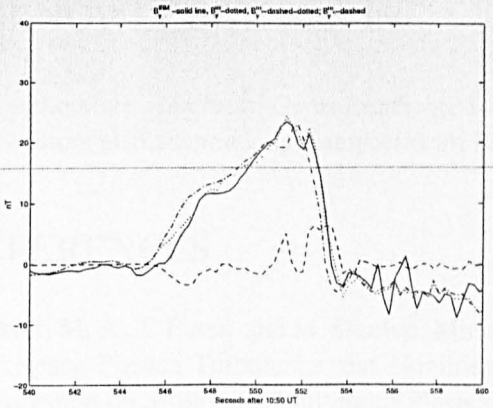

Figure D.10: Various contributions to the wave field of one of the SLAMS. The B_y component (GSE) of the magnetic field measured by *AMPTE IRM* (solid line), output of the identified model (dotted line), output of the linear (dashed-dotted line) and nonlinear (dashed line) contributions (from Coca *et al.* (2000)).

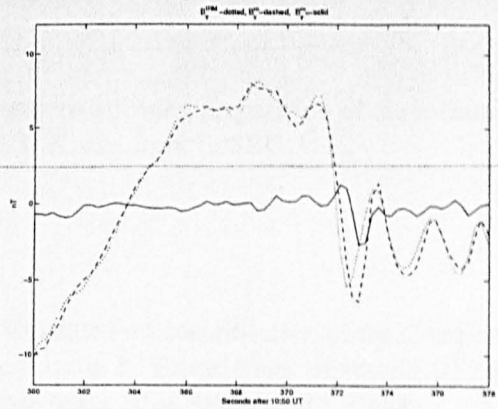

Figure D.11: Various contributions to the wave field for another SLAMS. The B_y component (GSE) of the magnetic field measured by *AMPTE IRM* (dotted line), output of the identified model (dashed line) and nonlinear contribution to the dynamics (solid line) (from Coca *et al.* (2000)).

The superposition of contributions for another SLAMS is plotted in Figure D.11. In this case the ULF wave-train is attached to the SLAMS on to the upstream edge. Again the linear part of the model can represent the wave field for the SLAMS and for the attached wave-train. The contribution of the nonlinear part (solid line) is negligible everywhere except at the interface between SLAMS and wave-train.

The explicit form of the Volterra model enables the calculation of all the orders of GFRF analytically. The magnitude of H_1 (linear part of GFRF) has been calculated from Coca2000. At lower frequencies which correspond to the SLAMS, the magnitude of $|H_1|$ exceeds 1 indicating the frequency range in which energy is transferred to the turbulence from the plasma via instabilities. At higher frequencies which correspond to the wave-trains, the values of $|H_1|$ are less than 1 revealing that damping of the waves occurs at these frequencies with the transfer of energy to the plasma. This enabled Coca2000 to derive a model for the evolution of foreshock turbulence which is in perfect accordance with theory. These theories concluded that plasma instabilities transfer energy to the frequency range which corresponds to SLAMS, resulting in the wave growth. Once these waves reach some finite amplitude nonlinear processes start to affect their dynamics. These nonlinear processes result in the steepening of the upstream edge of SLAMS. In the frequency domain, steepening can be represented as multi-wave coupling which results in the generation of higher harmonics. If some of these higher harmonics have spatial-temporal characteristics in the vicinity of any eigen plasma wave mode, this wave growth forms a wave-train (Sagdeev and Galeev, 1969). The magnitude of H_1 indicates that a wave-train transfers energy back to the plasma, removing energy from the SLAMS, which limits their growth.

SUMMARY

Analysis based on high order coherence functions cannot provide the same level of reliability as methods based on the identification of input-output models. Frequency domain identification of input-output models is easier to perform but it requires unrealistically long intervals if inclusion of cubic or higher terms is necessary. Time-domain identification requires short intervals $\sim$ 1000 points, however the technique of structure detection is more complex than techniques used in the frequency domain identification.

ACKNOWLEDGEMENTS

The authors are grateful to Carol Heathcote for discussions affecting preparation of the manuscript. The authors also acknowledge support from PPARC, U.K. and from EPSRC, U.K.

REFERENCES

Balikhin M. A., I. Bates, and M. Dunlop, Minimum Variance Free Identification of the Composition of Space Plasma Turbulence and Nonlinear Processes in it, Proceedings of the *CLUSTER II* Workshop on Multiscale/Multipoint Plasma Measurements, ESA **SP-449**, 287, 2000b.

Balikhin M. A., T. Dudok de Wit, L. J. C. Woolliscroft, S. N. Walker, H. St. C. K. Alleyne, V. Krasnosel'skikh, W. A. C. Mier-Jedrzejowicz, and W. Baumjohann, Experimental Determination of the Dispersion of Waves observed upstream of a Quasi–Perpendicular Shock, *Geophys. Res. Lett.*, **24**, 787-790, 1997a.

Balikhin M. A., and M. A. Gedalin, Comparative Analysis of Different Methods for Distinguishing Time of Temporal and Spatial Variations, Proceedings of START Conference, ESA **WPP-047**, 183–187, 1983.

Balikhin, M. A., S. Schwartz, S. N. Walker, H. St. C. K. Alleyne, M. Dunlop, and H. Lühr, Dual Spacecraft Observations of Standing Waves in the Magnetosheath, *J. Geophys. Res.*, in press, 2000a.

Balikhin M. A., Vinogradova T. V., Volkomirskaya L. *et al.*, Nonlinear Wave Dynamics in front of a Strong Shock, Proceedings of the International Workshop on Collisionless Shocks, Balatonfured, 210, 1987.

Balikhin M. A., L. J. C. Woolliscroft, H. St. C. K. Alleyne, M. Dunlop, and M. A. Gedalin, Determination of the Dispersion of Low Frequency Waves Downstream of a Quasi-Perpendicular Collisionless Shock, *Annales Geophysicae*, **15**, 143–151, 1997b.

Bertotti B., and D. Biskamp, Proceedings of a Study Group on *Collision Free Shocks in the Laboratory and Space*, held at ESPRIN, Frascati, Italy, ESPRO Spec. Pap. **SP-51**, 41, 1969.

Billings, S. A., and S. Chen, Extended Model Set, Global Data and Threshold Model Identification of Severely Nonlinear Systems, *Int. J. Control*, **50**, 1897-1923, 1989.

Billings, S. A., and W. S. F. Voon, Structure Detection and Model Validity Tests in the Identification of Nonlinear Systems, *IEE Proceedings*, **130**, 4, 193-199, 1983.

Billings, S. A., and Q. M. Zhu, Nonlinear Model Validation using Correlation Tests, *Int. J. Control*, **60**, 1107-1120, 1994.

Boaghe, O. M., M. A. Balikhin, S. A. Billings, and H. St. C. K. Alleyne, An Identification of Nonlinear Processes in the Magnetospheric Dynamics and Forecasting of D_{st} Index, Research Report 671, ACSE, Sheffield University (Submitted to J. Geophys. Res.), 1999.

Boyd S., and Chua L. O., Fading Memory and the Problem of Approximating Nonlinear Operators with Volterra Series, *IEEE Trans. Circuit Syst.*, **32 (11)**, 1150–1161, 1985.

Chisham G., S. J. Schwartz, Balikhin M. A., and M. Dunlop, AMPTE observations of mirror mode waves in the magnetosheath: Wavevector determination, *J. Geophys. Res.*, **104 (A1)** 437–447, 1999.

Coca *et al.*, Time Domain Identification of Nonlinear Processes in Space Plasma, Proceedings of the *CLUSTER II* Workshop on Multiscale/Multipoint Plasma Measurements, ESA **SP-449**, 111–118, 2000.

de Wit T. D., V. V. Krasnosel'skikh, T. Dunlop, and H. Lühr, Identifying Nonlinear Wave Interactions in Plasmas using Two-point Measurements: A Case Study of Short Large Amplitude Magnetic Structures (SLAMS), *J. Geophys. Res.*, **104 (A8)**, 17079–17090, 1999.

Fairfield D. H., Whistler Waves Observed Upstream from Collisionless Shock, *J. Geophys. Res.*, **79,** 1368, 1974.

Hoppe M. M., C. T. Russell, L. A. Frank, T. E. Eastman, and E. W. Greenstadt, Characteristics of the ULF Waves associated with Upstream Ion Beams, *J. Geophys. Res.*, **87**, 643, 1982.

Galeev A., V. V. Krasnosel'skikh, and V. Lobzin, Fine Structure of the Front of a Quasi-Perpendicular Supercritical Collisionless Shock Wave, *Sov. J. Plasma Phys.*, **14**, 697, 1988.

Kim, Y. C., and E. J. Powers, Digital Bispectral Analysis and its Application to Nonlinear Wave Interactions, *IEEE Trans. Plasma Sci.*, **PS-7**, 120, 1979.

Krasnosel'skikh V. V., Nonlinear Motions of a Plasma across a Magnetic Field, *Sov. Phys. Jetp*, **62**, 282, 1985.

Kravtchenko-Berejnoi V., V. Krasnosel'skikh, D. Mourenas, and F. Lefeuvre, Higher-order spectra and analysis of a non-linear dynamic model, *CLUSTER* Workshops, ESA **SP-371**, 61–67, 1995.

Leontaritis, I. J., and S. A. Billings, Input-Output Parametric Models for Nonlinear Systems, Part I: Deterministic Nonlinear Systems, *Int. J. Control*, **41**, 309-328, 1985a.

Leontaritis, I. J., and S. A. Billings, Input-Output Parametric Models for Nonlinear Systems, Part II: Stochastic Nonlinear Systems, *Int. J. Control*, **41**, 329-344, 1985b.

Leontaritis, I. J., and S. A. Billings, Model Selection and Validation Methods for Nonlinear Systems, *Int. J. Control*, **45**, 311-341, 1987.

McCaffrey D., I. Bates, M. Balikhin, H. St. C. K. Alleyne, and M. Dunlop, Experimental Method for Identification of Three Wave Coupling in Space Plasma, *Adv. Space Res.*, **25(7-8)**, 1571-1577, 2000.

Omidi, N., and D. Winske, Structure of the Magnetopause Inferred from One Dimensional Hybrid Simulations, *J. Geophys. Res.*, **100**, 11935-11955, 1995.

Orlowskii, D. S., C. T. Russell, D. Krauss-Varban, N. Omidi, and M. F. Thomsen, Damping and Spectral Formation of Upstream Whistlers, *J. Geophys. Res.*, **100**, 17117–17128, 1995.

Sagdeev, R. Z., and A. A. Galeev, Nonlinear Plasma Theory, Benjamin, *White Plains, N.Y. p.6.* 1969.

Schwartz S. J., D. Burgess, W. P. Wilkinson, R. L. Kessel, M. Dunlop, and H. Lühr, Observations of Short Large-Amplitude Magnetic-Structures at a Quasi-Parallel Shock, *J. Geophys. Res.*, **97**, 4209–4227, 1992.

Sentman D. D., M. F. Thomsen, S. Peter Gary, W. C. Feldman, and M. M. Hoppe, The Oblique Whistler Instability in the Earth's Foreshock, *J. Geophys. Res.*, **88,** 2048, 1983.

Song, P., C. T. Russell, and S. P. Gary, Identification of Low-Frequency Fluctuations in the Terrestrial Magnetosheath, *J. Geophys. Res.*, **99**, 6011, 1994.

Tidman D. A., and T. G. Northrop, Emission of Plasma Waves by the Earth's Bow Shock, *J. Geophys. Res.*, **73,** 1543, 1968.

Vaisberg, O. L., A. A. Galeev, S. I. Klimov, M. N. Nozdrachev, A. N. Omelchenko, and R. Z. Sagdeev, Investigation of Energy Dissipation Mechanism in Collisionless Shock Waves with High Mach Number, *Lett. to JETP*, **35**, 1, 25, 1982.

Walker, S. N., R. Huff, and M. A. Balikhin, An Investigation into Instrumental Nonlinear Effects, Proceedings of the *CLUSTER II* Workshop on Multiscale/Multipoint Plasma Measurements, ESA **SP-449**, 279–282, 2000.

Wu C. S., D. Wiske, Y. M. Zhou, S. T. Tsai, P. Rodriguez, M. Tanaka, K. Papadopulos, K. Akimoto, C. S. Lin, M. M. Leroy, and C. C. Goodrich, Microinstablitites Associated with a High Mach Number, Perpendicular Bow Shock, *Sp. Sci. Rev.*, **37**, 63, 1984.

Wong H. K., and M. L. Goldstein, Proton Beam Generation of Oblique Whistler Waves, *J. Geophys. Res.*, **93,** 4110, 1988.

Zakharov, V. E., S. L. Musher, and A. M. Rubenchik, Hamiltonian Approach to the Description of Nonlinear Plasma Phenomena, *Phys. Reports*, **129(5)**, 285–366, 1985.